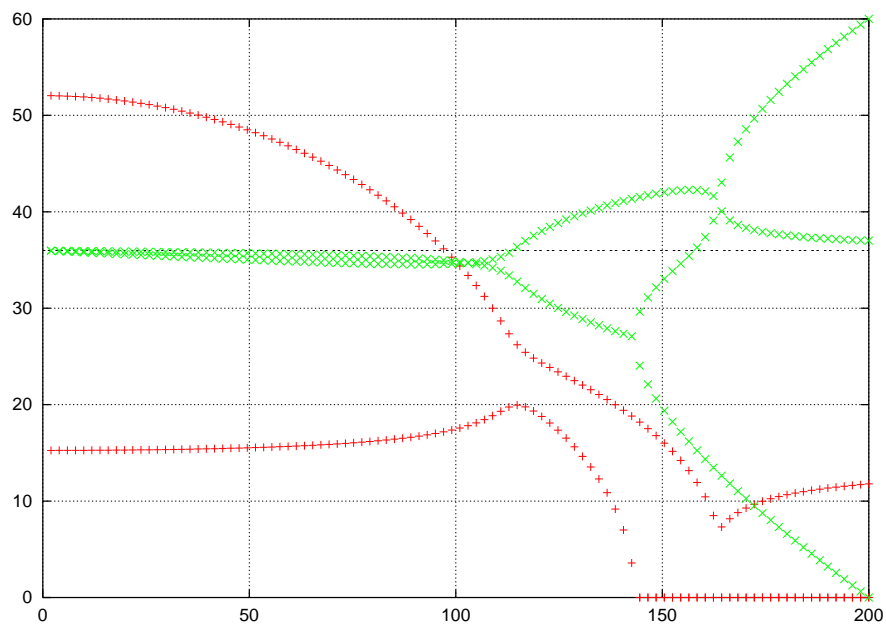


AE4930 Aeroelasticity



S. J. Hulshoff
HSL 0.36, Aerodynamics Group
Faculty of Aerospace Engineering, TU Delft
S.J.Hulshoff@TUDelft.NL

Version 11.1

Contents

1	Introduction	9
1.1	Background	9
1.2	Course Outline	11
1.3	Additional Course Information	13
1.3.1	Course format:	13
1.3.2	Prerequisite Concepts	14
1.3.3	Main References	14
1.3.4	Instructor Contact	14
1.4	Characteristics of Aeroelastic Problems	15
2	Simplified Aeroelastic Problems	21
2.1	The Typical Section	21
2.1.1	Simple Aerodynamic Models	24
2.1.2	Equations of motion for the typical section	25
2.1.3	Torsional Divergence	25
2.1.4	Control Reversal	27
2.1.5	Flutter of a Typical Section	28
2.1.6	Solution of the equations of motion	30
2.1.7	Mode Shapes	34
2.1.8	Conditions which determine the types of motion	34
2.1.9	Pines' Conditions for flutter	36
2.1.10	The effect of a low-frequency aerodynamic model	37
2.2	The Semi-Rigid Wing	39
2.2.1	Equations of motion for the Semi-rigid wing	40
2.3	Propeller Whirl Flutter	41
2.3.1	A Simplified model	42
2.3.2	Gyroscopic Coupling	43
2.3.3	Aerodynamic Coupling	43
2.4	Practice Problems	44
3	Unsteady Aerodynamics	47
3.1	Vorticity Dynamics	47
3.2	Compressibility effects	52
3.3	Viscous effects	54

3.4	Model Equations for Unsteady Flows	59
3.4.1	Navier-Stokes Equations	59
3.4.2	Boundary-Layer Equations	62
3.4.3	Euler Equations	63
3.4.4	Full Potential Equations	63
3.4.5	Small-Disturbance Potential Equation	65
3.4.6	Linear Potential Equation	66
3.5	Analytic Solutions	67
3.5.1	Incompressible Flows	67
3.5.2	Subsonic Compressible Flows	67
3.5.3	Transonic Flows	67
3.5.4	Supersonic Flows	67
3.6	Practice Problems	69
4	Analytic Solutions for Incompressible Flows	71
4.1	Problem definition	72
4.2	Far-Field Perturbation	73
4.3	Velocities on the $z = 0$ plane	73
4.4	Flow Tangency	75
4.5	Pressure Jump Across the Wake	75
4.6	Kutta Condition using Kelvin's Theorem	76
4.7	Harmonic Solutions	77
4.8	Harmonic Pitch and Plunge solutions	79
4.9	Indicial Response (Wagner's Function)	82
4.10	Vertical Step Gust Response (Küssner's Function)	83
4.11	Practice Problems	84
5	Analytic Solutions for Subsonic Compressible Flows	87
5.1	Steady Flow: The Prandtl-Glauert Correction	87
5.2	Unsteady Harmonic Solutions for $M < 1$	88
5.3	Piston theory	89
5.4	Indicial Responses for $M < 1$	92
5.5	Practice Problems	94
6	Analytic Solutions for Supersonic Flows	95
6.1	Problem definition	96
6.1.1	General approach:	97
6.2	Time Integration Limits	98
6.3	Spatial Integration Limits	99
6.4	Potential induced by the airfoil	99
6.5	Normal velocity at the Airfoil	100
6.6	Flow-Tangency Condition	101
6.7	Solutions for Harmonic Motion	101
6.8	Finite wings, Multiple Surfaces	102
6.9	Practice Problems	105

7	Arbitrary Unsteady Aerodynamic Responses	107
7.1	Indicial and Impulse Functions	108
7.2	Fourier Transforms	109
7.2.1	Computation of an arbitrary response	109
7.2.2	Re-expression of the incompressible results	109
7.2.3	Conversion to an Indicial response	110
7.2.4	Conversion from an Indicial response	111
7.3	State-Space Representations	111
7.4	Practice Problems	111
8	Compact Models of Structural Systems	113
8.1	Generalised Coordinates	114
8.2	Lagrange's Equations of Motion	115
8.3	Lagrange's Equations for a Flexible Aircraft	117
8.3.1	Options for efficient treatment	118
8.4	Methods for Constructing Compact Models	119
8.5	Lumped Parameter Method	120
8.5.1	Example Application	120
8.6	Rayleigh-Ritz (Assumed Mode) Method	122
8.6.1	Example Application	123
8.7	Practice Problems	125
9	Flutter Calculation Methods	127
9.1	Non-dimensionalisation	128
9.2	k method	129
9.2.1	Procedure	129
9.3	p-k method	131
9.3.1	Procedure	132
9.4	p method	133
9.5	Practice Problems	134
10	Dynamic Responses	135
10.1	Types of Dynamic Response problems	136
10.2	Dynamic Response Equations	136
10.3	Solution in the frequency domain: Fourier Transform	138
10.4	Solution in the time domain: Numerical Integration	139
10.5	Stochastic Response Analysis - PSD Technique	141
10.6	Practice Problems	145
11	Introduction to Computational Aeroelasticity	147
11.1	Treatment of CA	148
12	Computational structural dynamics	151
12.1	Rayleigh-Ritz finite-element formulation	152
12.2	Example: Formulation for an axially-loaded rod	153
12.3	Solution of the equations of motion	155

12.4 Numerical Integration multi-DOF systems	157
12.5 Newmark method	157
12.6 Efficient integration using modal superposition	158
12.7 Practice Problems	160
13 Computational Methods for Unsteady Flows	161
13.1 Linearised potential equation	163
13.1.1 Kernel-function method	163
13.1.2 Panel Methods	165
13.2 Small-disturbance potential equation	167
13.3 Euler and Navier-Stokes equations	168
13.4 Discretisation of the Euler and Navier Stokes equations	170
13.4.1 Semi-discrete approach	170
13.4.2 Fully-discrete approach	171
13.5 Dealing with moving meshes	171
13.5.1 The Geometric Conservation Law (GCL)	172
13.5.2 The Discrete Geometric Conservation Law (DGCL)	173
13.6 Example: A semi-discrete finite-difference method	173
13.6.1 Enforcing the DGCL (optional section)	175
13.7 Example: A semi-discrete finite-volume method	175
13.7.1 Enforcing the DGCL (optional section)	176
13.8 Example: A semi-discrete finite-element method (optional section)	177
13.9 Example: A space-time finite-element method (optional section)	178
13.10 Discretisation Error Analysis	180
13.10.1 Grid convergence studies	181
13.11 Phase and Amplitude Error Analysis	182
13.11.1 Adjoint-based error estimation	185
13.12 Example Unsteady Flow Solutions	186
13.13 Practice Problems	190
14 Computing Fluid-Structure interactions	191
14.1 Generalised force models from CFD computations	191
14.2 Coupling of fully-discretised fluids and structures	194
14.3 Partitioned Time Integration Techniques	195
14.3.1 Volume-continuous methods	196
14.3.2 Volume-discontinuous methods	196
14.3.3 Analysis of errors due to partitioning	197
14.3.4 Improved accuracy by extrapolation	201
14.4 Monolithic Time Integration Techniques	201
14.5 Efficiency of Monolithic and Partitioned Techniques	202
14.6 Practice Problems	206
14.7 Handy Formulae	206

15 Aeroelasticity in Aircraft Design	207
15.1 Requirements	207
15.2 Design Process	208
15.3 Wind Tunnel Testing Techniques	209
15.4 Ground Vibration Testing	210
15.5 Flight testing	211
15.5.1 Excitation and Measurement	211
15.5.2 Ground data processing and damping prediction	213

Chapter 1

Introduction

1.1 Background

The field of aeroelasticity considers phenomena in which interactions occur between aerodynamic flows and elastic structures. In this definition, the word “interaction” is significant. To be precise, we mean phenomena in which the aerodynamic forces are a function of the structural displacement, and the structural displacement is a function of the aerodynamic forces. This is easily demonstrated by an example, such as the glider shown below:

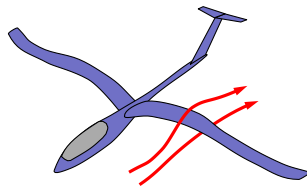


Figure 1.1: A flexible glider

If the glider’s wing is flexible, then we can expect it to deform. A change in shape, however, implies a change in the aerodynamic forces acting on it. In turn, these new forces will impose a new structural deflection. Therefore if we wish to predict the glider’s response, we must treat interactions by considering the complete fluid-structure system simultaneously.

The simultaneous analysis of fluids and structures can be complex. It is worthwhile from the scientific point of view, as such combined systems are often rich in unexpected and interesting behaviours. It can be essential from the engineering point of view, as unexpected behaviours are potentially undesirable ones.

Aeroelasticity is intimately connected with the field of aerospace engineering, where it has a major impact on configuration design. Its importance has grown

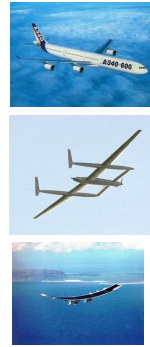
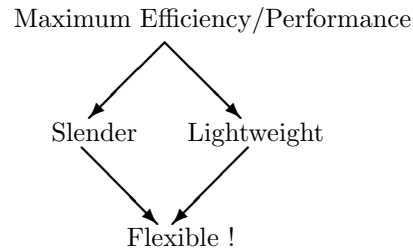
Modern Aircraft

Figure 1.2: Trends in high-performance aircraft

over the last few decades as the performance of aircraft has increased. High-performance aircraft tend to be light and slender, which implies reduced induced aerodynamic drag, but also increased flexibility. In addition, high operating speeds mean that the changes in aerodynamic force for a given amplitude of deflection are relatively large, leading to large-amplitude aeroelastic responses.

In the early days of aerospace engineering, the significance of aeroelastic effects was not completely recognised. Although the Wright brothers did investigate losses in thrust due to the flexibility of their propellers, the design of aircraft was mostly based on decoupled analysis until world war I. During the war, higher aircraft operating speeds brought several unexpected types of aeroelastic phenomena to light. These included those producing large static deflections, and several forms of self-sustained oscillations whose rate of growth could be dramatic. Often such phenomena lead to structural failure. This meant that they were difficult to diagnose (due to a lack of returning aircraft) and difficult to research (due to a lack of willing volunteers).

After world war I, the process of carrying out static and dynamic aeroelastic analysis using simplified models was established. These provided insight into why aeroelastic phenomena occurred, and allowed for the solution of problems such as aileron flutter through the use of mass balancing. At that point structural and aerodynamic models were too crude to be qualitatively accurate, however, especially for the more complex dynamic responses. In the 1930's it was recognised that unsteady aerodynamic effects played a substantial role dynamic aeroelastic response, which drove major developments in unsteady aerodynamic theory. In the same decade the basic techniques of flight flutter testing were established, although safety remained a substantial problem.

Before and during world war II aircraft entered new speed ranges, resulting in increased aerodynamic modelling complexity due to the effects of compressibility. They also employed more complex structural forms whose dynamics were difficult to predict. It was during this period that wind-tunnel testing evolved to the point where it became essential tool for aeroelastic analysis. With the invention of the jet engine, aircraft began operating in the transonic aerody-

namic regime. Here they experienced shock-induced aerodynamic phenomena which could promote aeroelastic instability. The aerodynamics of the transonic regime were found to be very difficult to predict accurately.

Since the 1950's digital computers have been used to support aeroelastic analysis. During the 1960s the first methods for predicting three-dimensional incompressible unsteady flows appeared, and during the 1970's, discrete structural prediction techniques advanced to the point where they could begin to predict the dynamics of realistic aircraft configurations. In the 1980's and 1990's, methods for computing inviscid transonic compressible flows on general geometries became widely available. Unfortunately, the accurate prediction of flows involving separation or shock boundary-layer interaction, which are of considerable interest in aeroelasticity, remains computationally intractable.

Aeroelasticity is a complex research field which there is active participation by both scientists and engineers. Their goal is not only to predict aeroelastic phenomena, but also to understand aeroelastic mechanisms well enough to control them. Therefore, a combination of techniques is presently in use. Where possible, simplified models are employed to develop maximum insight. Where practical, numerical computations are used to verify assumptions and make detailed changes in design. Wind-tunnel testing is employed to reduce the risk associated with new design concepts, while flight testing is used to deliver the final word on the characteristics of complete configurations.

Until recently, the role of aeroelasticity in aircraft design has been primarily directed towards analysing and correcting the aeroelastic deficiencies of existing design concepts. The push towards lighter construction techniques using active structures, however, is changing this role. As aeroelasticity becomes incorporated into multi-disciplinary design optimisation (MDO), the design problem is evolving from "how do we prevent this configuration from exhibiting instability" to "how can aerodynamics, structures and active controls be optimally combined to produce a configuration with maximum performance". Such challenges, along with those presented by the complex physical behaviours exhibited in many conditions of interest, will ensure that aeroelasticity remains a vibrant field for years to come.

1.2 Course Outline

This course will focus on the underlying analytical questions of aeroelasticity: how does one *predict* and *understand* the behaviour of an aeroelastic system? These two questions are not the same. One can perform a full aeroelastic simulation using hundreds of thousands of elements to discretise the structure, and tens of millions of elements for the fluid, and perhaps receive a reasonably accurate prediction of a particular aeroelastic response. But which of the factors taken into account are responsible for the observed response? More importantly, how can the results be translated in to a design action which ensures the desired behaviour over the complete range of operating conditions? In order develop the insight necessary to answer such questions, it is useful to simultaneously

At the end of this course you should:

- *Understand the physical processes which drive aeroelastic phenomena*
- *Be able to formulate and solve simple aeroelastic response and instability problems*
- *Be able to identify strengths and weaknesses of different aerodynamic and structural models for the analysis of a given aeroelastic condition*
- *Understand the basic design of computational aeroelastic solution techniques*
- *Be familiar with the role of aeroelasticity in aircraft design*

Figure 1.3: Course Goals

consider simplified (preferably analytic) models which condense complex physical interactions into conceptually manageable forms. This course will therefore examine the problem of aeroelasticity using models with varying levels of complexity. Familiarity with and comparison of these models will do much to achieve the course goals, which are summarized in figure 1.3.

The path we will take through the material of the course is shown in figure 1.4 (chapter numbers are indicated in brackets). We will start by considering simplified aeroelastic systems, specifically one or two degree-of-freedom structures with steady and quasi-steady aerodynamic models. These clearly do not contain all relevant physical effects, but are still general enough to exhibit some classic aeroelastic phenomena. Furthermore, the basic dynamic analysis techniques which will be presented are similar to those used for more complex physical models.

We will then increase the fidelity of our modelling by considering unsteady aerodynamics in detail. We will examine a range of theoretical aerodynamic models, each of which is representative of an unsteady physical phenomenon which contributes to aeroelastic response.

Next, we will investigate how general structures can be represented with using systems with modest numbers of degrees of freedom. Then we will reconsider dynamic response prediction in the context of these more general descriptions.

Following that, we will briefly review a number of high-fidelity computational techniques for computing the unsteady behaviour of both fluids and solids, including boundary-element, finite-element and finite-volume methods. We will then consider problems which arise when performing fully-coupled fluid-structure simulations. Finally, we will end with a summary of how the concepts described in the course are employed in the process of aircraft design.

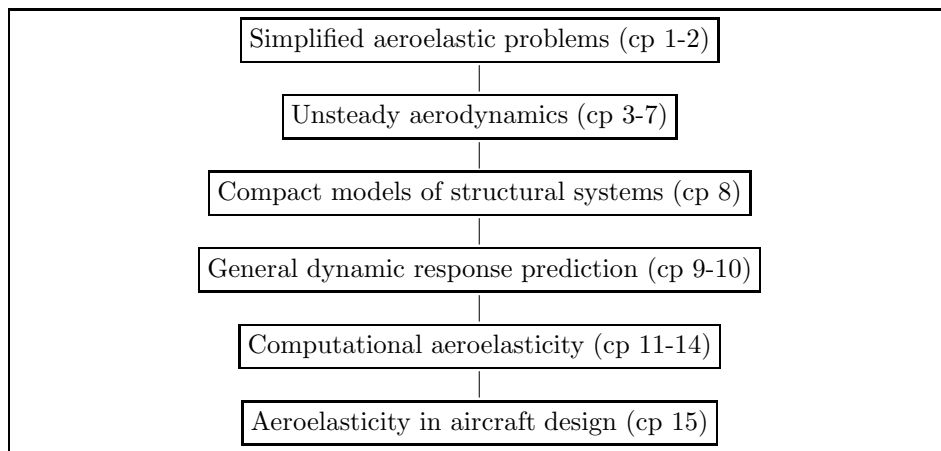


Figure 1.4: Course Content

1.3 Additional Course Information

1.3.1 Course format:

The course will consist of 14 lectures, an experimental demonstration, two projects and the final exam. In the lectures, course notes for the relevant sections will be passed out, and the key associated concepts and problems will be described and worked out. The experimental demonstration is short, and not mandatory. However, it is a chance to see some classic aeroelastic phenomena first hand.

Two projects will be given out. These primarily designed to reinforce the concepts treated in the course. They are not mandatory, but if completed and handed in they can count for up to 30% of your mark. You may also write a 100% final exam. Students who hand in projects but achieve a higher average mark on the exam will receive the exam mark instead. The marking scheme is summarised below:

- Project part 1: (15%)
Project part 2: (15%)
- Final examination:
(70%) - if project marks are highest
(100%) - if exam mark is highest

Students may work together on a project, but each student is expected to produce a unique report. (Near-) Identical reports will have their marks divided by the number of copies. Note that projects handed in late will not be graded.

Finally, there is a blackboard site where you can find announcements, information about the projects, practice exams, and some additional links and background information.

1.3.2 Prerequisite Concepts

Aeroelasticity is a truly multi-disciplinary topic, and thus relies on several prerequisite concepts. From aerodynamics, these include potential flow, the basics of compressible flow, and familiarity with thin airfoil theory. From structural mechanics, one should be comfortable with the concept of virtual work, Lagrange's equations of motion, and simple beam theory. You should also know how to analyse multiple degree-of-freedom vibrations, predict free and forced responses, and be familiar with Fourier analysis and the convolution of step and impulse responses.

1.3.3 Main References

The primary source of information for the material on the final exam are the course notes. The references listed below are useful for providing background information. Reference 1 highlights much of the material in the course, and contains several modern applications. Reference 2 is less up to date, but comprehensive, and perhaps easier to read than reference 1. Reference 3 is the easiest to read, and gives a good foundation for the course, but is less detailed than the other two. Do not confuse Reference 2 with another Dover book by Bisplinghoff and Ashley, titled "Principles of Aeroelasticity".

- **Introduction to Aircraft Aeroelasticity and Loads**, J.R. Wright and J.E. Cooper, Wiley (2007)
- **A Modern Course in Aeroelasticity**, 4th edition, E.H. Dowell (Editor), Kluwer Academic Publishers (2004)
- **Aeroelasticity**, C. S. Bisplinghoff, H. Ashley, and R. L. Halfman, Dover, (1955)
- **An introduction to the theory of Aeroelasticity**, Y. C. Fung, Dover (1955)

Many of the concepts presented in these notes appear in the previous course notes of Professor Zwaan, last published in 1999. Much of the material is also different, however. Please note that the exam and assignments are based on the current course notes.

1.3.4 Instructor Contact

I will be happy to help you with any material from the course, but please make an appointment before dropping by my office. You can contact me by telephone at +31-15-278-1538, or by email at S.J.Hulshoff@TUDelft.NL . I can also answer your questions directly by email.

1.4 Characteristics of Aeroelastic Problems

Before we continue with the rest of the material it is useful to first introduce precise terminology to describe different classes of aeroelastic problems.

Basically we will consider four types of problems, in two groups. The first group are called “Instability Boundary problems” (figure 1.5). These are concerned with determining the boundary which separates a stable fluid-structure interaction from an unstable one, and can be static or dynamic. Restricting interest to an instability boundary often allows simplifications in the analysis procedure. Not only can the solution search space be limited, but it is also often possible to use local linearizations of the governing equations. Static problems are a subset of instability boundary problems for which it is possible to ignore inertia effects. Dynamic problems are the more general type in which inertia effects must be included.

The second group of problems are called “Response problems” (figure 1.6). In this case one computes the response of the system to a given excitation. These problems can also be either static or dynamic. The last type includes every type of possible response, and is thus perfectly general. Therefore, a method developed for computing dynamic response problems can also be used to find instability boundaries. It just won’t be as efficient as a method which exploits the fact that it is looking for a boundary.

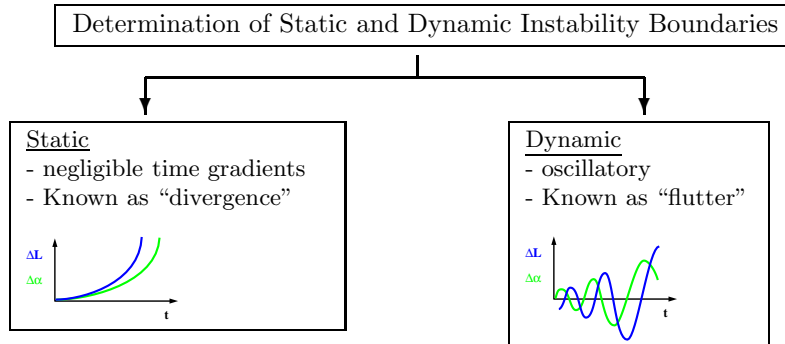


Figure 1.5: Instability problem types

Another way of visualising aeroelastic problem types is the famous Collar’s triangle, shown in figure 1.7. This shows the positioning of Aeroelastic problem types in relation to the forces considered within the model. Beside the aeroelastic problems, it is possible to locate several other classic aerospace problems on the diagram.

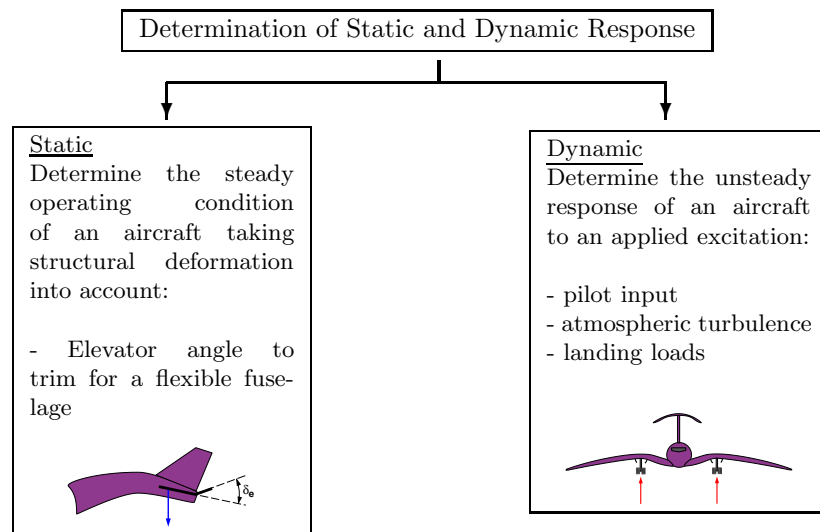


Figure 1.6: Response problem types

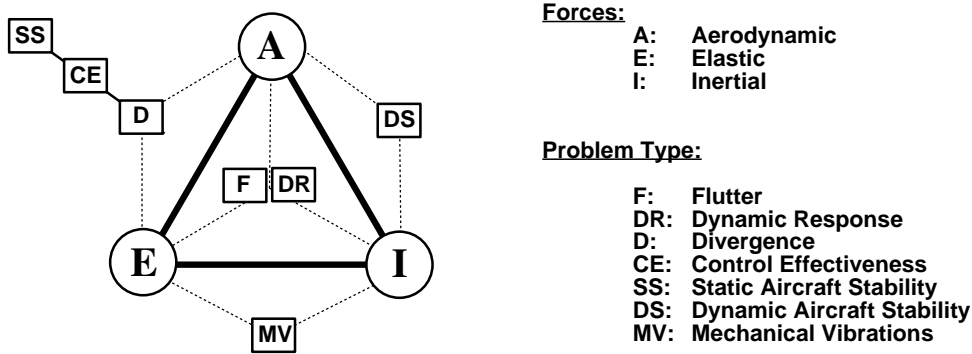


Figure 1.7: Collar's Triangle (1946)

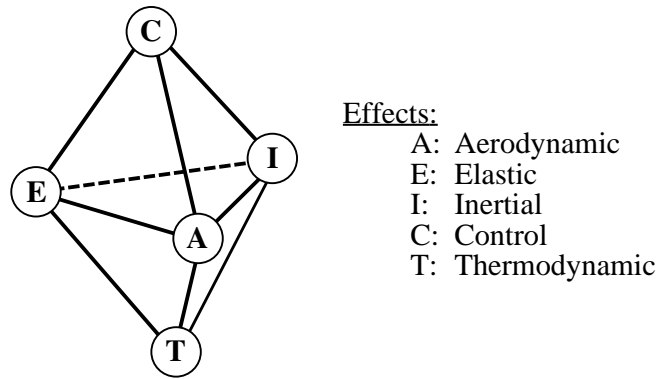


Figure 1.8: Friedmann's Hexahedron (1999)

The date on figure 1.7 gives you some idea of the context. Recently it has become fashionable to generalise this a bit, as shown in figure 1.8. This is because high-speed designs may also experience thermal coupling, and there is considerable ambition to optimise the response of multi-physics systems using advanced control concepts. These newer problems fall under the areas of Aeroservoelasticity (Aeroelasticity + high-gain control systems), and Aerothermoelasticity (Aeroelasticity + thermal effects).

A nice example of Aeroservoelastic engineering is the X-53, an aircraft which makes use of active leading and trailing edge controls to achieve aeroelastically deformed wing shapes with optimal performance (figure 1.9). This is a big contrast to the old way of doing things, (i.e. make the wing stiff enough to resist the moments incurred by control motion) and can lead to much lighter structures and increased control effectiveness. The latter is demonstrated figure



Figure 1.9: X53: control surfaces (upper) and in flight (lower)

1.10, which shows that for the X-53, the largest roll control authority is obtained using leading-edge outboard devices on a lighter, flexible wing.

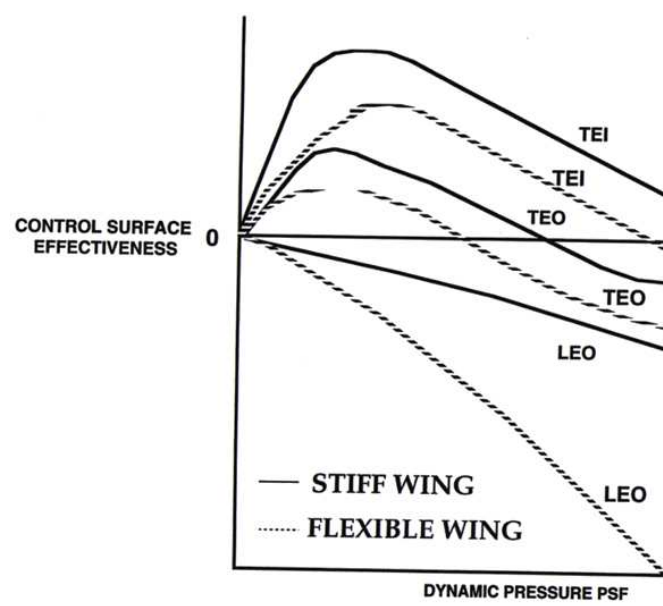


Figure 1.10: X53 control effectiveness for leading and trailing edge (LE, TE) inboard and outboard (I,O) devices

Chapter 2

Simplified Aeroelastic Problems

We will begin our look at aeroelastic analysis techniques using structural models which have only one or two degrees of freedom (DOF), and using only quasi-steady aerodynamics. This allows all the basic concepts of aeroelastic analysis to be introduced, however, and provides a first look at some of the physical phenomena that play a role in realistic systems. The models presented here may be too crude for use in detailed design, but they can still be applied in preliminary design stages as their simplicity allows the influence of design variables to be clearly identified.

We will start by describing simple structural and aerodynamic models for a typical airfoil section. Then approaches to deriving both static and dynamic aeroelastic boundaries will be given for the problems of divergence, control reversal and flutter. Afterwards we will briefly introduce two other simplified systems which can be used for preliminary analysis, namely the semi-rigid wing and a model for propeller whirl flutter.

2.1 The Typical Section

For a first demonstration of static and dynamic aeroelastic phenomena it is sufficient to consider a 2D airfoil section suspended using two springs as shown in figure 2.1 (right). This is sometimes used to approximate the characteristics of a complete wing by using its equivalent aerodynamic and structural properties at the 75% span section. The structural and geometric parameters of the typical section are given in figure 2.2. The center of rotation is referred to with EA, short for elastic axis. This terminology comes from three-dimensional wings, for which it may be thought of as the spanwise-running line which connects the rotation centres of each section. Note that vertical displacement, h is defined to be positive downwards. Also, in aerodynamics the chord c is used as a length scale. In aeroelasticity, the half-chord b is normally used instead (be careful not

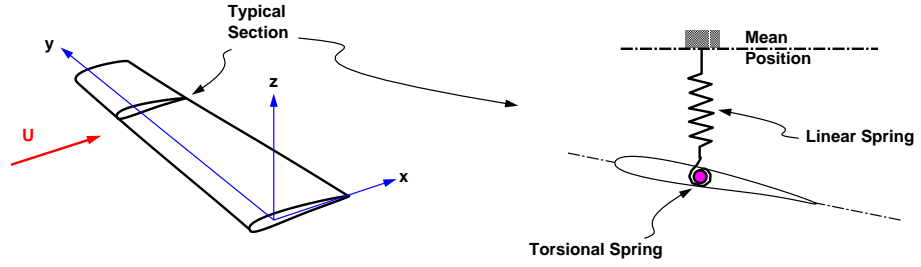
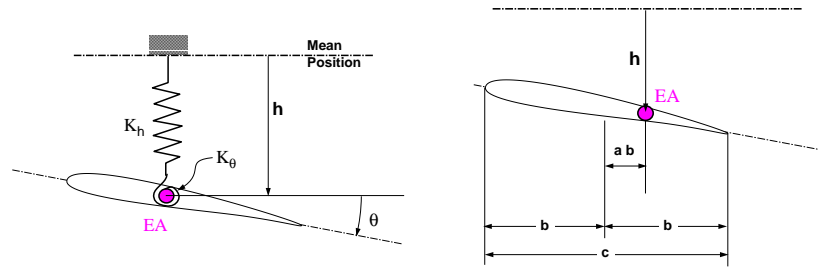


Figure 2.1: The Typical Section

**Structural Parameters**

EA: Elastic Axis
 h: Bending deflection (at EA)
 θ : Torsional deflection (about EA)
 K_h : Bending stiffness
 K_θ : Torsional stiffness

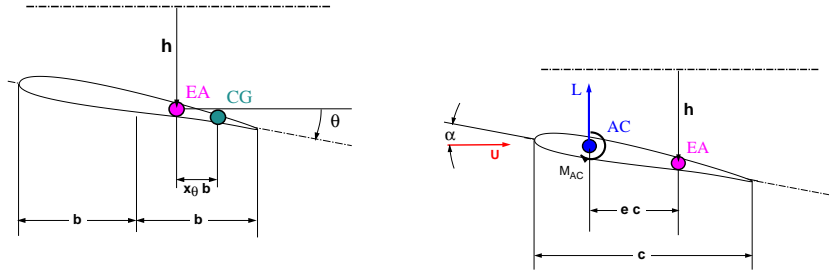
Geometric Parameters

b: Half chord
 c: Chord
 a: Displacement of EA from half chord
 S: Reference area

Figure 2.2: Structural and geometric parameters

to confuse b with wing span when working out problems).

We will use force and mass quantities such as L , M_{AC} , H , m , S_θ , and I_θ , defined in figures 2.3 and 2.3. These are sometimes considered to be local values on a three-dimensional wing, measured per unit span. This requires that the reference area, S , also be defined per unit span, i.e. $S = 2b$. We will occasionally work with derived quantities such as the uncoupled natural bending frequency, $\omega_h = \sqrt{K_h/m}$ and the uncoupled natural torsional frequency: $\omega_\theta = \sqrt{K_\theta/I_\theta}$. Be careful not to confuse these with two the natural frequencies of the *coupled* bending-torsion system. For problems involving control surfaces, we consider an alternate degree of freedom, δ , the control deflection, as shown in figure 2.4.

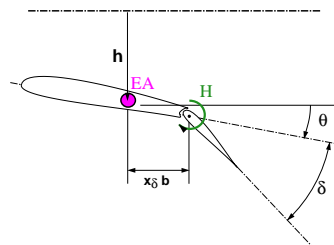
**Mass Parameters:**

CG: Center of Gravity
 x_θ : Displacement of CG from EA
 m : Mass
 S_θ : Static moment related to EA ($m x_\theta b$)
 $r_\theta b$: Radius of gyration about EA
 I_θ : Mass moment of inertia related to EA ($m r_\theta^2 b^2$)

Aerodynamic Parameters

U : Freestream velocity
AC: Aerodynamic center
 e : eccentricity factor
 α : Angle of attack
 L : Lift
 M_{AC} : Moment about AC (independent of α)
 q : Dynamic pressure ($\rho U^2 / 2$)

Figure 2.3: Inertial and aerodynamic parameters

**Control Surface Parameters**

δ : Control deflection
 $x_\delta b$: Hinge axis position
 H : Hinge moment
 S_δ : Static moment related to hinge axis
 I_δ : Mass moment of inertia related to hinge axis

Figure 2.4: Control surface parameters

2.1.1 Simple Aerodynamic Models

In the following sections we will only consider aerodynamic forces which are an instantaneous function of the local angle of attack. Although the forces may change in time due to changes in the angle of attack, they are not influenced by the time history of the flow.

We will use α to denote the instantaneous angle of attack measured from the zero lift line of the airfoil. Note that in general this not the same as θ , the pitch deflection angle. Be aware that in much of the aeroelastic literature, α is also used for the pitch deflection angle. This is due to the prevalence of linearised perturbation problems considered by early aeroelasticians.

Steady Aerodynamic Model

For the steady aerodynamic model, we assume that the lift and moment for the typical section in a freestream with density ρ and speed U is given by:

$$L(t) = qSC_{L_\alpha}\alpha(t) \quad (2.1)$$

$$M_{EA}(t) = 2bqS(C_{MAC} + eC_{L_\alpha}\alpha(t)) \quad (2.2)$$

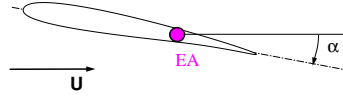


Figure 2.5: Steady angle of attack

Low-Frequency Aerodynamic Model

The low-frequency aerodynamic model is a little more advanced than the steady aerodynamic model, as it includes the vertical translation speed in angle of attack:

$$\alpha_{LF}(t) = \alpha(t) + \frac{\dot{h}(t)}{U} \quad (\text{Small-angle approximation}) \quad (2.3)$$

Thus:

$$L(t) = qSC_{L_\alpha} \left(\alpha(t) + \frac{\dot{h}(t)}{U} \right) \quad (2.4)$$

$$M_{EA}(t) = qSecC_{L_\alpha} \left(\alpha(t) + \frac{\dot{h}(t)}{U} \right) \quad (2.5)$$

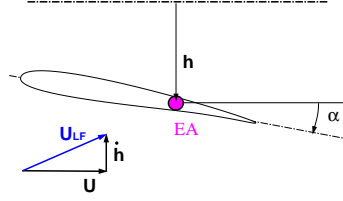


Figure 2.6: Quasi-steady Angle of attack

2.1.2 Equations of motion for the typical section

The equations of motion for the typical section can be derived using small-angle approximations and Lagrange's equations or more intuitively from a lumped-mass point of view. They express equilibrium in the vertical direction, and about the axis of rotation of the airfoil and control hinge:

$$\sum F_z = 0, \quad \sum M_{ElasticAxis} = 0, \quad \sum M_{Hinge} = 0 \quad (2.6)$$

In terms of the previously-derived parameters, these can be expressed:

$$m\ddot{h} + S_\theta\ddot{\theta} + S_\delta\ddot{\delta} + K_h h + L = 0 \quad (2.7)$$

$$S_\theta\ddot{h} + I_\theta\ddot{\theta} + (I_\delta + x_\delta b S_\delta)\ddot{\delta} + K_\theta\theta - M_{EA} = 0 \quad (2.8)$$

$$S_\delta\ddot{h} + (I_\delta + x_\delta b S_\delta)\ddot{\theta} + I_\delta\ddot{\delta} + K_\delta\delta - H = 0 \quad (2.9)$$

where θ and δ are small and the aerodynamic moment about the elastic axis is defined by:

$$M_{EA} = L(ec) + M_{AC} \quad (2.10)$$

Often simplified forms of the equations are used in order to clarify the roles of the structural and aerodynamic properties for certain classes of problems. For the static problem classes introduced in in chapter 1, for example, one may ignore the terms with time derivatives.

2.1.3 Torsional Divergence

Divergence was the first type of aeroelastic instability that was recognised and understood. If one considers the section shown below, it is obvious that a perturbation in angle of attack will tend to increase θ and thus also α and L . If the spring is strong enough to resist, there are no consequences. But as the dynamic pressure q increases, the aerodynamic forces become larger while the spring stiffness is unchanged. At a certain value of q , the aerodynamic moment balances the spring moment. The lowest speed at which this happens for a given density is the torsional divergence speed. Beyond this speed θ increases without bound in response to a perturbation.

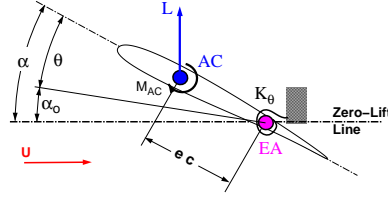


Figure 2.7: Typical section for the divergence problem

The divergence speed can be found by considering the equation of motion for a single degree of freedom. We will ignore inertial effects for this example, so it becomes a static instability boundary problem. Summing moments about the EA (positive nose-up):

$$\sum M = [C_{L_\alpha}(\alpha_o + \theta)e + C_{M_{AC}}]cqS - K_\theta\theta \quad (2.11)$$

For equilibrium, $\sum M = 0$, or:

$$\theta = \frac{cqS}{K_\theta} \frac{[C_{L_\alpha}\alpha_o e + C_{M_{AC}}]}{1 - \frac{C_{L_\alpha}ecqS}{K_\theta}} \quad (2.12)$$

examining the denominator, θ is seen to be unbounded when $C_{L_\alpha}ecqS = K_\theta$. This gives a certain value for $q_{divergence}$. It can be shown that this is an upper limit for q if one considers the stability of the system to small perturbations, for which we require:

$$\frac{\partial M}{\partial \theta} \leq 0 \quad (2.13)$$

Equation (2.13) simply says that if there is a positive perturbation in θ , then a negative (nose-down) opposing moment must be produced. Applying it to the moment equation leads immediately to:

$$1 - \frac{ecqS}{K_\theta}C_{L_\alpha} \geq 0 \quad (2.14)$$

from which can be concluded that the configuration is unconditionally stable if $e \leq 0$ (AC downstream of EA), but only conditionally stable if $e > 0$. The former is the case for weather vanes, while the latter is often true for realistic wings. We can also re-arrange (2.14) to obtain:

$$q \leq \frac{K_\theta}{C_{L_\alpha}ecS} \quad (2.15)$$

Which explicitly shows the configuration is limited to a maximum operating dynamic pressure as a function of aerodynamic and structural parameters.

2.1.4 Control Reversal

The actuation of trailing-edge control devices normally changes the pressure distribution so that the center of pressure shifts aft. Examining figure 2.8, it is clear that a positive control deflection will therefore give a nose-down pitching moment that tends to reduce the angle of attack of the configuration. A speed will be reached, $q_{reversal}$, where a positive control deflection decreases the angle of attack sufficiently to have no change in force. At speeds higher than this speed the control will act in the sense opposite to normal.

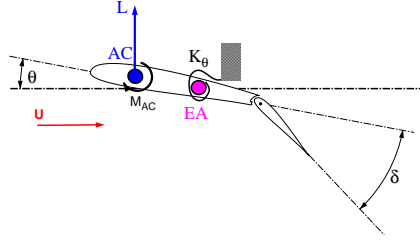


Figure 2.8: Typical section for the control reversal problem

At equilibrium:

$$\sum M = [(C_{L_\alpha}\theta + C_{L_\delta}\delta)e + C_{Mac_\delta}\delta]cqS - K_\theta\theta = 0 \quad (2.16)$$

solving for the ratio of structural twist to control deflection:

$$\frac{\theta}{\delta} = \frac{cqS}{K_\theta} \frac{C_{L_\delta}e + C_{Mac_\delta}}{1 - \frac{C_{L_\alpha}ecqS}{K_\theta}} \quad (2.17)$$

Control effectiveness is indicated by lift/(rigid-wing lift) :

$$\frac{L}{L^{(R)}} = \frac{(C_{L_\alpha}\theta + C_{L_\delta}\delta)}{C_{L_\delta}\delta} = \frac{1 + \frac{C_{L_\alpha}C_{Mac_\delta}cqS}{C_{L_\delta}K_\theta}}{1 - \frac{C_{L_\alpha}ecqS}{K_\theta}} \quad (2.18)$$

Noting $C_{L_\alpha}, C_{L_\delta}, S, c, K_\theta > 0$, and $C_{Mac_\delta} < 0$, there will be a $q > 0$ at which $\frac{L}{L^{(R)}}$ will switch from positive to negative, denoted as $q_{reversal}$:

$$q_{reversal} = -\frac{C_{L_\delta}K_\theta}{C_{L_\alpha}C_{Mac_\delta}cS} \quad (2.19)$$

Above this speed, the loss in lift due to (nose-down) structural deflection will be greater than the lift gained by (positive) control deflection



Figure 2.9: B-47

One famous example of unexpected control reversal cropping up in a design is that of the B-47 (figure 2.9). The torsion-strip-theory originally used did not predict aileron reversal within the envelope. It turned out that bending effects were significant as well, which is perhaps not surprising when you consider that the difference in wing-tip deflections between the maximum positive and negative loads is 11m for this aircraft. The early solution to this problem was to use roll spoilers, which have a relatively low $C_{Mac\delta}$. This is one of the reasons that roll spoilers are used on modern airliners, along with the fact that they are also quite effective when placed ahead of a flap.

Note that flight beyond $q_{reversal}$ can be made by actuating the controls in the opposite sense. To do so, however, the pilot would first need to spend a significant amount of time with little or no control while flying near the relatively high speed of $q_{reversal}$.

2.1.5 Flutter of a Typical Section

Flutter is a word used to describe self-sustained oscillations arising from fluid-structure interactions. It is normally implied that under certain conditions, the oscillations can grow without bound. The *flutter point* is defined as the point where a damped oscillation transitions to one growing in amplitude. A group of flutter points therefore forms a boundary between a region where one can expect to operate a vehicle “normally” from one where structural failure is likely. The region within the boundary is referred to as a *flutter envelope* (figure 2.10). Determination of the flutter envelope forms a major and mandatory part of aircraft certification, as it must be shown to be 15% larger than the aircraft’s flight envelope (10% if the aircraft has sustained damage).

The fact that the flutter point is a transition between damped and growing oscillations implies that the response at the flutter point is of constant amplitude. This idea is used repeatedly in analysis techniques, and often makes the problem of determining a flutter point easier than computing the general response of a configuration. In spite of this, determining the flutter boundary of an aircraft is a major job. One reason for this is the complexity of the aerodynamic phenomena which tend to exist in flutter conditions. Not only must unsteady aerodynamic effects be included, but the fact that the configuration is far from its normal operating point can lead to the appearance of difficult-to-deal-with features such as strong shocks and boundary-layer separation. In

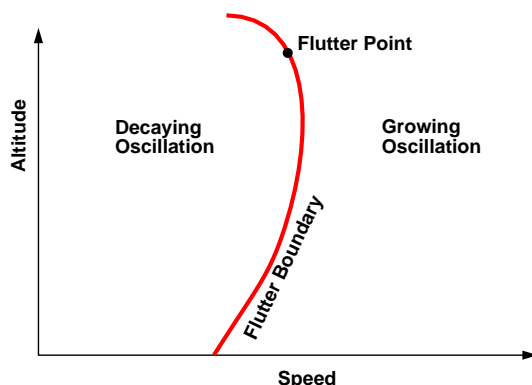


Figure 2.10: A flutter boundary

addition, one must normally consider several types of flutter modes, for which variations with fuel, payload and aircraft configuration must be established. The combination of these factors translates into a large number of flight cases which must be analysed.

To keep things simple, we start our analysis with the case of “Classical Flutter” which refers to a class of two-degree of freedom oscillations which are characteristic of 2D airfoil sections. Our approach will be to assume a solution of an amplified harmonic form, substitute the assumed solution into the equations of motion, and then solve for the unknown frequencies and amplification factors. Our task will then be to determine under which conditions the amplification factors transition from negative (damped case) to positive (growing case). The analysis is precise (within the bounds of the assumed simple aerodynamic and dynamic behaviours) but does not necessarily give a phenomenological answer to the question “What is flutter?”. For that, it is useful to appeal to energy concepts, which at the very least can account for the existence of the phenomena.

When an aircraft travels in relative motion to air, it is in fact contact with an energy reservoir. More succinctly, certain motions of the aircraft can extract work from the airstream. If the speed (and structural integrity) of the aircraft is maintained, such energy extractions will ultimately show up in the aircraft’s fuel bill. So how is energy transferred to the structure? In our analysis we will ignore the drag force, so that the transfer of energy must occur when the airfoil’s vertical speed vector is aligned with the lift vector. When the lift and vertical speed have the same sign, work is done on the structure (figure 2.11). When the lift opposes the motion, energy is extracted (this is similar to what occurs when pushing in and out of phase on a child’s swing).

If we consider an airfoil which can plunge but not pitch ($h \neq 0$, $\theta = 0$), the low-frequency aerodynamic model predicts that the motion is always damped (check this yourself). The key to classical flutter, therefore, is that the timing of the motion in θ and h must be such that over one cycle, the lift is on av-

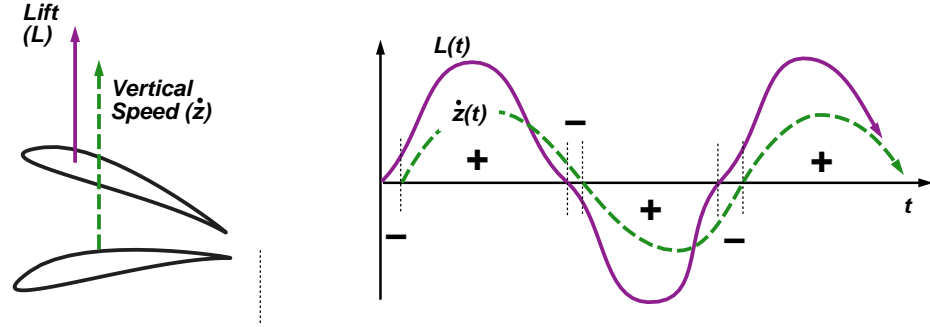


Figure 2.11: Timing of vertical motion and aerodynamic force

erage aligned with the airfoil motion, rather than opposing it (in other words $\int L(t)\dot{z}(t)dt > 0$). Such a situation is shown in figure 2.11.

Classical flutter with a growing amplitude can therefore occur with the proper timing of θ and h , which implies the proper timing of aerodynamic forces with structural motion. However, non-classical flutter modes are also possible. For example, single-degree-of-freedom flutter can occur when unsteady aerodynamic forces have a phase different from that applied by the steady aerodynamic model. A famous example is single-DOF control-surface flutter, which can occur in transonic conditions. In this case, shock movement as a function of δ is lagged such that the net aerodynamic damping is negative. Another possibility is the pitching airfoil at very low speeds, for which wake effects can also introduce negative damping.

Both of the single-degree-of-freedom cases above highlight the importance of unsteady aerodynamic effects in determining the timing of the forces and overall energy balance. Although in many cases the steady aerodynamic model we are about to use may perform reasonably, it can be insufficient for the conditions of most relevance for modern aircraft, the transonic regime. We will examine the reasons behind the limits of the steady aerodynamic model in Chapters 3-6.

2.1.6 Solution of the equations of motion

First we will consider the various motions possible for a 2-DOF (pitch and plunge) airfoil section with a steady aerodynamic model. To keep things simple, we will consider uncambered airfoils only ($C_{Mac} = 0$) so that the lift and moment about EA is:

$$L(t) = qSC_{L_\alpha}\theta(t) \quad (2.20)$$

$$M_{EA}(t) = e2bqSC_{L_\alpha}\theta(t) \quad (2.21)$$

The equations of motion can then be written:

$$m\ddot{h} + S_\theta\ddot{\theta} + K_h h + qSC_{L_\alpha}\theta(t) = 0 \quad (2.22)$$

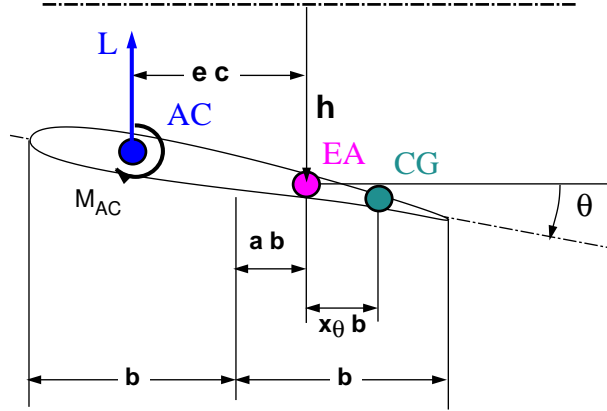


Figure 2.12: The typical section

$$S_\theta \ddot{h} + I_\theta \ddot{\theta} + K_\theta \theta - 2ebqSC_{L_\alpha} \theta(t) = 0 \quad (2.23)$$

or in matrix form (with $\{x\} = [h, \theta]^t$):

$$[M]\{\ddot{x}\} + ([K] - q[A_0])\{x\} = \{0\} \quad (2.24)$$

where

$$[M] = \begin{bmatrix} m & S_\theta \\ S_\theta & I_\theta \end{bmatrix} \quad [K] = \begin{bmatrix} K_h & 0 \\ 0 & K_\theta \end{bmatrix} \quad [A_0] = \begin{bmatrix} 0 & -SC_{L_\alpha} \\ 0 & 2SebC_{L_\alpha} \end{bmatrix} \quad (2.25)$$

This form is typical for the larger systems we will consider later in the course. To find solutions to the system, we begin by assuming that the 2 DOF response of the section, $\{x\} = [h, \theta]^T$, is of the form $\{x\} = \{\hat{x}\}e^{pt}$ so that:

$$h = \hat{h}e^{pt} \quad \text{and} \quad \theta = \hat{\theta}e^{pt} \quad \text{where} \quad p = (\sigma + i\omega)$$

This assumption therefore includes diverging, damped and neutral responses, both periodic and aperiodic. The equations of motion are then:

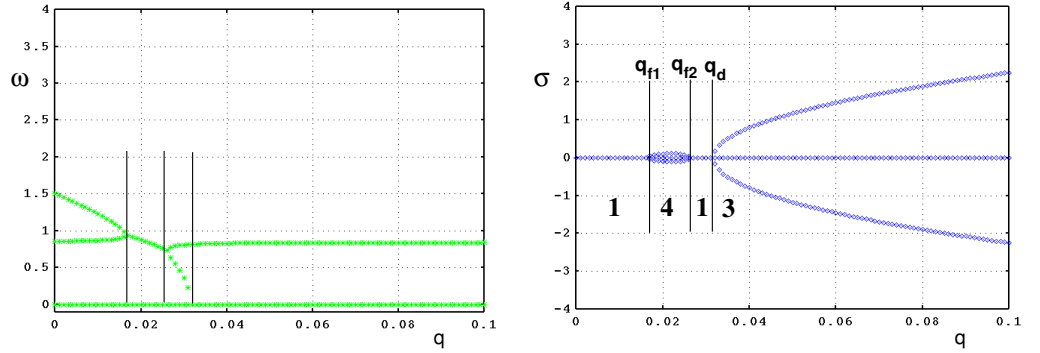
$$(mp^2 + K_h)\hat{h} + (S_\theta p^2 + qSC_{L_\alpha})\hat{\theta} = 0 \quad (2.26)$$

$$S_\theta p^2 \hat{h} + (I_\theta p^2 + K_\theta - 2ebqSC_{L_\alpha})\hat{\theta} = 0 \quad (2.27)$$

or

$$[[M]p^2 + ([K] - q[A_0])]\{x\} = 0 \quad (2.28)$$

where for the latter q , the dynamic pressure, has been separated out to indicate its importance as a parameter. For non-trivial $\{x\}$, the determinant of the

Figure 2.13: Flutter diagram for 2DOF section with $K_\theta = 0.05$, $x_\theta = 0.2$

coefficient matrix must be zero. This requirement leads to the *characteristic equation*, which can be written:

$$\begin{aligned}
 a_4 p^4 + a_2 p^2 + a_0 &= 0 \\
 a_4 &= mI_\theta - S_\theta^2 \\
 a_2 &= mK_\theta + I_\theta K_h - (2meb + S_\theta)qSC_{L_\alpha} \\
 a_0 &= K_h(K_\theta - 2ebqSC_{L_\alpha})
 \end{aligned}$$

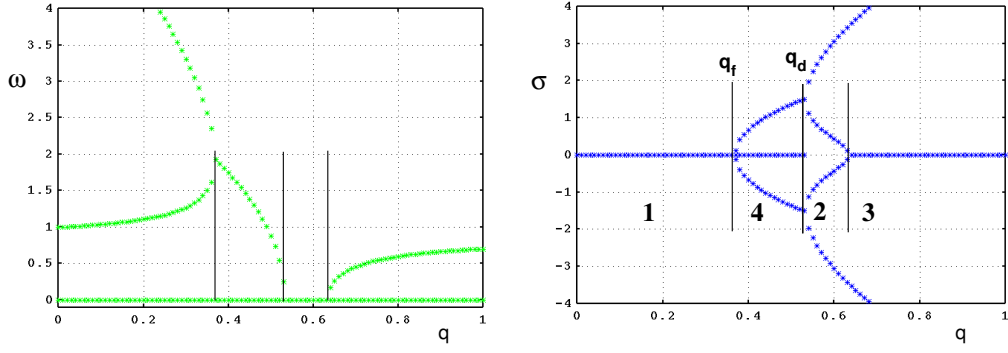
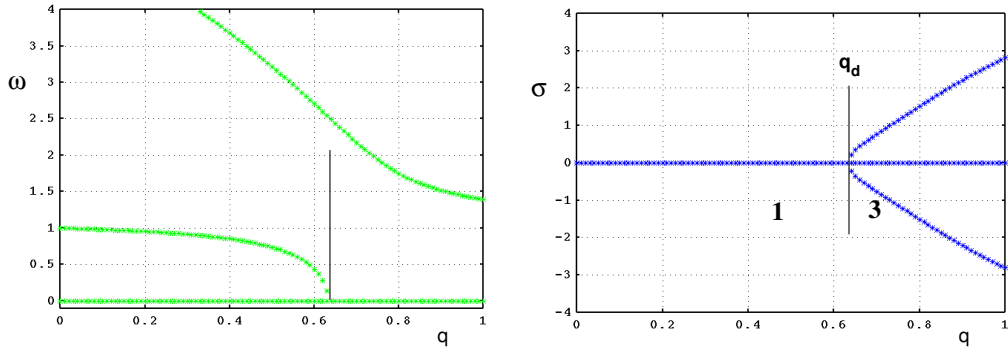
This can be solved for its roots:

$$p_{1..4} = (\sigma + i\omega)_{1..4} = \pm \sqrt{\frac{1}{2a_4}(-a_2 \pm \sqrt{a_2^2 - 4a_4a_0})} \quad (2.29)$$

so that the solution to the equations of motion can be written:

$$\{x_j\} = \{\hat{x}_j\}e^{(\sigma_j + i\omega_j)t} \quad ; \quad j = 1..4 \quad (2.30)$$

To get an idea of how the motion changes over the operating range of a given configuration, we can plot the components of p as a function of the dynamic pressure. Such diagrams are known as “flutter diagrams” and are frequently used to express the overall characteristics of a system (they can also be plotted with speed as the ordinate). Note that the imaginary component of p corresponds to the frequency of oscillation, while the real component corresponds to the growth rate. While plotting we reject p ’s with negative frequencies as unphysical solutions.

Figure 2.14: Flutter diagram for 2DOF section with $K_\theta = 1.0$, $x_\theta = 0.2$ Figure 2.15: Flutter diagram for 2DOF section with $K_\theta = 1.0$, $x_\theta = -0.1$

A number of distinct behaviours can be identified in figures 2.13 to 2.15. In figure 2.13, there are initially two constant-amplitude (neutral) modes with frequencies that decrease with increasing q (motion type I). Then the two frequency branches merge, and one decaying and one growing oscillatory mode appear (motion type II). The latter is a flutter mode, so that the dynamic pressure q_{f1} thus corresponds to a flutter boundary. As q is further increased, the motion becomes neutral again (q_{f2}). Increasing q further, the previous aperiodic ($\omega = 0$) modes, suddenly cease to be neutral (at q_d), and one starts experience positive growth rates while the other decays. The one with the positive growth rate corresponds to the dynamic version of the divergence mode we studied previously.

For figure 2.14, the stiffness of the configuration has been increased by a factor of 20. Initially the mode frequencies are therefore much larger, but these too decrease with increasing q . A flutter point is again encountered, but in this case it merges into the divergence mode without an intermediate stable region as q is increased.

For figure 2.15, the center of mass has been moved forward. The frequency branches remain well separated, and flutter does not occur. The divergence mode again appears at higher q .

The coalescing of frequency branches on flutter diagrams is often used as an indication of potential flutter problems. This is not proof that flutter is occurring, however, as σ must also be positive for one of the modes. Furthermore flutter can occur when the branches are separated, as we will see later in this chapter. For a full interpretation, both parts of the flutter diagram are required.

2.1.7 Mode Shapes

Associated with each value of p is a relative amplitude of pitch and plunge. It can be found by substituting the value of p into either equation (2.26) or (2.27) and solving for $\frac{\hat{\theta}}{\hat{h}}$. This ratio is sometimes referred to as the mode “shape”, for reasons that will become obvious when we consider continuous structural models. In fact if p is considered to be an eigenvalue of the system, then the mode shape is its corresponding eigenvector, where one component can be assumed to be unity and the other obtained through the ratio derived above. Note that the eigenvector, or mode shape, changes with dynamic pressure, as p itself is a function of dynamic pressure.

2.1.8 Conditions which determine the types of motion

In this section we will examine in more detail how the parameters of the problem effect the resulting motion types. We will assume that for a given configuration, the parameters are fixed, except for the dynamic pressure q . By definition, we would like to be sure that any undesirable motions occur at values of q which are outside the configuration’s normal range of operation.

We will focus our analysis on equation (2.29), as the form of p , (real, imaginary or complex), determines the type of motion present in the airfoil’s response.

Doing so we first note that a_4 must always be positive, as $r_\theta \geq x_\theta$. As a result, we need only consider four sets of conditions.

Set 1: $a_2^2 - 4a_4a_0 > 0$, $a_0 > 0$, $a_2 > 0$.

In this case:

$$p_{1..2}^2 = \frac{1}{2a_4} \left(-a_2 \pm \sqrt{(< a_2^2)} \right) = -\omega_1^2, -\omega_2^2$$

so that $p_{1..4} = \pm i\omega_1, \pm i\omega_2$. We reject negative frequencies as unphysical solutions, and are left with two neutral harmonic motions.

Set 2: $a_2^2 - 4a_4a_0 > 0$, $a_0 > 0$, $a_2 < 0$.

This is similar to set 1, but now the negative a_2 coefficient produces two positive p^2 , so that the p are pure real: $p_{1..4} = \pm\sigma_1, \pm\sigma_2$. Here we have two diverging and two converging aperiodic motions.

Set 3: $a_2^2 - 4a_4a_0 > 0$, $a_0 < 0$, $a_2 \pm$.

This set produces both of the motions defined above.

$$p_{1..2}^2 = \frac{1}{2a_4} \left(-a_2 \pm \sqrt{(> a_2^2)} \right) = r_1(-ve), r_2(+ve) \quad (2.31)$$

so that $p_{1..4} = \pm\sigma_1, \pm i\omega_2$. In this case, rejecting the negative frequency, we have one converging and one diverging aperiodic motion, and one neutral harmonic motion.

Set 4: $a_2^2 - 4a_4a_0 < 0$, $a_0 \pm$, $a_2 \pm$.

Finally, we have more general motions, defined by:

$$p_{1..2}^2 = \frac{1}{2a_4} (-a_2 \pm iK) = -m + in \quad (2.32)$$

This produces the following possible motions:

$$p = \begin{cases} \sigma_1 + i\omega_1 & \text{oscillatory diverging} \\ -\sigma_2 + i\omega_2 & \text{oscillatory converging} \\ \sigma_3 - i\omega_3 & \text{negative frequency - rejected} \\ -\sigma_4 - i\omega_4 & \text{negative frequency - rejected} \end{cases}$$

The above results are summarised in table 2.1.

$a_2^2 - 4a_4a_0$	> 0		< 0	
a_0	> 0		< 0	.
a_2	> 0	< 0	.	.
p^2	$-\omega_1^2, -\omega_2^2$	σ_1^2, σ_2^2	$\sigma^2, -\omega^2$	$-m \pm in$
p	$\pm i\omega_1, \pm i\omega_2$	$\pm \sigma_1, \pm \sigma_2$	$\pm \sigma, \pm i\omega$	$\pm \sigma \pm i\omega$
Type of Motion	Harmonic: 2 pos. freq. 2 neg. freq.	Aperiodic: 2 diverging 2 converging	Aperiodic: 1 diverging 1 converging Harmonic: 1 pos. freq. 1 neg. freq.	Oscillatory: 1 div. pos. freq. 1 conv. pos. freq. 1 div. neg. freq. 1 conv. neg. freq.
Type of motion	Neutral	Divergence	Diver./Neutral	Flutter
Set	1	2	3	4

Table 2.1: Responses of a typical section with a steady aerodynamic model

2.1.9 Pines' Conditions for flutter

Flutter can be defined as a self-sustained oscillation which, under certain conditions can grow in time. The *flutter point* is defined as the point where the self-sustained oscillation transitions from convergent to divergent motion. For a given typical section combined with a steady aerodynamic model, the motion will be a function of q (note how a_2 and a_0 are functions of q). For certain groups of parameters, there will be a flutter point, q_f , beyond which an oscillatory motion diverges. Given the local density (i.e. altitude and temperature) this can be converted into a flutter speed, V_f .

From the previous section, we can see that the type of motion we are interested in occurs under condition set 4. It can therefore be useful to re-express the condition $a_2^2 - 4a_4a_0 \leq 0$ in terms of the section's geometric and mass properties, with the assumption that the only flutter solutions of interest are for real and positive q_f . We define:

$$Q = \frac{qSbC_{L_\alpha}}{K_\theta} \quad (2.33)$$

and require it to be real and positive. We can then re-express $a_2^2 - 4a_4a_0 < 0$ as:

$$C_2Q^2 + C_1Q + C_0 < 0 \quad (2.34)$$

with:

$$C_2 = (x_\theta + 2e)^2 \quad (2.35)$$

$$C_1 = -2 \left[x_\theta + 2e + \left(\frac{w_h}{w_\theta} \right)^2 (x_\theta - 2e + 4e \frac{x_\theta^2}{r_\theta^2}) \right] \quad (2.36)$$

$$C_0 = \left[1 - \left(\frac{w_h}{w_\theta} \right)^2 \right]^2 + 4 \frac{x_\theta^2}{r_\theta^2} \left(\frac{w_h}{w_\theta} \right)^2 \quad (2.37)$$

We can find Q at the flutter boundary using the quadratic formula:

$$Q_1, Q_2 = \frac{-C_1 \pm \sqrt{C_1^2 - 4C_2C_0}}{2C_2} \quad (2.38)$$

Requiring Q to be real leads to:

$$C_1^2 - 4C_2C_0 > 0 \quad (2.39)$$

which can be expressed:

$$x_\theta \left[x_\theta + 2e - 2e \left(\frac{w_h}{w_\theta} \right)^2 \left(1 + 2e \frac{x_\theta}{r_\theta^2} \right) \right] > 0 \quad (2.40)$$

In order to derive a second condition we note that:

$$Q_1 + Q_2 = -C_1/C_2 \quad (2.41)$$

We consider the case where both Q_1, Q_2 are positive. Since C_2 is necessarily positive, C_1 should be negative. This leads to :

$$x_\theta + 2e + \left(\frac{w_h}{w_\theta} \right)^2 \left(x_\theta - 2e + 4e \frac{x_\theta^2}{r_\theta^2} \right) > 0 \quad (2.42)$$

Conditions (2.40) and (2.42) are known as Pine's conditions. They can be used to investigate the possibility of flutter for various combinations of geometric, stiffness, and inertial parameters.

2.1.10 The effect of a low-frequency aerodynamic model

Changing the aerodynamic model can have a profound effect on the observed flutter behaviour. This can be demonstrated just by considering the low-frequency aerodynamic model, which introduces an additional damping term, $[A_1]$, into the equations:

$$[M]\{\ddot{x}\} - \frac{q}{U}[A_1]\{\dot{x}\} + ([K] - q[A_0])\{x\} = \{0\} \quad (2.43)$$

where

$$[A_1] = \begin{bmatrix} -SC_{L_\alpha} & 0 \\ SecC_{L_\alpha} & 0 \end{bmatrix} \quad (2.44)$$

To solve the system we once again assume a solution of the form:

$$\{x\} = \{\hat{x}\}e^{pt} \quad (2.45)$$

Which leads to the characteristic equation:

$$a_4p^4 + a_3p^3 + a_2p^2 + a_1p + a_0 = 0 \quad (2.46)$$

$$(2.47)$$

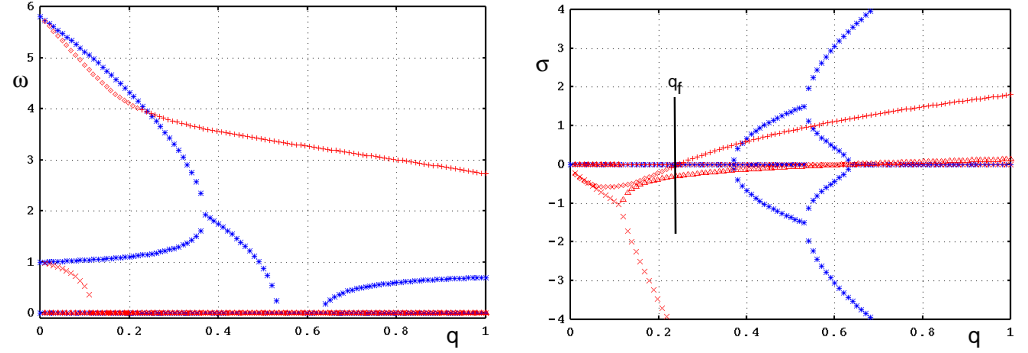


Figure 2.16: Flutter diagrams with the steady and low-frequency aerodynamic models (*) - steady aerodynamic model (x,+) - low-frequency aerodynamic model

where

$$a_4 = mI_\theta - S_\theta^2 \quad (2.48)$$

$$a_3 = \frac{q}{U} SC_{L_\alpha} (2ebS_\theta + I_\theta) \quad (2.49)$$

$$a_2 = mK_\theta + I_\theta K_h - (2meb + S_\theta)qsC_{L_\alpha} \quad (2.50)$$

$$a_1 = \frac{q}{U} SC_{L_\alpha} K_\theta \quad (2.51)$$

$$a_0 = K_h(K_\theta - 2ebqSC_{L_\alpha}) \quad (2.52)$$

As before, the roots of the characteristic equation define the motion types. Unfortunately, it is now a full-fourth order equation so it can not be so easily manipulated. We therefore resort to its numerical solution. Some example results are shown compared to their steady aerodynamic model counterparts in figure 2.16.

The low-frequency aerodynamic model results show the same initial behaviour of the mode frequency branches, but these become substantially different as q is increased. Note that there is no longer an intersection of the frequency branches. Examining the σ plot, we observe that at small q the motion is damped, as we might have anticipated from simple reasoning, but then for one oscillatory mode σ grows rapidly, so that the critical dynamic pressure is more than 30% less than that computed with the steady aerodynamic model.

2.2 The Semi-Rigid Wing

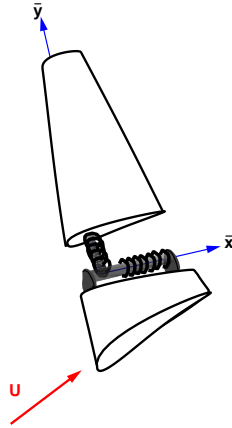


Figure 2.17: The Semi-Rigid Wing

Sweep is often used in high-speed aircraft, not only to raise the critical Mach number of a wing, but also to favourably affect its aeroelastic properties. A very simple model which can be used to illustrate this is the semi-rigid wing. This model combines bending and torsion with wing sweep as a parameter.

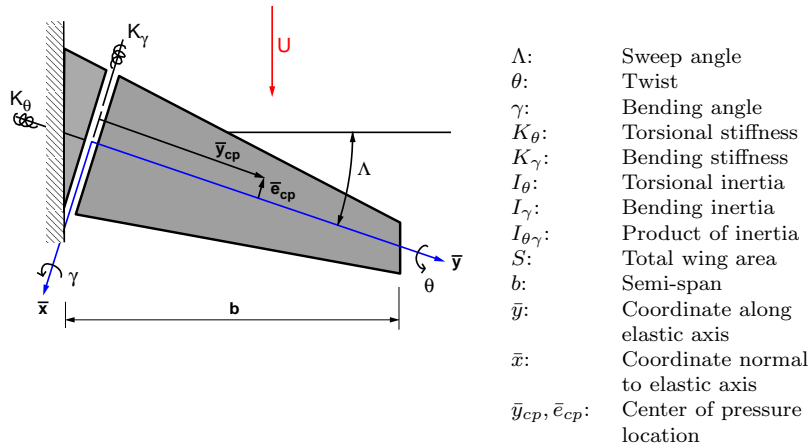


Figure 2.18: Semi-rigid wing parameters



Figure 2.19: X29 forward-swept aircraft

2.2.1 Equations of motion for the Semi-rigid wing

In this case we assume that the system is in equilibrium about both axes of rotation, so that:

$$\sum M_{\bar{x}} = 0, \quad \sum M_{\bar{y}} = 0 \quad (2.53)$$

$$I_{\theta}\ddot{\theta} - I_{\theta\gamma}\ddot{\gamma} + K_{\theta}\theta - L \bar{e}_{cp} = 0 \quad (2.54)$$

$$I_{\gamma}\ddot{\gamma} - I_{\theta\gamma}\ddot{\theta} + K_{\gamma}\gamma - L \bar{y}_{cp} = 0 \quad (2.55)$$

The lift is usually assumed to be a function of the time history of the local effective angle of attack:

$$L = L(\alpha(t)) \quad (2.56)$$

here $\alpha = \alpha_o + \alpha_d$, where α_o is the initial angle of attack, and α_d is the angle of attack due to deflection:

$$\alpha_d = \theta \cos(\Lambda) - \gamma \sin(\Lambda) \quad (2.57)$$

Following a procedure similar to that used for the typical section (see the problems at the end of this section), the divergence speed for the semi-rigid wing can be derived. Doing so reveals that forward-swept wings (e.g. figure 2.19) have lower divergence speeds. If aft sweep is used, there will be a point where the effect of bending cancels the effect of torsion and no divergence is obtained. This is referred to as the aeroisoclinic condition.

2.3 Propeller Whirl Flutter

Propeller whirl flutter arises with the correct synchronisation of aerodynamic forces with gyroscopic-coupled structural modes. It was first analysed as early as the late 1930's , but was not brought to the forefront until 1960, after two crashes of the Lockheed Electra 188 turboprop, a modified version of which is shown in figure 2.20. Both crashes occurred during passenger-carrying service.



Figure 2.20: Lockheed Electra turboprop

For these cases, it is believed that the whirl flutter mode also induced flutter in the main wing, leading to the wing's separation from the aircraft. Photos of a model of the aircraft before and after wind-tunnel testing are shown in figure 2.21.

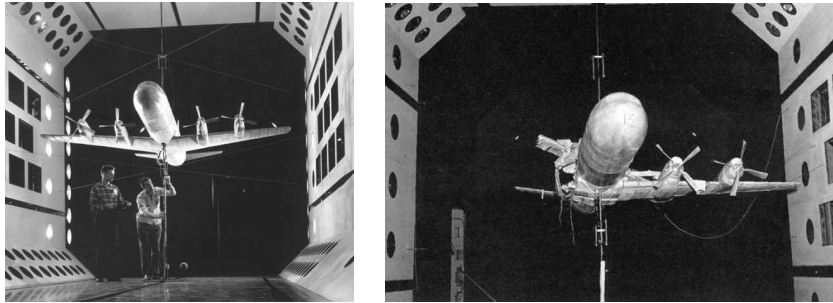


Figure 2.21: L188 model in the NASA Langley Transonic Dynamics Tunnel

We will examine the basics dynamics of whirl flutter by considering a simple two degree of freedom system, with appropriate simplifications. Although the following discussion is focused on the propeller whirl case, similar analyses could be carried out for other interesting configurations, including wind turbines and helicopter rotors.

2.3.1 A Simplified model

We consider a propellor rotating with a shaft at a very high angular velocity Ω (figure 2.22). The shaft is stiff, but is mounted such that it can deflect with the small angles ψ and θ . These motions are resisted by the structural stiffnesses K_ψ and K_θ . An additional aerodynamic force F_A operates at the propeller end of the shaft. The propeller is assumed to have 3 or more blades, so it can reasonably be approximated as a disk. Because Ω is large, we assume that the

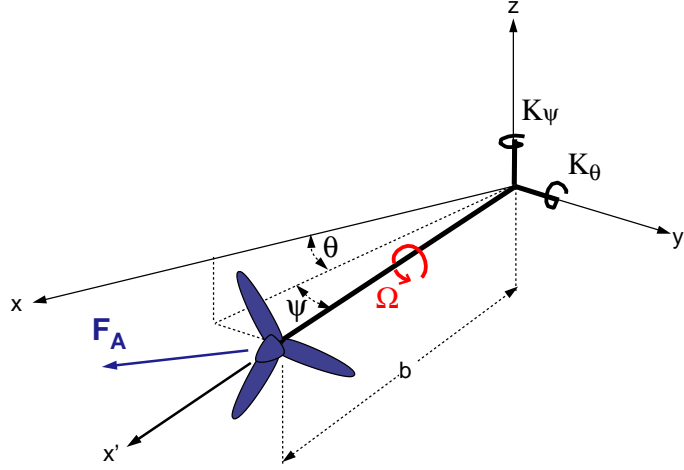


Figure 2.22: 2-DOF model of whirl flutter

angular momentum in rotor-fixed coordinates about the axis x' , H_Ω , is much larger than that of the other two directions, i.e.:

$$H_\Omega \gg H_{\dot{\psi}}, H_{\dot{\theta}} \quad (2.58)$$

as a consequence:

$$\frac{dH_\Omega}{dt} = 0 \quad (2.59)$$

Conservation of angular momentum requires:

$$\frac{d\vec{H}}{dt} + \vec{\omega} \times \vec{H} = \sum \vec{M} \quad (2.60)$$

where the vectors are measured with respect to a frame moving with $\vec{\omega} = (0, \dot{\theta}, \dot{\psi})$. For $\vec{\omega} \times (H_\Omega, 0, 0) \gg \vec{\omega} \times (0, H_{\dot{\theta}}, H_{\dot{\psi}})$ (2.60) becomes:

$$I_y \ddot{\theta} + I_x \Omega \dot{\psi} = -K_\theta \theta - F_{Az} b + M_{Ay} \quad (2.61)$$

$$I_z \ddot{\psi} - I_x \Omega \dot{\theta} = -K_\psi \psi + F_{Ay} b + M_{Az} \quad (2.62)$$

where \vec{F}_A and \vec{M}_A are the aerodynamic forces and moments, and b is the shaft length. These equations are coupled both gyroscopically and aerodynamically.

2.3.2 Gyroscopic Coupling

If the rotor operates in a vacuum ($F_A = M_A = 0$), the gyroscopic moment terms $I_x \Omega \dot{\psi}$ and $-I_x \Omega \dot{\theta}$ will act to produce two coupled motions:

1. a forward whirl mode (frequency higher than uncoupled frequencies)
2. a backward whirl mode (frequency lower than uncoupled frequencies)

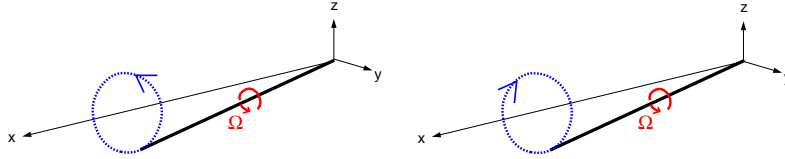


Figure 2.23: Forward (left) and backward (right) whirl modes

Both motions will be circular if $I_y = I_z$

2.3.3 Aerodynamic Coupling

Aerodynamic forcing can act to produce unstable (flutter) modes. How this occurs can be visualised using figure 2.24. Consider first the angle of attack

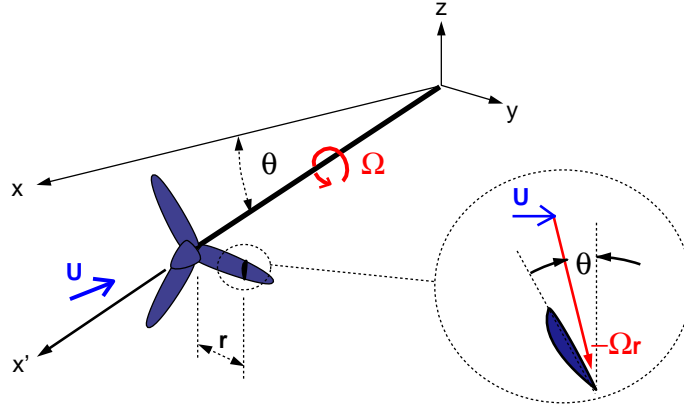


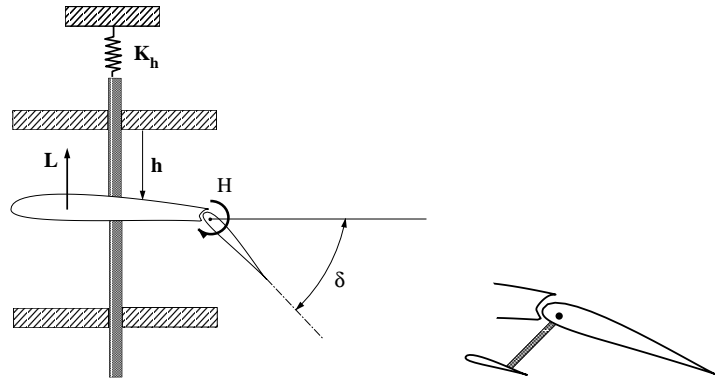
Figure 2.24: Aerodynamic Coupling

of a section on the up-going blade. If $\theta > 0$ is positive, the angle of attack will be increased. Conversely, the section angle of attack on down-going blade decreased for $\theta > 0$. This results in $M_{Az} < 0$ when $\psi = 0$ and $\theta = \theta_{max}$. The result is that the aerodynamic coupling tends to drive the backward whirl mode, and oppose the forward whirl mode.

2.4 Practice Problems

p2.4.1 Derive an expression for the $q_{divergence}$ of the semi-rigid wing (hint: first use the equations of motion and angle of attack equation to derive an explicit expression for α_d). Plot the variation of the divergence speed with wing sweep. Derive an expression for the aeroisoclinic condition.

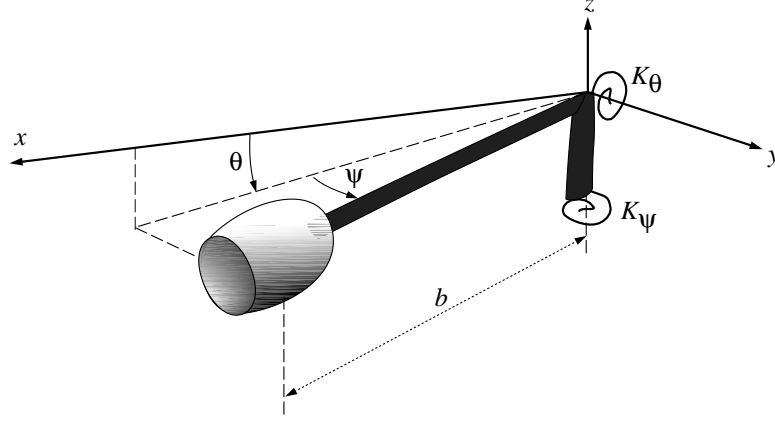
p2.4.2 An experimental setup for measuring control-surface flutter is shown in left part of the figure below. The airfoil section can translate in the vertical direction, but cannot rotate. Motion in the vertical direction is resisted by a spring, K_h . The control surface is free to rotate about its hinge ($K_\delta = 0$). The mass of the complete configuration is m , while the static moment and moment of inertia of the control surface at the hinge axis are S_δ and I_δ , respectively.



- Derive the characteristic equation for this configuration. Assume the lift is given by $L = [C_{L_\delta} \cdot \delta]qS$ and the aerodynamic hinge moment by $H = [C_{H_\delta} \cdot \delta]cqS$ (i.e. a steady aerodynamic model).
- What types of motion are possible if the experimenter forgets to hook up the spring ($K_h = 0$)?
- Assume an aerodynamic balance (see figure above, right) has been added to the control surface, such that the net aerodynamic hinge moment is zero ($C_{H_\delta} = 0$). Draw flutter diagrams for the configuration for both positive and negative values of S_δ (assume $K_h \neq 0$ and $S_\delta^2 < mI_\delta$).

p2.4.3 For the typical section with two degrees of freedom (θ, h), under what conditions is flutter possible if the AC lies ahead of the EA and the EA lies ahead of the CG?

p2.4.4



The motion of a ducted fan mounted on a wind-tunnel support stand is described by:

$$I_y \ddot{\theta} + I_x \Omega \dot{\psi} + K_\theta \theta - a b q \theta = 0$$

$$I_z \ddot{\psi} - I_x \Omega \dot{\theta} + K_\psi \psi - a b q \psi = 0$$

where a is the lift-curve slope of the engine nacelle, q is the dynamic pressure, and Ω is the engine rotation speed.

- a) Derive the characteristic equation for this system.
- b) Assume $I_z = I_y = 1$, $I_x = \frac{1}{\sqrt{2}}$, $K_\theta = K_\psi = 1$, $ab = 2$ and $\Omega = 2$. Would you permit this setup to be run at the test condition of $q = 1$?

Chapter 3

Unsteady Aerodynamics

In the previous chapter, it was demonstrated how energy can be added to the structural system if we have the correct phase between structural motion and aerodynamic forces. But what if the aerodynamic forces are themselves not in phase with the instantaneous position of the aerodynamic surfaces? This is precisely what occurs when the effects of unsteady aerodynamics are significant. In fact, not only may the relative phases be large, but the magnitudes of unsteady forces can also differ considerably from their quasi-steady counterparts. As a result, neglecting unsteady aerodynamic effects can result in substantial errors in predictions of aeroelastic behaviour.

There are several physical processes which contribute to unsteady aerodynamic effects. For airfoils, important examples include the influence of vortical convection, compressible effects such as time delays due to the finite speed of sound and shock movement, and viscous effects including flow separation and boundary-layer dynamics. We will begin this chapter with some qualitative descriptions of these phenomena. Then we will examine a hierarchy of model equations which can be used to predict all or some of their behaviour. We will finish by listing some of the analytic solutions which have been derived for these equations to date.

3.1 Vorticity Dynamics

If viscosity is neglected, one can show that the model equations for fluid flow express (among other things) the convection of vorticity along streamlines. The dynamics of such convecting vorticity can profoundly effect the forces generated on nearby solid bodies. To see why this is so, we will consider a thought experiment based on the theory of incompressible potential flow for an airfoil.

You should be familiar with the idea of the lift force on an airfoil being related with its value of “bound circulation”, often associated with a point vortex at the airfoil $1/4$ point. In steady aerodynamic theory, the value of the bound circulation is determined by the Kutta condition, a condition which

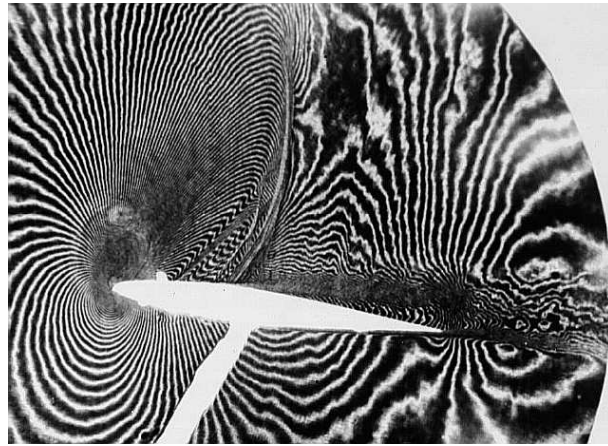


Figure 3.1: A flow with compressible effects (e.g. shocks), viscous effects (e.g. shock-boundary layer interaction, separation), and vorticity dynamics (e.g. wake and turbulent regions).

prevents a singularity from appearing at an airfoil's sharp trailing edge. It is useful to consider the Kutta condition in more detail. To start with, note that there is nothing in the potential flow equations themselves which dictate that no singularities can be present in the flow (in fact singularities are often used as building blocks to construct potential flow solutions). Thus the zero bound circulation solution shown in figure 3.2 is a perfectly valid one.

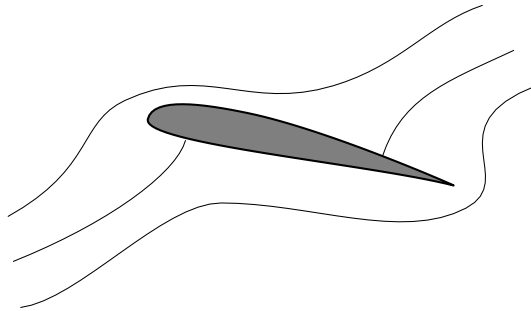


Figure 3.2: Zero-circulation potential flow solution

Now consider the *impulsive start* of an airfoil from rest. Initially, the flow pattern will indeed resemble figure 3.2. Zooming into the trailing edge, however, reveals some basic problems for a real viscous flow (figure 3.3). At the trailing edge, the sharp geometry will lead to velocities which tend towards infinity, implying very low pressures. Meanwhile, at the stagnation point on the rear

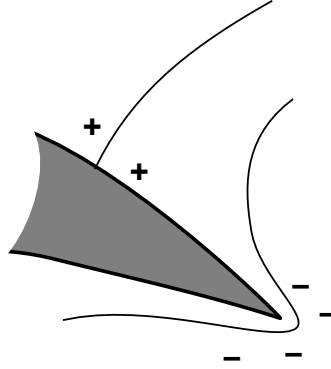


Figure 3.3: Pressure field of the zero-circulation potential flow solution

upper surface, the pressure reaches its highest possible value. Therefore the flow which tracks around the trailing edge towards the stagnation point experiences a severe adverse (positive) pressure gradient. From boundary layer theory, adverse pressure gradients in wall-bounded flows tend to induce separation. This can be seen by considering the boundary-layer streamwise momentum equation (see equation (3.7) later in this chapter) for a constant viscosity evaluated at the airfoil surface, where the velocities are zero due to the no-slip condition:

$$\mu \frac{\partial^2 u_i}{\partial x_1^2} = \frac{\partial p_e}{\partial x_i} \quad (3.1)$$

Where x_1 is the wall-normal direction. Thus in a positive pressure gradient, the second derivative of the profile in the normal direction also tends to be positive at the wall. This is characteristic of profiles near separation, as shown in figure 3.4.

Thus there is separation from the sharp trailing edge, leading to the formation of a vortex, known as the “starting vortex” above the airfoil (figure 3.5). This is in turn carried downstream with the flow (figure 3.6). Kelvin’s theorem states that the total vorticity within a closed contour which convects with the flow remains constant. If we draw this contour around the airfoil alone we recover the circulation of the bound vortex. If we draw it large enough to enclose both the bound and starting vortices, we see that the total vorticity must be zero (its value before the impulsive start) and that the starting vortex is equal and opposite in strength to the bound vortex.

While the starting vortex is in the immediate vicinity of the airfoil, its induced velocity field tends to lower the local angle of attack. The result is a lift value which is lower than that of the final steady-state value (in an incompressible inviscid flow, the initial value of airfoil lift is roughly half that of its final value). As the starting vortex convects downstream, its influence wanes so that the final steady lift value is approached asymptotically.

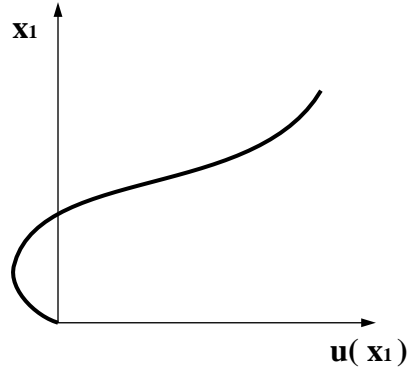


Figure 3.4: A profile with $\frac{\partial^2 u_i}{\partial x_1^2} > 0$ near the wall

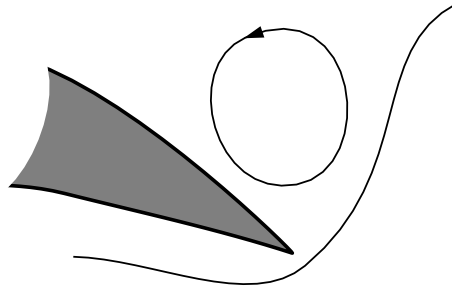


Figure 3.5: Formation of the starting vortex

Any change in circulation of an airfoil is associated with the shedding of vorticity with equal magnitude and opposite sign. If we consider an oscillating profile, it is clear that it must be continuously shedding vorticity increments (figure 3.7). The sign of these increments is determined by the position within the oscillation cycle. The resulting oscillatory wake can induce a significant phase lag and magnitude change of the aerodynamic forces relative to those computed with a purely steady theory.

The wake vorticity also induces a velocity field which influences the shape of the wake itself (remember vorticity is carried with the local velocity). This leads to complex wake shapes as time evolves, a factor which can considerably complicate numerical methods which rely on wake tracking.

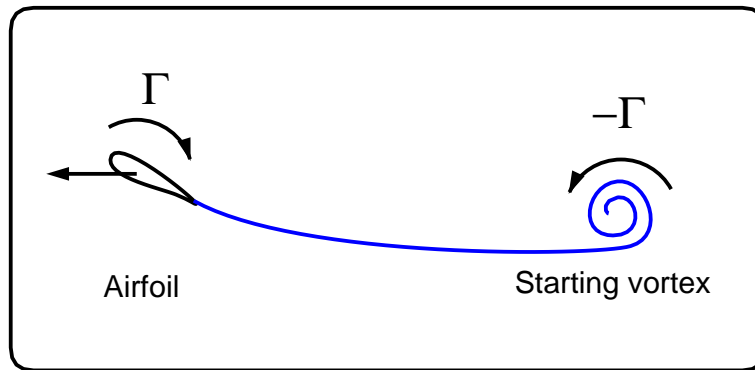


Figure 3.6: Circulation within an initial contour

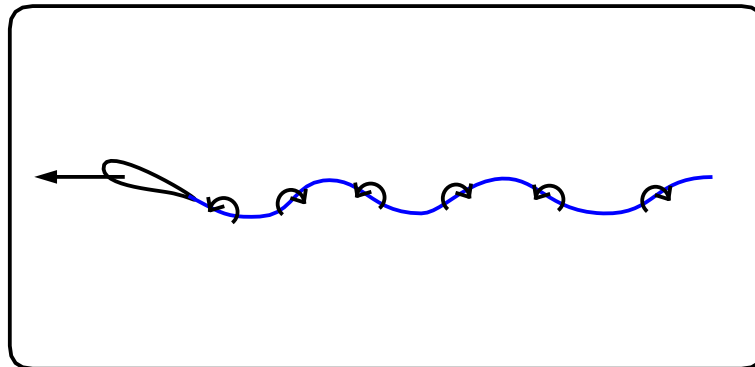


Figure 3.7: Wake vorticity due to oscillating airfoil

3.2 Compressibility effects

The inviscid compressible equations can also be used to show that acoustic waves propagate with the finite speeds $u + c$ and $u - c$, where u is the local flow velocity and c is the local value for the speed of sound. Steady supersonic airfoil theory demonstrates that for Mach numbers greater than one, this results in finite zones of influence and dependence in space. For unsteady flows, there are finite zones of influence and dependence in *space-time*, even in subsonic conditions.

Finite acoustic wave speeds imply that the state of a given point is influenced by its neighbours at different times. Consider the airfoil shown in figure 3.8. If

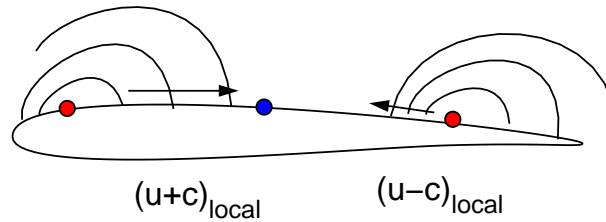


Figure 3.8: Acoustic wave propagation in a subsonic flow

the airfoil is moved suddenly, the three points shown in the figure will immediately begin to adjust their local states to the new boundary conditions. Their transients won't be complete, however, until the information reaching them from all other points on the airfoil remains fixed. The speed at which the information travels depends on the wave direction ($\pm c$) and on the local velocity produced by the flow u . If u is of a comparable size to c , then the point in the middle will hear from the downstream point at a much later time, resulting in a prolonged transient, and a complex local behaviour in time. Note that information travelling from the airfoil's wake can experience significant delays, resulting in significant response time lags.

As the Mach number is increased into the transonic region, shocks will begin to appear. A typical transonic pressure flow topology, and its associated pressure distribution is shown in figure 9. It is clear from the pressure distribution that the position of the shock has a strong influence on the the forces and moments, and thus the aeroelastic response. At very high excitation frequencies it is possible to show that the amplitude of shock movement is small, albeit with significant phase lag. At very low excitation frequencies one can expect a quasi-static transonic response. In between this range, where the majority of cases lie, shock dynamics are hard to predict. This is because they are determined by the time history of the acoustic wave pattern, which is even more complex when the flow contains embedded regions of supersonic flow. Figure 3.10 shows the time it takes for a signal travelling forward from the trailing edge of an airfoil to reach a given streamwise position. In the transonic case (right), the delay is significantly increased by the presence of the shock, as the information

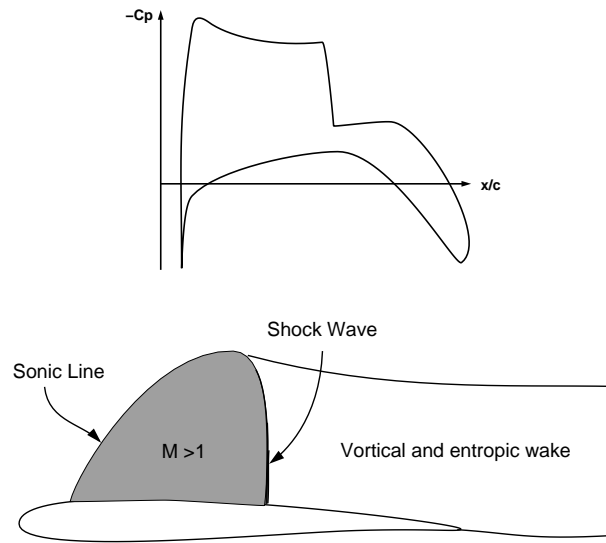


Figure 3.9: A typical transonic flow topology (below) and its associated pressure distribution (above)

must first travel around the supersonic region before reaching the points ahead of the shock. The time required for this is a strong function of the shock geometry, which is a function of the airfoil geometry (e.g. compare supercritical profiles to conventional ones). If the shock is moving, the transient becomes even more complex. The difficulty of predicting responses in the transonic regime is further highlighted by figures 11 and 12. which compare linearised theory to experiment for an oscillating flap as a function of the flow Mach number. The mean measured pressure coefficient, C_p , along with the in-phase C_p' and out-of-phase C_p'' measured and computed unsteady pressure perturbations are shown. Clearly the linearized theory does fairly well until transonic effects begin to appear $M = 0.85$, after which it becomes increasingly inaccurate.

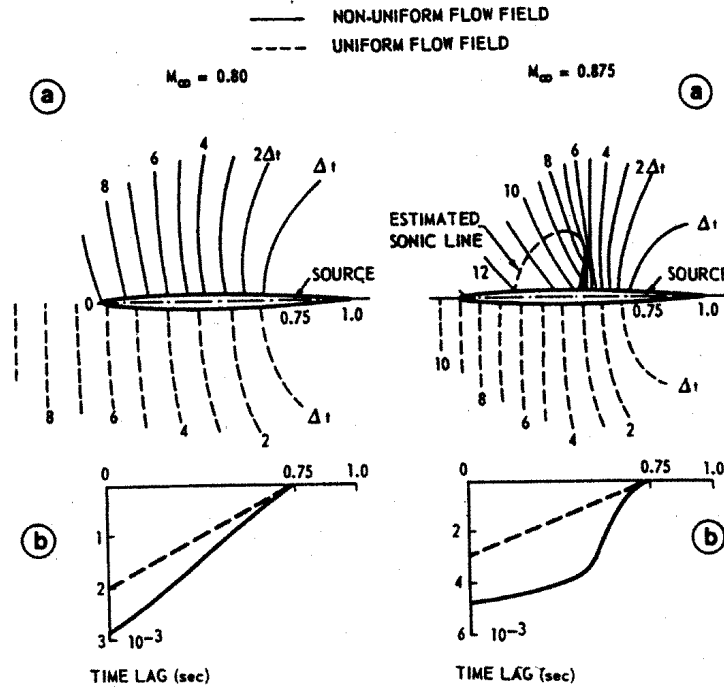


Figure 3.10: Time delays due to the presence of an airfoil (From Tijdeman, NLR TR 77090U)

3.3 Viscous effects

When analysing aerodynamic flows it is normally possible to ignore viscous effects except near the solid boundaries, where the complex dynamics of either the laminar or turbulent boundary layers ultimately determine the transient behaviour of the viscous drag. For thin wings, however, viscous drag may be only a minor contributor to the aeroelastic response. Still the effects of neglecting viscosity can be large, since they can also significantly affect the unsteady lift, as discussed in the examples below.

Returning first to the discussion of the Kutta condition in section 3.1, we note that the dynamics of the trailing separation can be influenced by the frequency of oscillation. At very high frequencies, it is possible to have a reduction in the effect of the Kutta condition via the appearance of a counter vortex near the trailing edge (figure 3.13). In this case the change in forces can be substantially reduced. The exact effect observed, however, will be a function of the trailing edge geometry and sharpness.

Assuming the Kutta condition is satisfied, the unsteady lift can still be affected by the transient response of the attached boundary layer over the wing. In

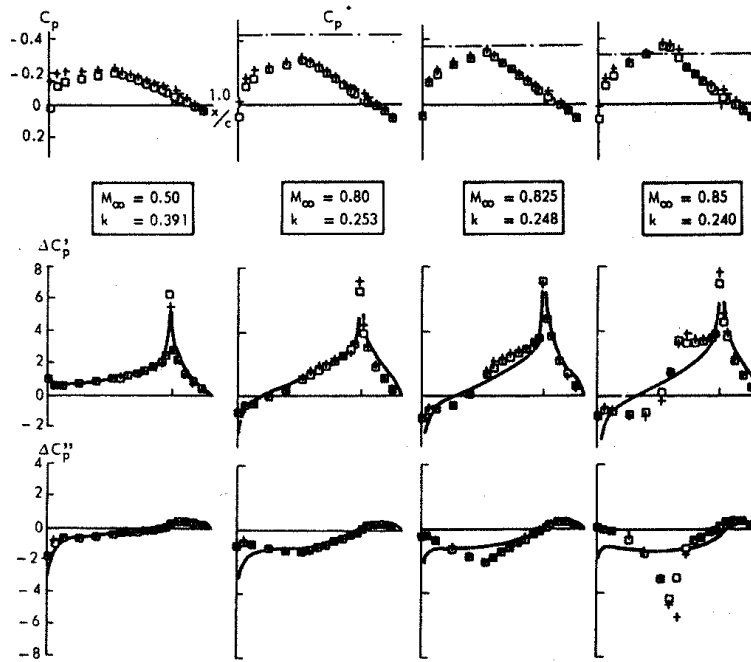


Figure 3.11: Pressure distributions for a NACA 64006 with an oscillating flap. Steady (upper) and real and imaginary components (lower) comparison of experiment (symbols) with linear theory (lines). (From Tijdeman, NLR TR 77090U)

steady flows, the upper surface boundary layer tends to thicken more rapidly than lower surface boundary layer as the angle of attack is increased. This results in a reduction in the effective camber of the section. (figure 3.14). This effect is further enhanced if a control surface is deflected. In unsteady flows, the decambering effect becomes a function of the boundary-layer dynamics, which is itself different from the main flow dynamics due to the relatively low-inertia near-wall flow.

If separation occurs, the forces and moments are much more directly affected. Conventional separation patterns include the leading and trailing edge separations shown in the left part of figure 3.15, and the transonic ones shown at right. The latter occur due to the strong adverse gradients encountered when passing through the shock wave, and can manifest themselves as either bubbles or complete separated regions. What makes it interesting is that the shock position is also a function of the separation pattern. These types of problems pose difficult challenges to even the most advanced computational techniques.

Under certain circumstances, it is possible to have a self-sustained oscillation which is driven by cycles of separation and re-attachment. A prominent example

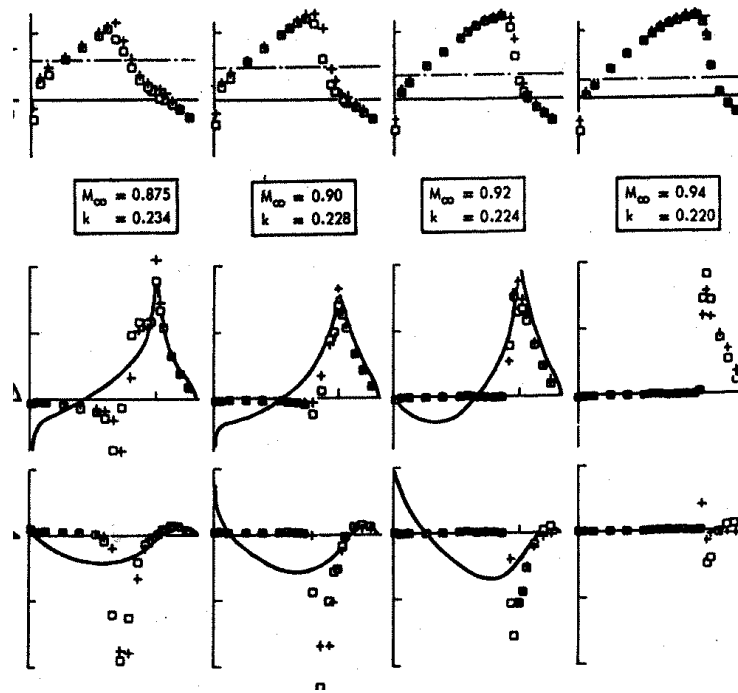


Figure 3.12: Pressure distributions for a NACA 64006 with an oscillating flap. Steady (upper) and real and imaginary components (lower) comparison of experiment (symbols) with linear theory (lines). (From Tijdeman, NLR TR 77090U)

of this is *dynamic stall*, where leading edge separation, vortex convection and re-attachment can provide significant pitching moment excitation. If the structure is flexible, its motion can in turn drive the dynamic stall cycle. The basic pattern is illustrated in figures 16 and 17. (Note that the letter indications do not correspond between the two figures).

Another type of self-sustained oscillation, known as *aerodynamic resonance*, can occur in transonic conditions. The basic cycle is shown in figure 18. As the shock moves aft, it strengthens, leading to boundary-layer separation. The resulting loss in circulation encourages the shock to move forward again, while the pressure field encourages aft movement of the lower shock. The cycle then alternates on both surfaces. What is remarkable about this self-sustained oscillation is that it can even happen when the structure is fixed.

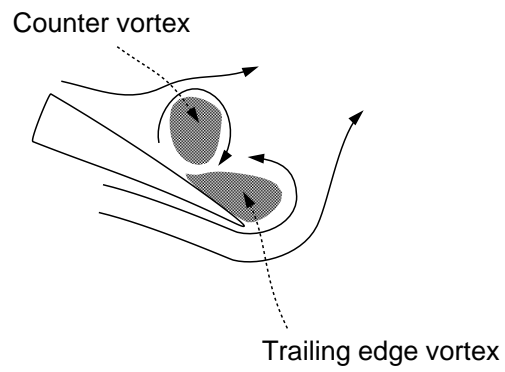


Figure 3.13: Reduction in the effectiveness of the Kutta condition

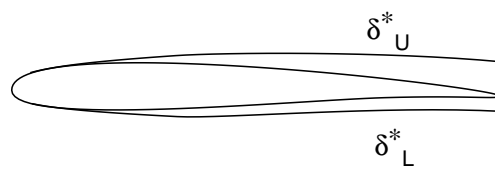


Figure 3.14: Viscous de-cambering effect

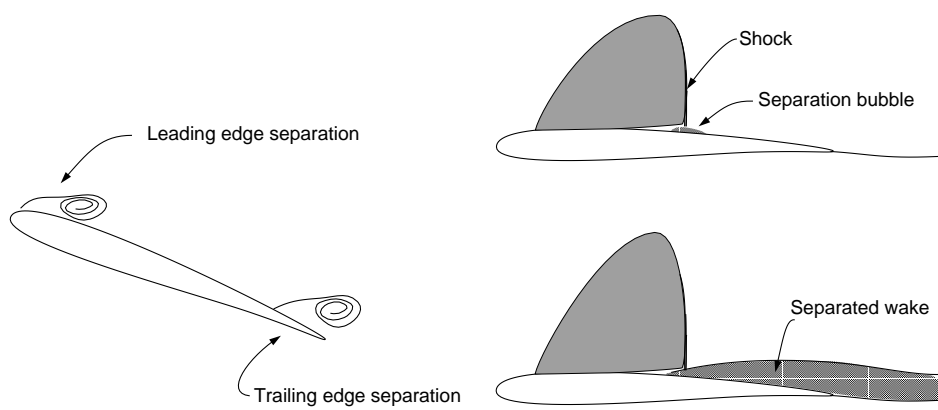


Figure 3.15: Conventional and transonic separation patterns

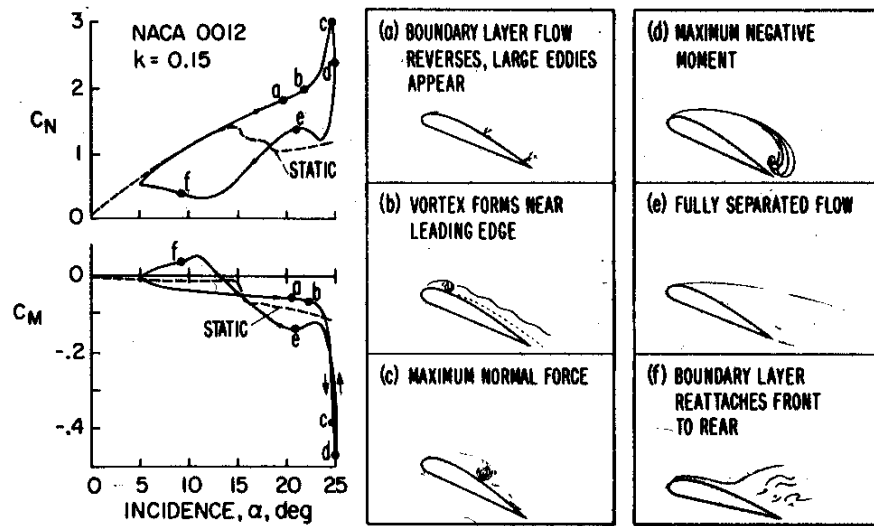


Figure 3.16: Dynamic Stall (1) From McCorskey, Journal of Fluid Engineering March 1977, 8-39

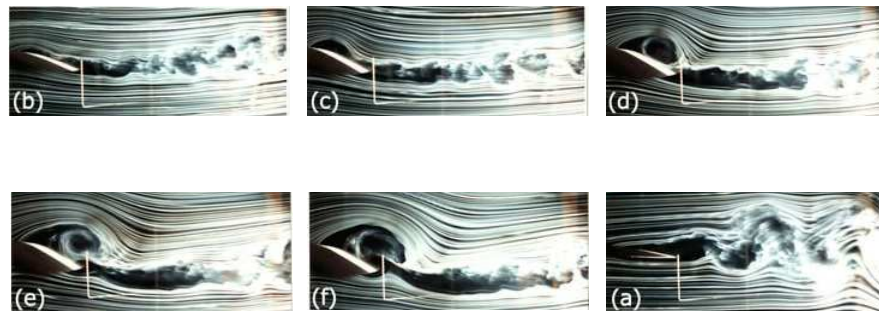


Figure 3.17: Dynamic Stall (2)

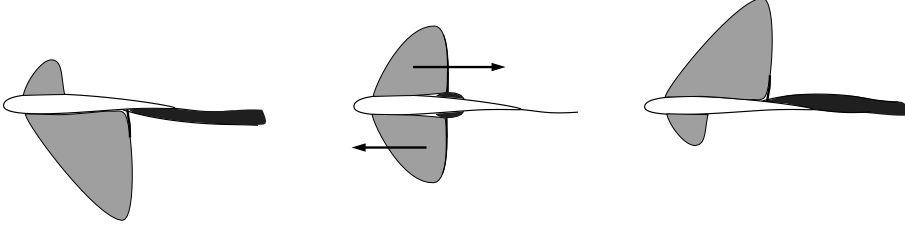


Figure 3.18: Aerodynamic resonance

3.4 Model Equations for Unsteady Flows

Here we will review the various sets of model equations which can be used to predict unsteady aerodynamic flows. Starting with the Navier-Stokes equations, models with varying levels of approximation will be described, and their advantages and disadvantages discussed. Figure 19 illustrates the hierarchical relationship between the model equations presented here.

3.4.1 Navier-Stokes Equations

The Navier-Stokes equations may be used to model all effects in homogeneous flows which may be described as a continuum. They express the conservation of mass, momentum, and energy for a viscous compressible fluid, and may be written in integral form for a moving control volume (figure 20) as:

$$\frac{d}{dt} \int_V W \, dV + \int_S (\vec{F}^i - \vec{F}^v - \dot{x}W) \cdot \vec{n} \, dS = 0 \quad (3.2)$$

$$W = \begin{bmatrix} \rho \\ \rho \vec{u} \\ \rho E \end{bmatrix}, \quad \vec{F}^i = \begin{bmatrix} \rho \vec{u} \\ \rho \vec{u} \vec{u} + p \bar{\bar{I}} \\ \rho \vec{u} H \end{bmatrix}, \quad \vec{F}^v = \begin{bmatrix} 0 \\ \bar{\bar{\tau}} \\ \bar{\bar{\tau}} \cdot \vec{u} - \vec{q} \end{bmatrix}$$

Here W is known as the state vector, and contains the unknown conservative variables density (ρ), momentum ($\rho \vec{u}$), and total specific energy (ρE), where \vec{u} is the local fluid velocity and $E = \epsilon + \frac{1}{2} |\vec{u}|^2$, the sum of internal and kinetic energies. The total enthalpy H , is given by $H = E + p/\rho$, where p is the local value of pressure.

The inviscid flux vector, \vec{F}^i , in combination with the term $\dot{x}W$, expresses the transport of the conserved variables across the control surface. It also includes the effect of the pressure acting on the control surface on the balance of momentum within the control volume. The viscous flux vector, \vec{F}^v , contains the effects of viscous stresses. These are described by the viscous stress tensor,

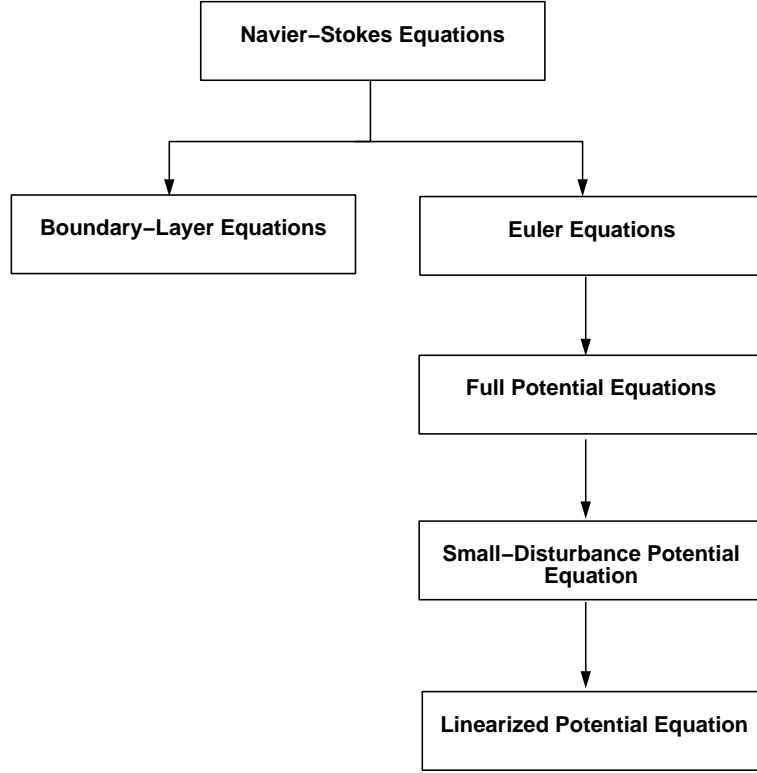


Figure 3.19: Models for unsteady aerodynamic flows

$\bar{\bar{\tau}}$, which has components given by:

$$\tau_{ij} = \mu \left[\frac{\partial u_i}{\partial x_j} + \frac{\partial u_j}{\partial x_i} \right] + \lambda \delta_{ij} \frac{\partial u_k}{\partial x_k} \quad (3.3)$$

where μ and λ are the viscosity coefficients. Normally λ is taken to be $2\mu/3$. The viscosity coefficients are functions of temperature, and for most circumstances their variation is determined experimentally.

To complete the system, a thermodynamic relation is required which relates the pressure to the remaining flow variables. For many aerodynamic flows, an ideal gas model may be used. In some specialized cases (e.g. re-entry vehicles) this assumption is inappropriate, and more elaborate thermodynamic relations must be employed.

Although a few specialized analytic solutions to the Navier-Stokes equations exist, numerical techniques must usually be used to solve flow problems of engineering interest. The computational cost of numerical simulations, however, is strongly affected by the enormous range of length scales present at the high Reynolds numbers typical of aerodynamic flows. This arises from the need to represent the effects of turbulence, for which relevant length scales can be several

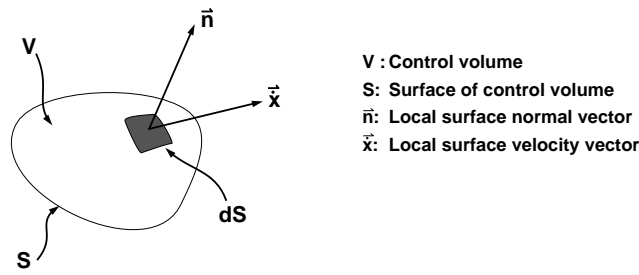


Figure 3.20: Nomenclature for a moving control volume

orders of magnitude smaller than the global scales of interest for an aeroelastic problem (airfoil chord, wing span etc.) Various approaches for dealing with this difficulty are summarized below:

DNS

DNS stands for direct numerical simulation, and refers broadly to computations which attempt to resolve all the turbulent lengths scales of a flow. These computations must be performed in three spatial dimensions in order to properly capture the dynamics of turbulence. Although feasible for low-Reynolds-number flows, the expense of DNS increases rapidly with Reynolds number. For the foreseeable future, DNS techniques will be impractical for direct application to aeroelastic problems. They will continue to play an important indirect role, however, in the the formulation of models of turbulent behaviour, which are required to exploit the techniques described in the next two sections.

LES

Large Eddy Simulation (LES) techniques make use of a sub-grid scale model (SGS) to eliminate the smallest turbulence length scales from consideration, while fully simulating the dynamics of the larger structures. This technique works well for free turbulent flows, where the dynamics of the smallest scales can be sufficiently well represented using simplified models. For wall-bounded flows, however, it can be difficult to model smaller scales accurately, due to the highly anisotropic nature of turbulent boundary layers. Although the development of accurate near-wall SGS models is an area of active research, presently DNS-like resolution is required near the wall in order to obtain accurate results. Consequently, LES computations remain too expensive to be routinely used for aeroelastic computations.

F/RANS

The classical approach to dealing with turbulence is based on the concept of averaging, as introduced by Reynolds in 1895. In summary, one may decompose

the quantities of interest in the flow, for example the pressure, $p(x, t)$, into mean and fluctuating components:

$$p(x, t) = \bar{p}(x, t) + p'(x, t) \quad (3.4)$$

where the mean value is given by averaging over a time scale, T :

$$\bar{p}(x, t) = \frac{1}{T} \int_t^{t+T} p(x, t) dt \quad (3.5)$$

where T must be chosen to be large compared to the time scale of turbulent fluctuations. Substitution of the mean and fluctuating components of each variable into the Navier-Stokes equations and averaging over time leads to the Reynolds-averaged Navier-Stokes equations (RANS) for incompressible flows, or the Favre-averaged Navier-Stokes equations for compressible flows. These equations contain additional terms arising from the correlation of the fluctuating solution components. The correlations represent new unknowns, the behavior of which must be described by an additional turbulence model.

There are numerous approaches to turbulence modelling, each of which has different ranges of applicability. Although reasonable results can be obtained for certain classes of flows, the development of turbulence models remains an active research area, as obtaining accurate results for arbitrary flow conditions can be difficult. When applied to unsteady flows, an additional problem arises in the choice of the averaging period, T . In practice, it may be difficult to separate the time scales of slowest turbulent fluctuations from those of the aeroelastic-induced flow unsteadiness. In such cases, the use of the time-averaging approach becomes questionable, and other modelling procedures must be applied.

In spite of the difficulties mentioned above, the application of the Reynolds or Favre-averaged Navier-Stokes equations to aeroelastic problems can produce useful results. However, for realistic three-dimensional aircraft geometries simulation costs remain relatively high, limiting their repeated use for aeroelastic design procedures.

3.4.2 Boundary-Layer Equations

The boundary-layer equations are an approximation of the Navier-Stokes equations based on the observation that in high Reynolds-number flows, viscous effects are usually confined to thin regions adjacent to solid boundaries. When the radius of curvature of such regions is large compared to their thickness, the local streamwise flow gradients can be considered to be much smaller than the gradients normal to the surface. This results in a considerable simplification of the momentum equation written for the direction normal to the surface:

$$\frac{\partial p}{\partial x_1} = 0 \quad (3.6)$$

while the remaining momentum equations collapse to:

$$\frac{\partial \rho u_i}{\partial t} + \frac{\partial}{\partial x_j} (\rho u_i u_j) = -\frac{\partial p_e}{\partial x_i} + \frac{\partial}{\partial x_1} \left(\mu \frac{\partial u_i}{\partial x_1} \right) \quad (3.7)$$

where x_1 is the direction normal to the surface, and p_e is the pressure of the flow at the edge of the boundary layer, which is that of the external inviscid flow. The resulting system, which includes the continuity and energy equations, is solved only within the thin viscous layer, with boundary conditions given by the no-slip condition at the wall, and the external flow velocities and pressures on the boundary layer edge. In many cases, the solution to the boundary layer equations may be found using marching techniques which exploit the parabolic character of the equations. This makes such techniques very efficient.

3.4.3 Euler Equations

The Euler equations can be obtained from the Navier-Stokes equations by directly eliminating the viscous terms (i.e. $\vec{F}^v = 0$ in (3.2)). From the point of view of aeroelasticity, this limits their application to problems where viscous effects do not significantly affect the forces and moments transferred to the aircraft structure. In practice, this requires attached flow, and shock Mach numbers below about 1.4 (in order to avoid significant shock/boundary-layer interactions).

Alternatively, the influence of viscous effects can be accounted for by solving the boundary-layer equations near solid walls based on an Euler solution for the external flow, and in turn correcting the Euler solution using the computed displacement thickness of the boundary layer. This approach is known as the viscous-inviscid interaction method, and can be used to treat attached flows, or those with small regions of separation.

The Euler equations are powerful in that they fully represent all of the inviscid effects associated with unsteady flow, including the convection of entropy and vorticity, and the propagation of information via acoustic waves. In the context of aeroelastic applications, the fact that vorticity dynamics are automatically included in the solution is a great advantage when considering complex wakes, or multiple-wake interactions. The solution of the unsteady Euler equations in three dimensions is still relatively expensive, but is certainly feasible for exploratory computations.

3.4.4 Full Potential Equations

The full potential equations can be derived from the Euler equations by assuming the flow to be irrotational and isentropic. To do so, we must first convert the integral form (3.2) with $\vec{F}^v = 0$ to a differential form. Leaving out the motion of the control volume for now, we can use Gauss's formula to convert the surface integral term to a volume integral:

$$\int_S \vec{F}^i \cdot \vec{n} \, dS = \int_V \nabla \cdot \vec{F} \, dV \quad (3.8)$$

As the size of the control volume is arbitrary, the complete volume integral (including the first term of (3.2)) can only be true if it is true for all points

within the volume, allowing us to write the differential form of the equations as:

$$\frac{\partial W}{\partial t} + \nabla \cdot \vec{F}^i = 0 . \quad (3.9)$$

Consider for a moment the continuity and momentum equations:

$$\frac{\partial \rho}{\partial t} + \nabla \cdot (\rho \vec{u}) = 0 \quad (3.10)$$

$$\frac{\partial \rho \vec{u}}{\partial t} + \nabla \cdot (\rho \vec{u} \otimes \vec{u}) + \nabla p = 0 \quad (3.11)$$

By subtracting the continuity equation from the momentum equation, and using the identity:

$$\vec{u} \cdot \nabla \vec{u} = \frac{1}{2} \nabla |\vec{u}|^2 + (\omega \times \vec{u}) \quad (3.12)$$

where ω is the local vorticity vector, $\nabla \times \vec{u}$, we can also express the momentum equation as:

$$\frac{\partial \vec{u}}{\partial t} + \frac{1}{2} \nabla |\vec{u}|^2 + (\omega \times \vec{u}) + \frac{1}{\rho} \nabla p = 0 \quad (3.13)$$

Recalling the second law of thermodynamics, which can be expressed in terms of the enthalpy, $h = \epsilon + p/\rho$, as:

$$dh = T ds + \frac{1}{\rho} dp \quad (3.14)$$

we then can express the momentum in terms of the total enthalpy, H , as:

$$\frac{\partial \vec{u}}{\partial t} + \nabla H = -(\omega \times \vec{u}) + T \nabla s = 0 \quad (3.15)$$

where T is the local temperature, and s is the local entropy. Equation (3.15) is known as Crocco's relation and is still exact within the framework of the Euler equations. Now we assume irrotational, isentropic flow, allowing us to replace the representation of the velocity field with the gradient of a scalar potential function, $\vec{u} = \nabla \Phi$. Equation (3.15) then becomes:

$$\frac{\partial \nabla \Phi}{\partial t} + \nabla H = 0 \quad (3.16)$$

or

$$\frac{\partial \Phi}{\partial t} + H = \text{const} \equiv H_\infty \quad (3.17)$$

We can use this equation to construct an explicit relationship between density and the potential function by using the isentropic formula for a perfect gas:

$$\frac{\rho}{\rho_\infty} = \left[\frac{h}{h_\infty} \right]^{\frac{1}{\gamma-1}} = \left[\frac{1}{h_\infty} \left(H_\infty - \frac{\partial \Phi}{\partial t} - \frac{|\nabla \Phi|^2}{2} \right) \right]^{\frac{1}{\gamma-1}} \quad (3.18)$$

Noting that $h = C_p T$ and $a = \sqrt{\gamma R T}$, this can be written as:

$$\frac{\rho}{\rho_\infty} = \left[1 + \frac{\gamma - 1}{2a_\infty^2} \left(U_\infty^2 - 2 \frac{\partial \Phi}{\partial t} - |\nabla \Phi|^2 \right) \right]^{\frac{1}{\gamma-1}} \quad (3.19)$$

Finally, we can also relate the potential function to the density via the continuity equation:

$$\frac{\partial \rho}{\partial t} + \nabla \cdot (\rho \nabla \Phi) = 0 \quad (3.20)$$

Equations (3.19) and (3.20) form a coupled non-linear system for only two unknowns, even for three-dimensional problems. These are the full potential equations, and represent a considerable simplification of the original Euler system. As a result, numerical schemes for the full potential equations are relatively inexpensive.

The assumptions used in deriving the full potential equations have two consequences. Firstly, the assumption of isentropic flow limits consideration to weak shocks, i. e. those with Mach numbers less than 1.3. Secondly, assuming the flow to be irrotational requires that vortical wakes be explicitly modelled, as opposed to being “captured” as part of the solution. This can be difficult to do in three dimensions, especially for situations which involve strong wake-wake interactions.

3.4.5 Small-Disturbance Potential Equation

To derive the small-disturbance potential equations, we consider the perturbations to the full potential equations for the case of a uniform freestream aligned with the x-axis:

$$\Phi = \Phi_\infty + \phi = U_\infty x + \phi \quad (3.21)$$

During the derivation, however, we note that that small terms which accompany $(1 - M^2)$ must be retained, as $(1 - M^2)$ is itself small in the transonic regime. This leads to the following non-linear equation for the disturbance potential:

$$\left[1 - M_\infty^2 - (\gamma + 1) M_\infty^2 b \frac{\partial \phi}{\partial x} \right] \frac{\partial^2 \phi}{\partial x^2} + \frac{\partial^2 \phi}{\partial y^2} + \frac{\partial^2 \phi}{\partial z^2} = \frac{1}{a_\infty^2} \left(2U_\infty \frac{\partial^2 \phi}{\partial x \partial t} + \frac{\partial^2 \phi}{\partial t^2} \right) \quad (3.22)$$

Equation (3.22) is still capable of representing shocks, although the assumption of small disturbances further limits its accuracy relative to the basic isentropic, irrotational flow restrictions. A significant advantage, however, is that the boundary conditions can now be linearised and applied on a reference plane instead of the true wing and wake surfaces. This eliminates the problem of dealing with moving grids for wings which change their shape.

In order to complete the description of the flow, we need to derive a equation relating the local value of the pressure to the small-disturbance potential. This

can be done by considering the momentum equation written using (3.21), and eliminating higher-order terms:

$$p - p_\infty = -\rho_\infty \left(\frac{\partial \phi}{\partial t} + U_\infty \frac{\partial \phi}{\partial x} \right) \quad (3.23)$$

Note that the equation for pressure is decoupled from (3.22), resulting in further reductions in computational work. The pressure may be computed as a post-processing step.

Equation (3.22), also known as the transonic small-disturbance (TSD) equation, has been widely used in aerodynamic analysis for transonic aeroelasticity, due to its relatively low computational cost.

3.4.6 Linear Potential Equation

If we assume $(1 - M^2)$ is large, we are justified in a full linearisation of the potential equations for small disturbances. Neglecting all higher-order terms leads us to:

$$\nabla^2 \phi - M_\infty^2 \frac{\partial^2 \phi}{\partial x^2} - \frac{1}{a_\infty^2} \left[\frac{\partial^2 \phi}{\partial t^2} + 2U_\infty \frac{\partial^2 \phi}{\partial x \partial t} \right] = 0 \quad (3.24)$$

Two limits of this equation are often employed:

Steady flow

Removing the time derivatives, we obtain:

$$(1 - M_\infty^2) \frac{\partial^2 \phi}{\partial x^2} + \frac{\partial^2 \phi}{\partial y^2} + \frac{\partial^2 \phi}{\partial z^2} = 0 \quad (3.25)$$

which is the classical Prandtl-Glauert equation for subsonic and supersonic steady flows.

Incompressible flow

Taking the limit of $a_\infty \rightarrow \infty$ gives us Laplace's equation:

$$\nabla^2 \phi = 0 \quad (3.26)$$

In this case, the time derivatives are lost from the equation for the perturbation potential. The problem remains unsteady, however, as the boundary conditions on the airfoil surface will be changing in time. Equation (3.26) is linear, which allows us to use superposition techniques in its solution. If the changing wake shape is not specified, however, determining its position may still require a non-linear iteration process.

3.5 Analytic Solutions

Below is a short list of analytic solutions for unsteady flows which are of relevance to aeroelasticity.

3.5.1 Incompressible Flows

- Birnbaum (1924), Theodorsen (1934); linearised incompressible potential flow for oscillating airfoils
- Wagner (1925); linearised incompressible potential flow for a step change in angle of attack

3.5.2 Subsonic Compressible Flows

- Possio (1938); Series solution of Integral equation for acceleration potential for a flat plate.
- Lomax (1953); Piston theory
- Balakrishnan (1998); Lin and Iliff (2000); Closed-form solutions of approximations to the Possio equation

3.5.3 Transonic Flows

- Stahara and Spreiter (1973), Isogai (1974), Dowel (1975); Linearisation of potential equation for $M \approx 1$. Good agreement for thin airfoils in shock-free flows.
- Tijdeman (1977) Local analysis at shock for frozen-Mach flows. Can use to investigate effects of shock movement
- Nixon (1979) Linearisation of small-disturbance equation using indicial function approach.

3.5.4 Supersonic Flows

- von Borbely (1942); Garrick and Rubinow (1946) Flat plates in Supersonic flow - integral equation solution.

In the chapters following this one we will examine selected analytic solutions for the simplest of the model equations. These have been chosen in order to consider the most important of the unsteady effects separately. Each solution can be used to provide reasonable predictions under a restricted set of conditions, but their chief advantage is that they help to develop insight into the relevant physical phenomena. The discussion of prediction methods for combined or more complex phenomena is deferred to later in the notes, where we will examine numerical solution methods for unsteady flows.

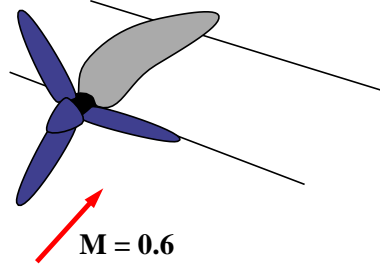
The analytic solutions we will consider are representative of some of the major results from unsteady aerodynamic theory over the past 80 years. In most cases, the full details of the solutions are too lengthy to be presented in their entirety, however, so we will omit some of the complex details where they do not interfere with understanding. For the exam, you will only be responsible for what is presented in class:

- Basic assumptions
- Governing equations
- Geometric simplifications
- Boundary conditions
- Outline of the solution procedure
- Interpretation of results

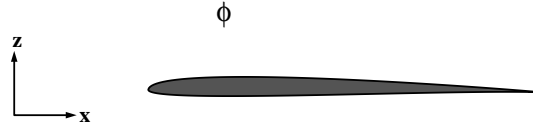
In addition, you should be able to solve simple problems employing the information above (see the practice problems in the chapters following this one).

3.6 Practice Problems

p3.6.5 Compare the advantages and disadvantages of applying the Euler equations versus the linear potential equation to the computation of whirl flutter in the propeller-wing-nacelle configuration shown below. Assume the configuration is operating with a freestream Mach number of 0.6.



p3.6.6 Consider a 2D thin airfoil moving in a uniform flow in the x direction, U_∞ , with a known perturbation potential, ϕ :



Using the momentum equation:

$$\frac{\partial \vec{u}}{\partial t} + (\vec{u} \cdot \nabla) \vec{u} + \frac{\nabla p}{\rho} = 0$$

derive the linearised expression for pressure:

$$p = p_\infty - \rho_\infty \left(\frac{\partial \phi}{\partial t} + U_\infty \frac{\partial \phi}{\partial x} \right)$$

Start by considering the x and z momentum equations for $\vec{u} = (U_\infty, 0) + (u', w')$, $\rho = \rho_\infty + \rho'$, $p = p_\infty + p'$ and eliminating the higher-order terms (Note that there are no spatial gradients in the mean-flow quantities). Then write the remaining equations as a vector equation in terms of $\nabla \phi$ and $\nabla p'$ and integrate it along a streamline.

Chapter 4

Analytic Solutions for Incompressible Flows

In this chapter we will examine potential-flow solutions for unsteady incompressible flows around thin airfoils. We will begin by considering a closed-form solution procedure for the problem of a harmonically oscillating airfoil, then review some solutions for step changes in angle of attack and step gusts.

The first solutions for the forces on a moving airfoil were produced in the the 1920's by aerodynamicists such as W. Birnbaum, H. Wagner, and H. Glauert. Their analyses established a clear strategy for solving unsteady aerodynamic problems, although their solution methods sometimes relied on series approximation techniques which did not always converge. In 1934, T. Theodorsen was able to express the solution to the harmonically oscillating airfoil problem explicitly in terms of Hankel functions. He also developed some of the first flutter analysis techniques incorporating the effects of unsteady aerodynamics. His solution to the oscillating airfoil problem has been widely used in the field of aeroelasticity.

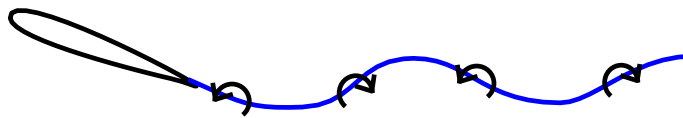


Figure 4.1: An unsteady airfoil and its wake

In the following sections we will consider solutions based on a vortex-sheet model for an moving airfoil and its wake. Note that due to the influence of convecting shed vorticity, we cannot omit the wake in an unsteady analysis. This contrasts with the 2D steady airfoil case, where the wake geometry is irrelevant so long as the Kutta condition is satisfied.

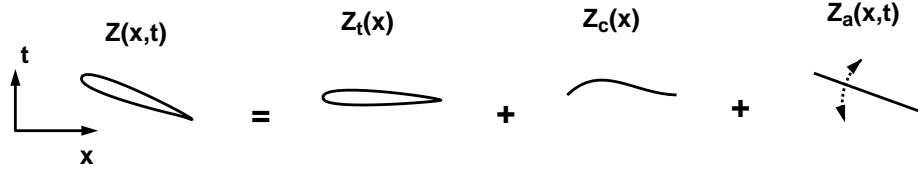


Figure 4.2: Decomposition of an unsteady airfoil problem

4.1 Problem definition

We will consider the linearized equations for the potential of an unsteady flow, which can be expressed as (see chapter 3):

$$\nabla^2 \phi = 0 \quad (4.1)$$

$$p - p_\infty = -\rho_\infty \left(\frac{\partial \phi}{\partial t} + U_\infty \frac{\partial \phi}{\partial x} \right) \quad (4.2)$$

Where ϕ is the perturbation potential and the ∞ denotes freestream conditions. To be consistent with the linearization of the potential, we will consider only small angle excursions, and a linearized airfoil geometry.

If we linearize the boundary conditions on the airfoil, the solution of an unsteady thin-airfoil problem can be broken up into its thickness (z_t), camber (z_c), and flat-plate (z_a) components, as shown in figure 4.2. As thickness and camber are not usually considered to be functions of time, their contributions can be obtained from standard steady thin-airfoil theory. Therefore, for the remainder of this analysis, we will focus on the solution for a moving flat plate. In doing so we will solve (4.1) and (4.2) subject to the following conditions:

1. Zero perturbation velocity in the far-field
2. Flow tangency on the airfoil surface
3. No pressure jump across the wake
4. Kutta condition using Kelvin's Theorem

The first of these conditions is simple enough, we require that the perturbation vanish when considering points far from the airfoil. The second is the standard no-flow-through-the-airfoil condition familiar from steady aerodynamic theory. The third is a new condition which arises from having to consider the wake in the problem, which of course cannot maintain a difference in pressure across it. The final condition represents an interpretation of the Kutta condition for unsteady flow, that the vorticity shed at the trailing edge must be equal and opposite in strength to the change in bound vorticity of the airfoil (see the previous chapter for a discussion).

In order to solve the problem we will represent the airfoil and its wake by a sheet of vortices of unknown strength, $\gamma(x, t)$, lying on the $z = 0$ plane, as

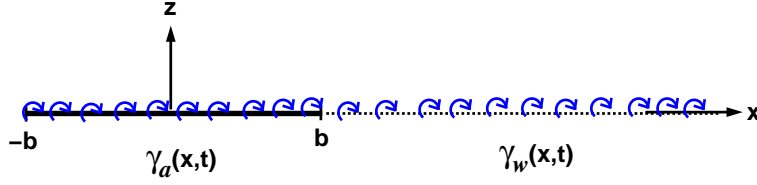


Figure 4.3: Replacement of airfoil and wake by a vortex sheet

shown in figure 4.3. Each of these vortices is a elementary solution of equation (4.1). This results in the following expression for the perturbation potential induced by the complete vortex sheet.

$$\phi(x, z) = - \int_{-b}^{\infty} \frac{\gamma(\xi)}{2\pi} \tan^{-1} \left(\frac{z}{x - \xi} \right) d\xi \quad (4.3)$$

The use of a vortex sheet exploits the linear nature of the governing equations to simplify the problem. As each of the infinitesimal point vortices in the vortex sheet satisfies the governing equations, then the entire vortex sheet satisfies the governing equations, even for arbitrary local strengths. To find the solution, it thus remains only to find the distribution of vortex strengths which satisfies the boundary conditions 1-4 above. We will derive mathematical expressions of these conditions in the following sections.

4.2 Far-Field Perturbation

To examine if our vortex sheet representation does indeed have a zero perturbation far from the airfoil, we start by deriving expressions for the perturbation velocities anywhere in the domain by differentiating the potential function for the vortex sheet:

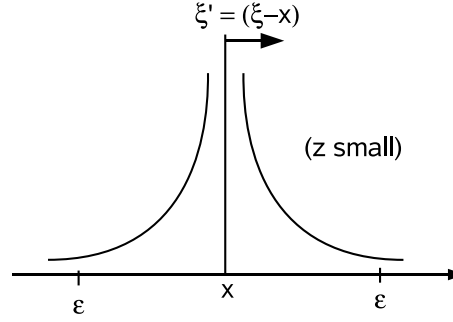
$$u(x, z) = \phi_x(x, z) = \int_{-b}^{\infty} \frac{\gamma(\xi)}{2\pi} \left(\frac{z}{(x - \xi)^2 + z^2} \right) d\xi \quad (4.4)$$

$$w(x, z) = \phi_z(x, z) = - \int_{-b}^{\infty} \frac{\gamma(\xi)}{2\pi} \left(\frac{x - \xi}{(x - \xi)^2 + z^2} \right) d\xi \quad (4.5)$$

Both of these components tend to zero in the far-field, as one would expect considering the behaviour of a single potential-flow vortex.

4.3 Velocities on the $z = 0$ plane

Before proceeding to the flow tangency and zero-wake pressure jump conditions, it is worthwhile first deriving the expressions for the local velocity at the surface

Figure 4.4: Integration in the region near x

of the vortex sheet. Taking the limit of the expressions for velocity (4.4) and (4.5) as $z \rightarrow 0$, we have:

$$u(x, 0) = \lim_{z \rightarrow 0} \int_{-b}^{\infty} \frac{\gamma(\xi)}{2\pi} \left(\frac{z}{(x - \xi)^2 + z^2} \right) d\xi \quad (4.6)$$

and

$$w(x, 0) = -\frac{1}{2\pi} \int_{-b}^{\infty} \left(\frac{\gamma(\xi)}{(x - \xi)} \right) d\xi \quad (4.7)$$

Note that the integral for $u(x, 0)$ tends to vanish except where $x \approx \xi$.

In order to find an expression for $u(x, 0)$, we restrict the range of integration to small region near x of width 2ϵ (figure 4.4). Introducing the intermediate variable $\xi' = \xi - x$:

$$u(x, 0) = \text{Lim}_{z \rightarrow 0} \int_{-\epsilon}^{+\epsilon} \frac{\gamma(\xi')}{2\pi} \left(\frac{z}{(\xi')^2 + z^2} \right) d\xi' \quad (4.8)$$

A Taylor series approximation for $\gamma(\xi')$ is:

$$\gamma(x - \epsilon \rightarrow x + \epsilon) = \gamma(x) + O(\epsilon) \quad (4.9)$$

Integrating and eliminating higher-order terms:

$$u(x, 0) = \text{Lim}_{\epsilon \rightarrow 0} \left\{ \frac{\gamma(x) + O(\epsilon)}{2\pi} \text{Lim}_{z \rightarrow 0} \left[\tan^{-1} \left(\frac{\epsilon}{z} \right) - \tan^{-1} \left(\frac{-\epsilon}{z} \right) \right] \right\} \quad (4.10)$$

We assume ϵ is small, but is still large compared with $z \rightarrow 0$. This leads to the following expression for the velocity above (+) and below (−) the vortex sheet:

$$u(x, \pm 0) = \pm \frac{\gamma(x)}{2} \quad (4.11)$$

Alternatively we can express the jump across the vortex sheet directly as:

$$\Delta u(x, 0) = \gamma(x) \quad (4.12)$$

4.4 Flow Tangency

Now that we have derived expressions for the velocity at $z = 0$, we can employ them directly in the application of the flow tangency condition. This requires that at the surface of the airfoil $\vec{V} \cdot \vec{n} = V_n = 0$, where

$$V_n = V_{n_{freestream}} + V_{n_{motion}} + V_{n_\gamma} \quad (4.13)$$

Here $V_{n_{freestream}}$ is the sheet-normal component of the freestream vector due to the instantaneous pitch angle of the airfoil, $V_{n_{motion}}$ is the normal velocity induced by the vertical motion of the airfoil, and V_{n_γ} is the local value of induced normal velocity due to the vortex sheet. Recalling that we are using small-angle approximations, we may replace $V_{n_{freestream}}$ and $V_{n_{motion}}$ with space and time derivatives of the local z coordinate of the sheet, as shown in figure 4.5. If

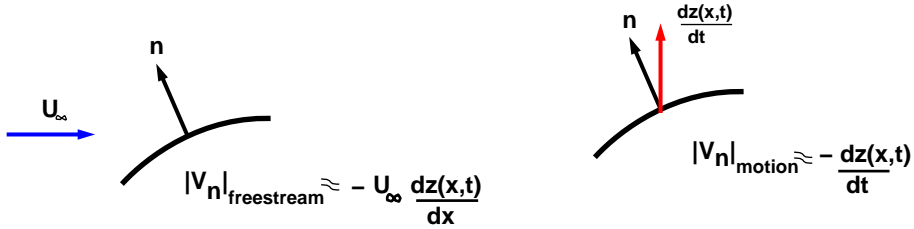


Figure 4.5: Geometric linearizations for the flow-tangency condition

we also note that for small angles $w \approx V_n$, the total vertical velocity due to freestream and motion, w_{FM} , may be expressed:

$$w_{FM}(x, t) \approx -U_\infty \frac{dz_a(x, t)}{dx} - \frac{dz_a(x, t)}{dt} \quad (4.14)$$

This allows us to express the flow tangency condition as:

$$w_{FM}(x, t) + w_\gamma(x, t) = 0 \quad (4.15)$$

or, by substituting our previous expressions, as:

$$-U_\infty \frac{dz(x, t)}{dx} - \frac{dz(x, t)}{dt} - \frac{1}{2\pi} \int_{-b}^b \frac{\gamma_a(\xi, t)}{x - \xi} d\xi - \frac{1}{2\pi} \int_b^\infty \frac{\gamma_w(\xi, t)}{x - \xi} d\xi = 0 \quad (4.16)$$

where $z_a(x, t)$ is the specified motion of the airfoil. Note that we have separated the integration of the velocity induced by the vortex sheet into components associated with the airfoil and wake.

4.5 Pressure Jump Across the Wake

In general, the wake is a free surface which will move to ensure that a pressure jump does not occur across it. In our model, we will assume that the excursions

of the wake in the vertical direction are so small that they can be neglected while enforcing the zero-pressure-jump condition. This assumption is quite reasonable when considering the relatively high forward velocities characteristic of most aircraft wings.

We can construct an expression for the pressure jump across the wake using (4.2):

$$p_u - p_l = -\rho_\infty \left[\frac{\partial \Delta \phi}{\partial t} + U_\infty \frac{\partial \Delta \phi}{\partial x} \right] \quad (4.17)$$

$$(4.18)$$

where $\Delta \phi = \phi_u - \phi_l$. This equation can be re-expressed in terms of γ if we note that:

$$\frac{\partial \Delta \phi(x)}{\partial x} = \Delta u(x) = \gamma(x) \quad (4.19)$$

Also, for $x < -b$, $\Delta \phi = 0$, so that for $x > -b$:

$$\Delta \phi(x) = \int_{-b}^x \frac{\partial \Delta \phi(\xi)}{\partial x} d\xi = \int_{-b}^x \gamma(\xi) d\xi \quad (4.20)$$

This leads to:

$$p_u - p_l = -\rho_\infty \left[U_\infty \gamma + \frac{\partial}{\partial t} \int_{-b}^x \gamma(\xi) d\xi \right] \quad (4.21)$$

The wake pressure condition then requires $p_u - p_l = 0$ for $x = b \rightarrow \infty$

4.6 Kutta Condition using Kelvin's Theorem

For our analysis, we assume that the Kutta condition is satisfied at each instant in time. As we saw in chapter 3, this implies that changes in the airfoil's condition will result in the shedding of vorticity from the trailing edge. In order to comply with Kelvin's theorem, we require that the shed vorticity is equal and opposite to the change in bound circulation over the airfoil. To express this mathematically, we start with an equation for the airfoil's bound circulation:

$$\Gamma(t) = \int_{-b}^b \gamma_a(\xi, t) d\xi \quad (4.22)$$

Consider an increment in vorticity shed from the trailing edge, as shown in figure 4.6. In terms of $\Gamma(t)$, Kelvin's theorem can be now expressed as:

$$\gamma_w(b, t) dx = -\frac{d\Gamma(t)}{dt} dt \quad (4.23)$$

If we consider infinitesimal time and space intervals, we can get the final expression for the magnitude of the vorticity shed instantaneously at the trailing edge:

$$\gamma_w(b, t) = -\frac{1}{U_\infty} \frac{d\Gamma(t)}{dt} \quad (4.24)$$

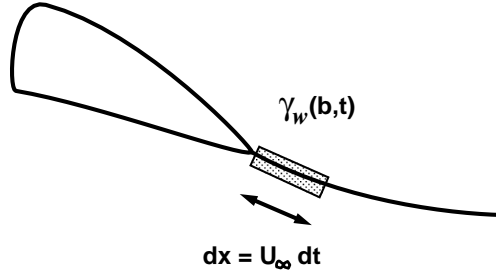


Figure 4.6:

4.7 Harmonic Solutions

We have already seen that the far-field condition is automatically satisfied though our choice of potential-flow singularities used to represent the airfoil and wake. For the case of harmonic motion, however, we can also show that if we assume that wake vorticity is convected with the freestream velocity, U_∞ , then the wake pressure condition is also automatically satisfied.

Let's begin by assuming a harmonic forms for the airfoil excitation and resulting solution:

$$w_{FM}(x, t) = \hat{w}_{FM}(x)e^{i\omega t}; \quad \gamma_a(x, t) = \hat{\gamma}_a(x)e^{i\omega t}; \quad \Gamma(t) = \hat{\Gamma}e^{i\omega t} \quad (4.25)$$

We also assume a harmonic response in the wake, so that:

$$\gamma_w(x, t) = \hat{\gamma}_w(x)e^{i\omega t} \quad (4.26)$$

allowing Kelvin's theorem to be expressed as:

$$\hat{\gamma}_w(b) = -\frac{i\omega}{U_\infty} \hat{\Gamma} \quad (4.27)$$

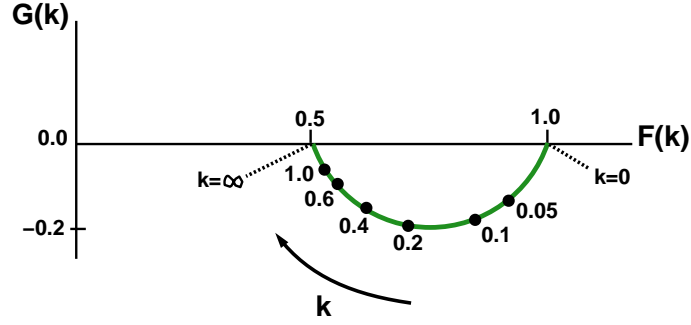
Assuming downstream convection of vorticity with U_∞ , the complex coefficient of the wake circulation distribution can then be expressed:

$$\hat{\gamma}_w(x) = -\frac{i\omega}{U_\infty} \hat{\Gamma} e^{\frac{i\omega}{U_\infty}(b-x)} \quad (4.28)$$

Now we substitute these expressions into the wake pressure condition $p_u - p_l = 0$. The second term in (4.21) can be expressed as:

$$\frac{\partial}{\partial t} \int_{-b}^x \gamma(\xi) d\xi = \frac{d\Gamma}{dt} + \frac{\partial}{\partial t} \int_b^x \gamma_w(\xi) d\xi \quad (4.29)$$

$$= \left(i\omega \hat{\Gamma} + i\omega \int_b^x \hat{\gamma}_w(\xi) d\xi \right) e^{i\omega t} \quad (4.30)$$

Figure 4.7: Components of Theodorsen's function $C(k) = F(k) + iG(k)$

Using the expression for $\hat{\gamma}_w(\xi)$ given by Kelvin's theorem:

$$\int_b^x \hat{\gamma}_w(\xi) d\xi = -\frac{i\omega \hat{\Gamma}}{U_\infty} \int_b^x e^{\frac{i\omega}{U_\infty}(b-\xi)} d\xi \quad (4.31)$$

Integration and substitution into the expression for the pressure change across the wake shows that the wake pressure condition is automatically satisfied.

Now we are left with just the expression for flow tangency (4.16), augmented by an explicit expression for the wake vorticity distribution (4.28) for harmonic flows. (4.16) evaluated for harmonic solutions can be combined with (4.28) to obtain the following expression for flow tangency on a harmonically oscillating airfoil:

$$\begin{aligned} -\frac{1}{2\pi} \int_{-b}^b \frac{\hat{\gamma}_a(\xi)}{x-\xi} d\xi + \frac{i\omega}{2\pi U_\infty} \hat{\Gamma} \int_b^\infty \frac{e^{i\omega(\frac{b-\xi}{U_\infty})}}{x-\xi} d\xi \\ = i\omega \hat{z}_a(x) + U_\infty \frac{\partial \hat{z}_a(x)}{\partial x} \end{aligned} \quad (4.32)$$

where $z_a(x, t) = \hat{z}_a(x)e^{i\omega t}$. This integral equation has been solved analytically for $\hat{\gamma}_a(x)$ Theodorsen (1934) and Schwarz (1940), with $\hat{z}_a(x)$ defined for a harmonically plunging and pitching flat plate. Solutions of the integral equation are usually expressed in terms of Theodorsen's function, $C(k)$:

$$C(k) = F(k) + iG(k) = \frac{H_1^{(2)}(k)}{H_1^{(2)}(k) + iH_0^{(2)}(k)} \quad (4.33)$$

where $H_n^{(2)}$ are nth-order Hankel functions of the second kind. Theodorsen's function is also known as the circulation function. The parameter $k \equiv (\omega b)/U_\infty$, is referred to as the *reduced frequency*. It expresses the ratio of periods for oscillation and (wake) convection. The variation of the components of $C(k)$ as a function of k is shown diagrammatically in figure 4.7.

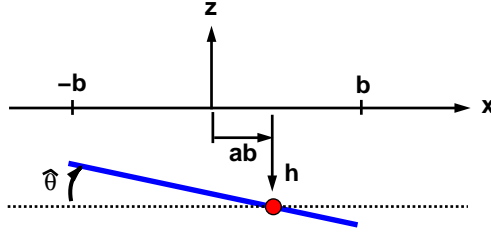


Figure 4.8: Flat plate undergoing combined pitch and plunge

4.8 Harmonic Pitch and Plunge solutions

Although their detailed derivation is beyond the scope of this course, it is useful to examine solutions to (32) for some basic cases. We first consider the solution for a flat plate undergoing combined harmonic pitching and plunging with a reduced frequency k , as shown in figure 4.8. For a center of pitch positioned at ab , the solution for the airfoil's lift and nose-up moment about the rotation for combined harmonic pitch can be written as:

$$\begin{aligned} L = \hat{L}e^{i\omega t} &= \pi\rho_\infty b^2[\ddot{h} + U_\infty\dot{\theta} - ba\ddot{\theta}] \\ &+ 2\pi\rho_\infty U_\infty bC(k)[\dot{h} + U_\infty\theta + b(\frac{1}{2} - a)\dot{\theta}] \end{aligned} \quad (4.34)$$

and :

$$\begin{aligned} M = \hat{M}e^{i\omega t} &= \pi\rho_\infty b^2[ba\ddot{h} - U_\infty b(\frac{1}{2} - a)\dot{\theta} - b^2(\frac{1}{8} + a^2)\ddot{\theta}] \\ &+ 2\pi\rho_\infty U_\infty b^2(a + \frac{1}{2})C(k)[\dot{h} + U_\infty\theta + b(\frac{1}{2} - a)\dot{\theta}] \end{aligned} \quad (4.35)$$

The first group of terms in both the lift and moment equations is known as the non-circulatory component of the response, while the second group of terms is known as the circulatory component, as it arises from the satisfaction of the Kutta condition. The non-circulant components are sometimes referred to as apparent mass terms, as they are proportional to accelerations felt by a fluid cylinder with radius b . Consider also the low k limit of the lift and moment expressions. At $k = 0$, all the rates disappear, $C(k) = 1$ (see figure 4.7), and the standard flat-plate solution is recovered (note $b = c/2$). We will often use an alternative notation for the lift and moment expressions, in terms of their unsteady (complex) coefficients:

$$\hat{L} = \pi\rho_\infty U_\infty^2 b \left[L_h(k) \frac{\hat{h}}{b} + L_\theta(k) \hat{\theta} \right] \quad (4.36)$$

$$\hat{M} = \pi\rho_\infty U_\infty^2 b^2 \left[M_h(k) \frac{\hat{h}}{b} + M_\theta(k) \hat{\theta} \right] \quad (4.37)$$

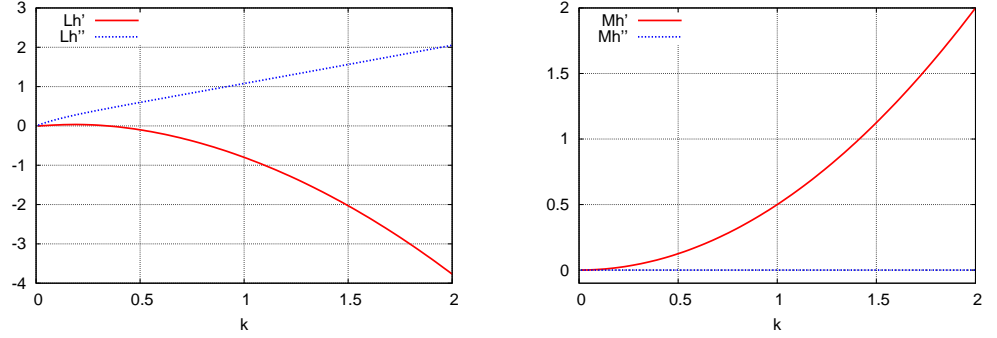


Figure 4.9: Unsteady lift and moment coefficients for a flat plate airfoil undergoing pure harmonic plunge

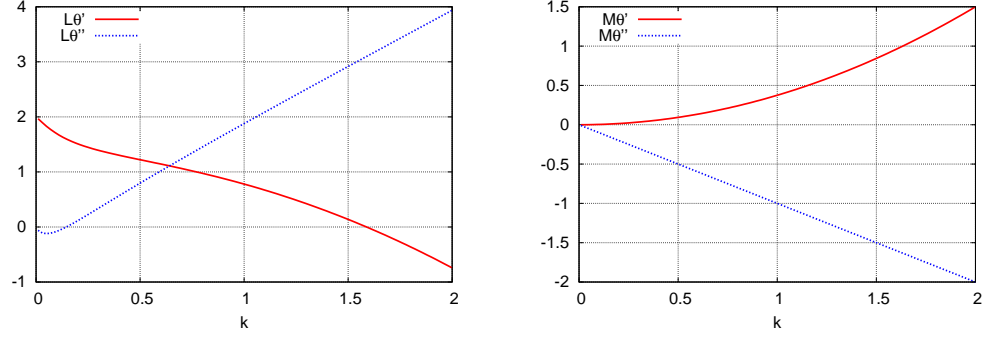


Figure 4.10: Unsteady lift and moment coefficients for a flat plate airfoil undergoing pure harmonic pitch

with \hat{M} measured nose-up positive relative to $x = ab$, and

$$L_h = -k^2 + C(k) [2ik] \quad (4.38)$$

$$L_\theta = ak^2 + ik + C(k) [2 + ik(1 - 2a)] \quad (4.39)$$

$$M_h = -ak^2 + C(k) [ik(1 + 2a)] \quad (4.40)$$

$$M_\theta = (a - \frac{1}{2})ik + (a^2 + \frac{1}{8})k^2 + C(k) \left[(2a + 1) + ik(\frac{1}{2} - 2a^2) \right] \quad (4.41)$$

The variation of the total lift and moment coefficients with k is shown in figures 4.9 and 4.10. In figure 4.10, the lift curve slope is seen to drop from its standard value of 2 fairly quickly with increasing k .

It is also possible to find expressions for the chordwise perturbations to the steady pressure distributions of the airfoil. For harmonic flows, these are

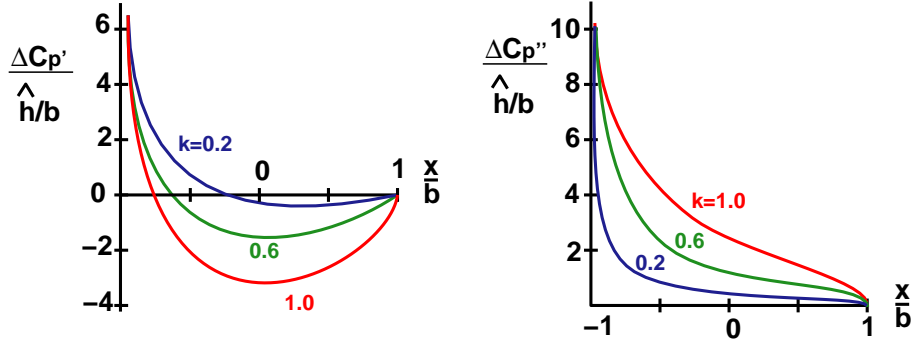


Figure 4.11: Pressure perturbations for a flat plate airfoil undergoing pure harmonic plunge

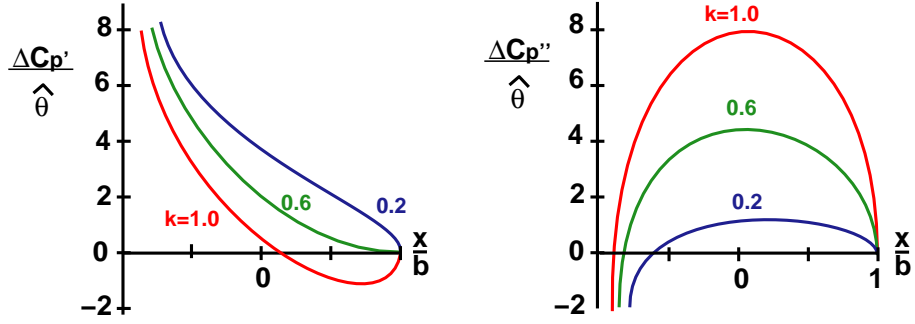


Figure 4.12: Pressure perturbations for a flat plate airfoil undergoing pure harmonic pitch

expressed as:

$$\Delta C_p(x, t) = (\Delta C_p'(x) + i\Delta C_p''(x)) e^{i\omega t} \quad (4.42)$$

The real and imaginary perturbations to the change in pressure across the plate, $\Delta C_p'$ and $\Delta C_p''$ are shown plotted as a function of chordwise position in figures 4.11 and 4.12. For the plunge case, real component $\Delta C_p'$ corresponds to the perturbation obtained when the plate is at its most downward position, while $\Delta C_p''$ corresponds to the mid-position while moving downwards. Each distribution shows the characteristic leading-edge singularity of flat plate steady solutions. Examination of the pure pitch perturbations reveals that they only resemble the steady flat plate pressure distribution at low k .

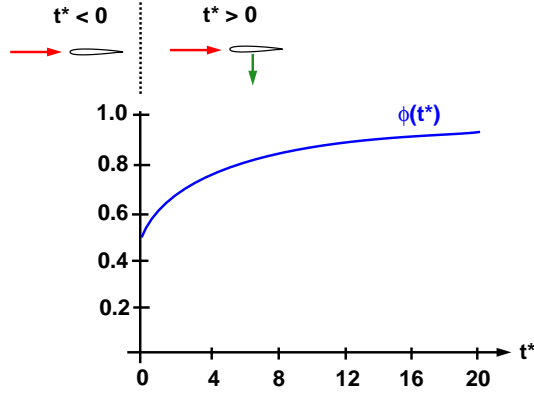


Figure 4.13: Wagner's indicial lift function

4.9 Indicial Response (Wagner's Function)

Although harmonic responses are clearly useful for analysing flutter instability boundaries, *indicial* (step) responses are often more convenient when considering arbitrary excitations. The solution for the indicial plunge response of a flat plate airfoil was first determined by Wagner in 1925. It can also be derived directly from the previously-presented harmonic plunge results using the following excitation:

$$w_{\frac{3}{4}c} = \begin{cases} 0 & t < 0 \\ -U_{\infty}\alpha_o & t > 0 \end{cases} \quad (4.43)$$

$$-U_{\infty}\alpha_o \quad t > 0 \quad (4.44)$$

The harmonic solution's non-circulatory component will provide a singular pulse at $t=0$, but otherwise it will have no contribution. The remainder of the response can be obtained by using a Fourier transform of the circulatory terms, resulting in:

$$L = 2\pi\rho_{\infty}U_{\infty}^2 b\alpha_o\phi(t^*) \quad (4.45)$$

where

$$\phi(t^*) = \frac{1}{2\pi} \int_{-\infty}^{\infty} \frac{C(k)}{ik} e^{ikt^*} dk ; \quad t^* = \frac{U_{\infty}t}{b} \quad (4.46)$$

In incompressible flow, the lift perturbation due to an indicial plunge acts at the quarter chord, so there is no perturbation to the moment about $c/4$. Wagner's indicial lift function can be approximated using:

$$\phi(t^*) \approx 1 - 0.165e^{-0.0455t^*} - 0.355e^{-0.3t^*} \quad (4.47)$$

4.10 Vertical Step Gust Response (Küssner's Function)

In an analogous manner, the response to a step gust is also very useful. Note that unlike the previous indicial plunge case, in this case the local angle of attack is not constant along the airfoil chord until the gust has past. This excitation can be expressed as (see figure 4.14).

$$w_G = 0 \quad x > U_\infty t - b \quad (4.48)$$

$$w_o \quad x < U_\infty t - b \quad (4.49)$$

The response to this excitation can be expressed in terms of Küssner's Function,

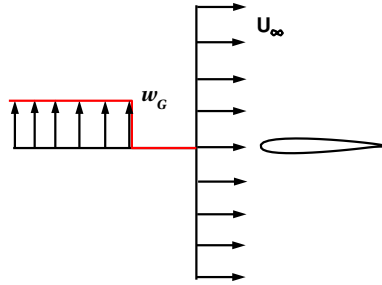


Figure 4.14: Step gust excitation

$\psi(t^*)$:

$$L = 2\pi\rho_\infty U_\infty b w_o \psi(t^*) \quad (4.50)$$

As for the indicial plunge case, $\psi(t^*)$ can be derived via a Fourier transform of the solution to a sinusoidal gust problem. It has the form shown in figure 4.15. Once again in incompressible flow the lift response acts at the quarter chord, so there is no perturbation to the moment about $c/4$. Küssner's step gust response function can be approximated by:

$$\psi(t^*) \approx 1 - 0.5e^{-0.13t^*} - 0.5e^{-t^*} \quad (4.51)$$

Note that the non-dimensional time, t^* , can also be interpreted as the number of half-chords travelled after the leading edge encounters the gust.

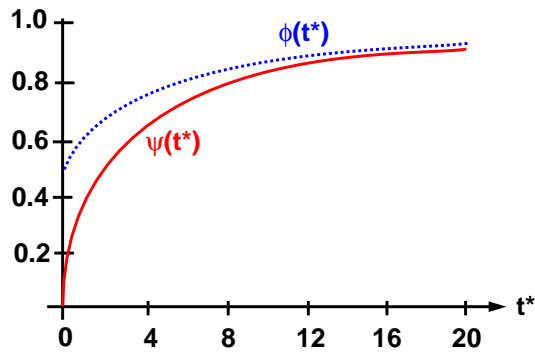


Figure 4.15: Küssner's step gust response function

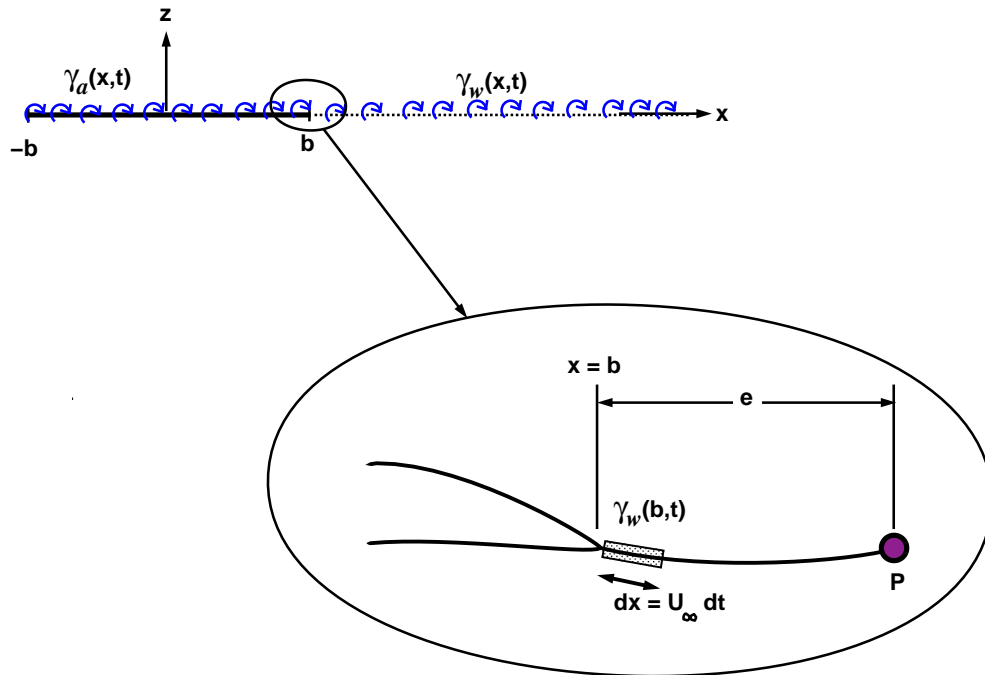
4.11 Practice Problems

p4.11.7 Sketch the pressure distributions for a harmonically plunging airfoil at 8 points in the cycle.

p4.11.8 Plot the quasi-steady aerodynamic model response in figure 4.9.

p4.11.9 Show that the wake pressure condition is automatically satisfied in the harmonic motion case using the definitions from sections 4.5 to 4.7.

p4.11.10 Consider a thin airfoil in an incompressible flow, as shown below:



If the airfoil deforms harmonically, so that the time-variant vorticity distribution on the airfoil surface is given by:

$$\gamma_a(x, t) = (x - b)^2(1 + 2i)e^{i\omega t} ; \quad -b \leq x \leq b$$

What is the vorticity as a function of time at the point P located a distance e behind the trailing edge [i.e. $\gamma_w(b + e, t)$]? Use assumptions consistent with the theory presented in class.

Chapter 5

Analytic Solutions for Subsonic Compressible Flows

5.1 Steady Flow: The Prandtl-Glauert Correction

The simplest equation describing compressible flows is the steady linear potential equation (see chapter 3), written below for two dimensions:

$$(1 - M_\infty^2) \frac{\partial^2 \phi}{\partial x^2} + \frac{\partial^2 \phi}{\partial y^2} = 0 \quad (5.1)$$

Comparing (5.1) to the linear potential equation for incompressible flow reveals that solutions to the former may be obtained from those of the latter if a simple coordinate transformation is applied. Specifically, The solution of (5.1) can be related to that of Laplace's equation for $\bar{\phi}(\xi, \eta) = \beta \phi(x, y)$ in the transformed coordinates $\xi = x$, $\eta = \beta y$; where $\beta = \sqrt{1 - M_\infty^2}$. Using this concept, it is possible to obtain forces and moments for a steady compressible flow by applying corrections to the forces and moments for the corresponding steady incompressible flow. For thin airfoils, the linearised, steady pressure coefficient can be shown to be (see an introductory aerodynamics text, such as Anderson):

$$Cp = -\frac{2u}{U_\infty} = -\frac{2}{U_\infty \beta} \frac{\partial \bar{\phi}}{\partial x} = \frac{Cp_o}{\beta} \quad (5.2)$$

where Cp_o is the pressure coefficient from the solution to Laplace's equation (i.e. the incompressible problem). The behaviour of the corrected lift curve slope over the complete Mach number range is illustrated in figure 5.1. The correction was first derived by Prandtl in the early 1920's and more formally

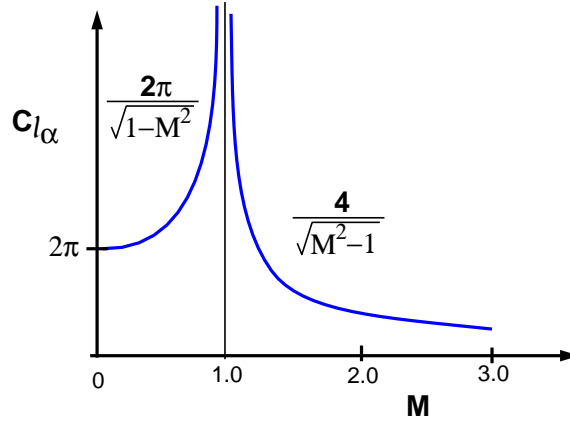


Figure 5.1: Prandtl-Glauert correction to the lift-curve slope of a flat-plate airfoil

by Glauert in 1928. It is important to note that since the linear potential equation for compressible flow (5.1) is obtained by ignoring time derivatives, the Prandtl-Glauert correction applies to steady flows only. Therefore, it can only be reasonably applied to aeroelastic problems if the frequencies of structural motion are small enough to allow the use of a steady aerodynamic model.

5.2 Unsteady Harmonic Solutions for $M < 1$

In 1938, Possio rewrote the unsteady linearized potential equation for compressible flows (equation 24 in chapter 3) in terms of the acceleration potential, and formulated the problem for the unsteady thin airfoil. This approach is more general than that described in chapter 4 as it includes the effects of time delays in addition to those of vorticity convection. Unfortunately, it has not been possible to derive closed form solutions to Possio's equation, so traditionally it has been solved using series-approximation techniques or other numerical methods. Recently, however, Balakrishnan (1998) Lin and Iliff (2000) have derived closed-form solutions to approximations to Poisson's equation. The Lin and Iliff (2000) approximation is given below (moment positive clockwise):

$$L_h = -k^2 + C(k) [2ik] + M^2 \log M \left[\frac{k^4}{2} - 2ik^3 C(k) - 2k^2 C(k)^2 \right] \quad (5.3)$$

$$\begin{aligned} L_\theta = & ak^2 + ik + C(k) [2 + ik(1 - 2a)] \\ & + M^2 \log M \left[-\frac{ik^3}{2} - \frac{k^4}{2} a + C(k) \left\{ -2k^2 - \left(\frac{1}{2} - 2a \right) ik^3 \right\} \right] \\ & + M^2 \log M [C(k)^2 \{ 2ik - (1 - 2a)k^2 \}] \end{aligned} \quad (5.4)$$

$$\begin{aligned}
M_h &= -ak^2 + C(k) [ik(1 + 2a)] \\
&\quad + M^2 \log M \left[-(1 + 2a)k^2 C(k)^2 - \left(\frac{1}{2} + 2a \right) ik^3 C(k) + \frac{k^4}{2} a \right] \quad (5.5)
\end{aligned}$$

$$\begin{aligned}
M_\theta &= \left(a - \frac{1}{2} \right) ik + \left(a^2 + \frac{1}{8} \right) k^2 + C(k) \left[(2a + 1) + ik \left(\frac{1}{2} - 2a^2 \right) \right] \\
&\quad + M^2 \log M \left[-\frac{aik^3}{2} - \frac{a^2 k^4}{2} + C(k) \left\{ (1 + 2a)ik - \left(\frac{1}{2} - 2a^2 \right) k^2 \right\} \right] \\
&\quad - M^2 \log M \left[C(k) \left\{ \left(\frac{1}{2} + 2a \right) k^2 - 2a^2 ik^3 \right\} \right] \quad (5.6)
\end{aligned}$$

Some results this approximation at a Mach number of 0.7 are shown compared to incompressible results in figures 5.2 and 5.3. The compressible effects can be seen to increase as a function of k . You can further investigate the influence of Mach number and the centre of rotation on your own by visiting:

<https://aerodynamics.lr.tudelft.nl/cgi-bin/lpfp>

5.3 Piston theory

If there are time delays, then information transfer is small for very fast motions. This concept allows a particularly simple aerodynamic theory to be derived. Consider the finite wing shown in figure 14.6. When the wing is impulsively plunged, then the interior of the wing initially acts as if the span and chord were infinite, since waves coming from the edges require time to propagate inwards. As a result, a simple 1D compression wave is generated on the lower surface of the wing, and a simple expansion wave is generated on the upper surface. From linearised acoustic theory, the initial pressure perturbation on the surface of a piston which is impulsively accelerated is:

$$p' = \rho_\infty a_\infty w_o \quad (5.7)$$

where w_o is the speed to which the piston is accelerated to, and a_∞ is the speed of sound in the fluid. This perturbation appears anti-symmetrically on the upper and lower surfaces so that $\Delta p = 2\rho_\infty a_\infty w_o$. The initial lift coefficient of the wing is then:

$$C_L(0) = \frac{(p'_{lower} - p'_{upper})S}{1/2\rho_\infty U^2 S} = \frac{4w_o}{M_\infty U} \quad (5.8)$$

These expressions provide a useful model for oscillations with very high frequencies at both subsonic and supersonic Mach numbers. Formally, the theory is accurate at large values of the product of Mach number and reduced frequency, Mk .

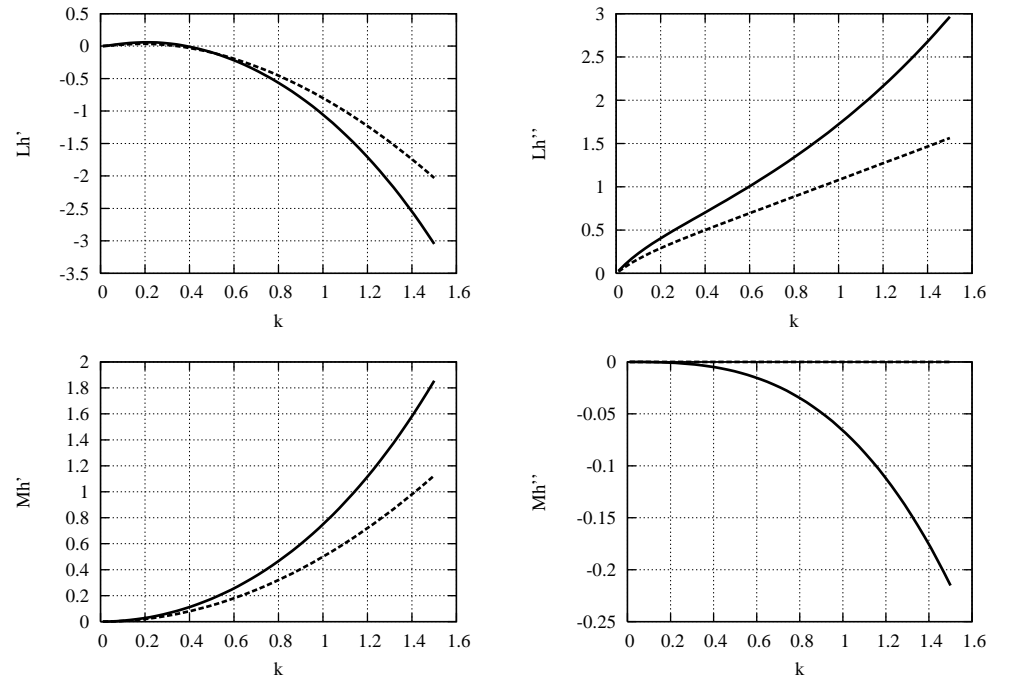


Figure 5.2: Plunging case - comparison of $M=0.7$ (solid) and $M=0$ (dashed) responses ($a=-1/2$).

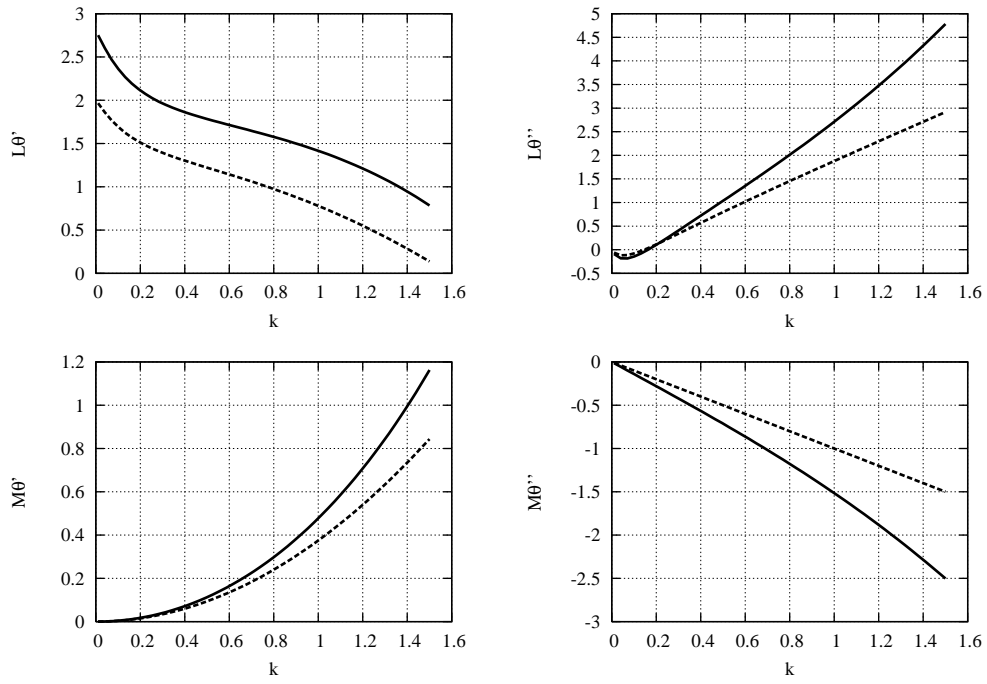


Figure 5.3: Pitching case - comparison of $M=0.7$ (solid) and $M=0$ (dashed) responses ($a=-1/2$).

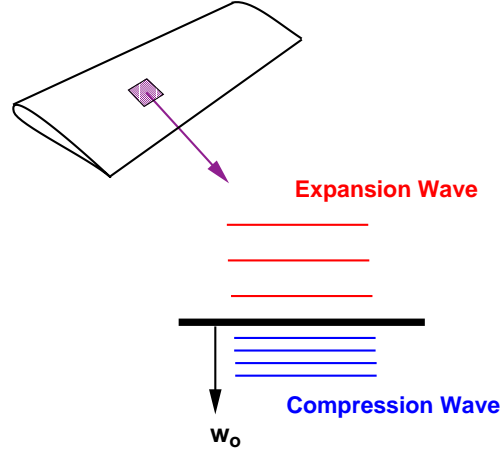


Figure 5.4: Piston theory

5.4 Indicial Responses for $M < 1$

It is also possible to compute indicial responses using unsteady linearized potential theory. These solutions are quite different from their incompressible counterparts, in that:

- The non-circulatory components are active after $t=0$, due to the finite times required for wave propagation.
- The solution is no longer singular at $t=0$; its initial peak can be predicted using “piston theory”.
- The circulatory response is no longer determined by $w_{\frac{3}{4}c}$
- The change in moment about the quarter chord is no longer zero.

Example responses for an indicial plunge at different Mach numbers are shown in figures 5.5 and 5.6, corresponding following definitions of lift and moment:

$$L = \pi \rho U_\infty^2 \frac{\dot{h}_o}{U_\infty} \Phi_c(t^*) \quad (5.9)$$

$$M = \pi \rho U_\infty^2 2b \frac{\dot{h}_o}{U_\infty} \Phi_{cM}(t^*) \quad (5.10)$$

After the initial piston theory response, there is an increasingly slow climb to the steady state value as the Mach number is increased. This is due to the increasing upstream propagation times of information describing the wake’s dynamics. For cases where linearised theory is adequate, the final large-time asymptotic value can be estimated using the Prandtl-Glauert factor $\frac{1}{\sqrt{1-M_\infty^2}}$.

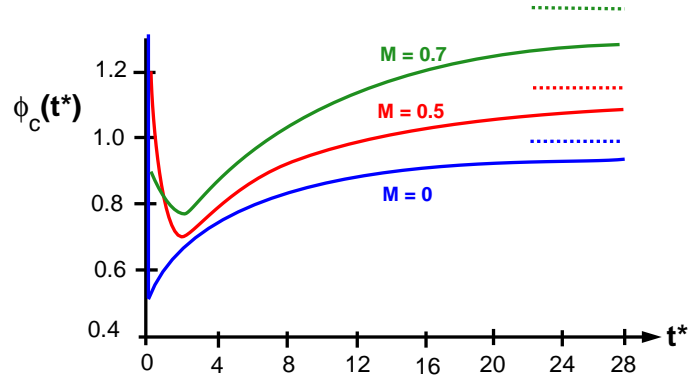


Figure 5.5: Indicial lift responses in compressible flow

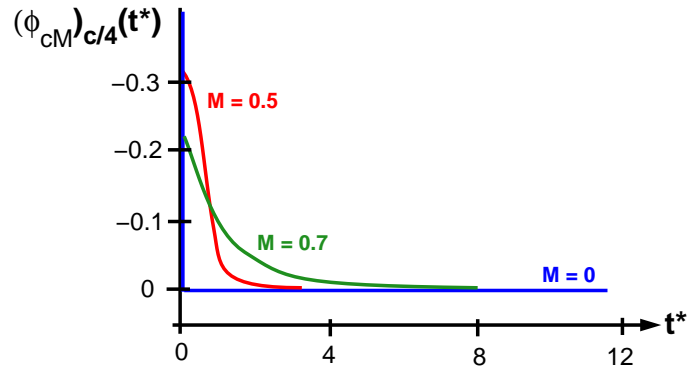


Figure 5.6: Indicial moment responses in compressible flow

5.5 Practice Problems

p5.5.11 Which of the real or imaginary components of L_h , L_t , M_h or M_t has the largest relative deviation from the incompressible unsteady flat-plate model corrected by the Prandtl-Glauert factor?

p5.5.12 Using piston theory and the Prandtl-Glauert correction, sketch the $M=0.5$ indicial plunge function for a finite wing with an incompressible lift-curve slope of 4. Give values for $t = 0$ and $t = \infty$.

Chapter 6

Analytic Solutions for Supersonic Flows

In this chapter we will consider solutions to the linear potential equation for supersonic flows. We will start by considering an isolated airfoil (figure 6.1). This case is quite different from the solutions we have considered up to now, as convecting vorticity in the wake has no influence on the airfoil's forces due to the former's restricted domain of influence. This allows us to concentrate on the analysis of time-delay effects. Note that in more general supersonic problems, such as those with highly swept or multiple lifting surfaces, convecting vorticity must again be taken into account. This will be discussed in more detail at the end of the chapter.

Although the unsteady supersonic airfoil problem was first solved by von Borbely in 1942, we will consider the later solution by Garrick and Rubinow (1946), because of its more physical interpretation. As for the incompressible case, we will exploit the linearity of the governing equations and solve the problem using a distribution of potential flow singularities. Once again, since each of the singularities is a solution to the governing equations, to solve the problem we only need to find the combination of their strengths which satisfies the boundary conditions.

The boundary conditions we need to consider are simpler than those of the incompressible case. Firstly, as the wake has no influence on the isolated airfoil, we may ignore Kelvin's theorem and the zero-pressure-change-across-the-wake condition. Secondly, although in the far-field the disturbance is finite and a function of the solution, we need not take it explicitly into account as it will be automatically provided once the singularity strengths are determined (this was also true for the incompressible case). This leaves us with only the flow-tangency condition to enforce.

Note that although the perturbation in the far-field is non-zero, for an earth-fixed observer, it is only non-zero for a finite time. This can be appreciated by imagining the airfoil in figure 6.1 passing over you. Initially you will feel

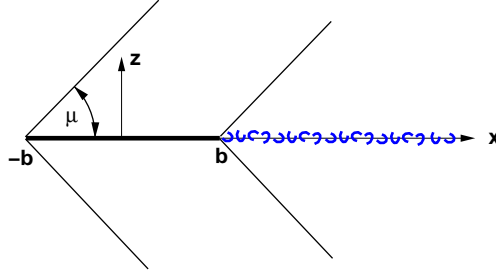


Figure 6.1: Thin airfoil in supersonic flow

the compression after you are passed by the wave emanating from the leading edge, and then expansion back to ambient pressure after you are passed by the wave emanating from the trailing edge. If you are sufficiently far away, the perturbation you feel due to the wake will be negligible.

6.1 Problem definition

As given in chapter 3, the linearised potential equations for unsteady compressible flows are:

$$\frac{\partial^2 \phi}{\partial x^2}(1 - M^2) + \frac{\partial^2 \phi}{\partial z^2} = \frac{1}{a^2} \left(\frac{\partial^2 \phi}{\partial t^2} + 2U \frac{\partial^2 \phi}{\partial t \partial x} \right) \quad (6.1)$$

$$p - p_\infty = -\rho_\infty \left(\frac{\partial \phi}{\partial t} + U_\infty \frac{\partial \phi}{\partial x} \right) \quad (6.2)$$

As for the incompressible case, the airfoil will be located in the $z = 0$ plane, so that the linearized flow tangency condition can be expressed:

$$\left. \frac{\partial \phi}{\partial z} \right|_{z=0} = w_{FM}(x, t) \quad (6.3)$$

Our intent is to represent the airfoil using a distribution of solutions to (6.1). A particularly useful one for this purpose is the source-pulse solution:

$$\phi_s(x, z, t) = \frac{A(\xi, \zeta, T)}{\sqrt{a^2(t - T)^2 - [(x - \xi) - U(t - T)]^2 - (z - \zeta)^2}} \quad (6.4)$$

$\phi_s(x, z, t)$ is the potential induced by a pulse of strength A at (ξ, ζ) and time T , measured at a point located at (x, z) at time t . Its effect can be visualised by considering the expanding sphere of the pulse disturbance front in the airfoil frame of reference, as shown in figure 6.2.

At time T the pulse is made, but due to the finite time of information propagation, it takes time for the surrounding regions to become aware of it. We use

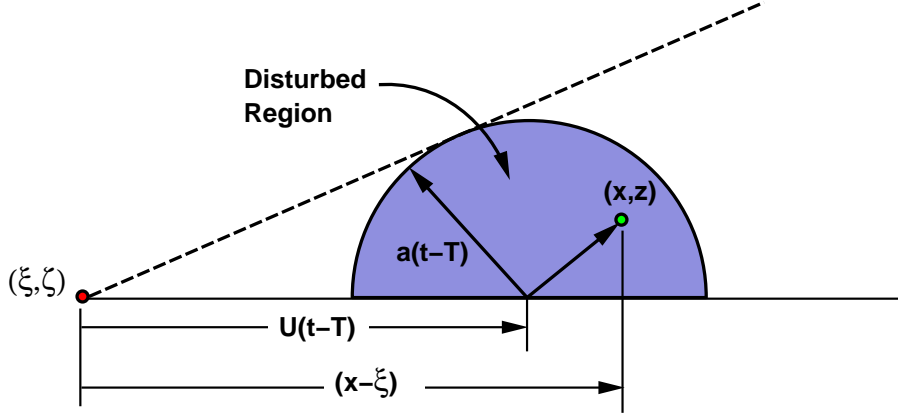


Figure 6.2: Expansion of a travelling pulse

the term “pulse disturbance front” to refer to the surface which separates points which are aware of the pulse from those who are not. The pulse disturbance front is a sphere (a cylinder in 2D problems) which expands with the speed of sound a . Since the airfoil is moving, however, the sphere is also convected downstream with a speed U . At a certain time, the disturbance front will expand and convect enough to reach (x, z) . After this time (x, z) is influenced by the pulse. Since $U > a$, however, after a certain time the sphere will be swept past (x, z) . After this time the effect of the pulse at (x, z) disappears. Note that points above the dashed line in figure 6.2 never feel the effect of the pulse. The dashed line therefore defines the limit of the pulse’s zone of influence. The cone obtained by revolving the dashed line around the x-axis is called the Mach cone (this becomes a wedge in 2D problems).

6.1.1 General approach:

We will represent the airfoil using a superposition of source pulses located on $z = 0$ between $x = -b$ and $x = +b$ (see figure 6.3). Then we will:

1. Derive a general expression for the potential at (x, z) due to source-pulses distributed along the airfoil
2. Derive $\frac{\partial \phi}{\partial z}$, and take the limit as $z \rightarrow 0 \pm$
3. Apply the flow-tangency condition to determine the source-pulse strength distribution
4. Evaluate $\frac{\partial \phi}{\partial t}$ and $\frac{\partial \phi}{\partial x}$ from the determined source-pulse potentials
5. Compute the pressure distribution, forces, and moments

As explained above, the effects of our component solutions are only felt over limited extents of time and space. Thus, in order to complete step 1, we must first establish formal limits of integration for the potential at (x, z) .

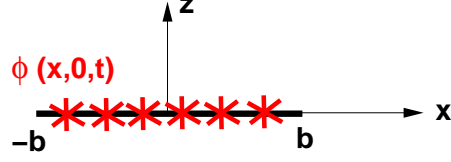


Figure 6.3: Source-pulse representation of a thin airfoil

6.2 Time Integration Limits

Consider the pulse disturbance front at two different times, τ_1 and τ_2 , as shown in figure 6.4. The point (x, z) first feels the potential of the pulse at τ_1 , when the expanding cylinder of the disturbance first makes contact. (x, z) is then kept within the cylinder as it expands and convects until τ_2 , when the expanding disturbance front is finally swept past (x, z) .

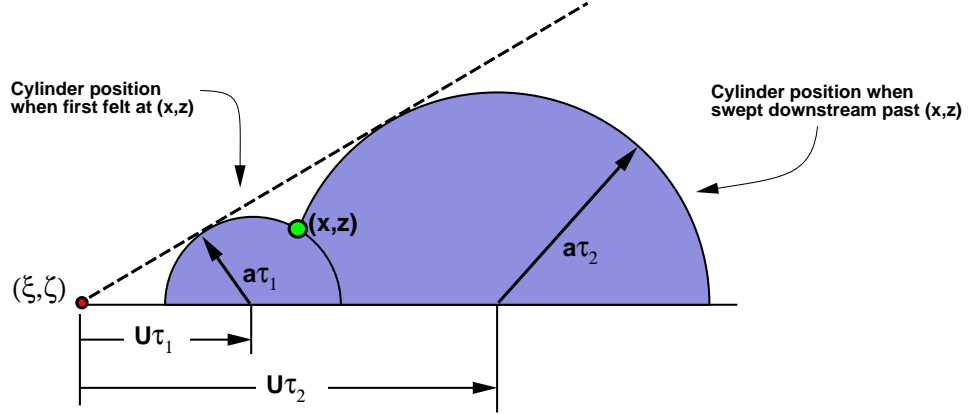


Figure 6.4: Times of influence for a travelling pulse

Mathematically, the interval within which the influence of the pulse is felt at (x, z) corresponds to when the expression for $\phi_s(x, z, t)$ is real. Defining $\tau = t - T$, we can determine the times τ_1, τ_2 between which the pulse is felt at

(x, z) by setting the denominator of the source function to zero:

$$\tau_1, \tau_2 = \frac{M(x - \xi) \mp \sqrt{(x - \xi)^2 - (M^2 - 1)(z - \zeta)^2}}{a(M^2 - 1)} \quad (6.5)$$

Thus when deriving an expression for the potential at (x, z) , we need only to integrate between times τ_1 and τ_2 .

6.3 Spatial Integration Limits

In the same way that we defined a rearward-looking Mach cone as containing the region of influence of a pulse, we can also construct a forward-looking Mach cone which defines the region of influence for a point. Such a forward-looking Mach cone is shown in figure 6.5. Note that the half-angle of the cone, μ (the Mach angle), is the same as that of the rearward-looking Mach cone.

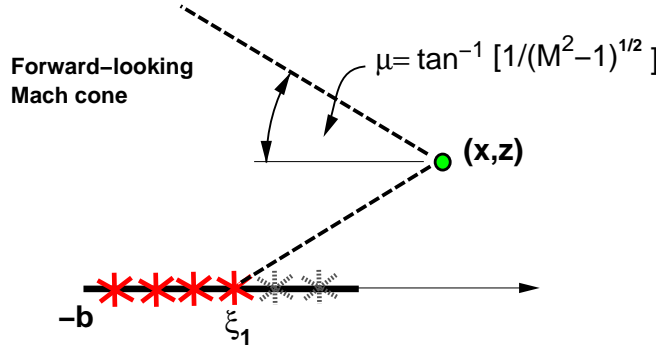


Figure 6.5: Spatial limits of integration for point (x, z)

With a little bit of geometry, we can establish the spatial limits of integration for sources on the airfoil which can influence the point (x, z) . If (x, z) is above the airfoil, then the limits are:

$$\xi = -b \quad \text{to} \quad \xi_1 = x - z\sqrt{M^2 - 1} \quad (6.6)$$

if (x, z) is below the airfoil, then the limits are:

$$\xi = -b \quad \text{to} \quad \xi_1 = x + z\sqrt{M^2 - 1} \quad (6.7)$$

6.4 Potential induced by the airfoil

Assuming we have a continuous distribution of sources on the airfoil running from $-b$ to b , we can then express the potential induced at (x, z) as:

$$\phi(x, z, t) = \int_{-b}^{\xi_1} \int_{\tau_1}^{\tau_2} \frac{A(\xi, 0, T) \, d\tau d\xi}{\sqrt{a^2(t - T)^2 - [(x - \xi) - U(t - T)]^2 - (z - \zeta)^2}} \quad (6.8)$$

which, noting that τ_1, τ_2 are the roots of the denominator of the source function, can also be expressed:

$$\phi(x, z, t) = \frac{1}{\sqrt{U^2 - a^2}} \int_{-b}^{\xi_1} \int_{\tau_1}^{\tau_2} \frac{\hat{A}(\xi, 0, t - \tau)}{\sqrt{(\tau - \tau_1)(\tau_2 - \tau)}} d\tau d\xi \quad (6.9)$$

where we have chosen to re-express the integral in terms of $\hat{A} = \sqrt{U^2 - a^2}A$. If we use an angle transformation defined in terms of an angle γ as :

$$\tau = \frac{(\tau_2 - \tau_1)}{2} \cos \gamma + \frac{(\tau_2 + \tau_1)}{2} \quad (6.10)$$

then after changing variables from τ to γ and substituting for $d\tau$ the denominator cancels perfectly, allowing us to simplify the expression to:

$$\begin{aligned} \phi(x, z, t) &= \frac{1}{\sqrt{U^2 - a^2}} \int_{-b}^{\xi_1} \int_0^\pi \hat{A} \left(\xi, 0, t - \frac{(\tau_2 - \tau_1)}{2} \cos \gamma - \frac{(\tau_2 + \tau_1)}{2} \right) d\gamma d\xi \end{aligned} \quad (6.11)$$

$$= \frac{1}{\sqrt{U^2 - a^2}} \int_{-b}^{\xi_1} \int_0^\pi \hat{A}(\xi, 0, T) d\gamma d\xi \quad (6.12)$$

where

$$T = t - \frac{M(x - \xi)}{a(M^2 - 1)} - \frac{\sqrt{(x - \xi)^2 - (M^2 - 1)z^2}}{a(M^2 - 1)} \cos \gamma \quad (6.13)$$

6.5 Normal velocity at the Airfoil

To evaluate $w = \frac{\partial \phi}{\partial z}$, we must consider the z -dependence of the limit ξ_1 and the time-delay variable, both of which are ultimately arguments to \hat{A} :

$$\begin{aligned} \frac{\partial \phi}{\partial z} &= \frac{1}{\sqrt{U^2 - a^2}} \left[\frac{\partial \xi_1}{\partial z} \int_0^\pi \hat{A}(\xi_1(z), T(t, \xi_1(z), z, \gamma)) d\gamma \right. \\ &\quad \left. + \int_{-b}^{\xi_1} \int_0^\pi \frac{\partial \hat{A}(\xi, T(t, \xi, z, \gamma))}{\partial z} d\gamma d\xi \right] \end{aligned} \quad (6.14)$$

which leads to:

$$\begin{aligned} \frac{\partial \phi}{\partial z} &= \frac{1}{\sqrt{U^2 - a^2}} \left[\frac{\partial \xi_1}{\partial z} \pi \hat{A} \left(\xi_1, t - \frac{Mz}{a\sqrt{M^2 - 1}} \right) \right. \\ &\quad \left. + \int_{-b}^{\xi_1} \int_0^\pi \frac{\partial \hat{A}((x - \xi)^2 - (M^2 - 1)z^2)^{-1/2}}{\partial T} \frac{1}{a(M^2 - 1)} (z \cos \gamma) d\gamma d\xi \right] \end{aligned} \quad (6.15)$$

Taking the limit as you approach the airfoil from the upper side:

$$\left. \frac{\partial \phi}{\partial z} \right|_{z=0^+} = -\frac{\pi}{a} \hat{A}(x, 0, t) \quad (6.16)$$

while the negative of this expression is true when approaching from the lower side (see the definition of ξ_1).

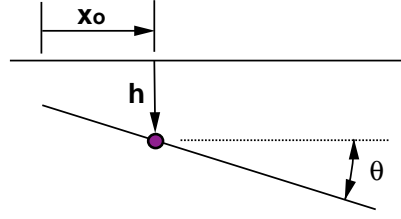


Figure 6.6: A pitching and plunging flat plate

6.6 Flow-Tangency Condition

From (6.16) we see that flow tangency can be expressed:

$$\hat{A}(x, 0, t) = -w_{FM}(x, t)a/\pi \quad (\text{upper side}) \quad (6.17)$$

$$= +w_{FM}(x, t)a/\pi \quad (\text{lower side}) \quad (6.18)$$

The source-pulse distribution is therefore directly related to the local vertical velocity! The resulting potential function at the airfoil is:

$$\phi(x, t) = \mp \frac{1}{\pi\sqrt{M^2-1}} \int_{-b}^x \int_{\tau_1}^{\tau_2} \frac{w_{FM}(\xi, t-\tau)}{\sqrt{(\tau-\tau_1)(\tau_2-\tau)}} d\tau d\xi \quad (6.19)$$

This expression can be used to find the force response of the airfoil to any given w_{FM} , by integration and substitution into the linearised pressure relation. In general it is integrated numerically, but it is also possible to integrate it analytically for the case of harmonic motion, as discussed in the next section.

6.7 Solutions for Harmonic Motion

To construct a harmonic solution we assume the following forms for the input and response:

$$\theta = \hat{\theta}e^{i\omega t}; \quad h = \hat{h}e^{i\omega t}; \quad w_{FM}(\xi, t-\tau) = \hat{w}_{FM}e^{i\omega(t-\tau)} \quad (6.20)$$

After some manipulation the potential at the airfoil can then be expressed as:

$$\phi(x, t) = \pm \frac{2b}{\sqrt{M^2-1}} \int_0^x \left[U\theta + \dot{h} + 2b(\xi - x_o)\dot{\theta} \right] I(\xi, x, M, \bar{\omega}) d\xi \quad (6.21)$$

$$\text{where: } I(\xi, x, M, \bar{\omega}) = e^{-i\bar{\omega}(x-\xi)} J_0 \left[\frac{\bar{\omega}}{M}(x-\xi) \right] \quad \text{and} \quad \bar{\omega} = \frac{\omega b}{U} \frac{2M^2}{M^2-1} \quad (6.22)$$

The details of the analytic procedure can be found in NACA report R846 by Garrick and Rubinow, or in the text by Bisplinghoff. The harmonic case can

also be derived very efficiently using a Laplace transform, as shown in the text by Fung.

The explicit expression for the potential can be differentiated with respect to time and space, and the results substituted into the linearised pressure relation to determine the pressure perturbation. This can be integrated along the chord to arrive at expressions for the airfoil's lift and moment, which are usually written compactly as:

$$L = 4\rho b U^2 k^2 e^{i\omega t} \left[\frac{\hat{h}}{b} (L_1 + iL_2) + \hat{\theta} (L_3 + iL_4) \right] \quad (6.23)$$

$$M = -4\rho b^2 U^2 k^2 e^{i\omega t} \left[\frac{\hat{h}}{b} (M_1 + iM_2) + \hat{\theta} (M_3 + iM_4) \right] \quad (6.24)$$

$$(6.25)$$

where $L_{1..4} = L_{1..4}(M, \bar{\omega})$ and $M_{1..4} = M_{1..4}(M, \bar{\omega})$ are coefficients dependent on $\bar{\omega}$ and M . Alternatively, the lift and moment can be expressed in terms of the L_h , M_h , L_θ , and M_θ coefficients introduced previously, which are then functions of k and M (note that $\bar{\omega}$ is essentially a modified reduced-frequency parameter). Figures 6.7 and 6.8 show the variation of these coefficients with Mach number and reduced frequency. Both the real and imaginary components of the response can be dramatically affected by these parameters. You are free to experiment for yourself using the program at:

<https://aerodynamics.lrr.tudelft.nl/cgi-bin/lpfp>

6.8 Finite wings, Multiple Surfaces

The 2D method described in the previous sections can readily be extended to 3D wings, provided that the leading edges of the 3D wing are “supersonic”. A wing with supersonic leading edges is shown in the left part of figure 6.9. A point P lying on the wing surface is only aware of pulses from the upper surface, as defined by its forward-looking Mach cone. There is no way a disturbance from the wake or the lower surface can reach it. The situation is different for a highly-swept wing operating at a low Mach number, as shown on the right. In this case, a disturbance on the lower surface near the forward edge of the wing will disturb the inflow region to point P (draw a rearward-looking Mach cone to convince yourself of this). This makes the integration procedure more complex, so it is normally necessary to resort to numerical methods. In the case shown, P is also influenced by a portion of the wake. Therefore, it is also necessary to impose the unsteady Kutta condition and the zero-pressure-change-across-the-wake condition in order to obtain the correct solution.

When multiple lifting surfaces are present, it can easily be the case that the wake of the upstream surface influences the forces and moments developed on downstream surfaces (see, for example, problem 6.4). Where this is the case, all

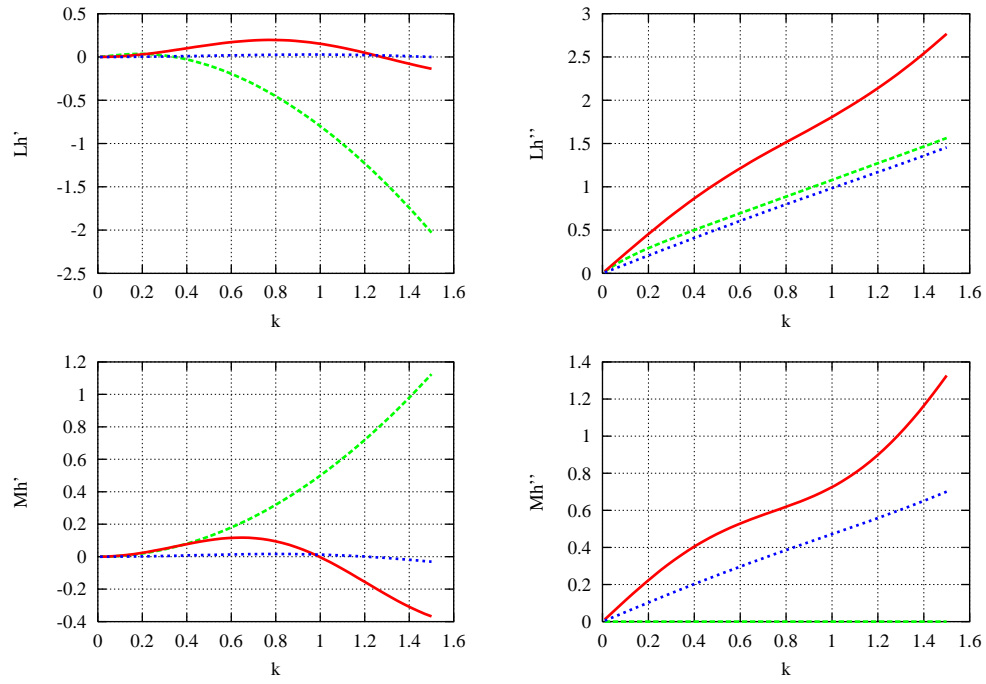


Figure 6.7: Plunging case - comparison of $M=2.0$ (solid), $M=4.0$ (dotted) and $M=0$ (dashed) responses ($a=-1/2$). (Supersonic values multiplied by π)

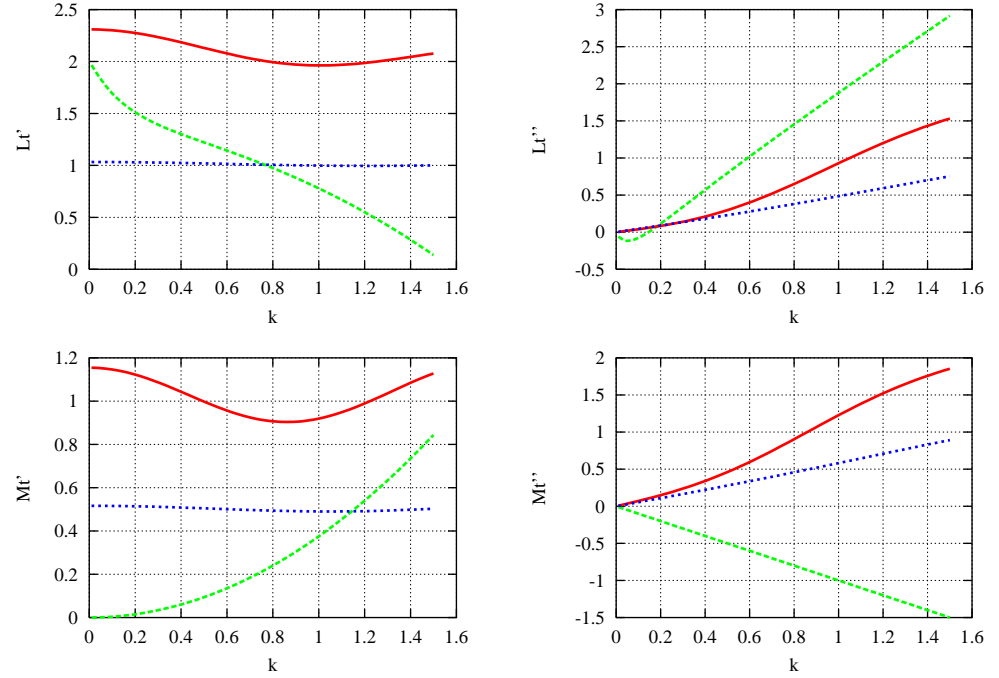


Figure 6.8: Pitching case - comparison of $M=2.0$ (solid), $M=4.0$ (dotted) and $M=0$ (dashed) responses ($a=-1/2$). (Supersonic values multiplied by π)

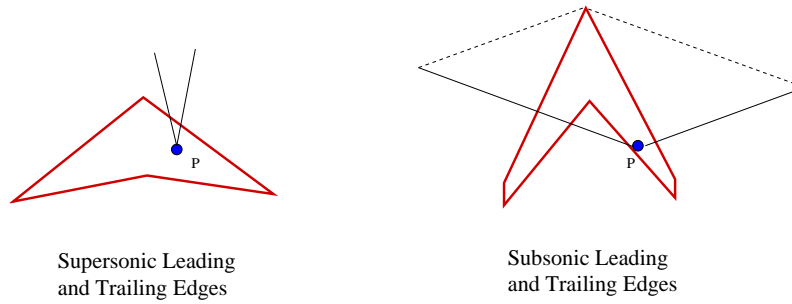


Figure 6.9: Zones of influence for finite wings

appropriate boundary conditions must be applied to the wake of the upstream surface.

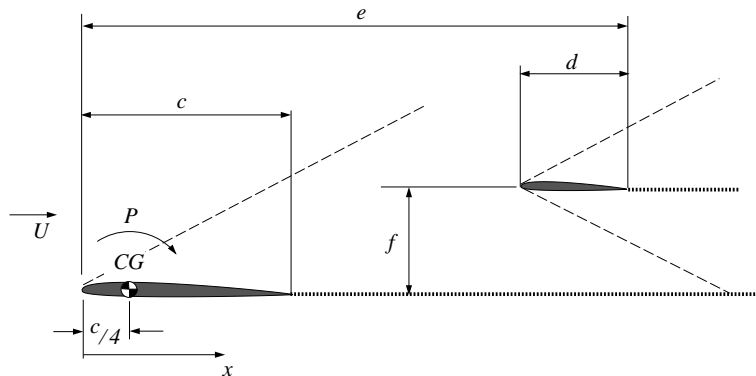
6.9 Practice Problems

p6.9.13 How long does a point (x, z) feel a pulse at (ξ, ζ, T) if (ξ, ζ) is on the forward-looking Mach cone of (x, z) ?

p6.9.14 Briefly outline how you could use linearised theory to determine the lift response of an airfoil to a sharp-edged gust in supersonic flow. Use equations from the notes.

p6.9.15 After how many half-chords travelled, s , ($s = U\Delta t/b$) should an indicially-plunged supersonic airfoil reach its steady-state lift?

p6.9.16 A wing-tail combination is travelling at a Mach number of $M = \sqrt{5}$, when it is subjected to a step plunge with amplitude \dot{h}_o at $t = 0$.



- Estimate the aerodynamic moment, P , about the CG at the initiation of the plunge.
- Assume the step plunge response is to be computed using a linear potential method. Calculate the length of the wing wake which must be included in the computation. What condition should be applied on the wake?

Chapter 7

Arbitrary Unsteady Aerodynamic Responses

Most of the analytic solutions we have considered up to now exploit mathematical simplifications inherent with the use of harmonic functions. Unsteady experimental data is also most often available in harmonic form, since it avoids the application of sudden or irregular forces, and allows the certainty of the data to be increased by averaging over several cycles.

If one is confronted with a problem where a non-harmonic response is required, one could in principle just use more complex versions of the same analytic or experimental procedures discussed up to now. This can be inconvenient, however, if many different types of responses must be considered, or if the exact form of the motion is itself determined by the solution of an aeroelastic interaction. It is often far smarter to directly use the harmonic motion results in a way which can provide predictions for aerodynamic responses to arbitrary motions.

A different reasoning might apply if one is using expensive numerical computations, or expensive flight tests to determine unsteady aerodynamic responses. In such cases one may wish to limit measurement times, and therefore limit the excitations considered to a few which contain a range of frequencies. One would still like to use the measured results to predict arbitrary responses, however, including pure harmonic ones if necessary for flutter computations or for comparison with harmonic experiments.

This section will describe how arbitrary responses can be computed from indicial, impulse, harmonic, and state-space responses. For the moment we will assume that the responses are linear, allowing us to use simple integral relations. It also is possible to treat fully non-linear responses using similar techniques, as we will see in a later chapter. In practice, however, the linear assumption is often used even when non-linear conditions are considered, as linearisations about non-linear base flows are often reasonably accurate for practical ranges of perturbations.

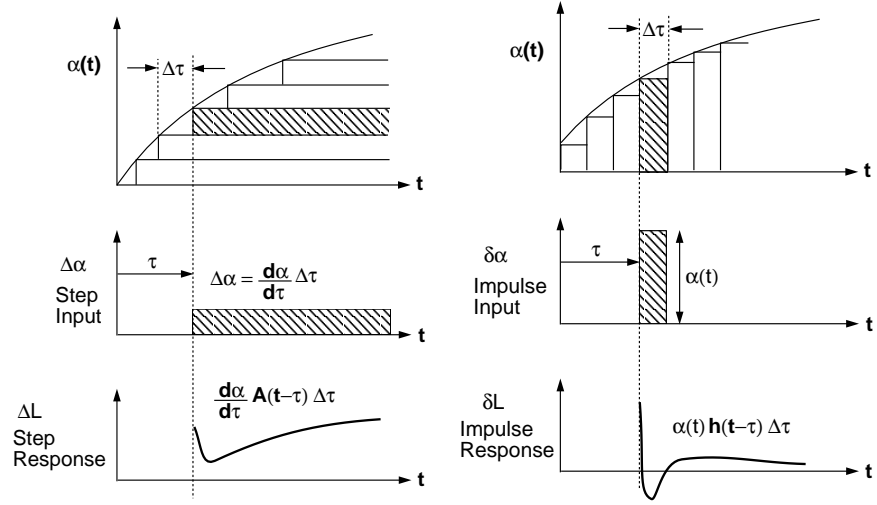


Figure 7.1: Convolution of step (left) and impulse (right) responses

7.1 Indicial and Impulse Functions

The response to an arbitrary input can be obtained by summing indicial (step) or impulse (spike) responses of a system. If the system has multiple inputs, one indicial or impulse function per input degree of freedom is required. Indicial and impulse functions are convenient for time-domain simulations where the final form of the response is unknown. When identifying responses using numerical methods (CFD), indicial inputs tend to be preferred over impulse responses due to their less singular nature. In some cases smoothed indicial functions are also used in order to limit the excitation of high-frequency spurious numerical modes within the solution.

Given an indicial response, one can obtain an arbitrary response by convolution using Duhamel's integral. Referring to figure 13.13(left), for a step change in angle of attack, $\Delta\alpha$, we may write:

$$L(t) = A(t)\Delta\alpha \quad (7.1)$$

where $A(t)$ is the indicial function. For a continuously changing $\alpha(t)$:

$$L(t) = A(t)\alpha(0) + \int_0^t \left(\frac{d\alpha}{dt} \right) (\tau) A(t - \tau) d\tau \quad (7.2)$$

A similar approach can be followed to compute arbitrary responses using impulse responses (figure 13.13(right)):

$$L(t) = \int_0^t \alpha(t) h(t - \tau) d\tau \quad (7.3)$$

where $h(t)$ is the aerodynamic impulse response.

7.2 Fourier Transforms

If one has a description of the aerodynamic forces in the frequency domain, Fourier transforms can be used to construct responses to arbitrary inputs. For reference, the definition of the Fourier transform pair is:

$$F(\omega) = \int_{-\infty}^{\infty} f(t)e^{-i\omega t} dt \quad (\text{Direct Fourier Transform}) \quad (7.4)$$

$$f(t) = \frac{1}{2\pi} \int_{-\infty}^{\infty} F(\omega)e^{i\omega t} d\omega \quad (\text{Inverse Fourier Transform}) \quad (7.5)$$

7.2.1 Computation of an arbitrary response

Assume we have an arbitrary input signal, for example an airfoil's instantaneous angle of attack, $\alpha(t)$, and unsteady results for the lift coefficient for a range of harmonic excitations, $C_{L\alpha}(\omega)$. To compute the arbitrary response, we first transform $\alpha(t)$ to the frequency domain using the direct transform to obtain $\alpha(\omega)$. Then we use the inverse transform to compute the time-domain lift response as:

$$L(t) = \frac{\rho U^2 S}{4\pi} \int_{-\infty}^{\infty} \alpha(\omega) C_{L\alpha}(\omega) e^{i\omega t} d\omega \quad (7.6)$$

We can think of taking the direct transform of $\alpha(t)$ as determining the harmonic components of α , and the inverse transform as a summation of each component multiplied by the $C_{L\alpha}$ at the corresponding frequency. Although we will consider analytic expressions here, in practice the procedure is often performed using fast Fourier transform (FFT) techniques.

7.2.2 Re-expression of the incompressible results

Using the above ideas we can re-express our results for the 2D flat plate in incompressible harmonic motion in order to compute arbitrary responses. Recall that the component of the lift response dependent on the flow time history can be expressed as a function of the motion of the three-quarter chord point:

$$L(t) = \pi \rho b^2 [\ddot{h}(t) + U_\infty \dot{\theta}(t) - ba\ddot{\theta}(t)] + 2\pi \rho U_\infty b C(k) [w_{\frac{3}{4}c}(t)] \quad (7.7)$$

where $k = \omega b/U_\infty$, and $w_{\frac{3}{4}c}(t)$ can be computed for any combination of pitch, θ , and plunge, h . If we focus on the second term, the frequency-domain representation of its input is:

$$W(k) = \int_{-\infty}^{\infty} w_{\frac{3}{4}c}(t) e^{-ikt^*} dt^* \quad (7.8)$$

where $t^* = \frac{tU_\infty}{b}$. $W(k)$ can be seen as the magnitude of a group of sinusoids with frequencies ranging from $-\infty$ to ∞ which add up to $w_{\frac{3}{4}c}(t)$.

Since our aerodynamic theory is linear, we can replace the second term in the lift expression with the sum of the responses to each one of the sinusoids:

$$L(t) = \pi \rho b^2 [\ddot{h}(t) + U_\infty \dot{\theta}(t) - ba\ddot{\theta}(t)] + \rho U_\infty b \int_{-\infty}^{\infty} C(k) W(k) e^{ikt^*} dk \quad (7.9)$$

This allows us to use the analytic expressions for $C(k)$ in the computation of arbitrary lift responses.

7.2.3 Conversion to an Indicial response

If we want to convert our frequency-domain representations to an indicial response, we need to compute the Fourier transform of a step input. This can be done by considering the limit as $a \rightarrow 0$ for a one-sided decaying exponential:

$$g(t) = \begin{cases} 0 & t < 0 \\ e^{-at} & t \geq 0 \end{cases} \quad (7.10)$$

$$e^{-at} \quad t \geq 0 \quad (7.11)$$

which for $a > 0$ has the Fourier transform:

$$G(w) = \frac{1}{a + i\omega} = \frac{a}{a^2 + \omega^2} - \frac{i\omega}{a^2 + \omega^2} \quad (7.12)$$

Since for $a \rightarrow 0$

$$\int_{-\infty}^{\infty} \frac{a}{a^2 + \omega^2} d\omega = \pi \quad (7.13)$$

the Fourier transform for a unit step is finally:

$$\pi \delta(\omega) + \frac{1}{i\omega} \quad (7.14)$$

To speed manipulation, however, we will consider the step function to be defined by (7.11) where a is very small but finite, so that its approximate transform is:

$$\frac{1}{i\omega} \quad (7.15)$$

This approximation allows us to express the indicial plunge lift response of a flat plate in incompressible flow as:

$$\phi(t^*) = \frac{1}{2\pi} \int_{-\infty}^{\infty} \frac{C(k)}{ik} e^{ikt^*} dk \quad (7.16)$$

where we have changed to the non-dimensional variables k and t^* , and have also ignored the initial infinite response peak arising from the apparent mass terms.

7.2.4 Conversion from an Indicial response

For the analysis of aeroelastic instability boundaries, it can be convenient to have the aerodynamic forces for harmonic motion. We can obtain these from an indicial response using the direct Fourier transform.

For example, we can derive an approximate relation for Theodorsen's function in the frequency domain using the approximation to the indicial function in the time domain using:

$$\frac{C(k)}{ik} = \int_{-\infty}^{\infty} \phi(t^*) e^{-ikt^*} dt^* \quad (7.17)$$

$$C(k) \approx 1 - \frac{0.165k}{k - 0.0455i} - \frac{0.335k}{k - 0.3i} \quad (7.18)$$

Note that this approximation contains spurious poles at $k = 0.0455i$ and $k = 0.3i$.

7.3 State-Space Representations

Control system designs often based on a “state space” approach, where the system is represented in terms of first-order differential equations in time:

$$\frac{d}{dt}\{x\} = [A]\{x\} \quad (7.19)$$

For steady aerodynamic models, one can easily cast the dynamic equations in this form by introducing additional variables for the derivatives of the structural DOFs (degrees of freedom). In the case of unsteady aerodynamics, however, a theoretically infinite number of additional variables would be required in order to express the applied forces in terms of multi-variate Taylor expansions.

Using sophisticated identification techniques, it is possible to produce reasonable approximations for the unsteady aerodynamic operators while keeping the number of additional variables relatively low, typically on the order of 10 times the number of structural DOFs. (see Silva and Raveh, AIAA Paper 2001-1213 for an example).

7.4 Practice Problems

p7.4.17 The Sears function expresses the response of an airfoil to a sinusoidal gust. Derive an approximation for the Sear's function, $S(k)$, using the approximation to Küssner's function given in chapter 4.

Chapter 8

Compact Models of Structural Systems

With modern computing facilities it is possible to resolve most of the detailed dynamics of structural systems. Yet compact (low-DOF) structural models are often used in practical aeroelastic computations, particularly during the preliminary design stage. To understand why this is so, let's consider the flutter analysis technique we discussed in chapter 2. A complex representation of a structure, such as that obtained by finite element analysis, will have many degrees of freedom, or a large vector of unknowns x . In principle such a system can also be treated with the standard flutter analysis technique, although it may be necessary to use specialised procedures for finding the p roots of large systems.

The problem arises when one tries to interpret the flutter diagrams. A very large number of modes will be generated, and correspondingly a large number of interactions will occur. A detailed analysis will be necessary to determine which modes are physically relevant. This will involve, among other procedures, rejecting modes of high spatial wave number due to their large associated numerical errors. Depending on how complex the retained modes are, however, it can still be a challenge deciding what is the most appropriate action to change the behaviour of the system. In contrast, if one can choose a reasonably-accurate compact representation of the system, the chances of developing design insight are far higher.

This chapter will address the question of how to construct compact representations of complex structural systems, such as those present in aircraft. We will start by discussing the concept of generalised coordinates, leading to a derivation of Lagrange's equations. These provide a straightforward way to determine the equations of motion in terms of compact sets of variables that are only indirectly related to local structural displacements. We will then specialise Lagrange's equations to the case of a free-flying vehicle, and discuss opportunities for their simplification.

Finally, two approaches to deriving compact structural models using Lagrange's equations will be demonstrated. The first of these, known as the lumped-parameter approach, makes intuitive use of local mass-spring systems. The second, known as the Rayleigh-Ritz approach, instead makes use of global modes which are known to be representative of the structure's motion. These methods are discussed in an introductory manner. For further information the reader is referred to one of many textbooks on the subject of structural dynamics.

8.1 Generalised Coordinates

The use of generalised rather than particle coordinates for representing the motion of a body can lead to substantial savings in the numbers of degrees of freedom required. For example, consider two representations of a rigid triangle moving in the x-y plane, as shown in figure 8.1.

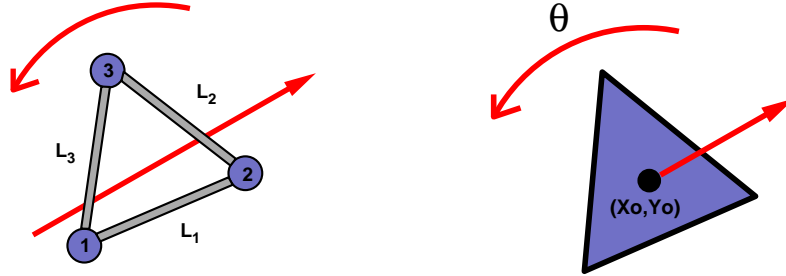


Figure 8.1: Particle (left) and generalised (right) coordinates

In figure 8.1 (left) the triangle is visualised as nodes connected by rigid bars. In order to describe its motion, we use the particle coordinates of the nodes as unknowns, and Newton's second law to describe their evolution. This leads to six equations of motion, as there are six particle coordinates:

$$\mathbf{r}_p = (x_p, y_p) \quad p = 1..3 \quad (8.1)$$

Since the bars are rigid, we also need to apply three constraints between the nodes of the form:

$$(x_2 - x_1)^2 + (y_2 - y_1)^2 = L_1^2, \dots \quad (8.2)$$

However, had we made a choice of non-particulate, generalised coordinates, such as the displacement of the centroid and the rotation angle of the triangle, $q_1 = X_o, q_2 = Y_o, q_3 = \theta$ we would immediately have arrived at only three equations of motion, without the need for constraints.

In the particle coordinate case, the additional constraints are holonomic, in that they can be written as explicit equations which express the behaviour of the particle coordinates in time. In theory these can also be used to reduce

the equations of motion to three. In many cases, however, constraints are non-holonomic and can be difficult to apply (e.g. inequalities forcing a fuel particle to remain in the fuel tank). By choosing our coordinates carefully, we can apply the constraints implicitly, thereby reducing the degrees of freedom while avoiding the need to deal with difficult constraints directly.

8.2 Lagrange's Equations of Motion

Once appropriate generalised coordinates have been chosen, how does one determine their associated equations of motion? This can be done by starting by defining a transformation between generalised and particle coordinates:

$$\mathbf{r}_p = \mathbf{r}_p(q_1, q_2, q_3 \dots q_N) \quad (8.3)$$

Using the chain rule, one may express a small change in a particle coordinate, $\delta \mathbf{r}_p$, as:

$$\delta \mathbf{r}_p = \sum_{i=1}^N \frac{\partial \mathbf{r}_p}{\partial q_i} \delta q_i \quad (8.4)$$

Similarly:

$$\dot{\mathbf{r}}_p = \sum_{i=1}^N \frac{\partial \mathbf{r}_p}{\partial q_i} \dot{q}_i \quad \text{from which:} \quad \frac{\partial \dot{\mathbf{r}}_p}{\partial \dot{q}_i} = \frac{\partial \mathbf{r}_p}{\partial q_i} \quad (8.5)$$

Consider Newton's second law for a system of M particles:

$$m_p \ddot{\mathbf{r}}_p - \mathbf{F}_p = 0 \quad p = 1 \dots M \quad (8.6)$$

We may write the virtual work expression for the system of particles as:

$$\sum_{p=1}^M (m_p \ddot{\mathbf{r}}_p - \mathbf{F}_p) \cdot \delta \mathbf{r}_p = 0 \quad (8.7)$$

The first term of this equation may be expressed:

$$\sum_{p=1}^M (m_p \ddot{\mathbf{r}}_p) \cdot \delta \mathbf{r}_p = \sum_{p=1}^M \left(\sum_{i=1}^N m_p \ddot{\mathbf{r}}_p \cdot \frac{\partial \mathbf{r}_p}{\partial q_i} \delta q_i \right) \quad (8.8)$$

$$= \sum_{i=1}^N \sum_{p=1}^M \left[\frac{d}{dt} \left(m_p \dot{\mathbf{r}}_p \cdot \frac{\partial \mathbf{r}_p}{\partial q_i} \right) - m_p \dot{\mathbf{r}}_p \cdot \frac{d}{dt} \left(\frac{\partial \mathbf{r}_p}{\partial q_i} \right) \right] \delta q_i \quad (8.9)$$

$$= \sum_{i=1}^N \sum_{p=1}^M \left[\frac{d}{dt} \left(m_p \dot{\mathbf{r}}_p \cdot \frac{\partial \dot{\mathbf{r}}_p}{\partial \dot{q}_i} \right) - m_p \dot{\mathbf{r}}_p \cdot \left(\frac{\partial \dot{\mathbf{r}}_p}{\partial \dot{q}_i} \right) \right] \delta q_i \quad (8.10)$$

$$= \sum_{i=1}^N \sum_{p=1}^M \left[\left(\frac{d}{dt} \left(\frac{\partial}{\partial \dot{q}_i} \right) - \frac{\partial}{\partial q_i} \right) \frac{m_p}{2} \dot{\mathbf{r}}_p \cdot \dot{\mathbf{r}}_p \right] \delta q_i \quad (8.11)$$

$$= \sum_{i=1}^N \left[\frac{d}{dt} \left(\frac{\partial T}{\partial \dot{q}_i} \right) - \frac{\partial T}{\partial q_i} \right] \delta q_i \quad (8.12)$$

where

$$T = \sum_{p=1}^M \frac{m_p}{2} \dot{\mathbf{r}}_p \cdot \dot{\mathbf{r}}_p \quad (8.13)$$

is the total kinetic energy of the system. So the first term of the virtual work expression for the system can now be expressed entirely in terms of the generalised coordinates as the kinetic energy of the system is a scalar that does not depend on what coordinates it is expressed in. The second term of the virtual work expression for the system can be written:

$$\sum_{p=1}^M \mathbf{F}_p \cdot \delta \mathbf{r}_p = \sum_{p=1}^M \mathbf{F}_p \cdot \sum_{i=1}^N \frac{\partial \mathbf{r}_p}{\partial q_i} \delta q_i = \sum_{i=1}^N \tilde{Q} \delta q_i \equiv \delta W \quad (8.14)$$

where \tilde{Q} is the net generalised force and δW is the virtual work.

It is ultimately required to express the behaviour of generalised forces directly in terms of generalised coordinates. In some cases this can be done directly, such as when they explicit change in potential (strain) energy: $U = U(q_1, q_2, \dots, q_N)$ or dissipation $D = D(\dot{q}_1, \dot{q}_2, \dots, \dot{q}_N)$. For these cases the virtual work can be expressed:

$$\delta W = -\delta U - \delta D + \sum_{i=1}^N Q \delta q_i \quad (8.15)$$

$$= \sum_{i=1}^N \left(Q - \frac{\partial U}{\partial q_i} - \frac{\partial D}{\partial \dot{q}_i} \right) \delta q_i \quad (8.16)$$

Substituting into the virtual work expression, and noting that by definition δq_i are arbitrary and independent, we can write:

$$\frac{d}{dt} \left(\frac{\partial T}{\partial \dot{q}_i} \right) - \frac{\partial T}{\partial q_i} + \frac{\partial U}{\partial q_i} + \frac{\partial D}{\partial \dot{q}_i} = Q_i, \quad i = 1, N \quad (8.17)$$

where:

- T : Kinetic energy
- U : Potential (strain) energy
- D : Rayleigh's dissipation function
- q_i : Generalised coordinate
- Q : Remaining generalised forces

Equations (8.17) are known as *Lagrange's equations* of motion.

8.3 Lagrange's Equations for a Flexible Aircraft

If one considers a flexible aircraft with deflections measured in an aircraft-fixed frame which is rotating relative to the inertial frame of reference, Lagrange's equations can take on a relatively complex form. Consider the following definitions, as shown in figure 8.2:

$$\mathbf{r} = \mathbf{s} + \mathbf{d} \quad (8.18)$$

$$\mathbf{r}' = \mathbf{r}'_o + \mathbf{r} \quad (8.19)$$

$$(8.20)$$

from which

$$\dot{\mathbf{r}}' = \dot{\mathbf{r}}'_o + \boldsymbol{\omega} \times \mathbf{r} + \frac{d\mathbf{r}}{dt} \quad (8.21)$$

- x, y, z : coordinates in local frame
- x', y', z' : coordinates in space-fixed frame
- \mathbf{r}'_o : vector giving position of the local coordinate origin
- \mathbf{r}' : vector giving position of an element in space-fixed frame
- \mathbf{r} : vector giving position of an element in local frame
- \mathbf{s} : undeflected position vector of an element in local frame
- \mathbf{d} : deformation vector of an element in local frame
- $\boldsymbol{\omega}$: angular velocity of local frame

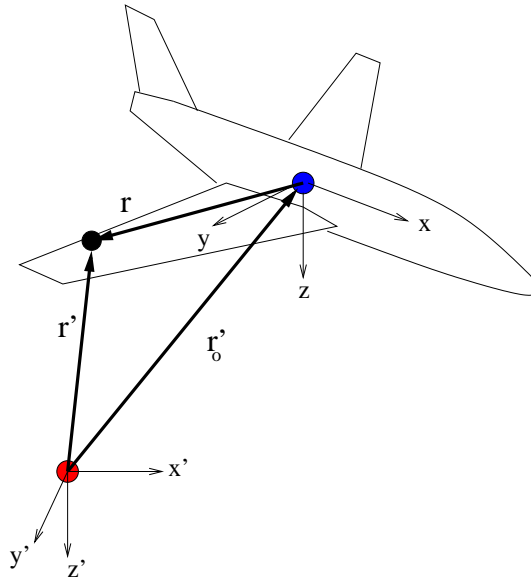


Figure 8.2: Local and space-fixed frames

The kinetic energy terms of Lagrange's equations then expand to:

$$T = \frac{1}{2} \int_V \dot{\mathbf{r}}' \cdot \dot{\mathbf{r}}' \rho dV \quad (8.22)$$

$$= \frac{1}{2} \int_V [\dot{\mathbf{r}}'_o \cdot \dot{\mathbf{r}}'_o + 2\dot{\mathbf{r}}'_o \cdot (\boldsymbol{\omega} \times \mathbf{r}) + (\boldsymbol{\omega} \times \mathbf{r}) \cdot (\boldsymbol{\omega} \times \mathbf{r})] \rho dV \quad (8.23)$$

$$+ 2\dot{\mathbf{r}}'_o \frac{d\mathbf{r}}{dt} + 2(\boldsymbol{\omega} \times \mathbf{r}) \frac{d\mathbf{r}}{dt} + \frac{d\mathbf{r}}{dt} \cdot \frac{d\mathbf{r}}{dt} \rho dV \quad (8.24)$$

where $\frac{d}{dt}$ denotes the time derivative in the local frame system and the dot denotes the time derivative in the space-fixed frame. (recall $\dot{\mathbf{r}} = \frac{d\mathbf{r}}{dt} + (\boldsymbol{\omega} \times \mathbf{r})$). The virtual work terms are:

$$\delta W = \int_S \mathbf{F} \cdot \delta \mathbf{r}'_o dS + \int_S \mathbf{s} \times \mathbf{F} \cdot \delta \left(\int_0^t \boldsymbol{\omega} dt \right) dS + \int_S \mathbf{F} \cdot \delta \mathbf{d} dS \quad (8.25)$$

Where S is the surface of the aircraft and \mathbf{F} is the force acting on the surface.

8.3.1 Options for efficient treatment

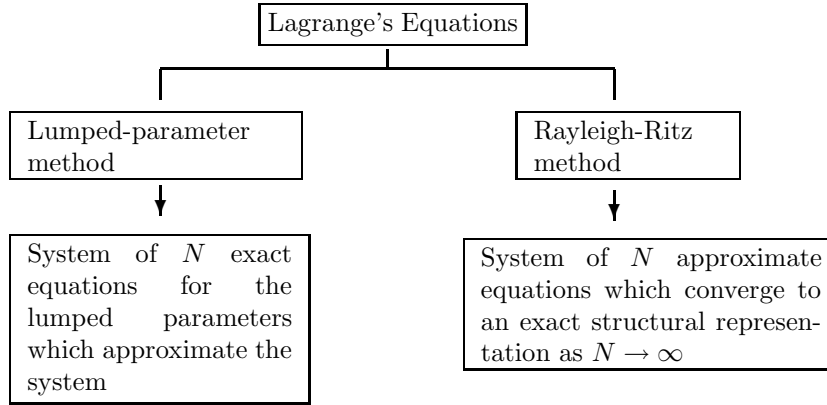
To keep things as simple as possible, a number of strategies are often applied:

1. Simplify the equations using orthogonal deformation modes as generalised coordinates
2. Linearise the equations for small $\boldsymbol{\omega}$
3. Assume that rigid-body dynamics are decoupled from aeroelastic effects (frequency separation) then:
 - Solve the rigid-body dynamics problem neglecting flexibility
 - Compute the resulting aeroelastic deformations

As well as reducing the number of terms in the equations, using orthogonal modes such as the free vibration modes can be useful from the conceptual and validation points of view. Linearizing the equations for small $\boldsymbol{\omega}$, on the other hand can lead to a loss of accuracy, so it is only appropriate for small excursions. Decoupling the rigid-body dynamics from aeroelastic motions is often done, but is inappropriate for many large, flexible aircraft. For example, the B747 has a short period mode ≈ 0.1 Hz while its fundamental symmetric wing bending mode is ≈ 1 Hz. This is relatively little separation for analysis purposes.

8.4 Methods for Constructing Compact Models

There are systematic methods for choosing generalised coordinates and deriving their equations of motion. We will consider two methods here, the lumped-parameter method and the Rayleigh-Ritz method.



We will start by consider their application to beam-like wings. Before we do so, it is worthwhile to review the following formulae for the kinetic and strain energies of a beam of length l , mass distribution $m(y)$, moment of inertia $I(y)$, and bending and torsional stiffness of $EI(y)$ and $GJ(y)$:

Kinetic and strain energies in bending

$$T = \int_0^l \frac{m}{2} \left(\frac{dw}{dt} \right)^2 dy \quad (8.26)$$

$$U = \int_0^l \frac{EI}{2} \left(\frac{d^2w}{dy^2} \right)^2 dy \quad w = w(y, t) = \text{bending deflection} \quad (8.27)$$

Kinetic and strain energies in torsion

$$T = \int_0^l \frac{I}{2} \left(\frac{d\theta}{dt} \right)^2 dy \quad (8.28)$$

$$U = \int_0^l \frac{GJ}{2} \left(\frac{d\theta}{dy} \right)^2 dy \quad \theta = \theta(y, t) = \text{torsional deflection} \quad (8.29)$$

8.5 Lumped Parameter Method

This straight-forward approach replaces the continuous system by a set of elastically coupled rigid elements: The degrees of freedom associated with each

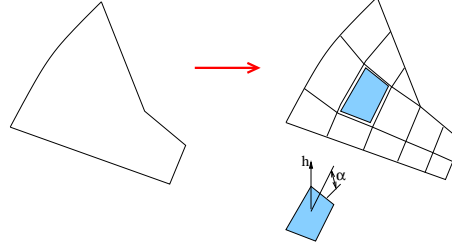


Figure 8.3: The lumped parameter method

element become the vector of generalised coordinates (Dimension N). To derive the equations of motion:

1. Express the total kinetic, potential, and dissipative energies of the system in terms of the generalised coordinates
2. Derive the generalised forces Q_i by considering the work done on the system by a virtual displacement of δq_i
3. Express Lagrange's equation for each generalised coordinate

(Note that for certain choices of generalised coordinates, the equations of motion can also be derived in a straight-forward way by applying force and moment equilibrium to each element.)

8.5.1 Example Application

Consider the two-degree-of-freedom system shown below, with masses m_1 and m_2 , springs with constants k_1 and k_2 , dampers with constants c_1 and c_2 , and applied force $F_2(t)$ (figure 1). The first step is to define the generalised coordinates. A good choice is $q_1 = x_1$, and $q_2 = x_2$. Next, we have to define each component of the total energy:

$$T = \frac{1}{2}[m_1\dot{x}_1^2 + m_2\dot{x}_2^2] \quad (\text{Kinetic}) \quad (8.30)$$

$$U = \frac{1}{2}[k_1x_1^2 + k_2(x_1 - x_2)^2] \quad (\text{Potential}) \quad (8.31)$$

$$D = \frac{1}{2}[c_1\dot{x}_1^2 + c_2(\dot{x}_1 - \dot{x}_2)^2] \quad (\text{Dissipative}) \quad (8.32)$$

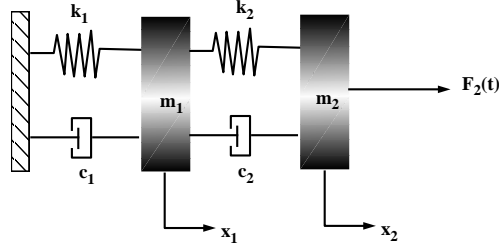


Figure 8.4: A 2 DOF Forced System

Then we need to consider the virtual work done by the force F_p . From the expression for δW on slide 8-7, we can express the generalised force as:

$$Q_i = \sum_{p=1}^M \mathbf{F}_p \frac{\partial \mathbf{r}_p}{\partial q_i} \quad (8.33)$$

From our definition of the generalised coordinates, we find that $Q_1 = 0$, and $Q_2 = F_2(t)$. The final step is to substitute our expressions into Lagrange's equation:

$$\frac{d}{dt} \left(\frac{\partial T}{\partial \dot{q}_i} \right) - \frac{\partial T}{\partial q_i} + \frac{\partial U}{\partial q_i} + \frac{\partial D}{\partial \dot{q}_i} = Q_i, \quad i = 1, N \quad (8.34)$$

For $i = 1$, this produces:

$$m_1 \ddot{x}_1 + k_1 x_1 + k_2 (x_1 - x_2) + c_1 \dot{x}_1 + c_2 (\dot{x}_1 - \dot{x}_2) = 0 \quad (8.35)$$

While for $i = 2$:

$$m_2 \ddot{x}_2 + k_2 (x_2 - x_1) + c_2 (\dot{x}_2 - \dot{x}_1) = F_2(t) \quad (8.36)$$

You can verify these equations using a direct application of Newton's second law.

8.6 Rayleigh-Ritz (Assumed Mode) Method

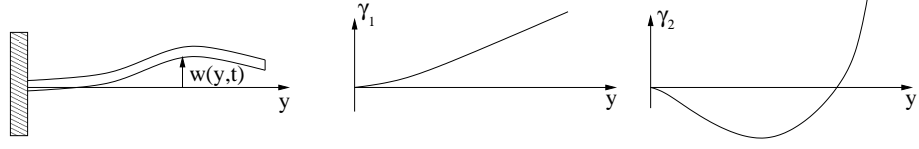


Figure 8.5: The Rayleigh-Ritz method

In this case, the deflections are expressed in terms of a finite set of assumed modes, the amplitudes of which are the generalised coordinates:

$$w(y, t) = \sum_{i=1}^N \gamma_i(y) q_i(t) \quad (8.37)$$

where $w(y, t)$ is the local deflection and $\gamma_i(y)$ is the assumed mode. To derive the equations of motion:

1. Assume N modes of unknown amplitude which satisfy the boundary conditions and are linearly independent
2. Express the total kinetic, potential, and dissipative energies of the system in terms of the assumed modes and generalised coordinates
3. Derive the generalised forces Q_i by considering the work done on the system by a virtual displacement of δq_i
4. Express Lagrange's equation for each generalised coordinate

In general, when applied to a system with zero damping, the Rayleigh-Ritz method will produce a system of the form:

$$\sum_{j=1}^N M_{ij} \ddot{q}_j + \sum_{j=1}^N K_{ij} q_j = Q_i(t), \quad i = 1, N \quad (8.38)$$

This system can be considerably simplified if the chosen modes have the property of orthogonality:

$$\int_0^l \gamma_i(y) \gamma_j(y) dy \neq 0 \text{ for } i = j \quad (8.39)$$

$$= 0 \text{ for } i \neq j \quad (8.40)$$

Orthogonal modes can be obtained by choosing $\gamma_i(y)$ to be the undamped free-vibration modes of the structure

8.6.1 Example Application

Consider a bending wing of length l which has its root fixed to a wind-tunnel wall (figure 2). The wing has a mass distribution $m(y)$, and stiffness distribution $EI(y)$. The lift acting on the wing is $L(y, t)$, and the resulting deflection is $w(y, t)$. We wish to derive the equations of motion of the wing in terms of N assumed modes γ_i , where $i = 1..N$. We will assume the local deflection can

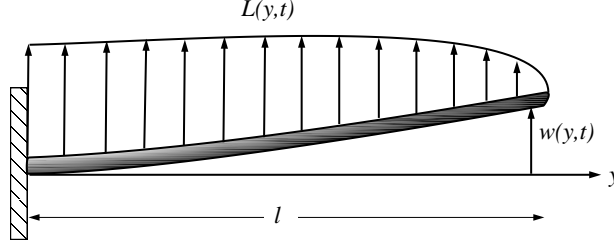


Figure 8.6: A Bending Wing

be written as a linear combination of assumed mode shapes, the amplitudes of which vary in time:

$$w(y, t) = \sum_{i=1}^N \gamma_i(y) q_i(t) \quad (8.41)$$

The kinetic and strain energy of the beam are given by:

$$T = \frac{1}{2} \int_0^l m(y) \dot{w}^2(y, t) dy \quad (\text{Kinetic}) \quad (8.42)$$

$$U = \frac{1}{2} \int_0^l EI(y) (w'')^2(y, t) dy \quad (\text{Strain}) \quad (8.43)$$

Here $\dot{}$ denotes the time derivative, and $'$ denotes $\frac{d}{dy}$. The above equations can be re-expressed in terms of the assumed modes as:

$$T = \frac{1}{2} \int_0^l m(y) \left(\sum_{i=1}^N \gamma_i(y) \dot{q}_i \right) \left(\sum_{i=1}^N \gamma_i(y) \dot{q}_i \right) dy \quad (8.44)$$

$$= \frac{1}{2} \sum_{i=1}^N \sum_{j=1}^N \dot{q}_i \dot{q}_j \int_0^l m(y) \gamma_i(y) \gamma_j(y) dy \quad (8.45)$$

$$= \frac{1}{2} \sum_{i=1}^N \sum_{j=1}^N M_{ij} \dot{q}_i \dot{q}_j; \quad \text{where} \quad M_{ij} = \int_0^l m(y) \gamma_i(y) \gamma_j(y) dy \quad (8.46)$$

Similarly for the strain energy:

$$U = \frac{1}{2} \sum_{i=1}^N \sum_{j=1}^N K_{ij} q_i q_j; \quad \text{where} \quad K_{ij} = \int_0^l EI(y) \gamma_i''(y) \gamma_j''(y) dy \quad (8.47)$$

Finally, we define the i th generalised force by considering the work done by $L(y, t)$ for a generalised displacement δq_i :

$$Q_i(t)\delta q_i(t) = \int_0^l (L(y, t)\delta w(t))dy \quad (8.48)$$

$$= \int_0^l L(y, t)\gamma_i(y)\delta q_i(t)dy \quad (8.49)$$

or:

$$Q_i(t) = \int_0^l L(y, t)\gamma_i(y)dy \quad (8.50)$$

Substituting these expressions into Lagrange's equation yields the following system of N equations:

$$\sum_{j=1}^N M_{ij}\ddot{q}_j + \sum_{j=1}^N K_{ij}q_j = Q_i(t) \quad (8.51)$$

As $N \rightarrow \infty$, this system will approximate the dynamics of the continuous beam. Often, however, only a few modes will suffice, especially if one is primarily interested in the lower-frequency structural modes. For the latter case, a good choice for the γ_i are the beam's natural modes. As an alternative, Bisplinghoff gives the following polynomial formula for a bending beam:

$$\gamma_i(y) = 1 - (i+3)\frac{y}{l} - \left(1 - \frac{y}{l}\right)^{i+3} \quad (8.52)$$

8.7 Practice Problems

p8.7.18 Derive the equations of motion for the lumped-parameter model of a cantilever beam subject to torsion as shown below. Find the natural modes of the system and verify that they are orthogonal.

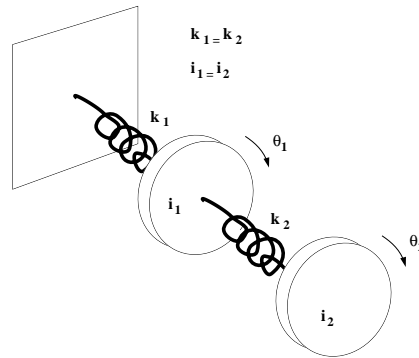


Figure 8.7: Lumped-parameter model

p8.7.19 Consider the continuous beam subjected to torsion shown below. Apply the Rayleigh-Ritz method with two assumed modes to determine the natural modes of the beam. How do these compare with those obtained from the lumped-parameter model approach in question 1?

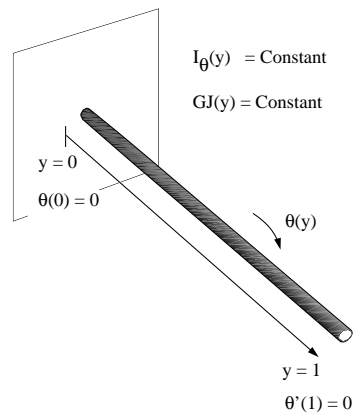


Figure 8.8: Continuous beam

Chapter 9

Flutter Calculation Methods

In the last few chapters, we have considered more advanced representations for unsteady aerodynamic forces and structural systems. Now we return to the problem of flutter prediction. Like the simple two-degree-of-freedom examples of chapter 2, our more advanced representations still lead to a system of second-order differential equations, although now expressed in terms of generalised coordinates:

$$[M]\{\ddot{q}\} + [D]\{\dot{q}\} + [K]\{q\} = \{Q_A\} \quad (9.1)$$

where:

- $[M]$: Mass matrix
- $[D]$: Structural damping matrix
- $[K]$: Stiffness matrix
- $\{q\}$: Vector of Generalised Coordinates
- $\{Q_A\}$: Generalised aerodynamic forces

In chapter 2 we produced flutter diagrams by assuming a solution of the form $\{q\} = \{\hat{q}\}e^{pt}$, and solving the resulting characteristic equation for p . That can still be done here, provided that the aerodynamic forces Q_A , can be explicitly expressed as algebraic functions of $\{q\}$. This is the case for the simple aerodynamic models considered in chapter 2, as well as the state-space approximations described in chapter 7. It is not the case when only pure harmonic results are available, or when the analytic solution is expressed in terms of transcendental functions, or when the data is available only in tabular form from either experiments or CFD computations. In these circumstances, more general flutter-calculation methods are required.

A brute-force approach is to add a harmonic forcing term $F(t)$ to the equations and evaluate the system response as a function of operating conditions

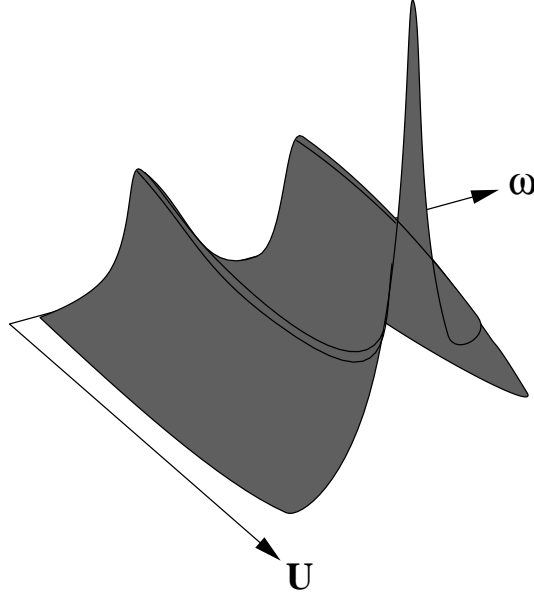


Figure 9.1: Brute-force amplitude analysis

(e.g. the flight speed U) and the frequency, ω , of $F(t)$. Typically this results in system response amplitude plots such as that shown in figure 9.1. Although this procedure is analogous to those used in flight flutter testing, it is quite inefficient from the numerical point of view as it requires harmonic time-domain simulations for each point in the $U - \omega$ plane.

Fortunately there are a number of more efficient methods, the most common of which will be described in this chapter. Each of these avoids the costs of the brute-force approach by directly generating an approximate flutter diagram. The first two methods considered, the k method and p-k method, assume that only harmonic aerodynamic data are available. This is sufficient for the prediction of flutter boundaries, as we know that at each flutter point, the response will be purely harmonic. The last method we consider, the p method, is more general in that it can also predict the response away from the flutter boundary, but requires enough aerodynamic data to construct an approximate model for Q_A as a function of p .

9.1 Non-dimensionalisation

For the remainder of this chapter, we will employ a non-dimensional expression for p :

$$p = \frac{b}{U}(\sigma + i\omega) = \delta + ik \quad (9.2)$$

and assume solutions of the form $\{q\} = \{\hat{q}\}e^{p\frac{U}{b}}$. The dynamic equations of motion can then be written as:

$$\left[\frac{U^2}{b^2}[M]p^2 + \frac{U}{b}[D]p + [K] \right] \{\hat{q}\} = \frac{1}{2}\rho U^2[A(p)]\{\hat{q}\} \quad (9.3)$$

Where $A(p)$ is also a function of the Mach number M_∞ and the Reynolds number Re . In general, $A(p)$ can be non-linear, and need not be expressed in terms of explicit functions.

9.2 k method

The k method arose during the 1940's as a technique to efficiently make use of pure harmonic aerodynamic data during flutter analysis. The idea is simply to add a fictitious structural damping term to the equations, and then to determine its required value in order to keep the response purely harmonic. The flutter boundary is then determined by finding the point at which the required fictitious damping becomes zero. Note that since the response is always kept purely harmonic, the use of harmonic aerodynamic data is justified throughout the analysis.

9.2.1 Procedure

If we assume a fictitious structural damping, g , and a purely harmonic response $p = ik$, the equations of motion become:

$$(-\omega^2[M] + (1 + ig)[K]) \{\hat{q}\} = \frac{1}{2}\rho U^2[A(k)]\{\hat{q}\} \quad (9.4)$$

We can then set up the following eigenvalue problem:

$$[K]^{-1} \left([M] + \frac{1}{2}\rho b^2[A(k)/k^2] \right) \{\hat{q}\} = \frac{1 + ig}{\omega^2} \{\hat{q}\} \quad (9.5)$$

or:

$$[B(k)]\{\hat{q}\} = \lambda\{\hat{q}\}, \quad \lambda = \frac{1 + ig}{\omega^2} \quad (9.6)$$

where $[B(k)]$ and $\lambda = \lambda' + i\lambda''$ are, in general, complex. Now to generate a point on the k method's "flutter diagram", we follow the following procedure:

1. Choose an altitude, which results in a value for ρ
2. Choose k and calculate $[B(k)]$, which will include the aerodynamic data at frequency k
3. Compute the eigenvalues for each mode $\lambda_1 \dots \lambda_N$
4. Compute the frequency of each mode $\omega_i = 1/\sqrt{\lambda_i'}$

5. Compute the flight speed $U_i = \omega_i b/k$, and fictitious damping $g_i = \omega_i^2 \lambda_i''$ corresponding to each mode

This procedure is repeated at the same altitude for different k 's, which generates diagrams similar to that shown in figure 9.2 (note that a constant k is a straight line on the $U - \omega$ plane). An estimate for the flutter speed, U_F , can be obtained by interpolation using two values near $g_i = 0$.

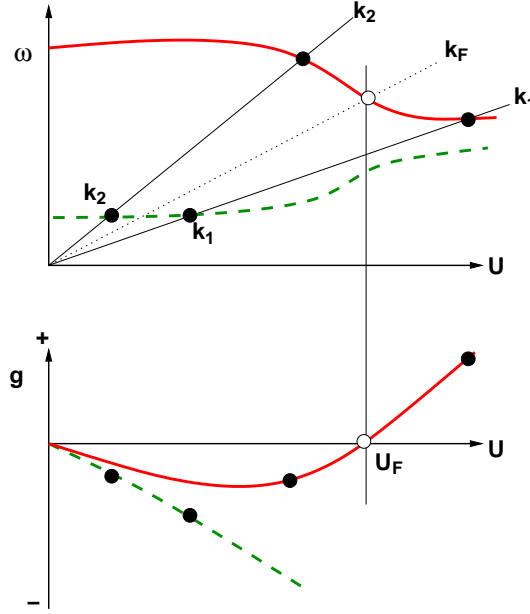


Figure 9.2: k-method diagrams for a two-mode problem

The k method is efficient when the aerodynamic forces do not vary significantly with M_∞ or Re , as it then allows the flutter point to be found after a small number of order N eigenvalue problems, where N is the number of generalised coordinates. It is worth noting that at the flutter point, no additional sources of error are present, so the flutter solution is exact.

When the aerodynamic forces do vary significantly with M_∞ or Re , additional iterations are required. This is because the flight velocity is determined from the computation after $A(k)$ has been specified. Additionally, when flight control systems are involved for which the frequency parameter is ω instead of k , an additional interpolation step has to be made to match both parameters. This can make the application of the k method unwieldy in general design cases. Outside of these efficiency issues, the k method suffers from practical problems in implementation and interpretation. These include difficulties associated with connecting the solution pairs in the flutter diagram to form sensible frequency and damping curves, especially when the curves merge. In some cases it is

necessary to calculate the eigenvectors and to inspect their development along the frequency and damping curves. Another problem is the appearance of more frequency and damping solutions than the number of degrees of freedom. An example of such anomalous results is shown in figure 9.3. This phenomenon typically occurs when the aerodynamic forces are large with respect to inertia and stiffness forces, for example in cases with free rotation of control surfaces.

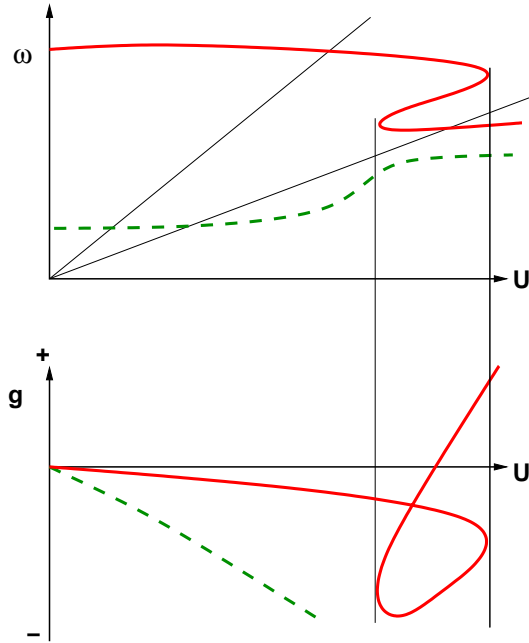


Figure 9.3: Non-physical behaviour of k-method diagrams

9.3 p-k method

The p-k method emerged in the mid 1960's as an alternative to the k method with better properties for aerospace problems. It is based on the assumption that we may approximate the aerodynamics of sinusoidal motions with slowly increasing or decreasing amplitudes using purely harmonic aerodynamic results. i.e. that:

$$[A(p)] = [A(\delta + ik, M_\infty, Re, \dots)] \approx [A(k, M_\infty, Re, \dots)] \quad (9.7)$$

The full equations of motion are then used to determine the correct value of p for each mode at a given flight condition.

9.3.1 Procedure

With our assumed form of the aerodynamic forces, the equations of motion can be written:

$$\left[\frac{U^2}{b^2} [M] p^2 + \frac{U}{b} [D] p + [K] \right] \{\hat{q}\} = \frac{1}{2} \rho U^2 [A(k, M_\infty, \dots)] \{\hat{q}\} \quad (9.8)$$

or

$$[F(p, k)] \{\hat{q}\} = 0 \quad (9.9)$$

where $p = \delta + ik$. This equation can be used to determine values of p . Normally an iterative solution method is used, with guesses for p determined from the previously analysed flight condition. The most common technique is known as “determinant iteration” (see Hassig, H, “An Approximate true damping solution of the flutter equation by determinant iteration”, J. Aircraft, Vol. 8, No. 11, Nov. 1971).

The basic procedure is as follows. First the mode which will be tracked is chosen, along with a starting value for U near $U = 0$. The Mach and Reynolds number are then computed for that U . A first guess, p_1 , can be made using the natural frequency of the mode in the absence of aerodynamic forces. Another initial guess, p_2 , can be made by adding a small value of damping to p_1 . Then the following sequence of steps is performed:

1. Compute or interpolate for $[A(k_1, M_\infty, \dots)]$ and $[A(k_2, M_\infty, \dots)]$.
2. Compute the determinants $F_1 = | [F(p_1, k_1)] |$ and $F_2 = | [F(p_2, k_2)] |$
3. Update p using: $p_3 = \frac{p_2 F_1 - p_1 F_2}{F_1 - F_2}$;
4. Set $p_1 = p_2$ and $p_2 = p_3$, then repeat from step 1 until converged
5. Choose the next flight condition ($\rho, U, M_\infty, Re, \dots$)
6. Choose two new values of p based on extrapolation from the previous flight conditions
7. Return to step 1 and repeat to find the new p at the next flight condition

Once the mode is tracked through its desired range, a different mode is selected and the entire procedure is repeated. The formula for p_3 in step 3 can be derived using the diagram shown in figure 9.4. Note that only one determinant evaluation is required per iteration as after the procedure is started, as F_1 can be taken from the previous iteration.

Although the process of finding a values of p can be costly for complex F , this must be compared with the high cost of finding eigenvalues for large systems as required by the k method. Additionally, no further iteration is required by the p - k method to incorporate Mach or Reynolds number effects. An additional

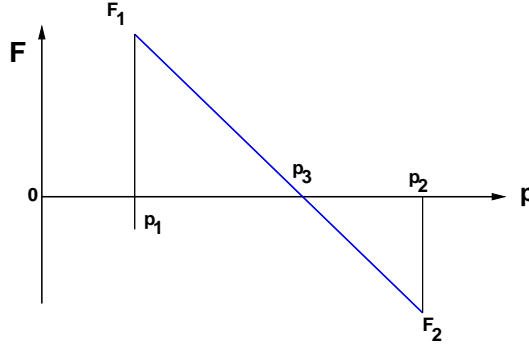


Figure 9.4: The determinant iteration procedure

control transfer function $[H(p)]\{\hat{q}\}$, can also be easily incorporated. In general, the flutter diagrams from the p-k method are much closer to those of the actual system than those obtained via the k method. They are still only exact, however, at the flutter point.

9.4 p method

If we want flutter diagrams which are accurate over the complete range of conditions, we will be forced to construct an approximate expression for $[A(p)]$ which is accurate for decaying or growing motions. One of the major complicating factors in doing so is representing the time lags inherent in unsteady aerodynamic responses.

Once $[A(p)]$ is specified, the resulting system can be solved using the same determinant iteration procedure used in the p-k method. Alternatively, $A[(p)]$ can be expressed in the time domain using an inverse Laplace transform, and the solution carried out as an eigenvalue problem in state space. The dimension of state-space problem is usually higher, as new state variables have to be introduced to properly represent the aerodynamic lag modes.

Approximate models for $[A(p)]$ are typically of the form:

$$\left[A_{0ij}(M_\infty) + A_{1ij}(M_\infty)p + A_{2ij}p^2 + \sum_{l=1}^L \frac{A_{(l+2)ij}(M_\infty)p}{\beta_{lij} + p} \right] \quad (9.10)$$

- The first three terms are instantaneous in nature and are often referred to as aerodynamic stiffness, damping and mass terms
- Terms $l = 1$ to L approximate aerodynamic lag effects
- Coefficients A_{ij}, β_{lij} can be determined by fitting to computed or experimental results

- A_{2ij} is usually zero, except for incompressible flow

It is instructive to compare the lag effect terms above to the approximation for Theodorsen's function given in chapter 7 (Note that the latter approximation accounts for the circulatory part of the response only).

The main advantage of the p method is that it can accurately represent non-harmonic aerodynamic responses, including converging, diverging and aperiodic motions. In its state-space form, it is also effective for control system design. Its disadvantage is that it can require a complex procedure for accurately approximating the aerodynamic forces, and its state-space approximations can lead to very large eigenvalue problems. Also, the p method will find a slightly different value of flutter speed than determined using k and p-k methods, due to additional interpolation errors in the aerodynamic forces.

9.5 Practice Problems

p9.5.20 Consider the following single-DOF system:

$$[M]\ddot{q} + [K]q = \frac{1}{2}\rho U^2[A]q$$

with $\rho = 1$, $b = 1$, $M = 2$, and $K = 1$.

Given the following two experimental results:

$$\begin{aligned} k = 1 & \quad A(k) = 4 + 2i \\ k = 2 & \quad A(k) = 2 - 4i \end{aligned}$$

compute the flutter speed of the system using the k method.

p9.5.21 For the single DOF system described above, use the p-k method to estimate $p = \delta + ik$ at $U=0.4$. Use an assumed value of $\delta_1 = -0.1$ with the experimental $A(k)$ for $k = 1$, and $\delta_2 = 0.1$ with the experimental $A(k)$ for $k = 2$. Perform a single step of determinant iteration.

Chapter 10

Dynamic Responses

The need to ensure aeroelastic instabilities occur outside of an aircraft's flight envelop is self-evident, and is a natural concern for aeroelasticians. There are also many important aeroelastic design problems, however, which occur well away from instability boundaries. The most common of these are related to achieving desired dynamic response characteristics. Such problems are becoming more and more prevalent as we move towards lighter, more flexible structures, particularly when active control systems are used.

The sources of excitation for dynamic responses are varied. They include atmospheric turbulence, manual or automated control deflections, water or ground forces transmitted through the landing gear, or unsteady aerodynamic interference occurring between aircraft components. In some cases failure modes associated with dynamic responses can be critical. This can be due to the possibility of structural failure, as is the case for tail surfaces subjected to strong atmospheric gusts (figure 10.1). Alternatively, an undesired elastic response could lead to loss of control.

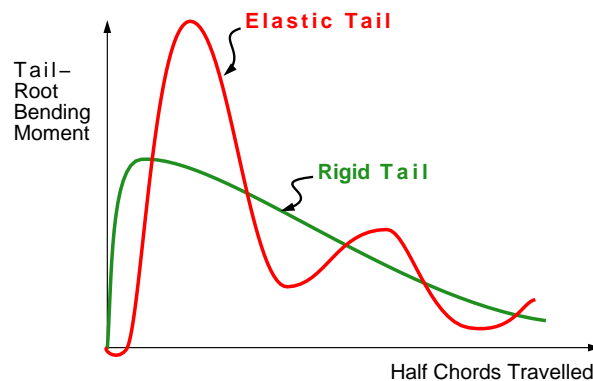


Figure 10.1: Response of a tail to sharp-edge gust

Analysis of cases with less severe consequences can also be useful. Passenger comfort, for example, is affected by the details of response to atmospheric turbulence. On the other hand, non-critical dynamic responses can also be measured and used by aeroelasticians in order to validate the numerical models they have developed.

From the analysis point of view, dynamic response problems are more general than dynamic instability problems, as we can no longer exploit the simplifications inherent in assuming undamped harmonic solutions. In fact, the complexity of modern aircraft structural and control systems, coupled with the difficulties of accurately predicting unsteady aerodynamic flows, means that dynamic response problems can pose a significant challenge.

10.1 Types of Dynamic Response problems

We can broadly divide dynamic response problems into two classes, deterministic and stochastic. In the first class the excitation is known precisely. Examples include specified control deflections, idealised test gusts or measured forces from initial touchdown. Such problems may be treated directly by time-domain simulations. If the system is linear, we can also treat the problem using frequency-domain techniques, providing another viewpoint which often aids interpretation.

The second class of problems are those with excitations which are only quantified statistically. Examples include general atmospheric turbulence or landing loads imparted by water or uneven terrain. In recent years a number of advanced techniques for analysing such stochastic systems have been developed. We will limit our discussions to simple stochastic problems, however, which can be treated using frequency-domain techniques. An overview of problems and their analysis appears in figure 10.2.

10.2 Dynamic Response Equations

Most aeroelastic systems can be expressed as a system of equations of the form:

$$[M]\{\ddot{q}\} + [D]\{\dot{q}\} + [K]\{q\} = \frac{1}{2}\rho U^2 \{A(t, q, v, M_\infty, Re)\} + \{E(t)\} \quad (10.1)$$

- $[M]$: Mass matrix
- $[D]$: Structural damping matrix
- $[K]$: Stiffness matrix
- $\{A(t..)\}$: Aerodynamic forces
- $\{q\}$: Vector of generalised deformation coordinates
- $\{v\}$: Vector of external aerodynamic excitations
- $\{E(t)\}$: External mechanical forces (e.g landing gear)

Here $\{A(t)\}$ defines the combined unsteady aerodynamic forces arising from both excitation (gusts) and deformation. For a truly general analysis, this must

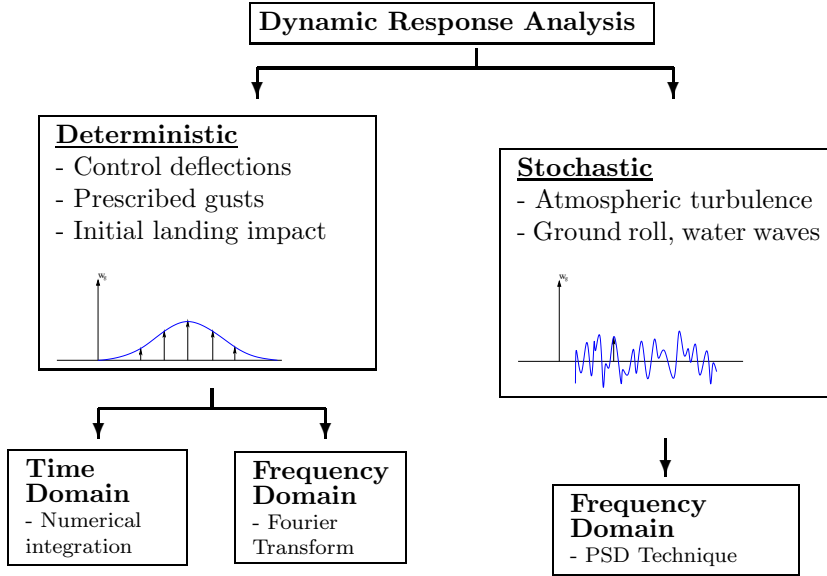


Figure 10.2: Dynamic Response Analysis

be determined together with the response. The most practical way to do so is using time integration methods.

If the aerodynamic interaction between the excitation and the responding configuration is low, we can split $\{A(t)\}$ into excitation and response components. This allows the use of simplified analysis techniques. The assumption can be expressed as the independence of the aerodynamic forces due to excitation (v) from those arising due to deformation (q). This results in the following equations of motion:

$$[M]\{\ddot{q}\} + [D]\{\dot{q}\} + [K]\{q\} = \frac{1}{2}\rho U^2 ([A(t)]\{q\} + [A_e(t)]\{v\}) + \{E(t)\} \quad (10.2)$$

$[A(t)]$: Aerodynamic forces due to $\{q\}$
 $[A_e(t)]$: Aerodynamic forces due to $\{v\}$

A common example is the *frozen gust* assumption, where the gust is represented by a vertical velocity distribution fixed in space, assumed to remain constant during the passage of the wing (figure 10.3). For certification purposes, standardised gusts, such as the sharp-edged and (1-cosine) gusts may be used to establish minimum response criteria (figure 10.4).

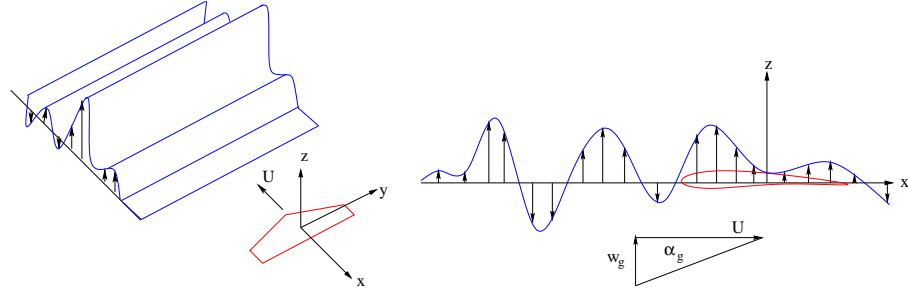


Figure 10.3: Frozen gust assumption

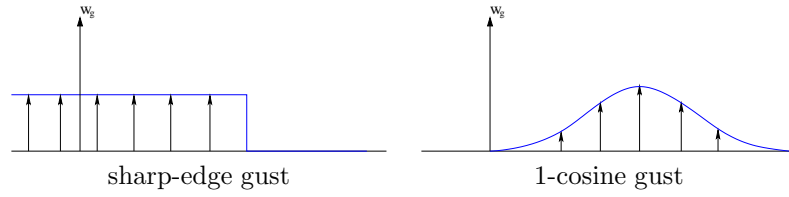


Figure 10.4: Standardised gusts

10.3 Solution in the frequency domain: Fourier Transform

If we can separate the aerodynamic forces as described in the previous section, then equation (10.2) can be expressed for a single harmonic frequency as:

$$\left(-\omega^2[M] + i\omega[D] + [K] - \frac{1}{2}\rho U^2[A(k)] \right) \{\hat{q}\} = \frac{1}{2}\rho U^2\{A_e(k)\}\{\hat{v}\} \quad (10.3)$$

or equivalently:

$$[D_q(\omega)]\{\hat{q}\} = [D_v(\omega)]\{\hat{v}\} \quad (10.4)$$

The ratio of output to input is then given by:

$$[H(\omega)] = [D_q]^{-1}[D_v] \quad (10.5)$$

$[H(\omega)]$ is known as the mechanical admittance. It can be pre-computed before considering a specific gust problem using harmonic experimental, analytic or numeric data. Assuming $[H(\omega)]$ has been defined, we can compute the response to an arbitrary gust using the following procedure:

Step 1: Transform $\{v\}$ from time to frequency domain:

$$\{v(\omega)\} = \int_{-\infty}^{\infty} \{v(t)\} e^{-i\omega t} dt \quad (10.6)$$

Step 2: Compute response in frequency domain:

$$\{q(\omega)\} = [H(\omega)]\{v(\omega)\} \quad (10.7)$$

Step 3: Return response to time domain

$$\{q(t)\} = \frac{1}{2\pi} \int_{-\infty}^{\infty} \{q(\omega)\} e^{i\omega t} d\omega \quad (10.8)$$

In practice fast Fourier transforms are often used to perform these steps.

10.4 Solution in the time domain: Numerical Integration

There is a wide range of numerical methods available for the integration of systems of ODE's. These are typically based on either finite-difference or variational techniques. Some of these methods require expressing the system of N second-order equations as a system of $2N$ first-order ODE's. This can be done by introducing the state vector $r = \{q_1, \dot{q}_1, \dots, B_1, B_2, \dots\}^t$, and the corresponding excitation vector $v = \{v_1, v'_1, \dots\}^t$, where the extra state variables B_1, B_2 are usually required in order to properly simulate aerodynamic lag modes. The final system of first-order equations can be expressed:

$$\dot{r} = [A]r + [B]v \quad (10.9)$$

A typical numerical integration technique is the finite difference “ θ -method”:

$$r^{n+1} = r^n + \Delta t [(1 - \theta)([A]r + [B]v)^n + \theta([A]r + [B]v)^{n+1}] \quad (10.10)$$

The above formula allows the solution at $t = t^n + 1$ to be computed from that at $t = t^n$. This formula is applied recursively to advance the solution in time. For $\theta = 0$, the method reduces to Euler explicit integration, while for $\theta = 1$, Euler implicit integration is obtained. Both of these are $O(\Delta t)$ accurate in time. The trapezoidal method, which is $O(\Delta t^2)$ accurate in time, is obtained when $\theta = \frac{1}{2}$.

Example: Numerical integration of a 2 DOF System:

The equations of motion for our standard 2 DOF (h, θ) representative section with a low-frequency aerodynamic model (see chapter 2) can be written:

$$[M]\dot{r} + [C]r = v \quad (10.11)$$

where

$$r = \{h, \dot{h}, \theta, \dot{\theta}\}^t,$$

$$v = \{0, -C_{L_\alpha} q S w(t)/U, 0, C_{L_\alpha} q S e c w(t)/U\}^t,$$

and:

$$[M] = \begin{bmatrix} 1 & 0 & 0 & 0 \\ 0 & m & 0 & S_\theta \\ 0 & 0 & 1 & 0 \\ 0 & S_\theta & 0 & I_\theta \end{bmatrix} \quad (10.12)$$

$$[C] = \begin{bmatrix} 0 & -1 & 0 & 0 \\ K_h & C_{L_\alpha} q S/U & C_{L_\alpha} q S & 0 \\ 0 & 0 & 0 & -1 \\ 0 & -C_{L_\alpha} q S e c/U & K_\theta - C_{L_\alpha} q S e c & 0 \end{bmatrix} \quad (10.13)$$

We will consider some dynamic responses for a section with the following properties:

$$\begin{aligned} \rho &= 0.53 \text{ kg/m}^3 \\ e &= 0.2, c = 6 \text{ m} \\ m &= 400 \text{ kg/m} \\ S_\theta &= 180 \text{ kg m/m} \\ I_\theta &= 200 \text{ kg m}^2/\text{m} \\ K_h &= 1 \times 10^5 \text{ N/m/m}, \\ K_\theta &= 3 \times 10^5 \text{ N m/m} \end{aligned}$$

For reference, the associated flutter diagram is shown in figure 10.5.

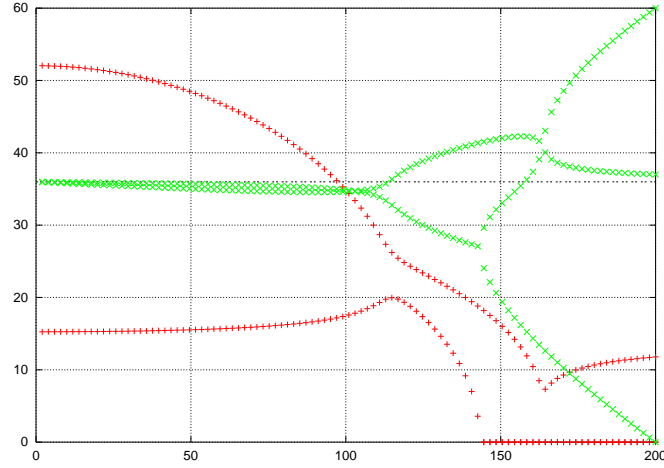
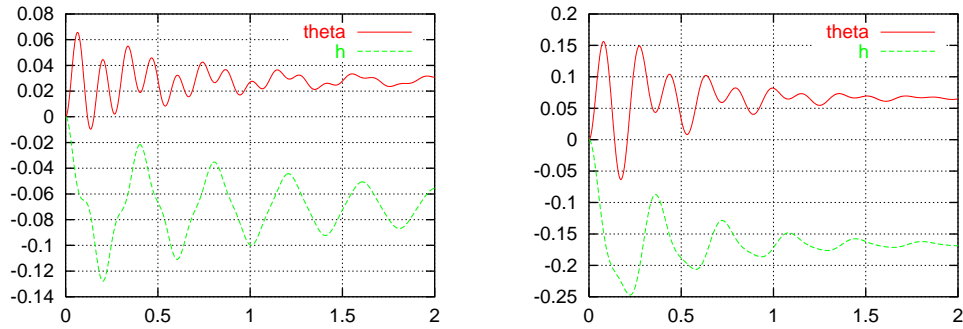
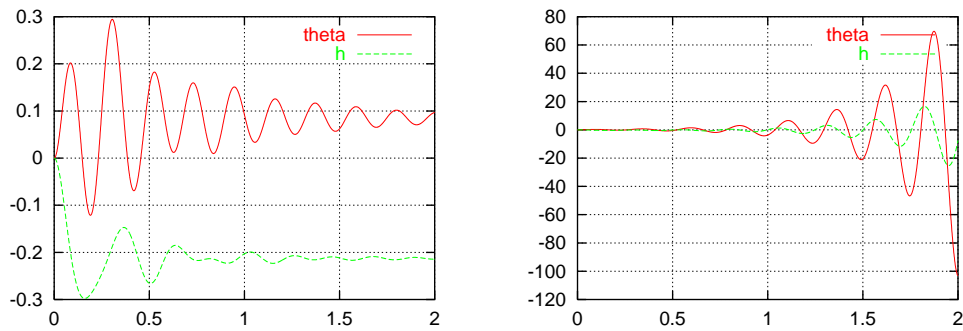


Figure 10.5: Flutter Diagram (low-frequency aerodynamic model)

Figures 10.6 and 10.7 show the response of the system to a sharp-edged gust with a magnitude of 10 m/s encountered at $t = 0$. Initially there is increased damping

Figure 10.6: Responses at $U=60$ m/s and $U=100$ m/s

as the velocity is increased, as can be anticipated from the flutter diagram. As

Figure 10.7: Responses at $U=110$ m/s and $U=120$ m/s

the speed is increased further however, the damping decreases until the system becomes unstable. Depending on the maximum allowed strain of the structure, the 100 and 110 m/s cases may already be critical, as these produce relatively large excursions.

10.5 Stochastic Response Analysis - PSD Technique

Many types of excitations, including atmospheric turbulence, can be appropriately modelled as random processes. In such cases it is best to define their properties in terms of average quantities such as:

the mean value of a variable:

$$\bar{x} = \lim_{T \rightarrow \infty} \frac{1}{2T} \int_{-T}^T x(t) dt \quad (10.14)$$

and the mean square value (or power) of a variable:

$$\bar{x^2} = \lim_{T \rightarrow \infty} \frac{1}{2T} \int_{-T}^T x^2(t) dt \quad (10.15)$$

The mean square value can also be expressed in terms of the Power Spectral Density (PSD) function:

$$\bar{x^2} = \int_0^\infty \Phi_x(\omega) d\omega \quad (10.16)$$

where:

$$\Phi_x(\omega) = \frac{2\pi X(i\omega)X(-i\omega)}{T} \quad (10.17)$$

and

$$X(i\omega) = \frac{1}{2\pi} \int_{-T}^T x(t) e^{-i\omega t} dt \quad (10.18)$$

The function $\Phi_x(\omega)$ may be thought of the distribution of power across the frequency domain. Expression (10.16) can be derived using the autocorrelation function for x assuming it to be defined by a processes which is statistically stationary (its statistical properties are independent of time) homogeneous (its statistical properties are independent of space) and isotropic (its statistical properties are independent of direction) [see “Aeroelasticity” by Bisplinghoff et al, appendix C].

Power Spectral Density Technique

If we assume that the response to the excitation is also a random function, then it can be shown that for a linear system:

$$\Phi_r(\omega) = |H_{rw}(\omega)|^2 \Phi_x(\omega) \quad (10.19)$$

where:

- $\Phi_r(\omega)$: response power spectral density
- $\Phi_x(\omega)$: input (e.g gust velocity) power spectral density
- $H_{rx}(\omega)$ mechanical admittance

This means that given the PSD of an input signal, we can quickly get an idea of the power frequency distribution of the output if we have the system’s mechanical admittance. The complete analysis can be summarised as:

1. Obtain the input PSD , $\Phi_x(\omega)$
2. Determine $H_{rx}(\omega)$ for the system
3. Multiply $|H_{rx}(\omega)|^2$ by $\Phi_x(\omega)$ to obtain response PSD, $\Phi_r(\omega)$

An example of two commonly-used input PSD functions for atmospheric turbulence are shown in figure 10.8. Both of these are biased towards low frequencies,

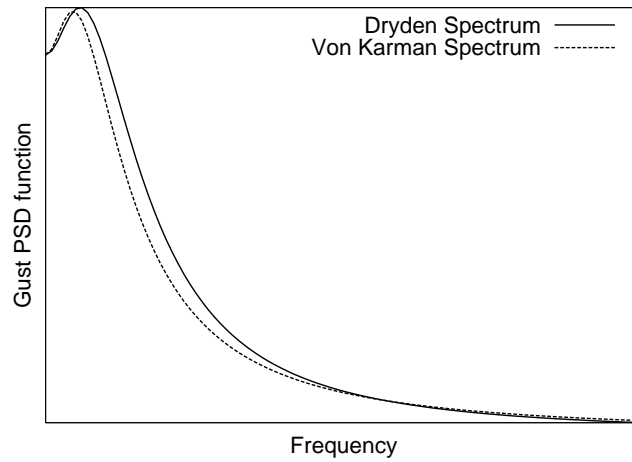


Figure 10.8: Standard PSD functions for atmospheric turbulence

indicating atmospheric turbulence tends to excite low-frequency modes most effectively. This is shown in figure 10.9, where the admittance function of the 2DOF representative section is plotted with an input PSD for atmospheric turbulence and the corresponding output PSD. The input PSD is seen to act as a filter which tends to enhance the relative power of the low-frequency mode.

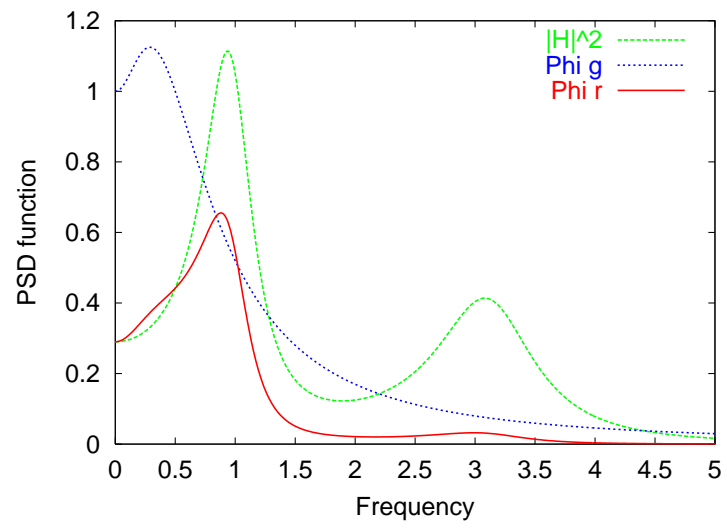


Figure 10.9: PSD response to atmospheric turbulence

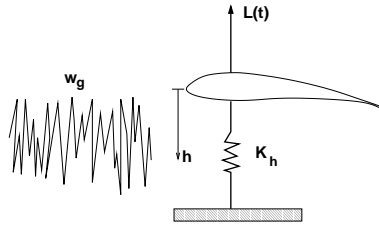
10.6 Practice Problems

p10.6.22 An wing with mass m enters a stochastic gust field with a power spectral density, $\Phi_g(\omega)$, approximated by:

$$\Phi_g(\omega) = \frac{A}{B + \omega^2}$$

The wing moves with a single degree of freedom, h , and is supported by a spring K_h . Its lift may be approximated by:

$$L(t) = C_{L_\alpha} q S \left(\frac{\dot{h}}{U} + \frac{w_g}{U} \right)$$



Compute the mechanical admittance, $H(\omega)$, and the PSD of the response, $\Phi_r(\omega)$. If A and B are positive, will increasing K_h increase or decrease the maximum response amplitude? Use sketches of $H(\omega)$ and $\Phi_g(\omega)$ to illustrate your answer.

p10.6.23 Consider the single DOF plunging airfoil of the previous problem. Using the frozen gust assumption and results from unsteady incompressible flat-plate theory, express the response PSD as a function of reduced frequency for an arbitrary gust PSD function, $\Phi(k)$. Assume that the lift due to a harmonic gust with amplitude \hat{w} can be expressed:

$$L_g = 2\pi\rho U b [S(k)] \hat{w}$$

Chapter 11

Introduction to Computational Aeroelasticity

In this short chapter we review some advantages and disadvantages of performing high-fidelity numerical simulations of the flow and structure in order to estimate the aeroelastic performance of a configuration. Methods for doing so will be considered in the following chapters.

With the widespread availability of computing facilities, one might ask with justification, why would we not always approach aeroelastic problems using highly-detailed numerical simulations? After all, these do not employ geometric simplifications, and can automatically account for non-linear effects in both the flow and the structure. Indeed these are powerful advantages which have motivated the increasing use of numerical simulations in industry.

However it is worthwhile to acknowledge some of the limitations of the current state-of-the art. A prime motivation for the use of high-fidelity numerical simulations is the fact that many aeroelastic phenomena of interest occur in off-design conditions (e.g. flutter), which requires the use of sophisticated modelling techniques. This has two consequences:

High computational cost

The high cost of aeroelastic simulations is primarily associated with the need to resolve unsteady flow phenomena. For models applicable to off-design conditions a full volume mesh is normally required, which must in turn be sufficiently resolved to track features which are moving relative to the mesh. Also the simulation must be time accurate, and performed for the relatively long time intervals associated with structural vibrations. This means that individual aeroelastic simulations tend to be far more expensive than their steady design-point counterparts.

Not only is the cost of individual simulations high, but many of them must be

performed. To establish a flutter envelope, for example, a wide range of airspeed-altitude combinations must be considered, and at each of these, several inertial loading scenarios (fuel, payload) must be simulated.

Difficulties with Validation

Each aeroelastic simulation is subject to:

- Flow / turbulence modelling errors
- Nonlinear structural modelling errors
- Grid and time step dependent errors
- Fluid-structure coupling errors

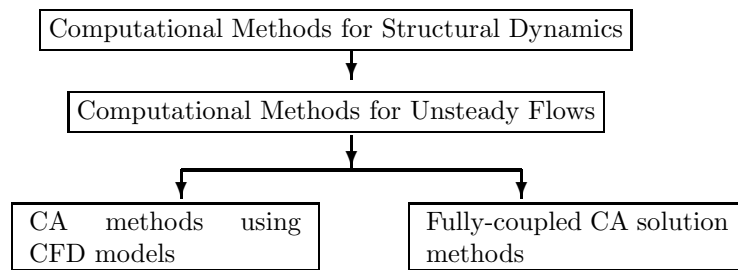
Of these, the flow and structural modelling errors are normally the most significant. In particular, off-design flow problems including separation and shock-boundary layer interaction are particularly difficult to compute, even using the most advanced analysis methods. This means that experimental validation is often required.

Ground vibration tests can provide a reasonable means to validate the fidelity of a structural model from the aeroelastic viewpoint. Unsteady-flow experiments, however, are complex and are carried out much less frequently. Fully-coupled aeroelastic experiments are very difficult to perform reliably and are relatively rare.

Given these difficulties, the objective of multidisciplinary design optimisation (MDO) including off-cruise conditions is indeed an ambitious one. As design loops require a significantly higher number of computations than standard aeroelastic analyses, simplified models are still widely used. Adjoint-based optimisation methods have potential for lowering this cost, so these will likely see increasing application in the future.

11.1 Treatment of CA

Our look at computational aeroelasticity over the next three chapters (CA) is summarised in the following diagram:



Chapter 12

Computational structural dynamics

The methods we considered in chapter 8 for deriving representations of continuous structures can be awkward to apply to complex configurations which feature multiple structural and inertial components (figure 12.1). Many of the concepts we have used, however, can still be applied on a more local level. In this chapter we will the main concepts of the finite element method when used for structural dynamic problems. In order to build on the concepts we have already developed, we will limit the discussion to semi-discrete finite-element methods obtained by application of the Rayleigh-Ritz method and Lagrange's equation. Time discretisation will be treated with standard time-marching methods. We note that what we consider forms a mere subset of available finite-element techniques.

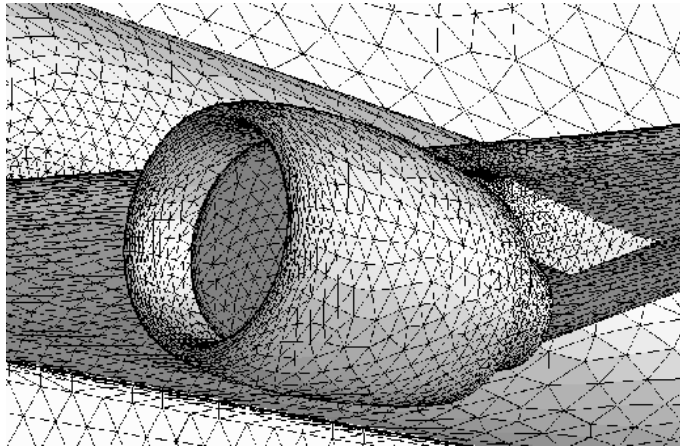


Figure 12.1:

12.1 Rayleigh-Ritz finite-element formulation

The defining characteristic of finite-element methods is their locality. In other words, the solution within each element is defined purely in terms of unknowns associated with the element or its immediate neighbours. This feature simplifies integrations since only one element contribution need be considered at a time. It also results in large but sparse matrices, for which a number of powerful algebraic solution techniques have been developed.

An example finite-element method can be obtained by considering the Rayleigh-Ritz method of chapter 8, but with “assumed modes” (referred to from now on as *shape functions*) defined only in the immediate vicinity of an element 12.2. This allows large local deviations in the solution to be represented accurately without affecting the quality of the solution interpolation in the remaining regions.

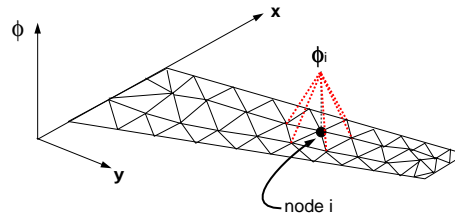


Figure 12.2:

We can summarise the discretisation process using the following steps:

1. Discretize the domain into a number of elements
2. Choose the shape functions which will represent the local solution (structural deflection)
3. Find the contributions of an element to Lagrange's equation expressed in terms of the nodal unknowns
4. Transform the local contributions of each element to the global coordinate system, and assemble the global mass and stiffness matrix
5. Apply the boundary conditions and generalized forces

This procedure will result a system of equations for the unknown nodal displacements, u , of the form:

$$[M]\{\ddot{u}\} + [K]\{u\} = \{f(t)\} \quad (12.1)$$

An illustrative example is given in the next section.

12.2 Example: Formulation for an axially-loaded rod

Steps 1 and 2: Introduce elements and shape functions

The bar is first divided into elements e , $e + 1$ etc. We will assume the solution will be interpolated within element e by two “tent-like” linear shape functions, one centered at node i on the left side of the element and one centered at node $i + 1$ on the right.

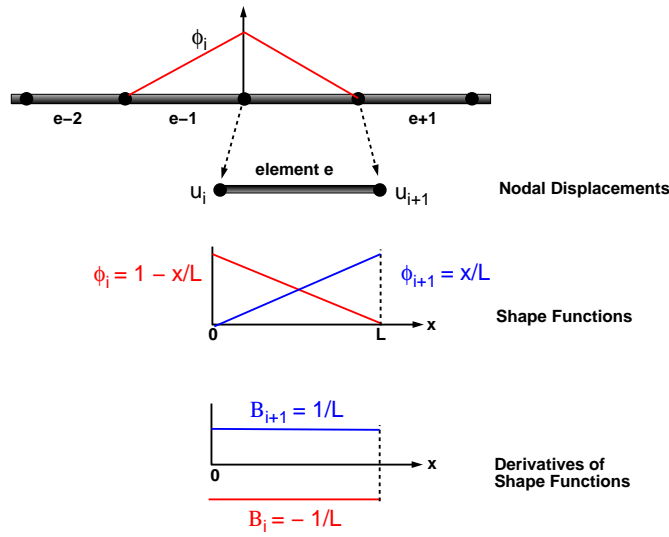


Figure 12.3:

Step 3: Compute the Element contribution to Lagrange's equations

Assume that ρ (density) A (cross-sectional area) E (modulus of elasticity) constant. The kinetic energy is then defined as:

$$T = \frac{1}{2} \int_v \rho \dot{u}^2 dV = \frac{\rho A}{2} \int_0^L (\dot{u}_i \phi_i + \dot{u}_{i+1} \phi_{i+1})^2 dx \quad (12.2)$$

Recalling the first term from Lagrange's equation, it is convenient to define an *element* mass matrix as:

$$Me_{ij} = \rho A \int_0^L \phi_i \phi_j dx ; \quad i = i, i + 1; \quad j = i, i + 1 \quad (12.3)$$

which for this example is:

$$Me = \frac{\rho AL}{6} \begin{bmatrix} 2 & 1 \\ 1 & 2 \end{bmatrix} \quad (\text{symmetric}) \quad (12.4)$$

We can then define the strain energy as:

$$U = \frac{1}{2} \int_v E u'^2 dV = \frac{EA}{2} \int_0^L (u_i B_i + u_{i+1} B_{i+1})^2 dx \quad (12.5)$$

and define an *element* stiffness matrix to be:

$$Ke_{ij} = EA \int_0^L B_i B_j dx \quad ; \quad i = i, i+1; \quad j = i, i+1 \quad (12.6)$$

which for this example is:

$$Ke = \frac{EA}{L} \begin{bmatrix} 1 & -1 \\ -1 & 1 \end{bmatrix} \quad (\text{symmetric}) \quad (12.7)$$

Step 4: Assemble the global mass and stiffness matrix

Each equation in the global system represents a Lagrange equation for the generalised displacement $u_i \phi_i$. Since the ϕ_i are chosen with *local support*, the i th equation can be obtained by simply adding (Assembling) the contributions of the elements to the left and right of node i . This can be done by "overlapping" the element mass and stiffness matrices as shown in figure 12.4.

$$\mathbf{M} = \frac{\rho AL}{6} \begin{bmatrix} \text{diagonal hatching} & & & \\ & \begin{bmatrix} 4 & 1 \\ 1 & 4 \end{bmatrix} & & \\ & & \text{diagonal hatching} & \\ & & & \text{diagonal hatching} \end{bmatrix}$$

The central 2x2 submatrix is labeled \mathbf{Me}_{i+1} in blue. The top-right element of this submatrix is labeled \mathbf{Me}_i .

Figure 12.4: Assembly of the global mass matrix

The final result is a produces a system of the form:

$$[M]\{\ddot{u}\} + [K]\{u\} = \{F\} \quad (12.8)$$

where the i th row of the system expresses Lagrange's equation for the generalised coordinate u_i :

$$\frac{d}{dt} \left[\frac{\partial T}{\partial \dot{u}_i} \right] - \frac{\partial T}{\partial u_i} + \frac{\partial U}{\partial u_i} = Q_i \quad (12.9)$$

Step 5: Apply the B.C's and generalised forces

Constraints such as $u(0) = 0$ can be introduced to eliminate variables from the system. Due to the form chosen for ϕ_i , the generalised forces, Q_i , are simply the the external forces applied at each node.

12.3 Solution of the equations of motion

Once the basic semi-discrete system has been defined, we must define a time integration method to advance the system in time. There are a large number of available methods, each of which have different accuracy and stability properties. When performing computations with possible physical instabilities, it is important to understand how introducing a discrete time march modifies the solution in time. In a flutter simulation, for example, it can be difficult to tell if the instability arises due to numerical or physical mode amplification.

It is therefore useful to gain insight into how such methods behave, by considering a simple single degree of freedom model systems. Consider the following equation of motion:

$$m\ddot{u} + ku = 0 \quad (12.10)$$

This can also be written as a system of two first-order ODE's:

$$\frac{d}{dt} \begin{Bmatrix} u \\ \dot{u} \end{Bmatrix} = \begin{bmatrix} 0 & 1 \\ -k/m & 0 \end{bmatrix} \begin{Bmatrix} u \\ \dot{u} \end{Bmatrix} \quad (12.11)$$

The solution of this system is a constant-amplitude oscillation with frequency $\sqrt{k/m}$.

Now assume we will advance the system in time using the Explicit Euler integration technique, which is defined by a simple first-order Taylor series expansion in time. In the following, we will assume that the solution is advanced with a constant time-step Δt . We denote the current time level by n so that $t_n = n\Delta t$. Considering a step from n to $n+1$ with the Explicit Euler technique, the discrete version of our system can be written:

$$u^{n+1} = u^n + \Delta t \dot{u}^n \quad (12.12)$$

$$\dot{u}^{n+1} = \dot{u}^n - \Delta t \frac{k}{m} u^n \quad (12.13)$$

or:

$$\begin{Bmatrix} u \\ \dot{u} \end{Bmatrix}^{n+1} = [C] \begin{Bmatrix} u \\ \dot{u} \end{Bmatrix}^n \quad \text{where} \quad [C] = \begin{bmatrix} 1 & \Delta t \\ -\Delta t(k/m) & 1 \end{bmatrix} \quad (12.14)$$

Using $[X]$, the matrix of right eigenvectors of $[C]$, we can also express this system in “modal coordinates” w_1, w_2 as:

$$\begin{Bmatrix} w_1 \\ w_2 \end{Bmatrix}^{n+1} = [X]^{-1} \begin{Bmatrix} u \\ \dot{u} \end{Bmatrix}^{n+1} = [X]^{-1}[C][X][X]^{-1} \begin{Bmatrix} u \\ \dot{u} \end{Bmatrix}^n \quad (12.15)$$

$$= \begin{bmatrix} \sigma_1 & 0 \\ 0 & \sigma_2 \end{bmatrix} \begin{Bmatrix} w_1 \\ w_2 \end{Bmatrix}^n \quad (12.16)$$

where σ_1, σ_2 are the eigenvalues of $[C]$. The transformation to diagonal form using the matrix of eigenvalues is known as the similarity transform. For the Euler explicit case:

$$\sigma_{1,2} = 1 \pm \Delta t \sqrt{-k/m} \quad (12.17)$$

Since $w_{1,2}^{n+1} = (\sigma_{1,2})w_{1,2}^n$, and $|\sigma_{1,2}| > 1$ we can conclude that the numerically integrated response is growing in time. This is in contrast to the original semi-discrete one DOF system, which has constant amplitude and frequency. It can also be seen that The error is first-order in Δt , consistent with the order of the truncation error in the Taylor series.

A similar analysis of the implicit Euler method produces:

$$\sigma_{1,2} = \frac{1 \pm \Delta t \sqrt{-k/m}}{1 + \Delta t^2 k/m} \quad (12.18)$$

This method is also first-order accurate, but in this case, $|\sigma_{1,2}| < 1$ so that the amplitude is decreased each time step. One has to be aware of this type of error during a computation, as this damping introduced by the time march can stabilise an otherwise unstable mode.

In general, all numerical integration methods produce either amplitude errors (signal growth or dissipation) or phase errors (time leads or lags) or both, depending on their design. We may express the amplitude error per time step (local amplitude error) as:

$$e_{amp} = 1 - |\sigma| \quad (12.19)$$

while the local phase error is:

$$e_{pse} = \omega \Delta t - \arg(\sigma) \quad (12.20)$$

where for the system considered, $\omega = \sqrt{k/m}$. If the method is *consistent*, e_{amp} and e_{pse} will reduce with $(\Delta t)^m$, where m is the order of the method.

Although the phase and amplitude errors of the Euler explicit and Euler implicit methods are similar, in the case of the explicit method, the amplitudes are growing with each time step. Repeated application of the explicit method by taking multiple time steps will thus result in an exponential growth in the amplitude. This phenomena is known as (linear) numerical instability. For the Euler implicit method, the solution will remain bounded after multiple time

steps (with an amplitude tending to zero). It is said to be (linearly) stable for this problem.

In general, numerical time-integration techniques applied to either analytic or discretised systems will produce solutions which are either linearly stable, unstable, or conditionally stable. In the latter case, there is normally a maximum time step with which the system can be advanced and remain stable. For structural problems, an implicit method is usually required to ensure unconditional linear stability.

12.4 Numerical Integration multi-DOF systems

Now consider a system such as what would be obtained by application of the finite-element method described in the previous section:

$$[M]\{\ddot{u}\} + [K]\{u\} = 0 \quad (12.21)$$

for such a case it is clear that the eigenvalues which characterise the behaviour of the numerically time-integrated solution will be functions of $[M]$ and $[K]$. Therefore, the type of spatial discretisation used also effects the resulting amplitude errors (stability) and phase errors of the solution. Multiple-DOF systems produce multiple modes, each with an associated oscillation period.

If the oscillation periods are close to each other, then conditionally-stable explicit methods may be preferred, since they require far less work per time step than implicit methods. If the oscillation periods are far apart in magnitude (i.e. the matrix resulting from the discretisation is stiff), then unconditionally stable implicit methods are generally preferred. This is because typically only the lower frequency modes are of interest, and implicit methods permit the use of large time steps. In contrast, a conditionally-stable explicit method would be forced to march at the time-step required to prevent instability of the highest-frequency mode.

12.5 Newmark method

The Newmark time integration method commonly used in structural dynamic applications. For the system:

$$[M]\{\ddot{u}\} + [C]\{\dot{u}\} + [K]\{u\} = \{f(t)\} \quad (12.22)$$

An implicit method can be defined based on the satisfaction of equilibrium at t^{n+1} :

$$[M]\{\ddot{u}_{n+1}\} + [C]\{\dot{u}_{n+1}\} + [K]\{u_{n+1}\} = \{f(t_{n+1})\} \quad (12.23)$$

and two Taylor series expansions in terms of the anticipated value of acceleration at the next time step:

$$u_{n+1} = u_n + \Delta t \dot{u}_n + \frac{\Delta t^2}{2} [(1 - 2\beta)\ddot{u}_n + 2\beta\ddot{u}_{n+1}] \quad (12.24)$$

$$\dot{u}_{n+1} = \dot{u}_n + \Delta t [(1 - \gamma)\ddot{u}_n + \gamma\ddot{u}_{n+1}] \quad (12.25)$$

The Newmark method is unconditionally stable (no amplitude growth) when $2\beta \geq \gamma \geq \frac{1}{2}$. It is similar to trapezoidal integration when $\beta = \frac{1}{4}$, and $\gamma = \frac{1}{2}$.

12.6 Efficient integration using modal superposition

If you will repeatedly be advancing a structural discretisation in time, it is often worthwhile to first solve for the natural modes of the structure, and then construct a decoupled dynamic system based on the natural modes.

To solve for the natural modes, we assume a harmonic solution: $\{u\} = \{\hat{u}\}e^{i\omega t}$. Substituting into the equations of motion leads to:

$$([K] - \omega^2[M])\{\hat{u}\} = 0 \quad (12.26)$$

This generalised eigenvalue problem can be solved for the eigenvalues, ω^2 , and the eigenvectors (or natural modes) Φ_i . The latter are normalised so that $[\Phi]^t[M][\Phi] = I$, where $[\Phi]$ is the matrix of eigenvectors (orthonormal modes).

We can then use orthogonal properties of the modes to decouple the dynamic system, by noting the matrix of orthonormal modes, $[\Phi]$ has the following property:

$$[\Phi]^t[K][\Phi] = [\Lambda] = \begin{bmatrix} \omega_1^2 & . & . & . \\ . & \omega_2^2 & . & . \\ . & . & \ddots & . \\ . & . & . & \omega_N^2 \end{bmatrix} \quad (12.27)$$

$$(12.28)$$

while by definition:

$$[\Phi]^t[M][\Phi] = [I] \quad (12.29)$$

so that if we define generalized coordinates $\{q\}$ by:

$$\{u\} = [\Phi]\{q\} \quad (12.30)$$

the equations of motion can be expressed:

$$[I]\{\ddot{q}\} + [\Lambda]\{q\} = [\Phi]^t\{f(t)\} \quad (12.31)$$

which is a decoupled system in *modal coordinates*.

A damping term $[C]\{\dot{u}\}$ may also be included in the system provided that it is of the form:

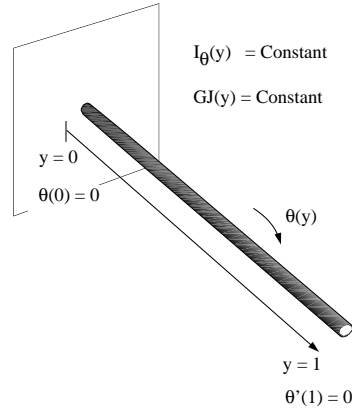
$$[C] = \alpha[M] + \beta[K] \quad (12.32)$$

Overall, using modal superposition can substantially reduce the cost of numerical integration. Furthermore, we can now choose to retain only the low-frequency modes. This approach to reduced-order modelling procedure allows us to perform compact computations which retain the most important behaviours present in a complex geometry.

12.7 Practice Problems

p12.7.24 Derive the element mass and stiffness matrices for a bar element loaded in torsion using linear shape functions.

p12.7.25 Compute the torsional normal modes of the cantilever bar shown in the figure below. Use two finite elements with linear shape functions.



p12.7.26 Compute the forced response $\theta(y, t)$, of the bar in question 2 to a torque $T = A \sin(\omega t)$ applied at $y = l$. Use the results of question 2 and the modal superposition approach.

p12.7.27 Consider a single DOF system given by:

$$m\ddot{u} + ku = 0$$

and a trapezoidal direct integration method to advance this system in time based on the equations:

$$\begin{aligned} u^{n+1} &= u^n + \frac{\Delta t}{2}(\dot{u}^{n+1} + \dot{u}^n) \\ \dot{u}^{n+1} &= \dot{u}^n - \frac{\Delta t k}{2m}(u^{n+1} + u^n) \end{aligned}$$

Compute the phase and amplitude errors produced by this method per time step when $k/m = 1$ and $\Delta t = 0.1$.

Chapter 13

Computational Methods for Unsteady Flows

This chapter will provide an overview of computational methods currently used to predict unsteady aerodynamic forces for aeroelastic analyses. We will begin by considering methods for the linearised potential equation. These are still in wide use for preliminary design, as they can give a first estimation of the critical points for a configuration, which can later be examined in detail using more sophisticated methods. The typical level of fidelity achieved for classical flutter problems is illustrated in figure 13.1, which shows a non-dimensional flutter speed versus Mach number. Comparison of linear and non-linear results

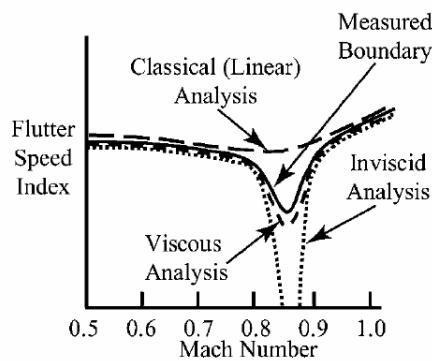


Figure 13.1: Flutter speeds predicted with different aerodynamic models (from Schuster et al, J. of Aircraft (40) 5 , 2003)

also gives an indication of the sensitivity of the design to non-linear effects.

In the transonic region, non-linear prediction methods are typically required in order to predict the flow with acceptable accuracy. In addition to providing

better predictions of classical flutter modes, non-linear methods can also be used to consider responses which are purely dependent on phenomena which cannot be computed with linear methods. Examples include aileron buzz and stall flutter, although the truly accurate computation of these phenomena remains a considerable challenge.

In our description of non-linear methods, we will first consider the small-disturbance potential equation, and then move on to the Euler and Navier-Stokes equations, for which we will also discuss the analysis of numerical errors. We will not discuss methods for the full-potential equations, as these are similar in form to methods for the Euler equations. Figure 13.2 presents an overview of the models, concepts, and methods considered in this chapter.

Aerodynamic Model	Important Concepts	Example Methods
Linearised Potential	<div>Superposition</div> <div>Wake / time delay treatment</div>	<div>Kernel Function</div> <div>Panel</div>
Small-Disturbance Potential	<div>Linearised moving-wall B.C.s</div>	<div>Finite Difference</div>
Euler / Navier-Stokes	<div>Moving meshes and the DGCL</div> <div>Methods for error estimation</div>	<div>Finite Difference</div> <div>Finite Volume</div> <div>Finite Element</div>

Figure 13.2: Models, concepts and example methods considered in chapter 13

13.1 Linearised potential equation

Methods for the linearised potential equation are not only attractive for their computational speed, but also for the ease with which they can be validated using exact solutions. In industry, these methods remain popular due to the wealth of experience built up with their use. Linearised methods are also good candidates for inverse design procedures, although the sensitive nature of the flutter problem still makes the development of robust inverse algorithms a challenge.

Many solution methods for linear equations make use of superposition. For the linearised potential equation, surface-singularity approaches are particularly popular. These can be based on either the velocity- or acceleration-potential form of the equations. The velocity-potential form of the equations was introduced in chapter 3, and can be written:

$$\nabla^2 \phi - M_\infty^2 \frac{\partial^2 \phi}{\partial x^2} - \frac{1}{a_\infty^2} \left[\frac{\partial^2 \phi}{\partial t^2} + 2U_\infty \frac{\partial^2 \phi}{\partial x \partial t} \right] = 0 \quad (13.1)$$

$$(13.2)$$

$$p - p_\infty = -\rho \left(\frac{\partial \phi}{\partial t} + U_\infty \frac{\partial \phi}{\partial x} \right) \quad (13.3)$$

The acceleration-potential form can be obtained by defining ψ , the acceleration potential, as:

$$\psi = \frac{\partial \phi}{\partial t} + U_\infty \frac{\partial \phi}{\partial x} \quad (13.4)$$

For a harmonic solution $\psi = \hat{\psi}(x, y, z)e^{i\omega t}$, the linearised potential equations can be expressed in terms of acceleration potential as:

$$\nabla^2 \hat{\psi} - M_\infty^2 \frac{\partial^2 \hat{\psi}}{\partial x^2} - 2i\omega \frac{M_\infty}{a_\infty} \frac{\partial \hat{\psi}}{\partial x} + \frac{\omega^2}{a_\infty^2} \hat{\psi} = 0 \quad (13.5)$$

$$p - p_\infty = -\rho \hat{\psi} \quad (13.6)$$

The first equation is similar to the velocity-potential form for harmonic motions. The second equation is now much more convenient for the application of wake boundary conditions. In this case the $\Delta p = 0$ wake condition can be simply expressed as $\psi = 0$ on the wake surface.

13.1.1 Kernel-function method

Consider the isolated wing geometry of figure 13.3. If we assume the solution is harmonic, it is possible to express the vertical velocity at all points on the wing as:

$$w(x, y) = \hat{w}(x, y)e^{i\omega t} \quad (13.7)$$

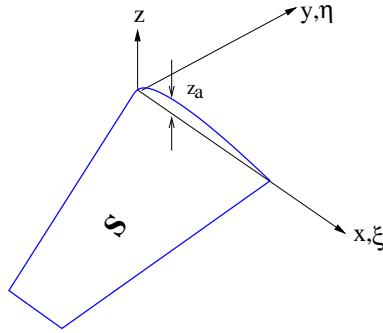


Figure 13.3: Basic wing geometry

where:

$$\hat{w}(x, y) = \int_S \Delta \hat{\psi}(\xi, \eta) K(x - \xi, y - \eta, k, M_\infty) d\xi d\eta \quad (13.8)$$

and K , known as the kernel function, is a (rather complicated) analytic expression which can be derived for thin wings with planar wakes. In order to solve the problem we may choose:

$$\Delta \hat{\psi}(x, y) = \sum_{i=1}^n \sum_{j=1}^m \hat{a}_{ij} f_i(x) g_j(y) \quad (13.9)$$

where $f_i(x)$ and $g_j(y)$ are assumed continuous functions which satisfy the pres-

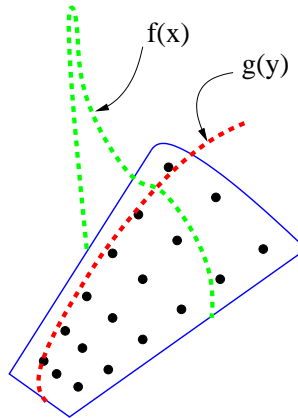


Figure 13.4: Assumed forms for the kernel function method

sure boundary conditions on the edges of the wing (singular at leading edge,

zero at the tips and trailing edges). Example functions are illustrated in figure 13.4. The \hat{a}_{ij} coefficients can be found by enforcing flow tangency condition at $n \times m$ control points using the integral equation for w and the assumed form for $\Delta\hat{\psi}(x, y)$. This leads to a system of $(n \times m)$ equations for the unknown coefficients. Note that the wake need not be included in the integration since $\Delta\hat{\psi}_{wake} = 0$. This is because all of the assumed harmonic wake-lag effects are already encapsulated in the definition of K .

13.1.2 Panel Methods

The kernel-function approach is extremely efficient, but it is restricted to simple, thin wings. Alternatively, panel methods can be used if more complex geometries are to be considered. Panel methods can be formulated in the time domain, using the velocity-potential form of the equations. Vorticity convection in the wake is then treated explicitly. The general steps in the procedure are

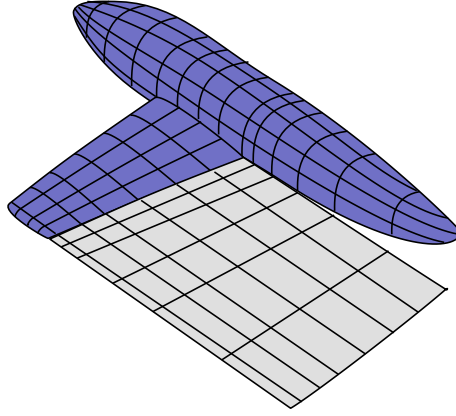


Figure 13.5: Layout of a panel method

(see figure 13.5):

1. The surface of the wing or body and its associated wake is discretised into a series of panels with surface singularity distributions of unknown strength.
2. The potential induced at a point due a given panel is then expressed in terms of the panel's p unknown singularity-strength coefficients.
3. If there are N panels, a system of $N * p$ equations can be formed by enforcing flow tangency at p control points on each panel. Since the PDE is linear, the local normal velocity is simply the sum of the contributions from all the panels.
4. The position of the wake is updated so that $\Delta p_{wake} = 0$

For incompressible flows, or harmonic compressible flows, the potential induced by a panel can be expressed simply. For arbitrary compressible flows, time delays must be taken into account, which complicates implementation. An equally important problem is the determination of the wake position, as it can experience significant distortions in regions of high vorticity, such as near wing tips (figure 13.6). It is possible to find the wake position using non-linear iteration procedures, but these are generally unreliable if the wing is significantly loaded. A robust alternative is to use a fixed reference wake, and solve for small normal displacements from the wake as a function of time. This can be quite accurate at the low reduced frequencies which are often crucial in aircraft configuration analysis.

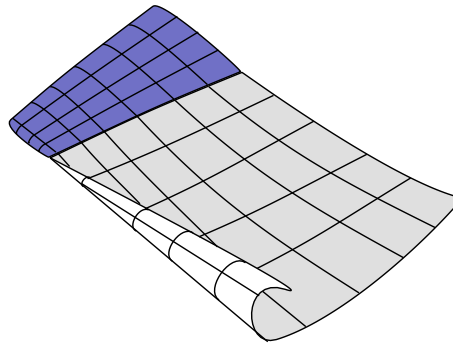


Figure 13.6: Concentration of wake vorticity

The singular behaviour of the potential solution in the immediate vicinity of the panels means that wake-body interactions, such as produced by propellers mounted ahead of wings, are difficult to treat accurately. Robust analysis of such problems requires the solution of the Euler or Navier-Stokes equations, which can capture arbitrary vortical phenomena within their solutions.

13.2 Small-disturbance potential equation

The earliest methods which could predict transonic flutter were based on the small-disturbance potential equation, the simplest model which can include the effects of shock motion. Since many companies have extensive experience with its use, the small-disturbance potential equation (also known as transonic small disturbance (TSD) equation), is still often applied for preliminary transonic analysis. The small-disturbance potential equations can be written:

$$\left[1 - M_\infty^2 - (\gamma + 1)M_\infty^2 b \frac{\partial \phi}{\partial x}\right] \frac{\partial^2 \phi}{\partial x^2} + \frac{\partial^2 \phi}{\partial y^2} + \frac{\partial^2 \phi}{\partial z^2} \quad (13.10)$$

$$- \frac{1}{a_\infty^2} \left(2U_\infty \frac{\partial^2 \phi}{\partial x \partial t} + \frac{\partial^2 \phi}{\partial t^2} \right) = 0$$

$$p - p_\infty = -\rho \left(\frac{\partial \phi}{\partial t} + U_\infty \frac{\partial \phi}{\partial x} \right) \quad (13.11)$$

Since the main equation is non-linear, superposition cannot be used. This means that the entire flow domain must be discretised (figure 13.7). As we are considering small disturbances, however, it is customary to linearise the boundary conditions. The latter is an extremely convenient simplification, as then the application of flow tangency on the airfoil surface does not require distortion of the grid in order to account for structural deformations. A popular

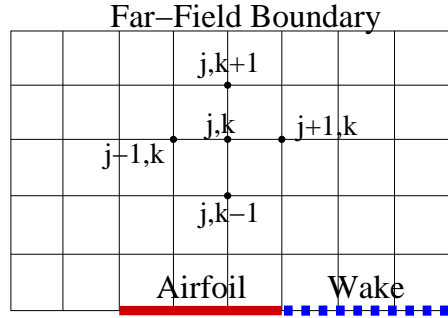


Figure 13.7: Discretisation for the small-disturbance potential equation

discretisation option is to apply finite differences simultaneously in space and time, where derivatives are replaced by approximate expressions derived from Taylor series expansions such as:

$$\phi_{xx_{ij}} = \frac{\phi_{j-1,k} - 2\phi_{j,k} + \phi_{j+1,k}}{\Delta x^2} + O(\Delta x^2) \quad (13.12)$$

Cartesian meshes can be used for simplicity, although transformed meshes are sometimes used to place the far-field boundary at infinity. Once discretised, the following boundary conditions are applied:

- Linearised flow tangency on the airfoil surface (ϕ_z^\pm is prescribed by the airfoil motion)
- Linearised change in pressure across the wake surface is zero
- The perturbation is zero at the far field

An implicit discretisation is then obtained in terms of the unknowns at the next time level. This is typically solved using a sub-iteration techniques to remove linearisation errors in time.

13.3 Euler and Navier-Stokes equations

The 1980's saw the introduction of the first reliable numerical methods for the compressible Euler and Navier-Stokes equations. These have only recently come into common use for aeroelastic analysis, however, due to their relatively high cost when used for low-frequency unsteady simulations. The Euler equations represent a considerable step up from potential-based methods (including full potential methods), as they admit vorticity directly into their solutions, and can therefore capture complex wake interactions occurring between aerodynamic components. In addition they automatically include the effects of time delays, and include such features such as non-isentropic shock waves, non-linear expansion waves, and contact surfaces. The Euler equations are still limited, of

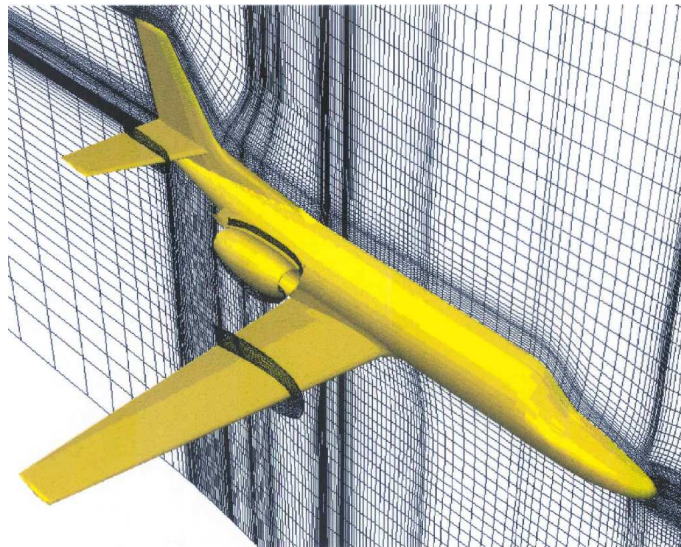


Figure 13.8: An Euler mesh for unsteady aerodynamic computations

course, as they do not include the effects of viscosity. In theory this means that

they also do not enforce the Kutta condition, but in practice this is enforced automatically due to the necessary presence of finite amounts of numerical dissipation.

When other viscous effects must be considered, the Reynolds-averaged Navier-Stokes equations are normally used. This raises an important issue concerning the fidelity of turbulence models used to predict unsteady flows. A lack of unsteady data makes such models difficult to calibrate, and often models calibrated using steady data are used. Another problem occurs if the turbulent fluctuations of the largest eddies approaches the time scales of the structural vibration. In this case the assumptions underlying the Reynolds-averaged approach are compromised, and one formally should switch to large-eddy simulation. Due to resolution requirements, however *accurate* LES is currently not possible at the Reynolds numbers of interest to aircraft applications.

In contrast to the small-disturbance equations, in most cases it is inappropriate to linearise the boundary conditions for the Euler and Navier-Stokes equations. This adds considerable complication to the solution procedure, as the discretisation must be general enough to treat deforming domains (figure 13.9). Aside from the complication of implementation, it has been demonstrated that

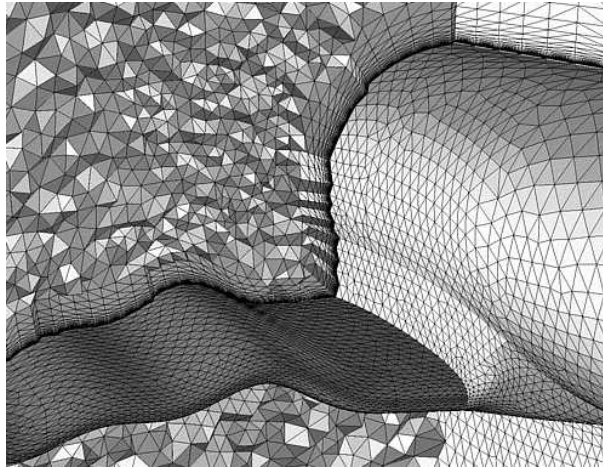


Figure 13.9: A mesh with a deforming boundary

algorithms which discretely enforce conservation in the unsteady sense usually deliver superior accuracy, making this an additional criteria in method design.

As far as wall boundary conditions are concerned, for the Euler equations it is sufficient to apply the flow-tangency condition at the wall, while for the Navier-Stokes equations no-slip conditions are required. Typically this is done using methods similar to those used for steady flows, but accounting for wall movement. At far field boundaries, however, the enforcement of boundary conditions in unsteady flows can be far more complicated than for steady problems.

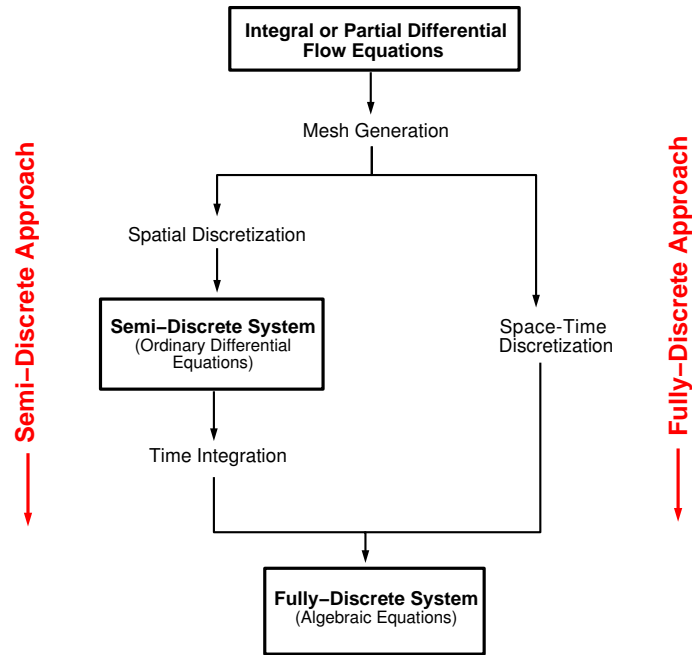


Figure 13.10: Options for discretisation

Due to computational cost the domain of the problem must remain limited, which means that important influences of physical phenomena (such as convecting wake vorticity) can be lost as they leave the domain. This contrasts with steady problems, which typically have uniform far-field conditions. The latter can be represented by relatively simple procedures, provided solution-error transients can be properly expelled.

13.4 Discretisation of the Euler and Navier Stokes equations

In general, either semi- or fully-discrete approaches can be applied using either the Finite-difference, Finite-volume, or Finite-element method. An overview is given in figure 13.10.

13.4.1 Semi-discrete approach

In the semi-discrete approach, a finite-difference, volume or element method is first applied to the spatial part of the partial differential equations (PDE). This results in a system of ordinary differential equations (ODE) for the unknown

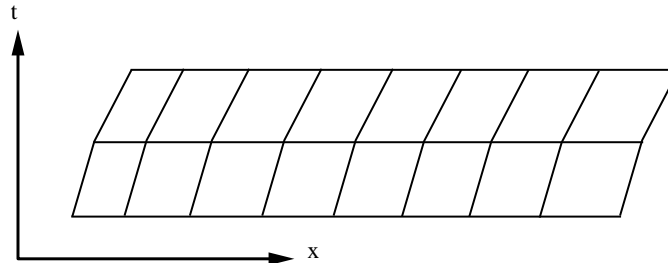
discrete solution values as a function of time. These are integrated using either explicit or implicit time-integration methods.

For unsteady problems the solution accuracy is a function of both the spatial discretisation and time integration method. This is different from when steady-flow problems are considered, for which the accuracy of the time integration method normally used to solve the non-linear problem is unimportant.

In general, explicit time-integration methods (e.g. MacCormack, Runge-Kutta) are restricted for stability reasons to small time steps, on the order of the time necessary for an acoustic wave to traverse the smallest cell. Implicit time-integration methods (e.g. Trapezoidal) are stable for much larger time steps but require more work per time step than explicit methods. Implicit time-integration methods are often preferred, as the time scales of fluid-structure interactions are usually much greater than the acoustic scale of the smallest mesh cell, particularly for viscous calculations.

13.4.2 Fully-discrete approach

In the fully-discrete approach a finite-difference, volume or element method is applied simultaneously to the spatial and temporal parts of the PDE. This leads directly to a (non-linear) algebraic system for the unknown nodal values. Fully-discrete discretisations (also known as space-time discretisations) can be advantageous from an implementation point of view, since they naturally include mesh motion. This is illustrated in figure 13.11, which shows space-time elements for a one-dimensional domain moving to the right as time advances.



A moving 1D mesh in space-time

Figure 13.11: Fully-discrete approach

13.5 Dealing with moving meshes

Typically the equations of fluid mechanics are in Eulerian form, that is they are derived for a control volume which is fixed in space. This is inconvenient if the boundary of the domain is changing due to, for example, the movement of an

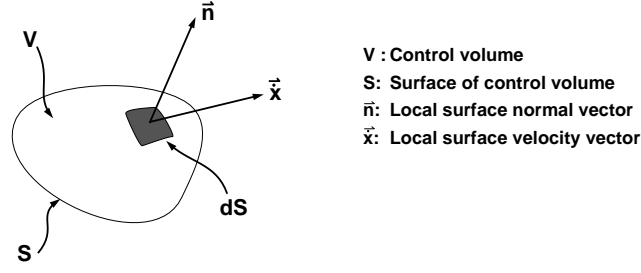


Figure 13.12: A moving control volume

elastic wing. An alternative is to use a Lagrangian formulation, where the mesh follows the fluid particles (and thus the fluid boundary). This is impractical for most flows due to the large distortions associated with tracking fast-moving particles. In fact, we need to be able to choose the mesh geometry arbitrarily, in order to control mesh quality as the boundary deforms. This leads to the concept of the Arbitrary Lagrangian-Eulerian (ALE) formulation. This is most easily expressed by directly applying the Reynolds Transport theorem for a moving control volume to the Euler or Navier-Stokes equations. Referring to figure 13.13, this results in:

$$\frac{d}{dt} \int_V W \, dV + \int_S (\vec{F}^i - \vec{F}^v - \vec{x}W) \cdot \vec{n} \, dS = 0 \quad (13.13)$$

Here W represents the flow state vector:

$$W = \begin{bmatrix} \rho \\ \rho \vec{u} \\ \rho E \end{bmatrix} \quad (13.14)$$

which contains components of density, specific momentum, and specific total energy. The flux vector is defined by $\vec{F}^i - \vec{F}^v$, where \vec{F}^i and \vec{F}^v are the inviscid and viscous contributions. Finally, \vec{x} denotes the local surface velocity of the control volume. Note that (13.13) reverts to the Lagrangian description for $\vec{x} = \vec{u}$ and the Eulerian for $\vec{x} = 0$. In practice we will instead associate \vec{x} with the movement of the mesh, as it changes position to represent aeroelastically-deformed geometries.

13.5.1 The Geometric Conservation Law (GCL)

Consider the ALE formulation (13.13) for a constant $W = W^*$:

$$\frac{d}{dt} \int_V W^* \, dV + \int_S (\vec{F}^i(W^*) - \vec{x}W^*) \cdot \vec{n} \, dS = 0 \quad (13.15)$$

In this case, the viscous fluxes $\vec{F}^v(W^*) = 0$, and the inviscid fluxes are constant. Since for a closed cell, $\int_S \vec{n} dS = 0$:

$$\frac{d}{dt} \int_V dV = \int_S \dot{x} \cdot \vec{n} dS \quad \text{GCL (Integral form)} \quad (13.16)$$

This relation is called the Geometric Conservation Law (GCL), as it can be interpreted physically as “The change in V must equal the volume swept out by its surface”.

13.5.2 The Discrete Geometric Conservation Law (DGCL)

In the design of steady solution methods, it has long been known that methods which are discretely conservative (those which conserve the total mass, momentum, and energy exactly), tend to produce more accurate results. This becomes crucial when discontinuous solutions are present, as their description is tied to the integral rather than the differential form of the equations. In recent years, it has also become clear that discrete enforcement of the geometric conservation law is desirable for methods which use moving meshes. Although the idea of enforcing the DGCL dates back to Thomas and Lombard (AIAA J. 1979 18:1030-1037), comprehensive analyses of its advantages were first made in a series of results published by Farhat et al between 2000 and 2001. First, Guillard and Farhat (Comput. Methods Appl. Mech Engrg. 2000 190:1496-1482) showed that for a p -order accurate scheme, enforcing the p -discrete DGCL will ensure *at least* 1st-order accuracy on a moving mesh. Then, Farhat and Geuzaine (AIAA paper 2001-2607) showed that the second-order three-point backward-difference time-integration scheme maintains its accuracy on a moving mesh if the DGCL is enforced. Finally, in Farhat, Geuzaine and Grandmont (J. Comp. Physics 2001 174:669-694) it is proposed that the DGCL is a necessary and sufficient condition for preserving the nonlinear stability of fixed-mesh methods when generalised to moving-mesh problems.

In the following sections, some example discretisations for moving meshes will be presented. The details of enforcement of the DGCL will also be discussed. Note that the details of the enforcement of the DGCL are considered additional material for this course, and are not required knowledge for the exam.

13.6 Example: A semi-discrete finite-difference method

As the application of multidimensional finite-difference relations is inconvenient, normally finite-difference techniques are implemented using a curvilinear transform, which maps the mesh onto a Cartesian reference mesh. When moving meshes are used, this transformation must be time-varying. The finite-difference

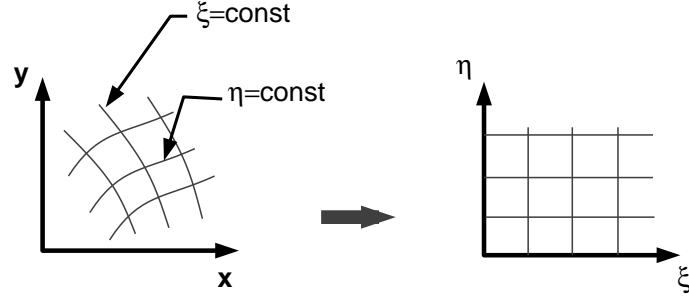


Figure 13.13: Curvilinear coordinate transform

discretisation is then applied to the transformed equations on the fixed reference mesh. Consider the divergence form of the Euler equations:

$$\frac{dW}{dt} + \vec{\nabla} \cdot \vec{F} = 0 \quad \text{or in 2D:} \quad W_t + f_x + g_y = 0 \quad (13.17)$$

where f_x are the flux components g_y in two dimensions. The transformed equations can be obtained using the chain rule, and are thus expressed in terms of the metrics of the transformation ($\xi_t, \xi_x, \xi_y, \eta_t$ etc.):

$$W_t + W_\xi \xi_t + W_\eta \eta_t + f_\xi \xi_x + f_\eta \eta_x + g_\xi \xi_y + g_\eta \eta_y = 0 \quad (13.18)$$

(Note that dissipative terms which vanish in the limit of zero mesh size are often added to (13.18) to improve the stability of the numerical solution procedure). To evaluate the metrics of the transformation, note:

$$\begin{bmatrix} dt \\ dx \\ dy \end{bmatrix} = \begin{bmatrix} 1 & \xi_t & \eta_t \\ 0 & \xi_x & \eta_x \\ 0 & \xi_y & \eta_y \end{bmatrix} \begin{bmatrix} d\tau \\ d\xi \\ d\eta \end{bmatrix} \quad (13.19)$$

and:

$$\begin{bmatrix} d\tau \\ d\xi \\ d\eta \end{bmatrix} = \begin{bmatrix} 1 & x_\tau & y_\tau \\ 0 & x_\xi & y_\xi \\ 0 & x_\eta & y_\eta \end{bmatrix} \begin{bmatrix} dt \\ dx \\ dy \end{bmatrix} \quad (13.20)$$

By comparison, the second matrix of metrics is equivalent to the inverse of the first. This leads to:

$$\begin{bmatrix} 1 & \xi_t & \eta_t \\ 0 & \xi_x & \eta_x \\ 0 & \xi_y & \eta_y \end{bmatrix} = J^{-1} \begin{bmatrix} J & (y_\tau x_\eta - x_\tau y_\eta) & (x_\tau y_\xi - y_\tau x_\xi) \\ 0 & y_\eta & -y_\xi \\ 0 & -x_\eta & x_\xi \end{bmatrix} \quad (13.21)$$

where $J = (x_\xi y_\eta - y_\xi x_\eta)$ is the Jacobian of the transformation. The expressions for x_ξ, y_τ, y_η etc. can easily be evaluated on the fixed (Cartesian) reference mesh.

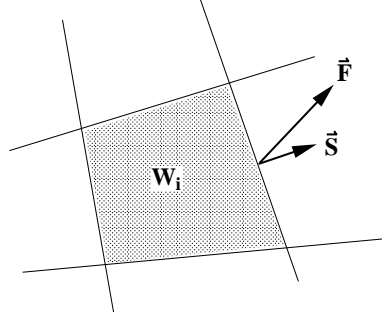


Figure 13.14: A single cell of a finite-volume discretisation

13.6.1 Enforcing the DGCL (optional section)

In order to satisfy the DGCL, the Jacobian is updated separately by integrating a transformed version of the geometric conservation law:

$$J_t + (J\xi_t)_\xi + (J\eta_t)_\eta = 0 \quad (13.22)$$

Ensuring the time and space discretisation for this relation is identical to that of the flow equations enforces the DGCL (see Thomas and Lombard AIAA J. 1979 18:1030-1037 for more details).

13.7 Example: A semi-discrete finite-volume method

A moving-mesh finite-volume method can be derived directly from (13.13), that is the conservation laws written for an arbitrarily-moving control volume:

$$\frac{d}{dt} \int_V W \, dV + \int_S (\vec{F} - \vec{x}W) \cdot \vec{n} \, dS = 0 \quad (13.23)$$

By defining cell-averaged solution values:

$$W_i = \frac{1}{V_i} \int_{V_i} W \, dV \quad (13.24)$$

The conservation laws can be applied directly to each cell (figure 13.14), resulting in a system of ODEs for the time evolution of the average values:

$$\frac{d}{dt} (V_i W_i) = - \sum_{m=1}^M (\vec{F}_m - W_m \vec{x}_m) \cdot \vec{S}_m \quad (13.25)$$

where $\vec{S}_m = \vec{n}_m \cdot |S_m|$. These can be integrated using standard time-integration techniques, although some care must be taken to satisfy the DGCL.

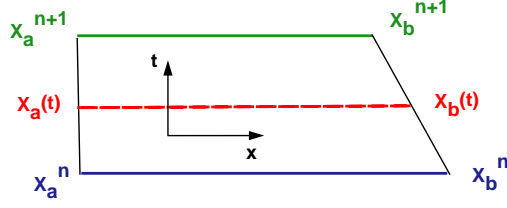


Figure 13.15: Movement of the side of a control volume in space-time

13.7.1 Enforcing the DGCL (optional section)

The finite-volume version of the DGCL can be expressed:

$$(V_i^{n+1} - V_i^n) = \int_{t^n}^{t^{n+1}} \sum_{m=1}^M \vec{x}_m \cdot \vec{S}_m = 0 \quad (13.26)$$

Normally it is chosen to compute V_i^{n+1} and V_i^n exactly from the given mesh deformation data, and then formulate the right-hand side in a way which satisfies the DGCL. How this is done depends on both the spatial and temporal discretisation. Consider a single (flat) side of a 2D cell as shown in figure 13.15, combined with a first-order accurate time-integration scheme, and define:

$$I_{ab} = \int_{t^n}^{t^{n+1}} \int_a^b \dot{x} \cdot \vec{n} \, ds \, dt \quad (13.27)$$

A linear parameterisation for the mesh movement can be made as:

$$x(t) = \alpha x_a(t) + (1 - \alpha)x_b(t) \quad \alpha \in [0, 1] \quad (13.28)$$

$$\dot{x}(t) = \alpha \dot{x}_a(t) + (1 - \alpha)\dot{x}_b(t) \quad (13.29)$$

$$x_a(t) = \delta(t)x_a^{n+1} + (1 - \delta(t))x_a^n \quad \delta \in [0, 1] \quad (13.30)$$

$$x_b(t) = \delta(t)x_b^{n+1} + (1 - \delta(t))x_b^n \quad (13.31)$$

Then, noting \vec{n} is a function of time but not α , and $ds = l d\alpha$:

$$I_{ab} = \int_{t^n}^{t^{n+1}} \int_0^1 (\alpha \dot{x}_a + (1 - \alpha)\dot{x}_b) \, \vec{n} l \, d\alpha \, dt \quad (13.32)$$

$$= \int_{t^n}^{t^{n+1}} \frac{1}{2} (\dot{x}_a + \dot{x}_b) H(x_a - x_b) \, dt \quad (13.33)$$

where $H = \begin{pmatrix} 0 & -1 \\ 1 & 0 \end{pmatrix}$ converts the vector between the two endpoints to the normal area, $\vec{n}l$. Substituting our parameterisations, and noting $dt = \Delta t d\delta$,

$$I_{ab} = \frac{1}{2} \int_0^1 ((x_a^{n+1} - x_a^n) + (x_b^{n+1} - x_b^n)) H \, d\delta \quad (13.34)$$

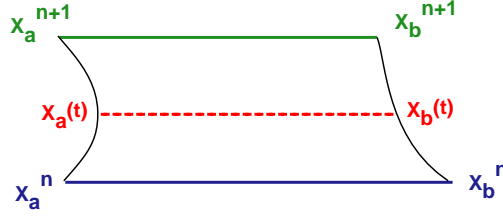


Figure 13.16: Higher-order variation in time

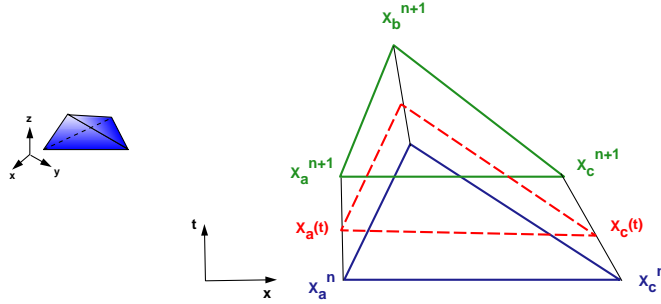


Figure 13.17: Three-dimensional DGCL

which has an integrand which is linear in δ . Therefore, I_{ab} can be evaluated exactly using the mid-point rule. The DGCL is thus satisfied in this case if the configuration used for evaluating the flux integral is at $x^{n+\frac{1}{2}}$. A higher-order time-integration scheme requires a higher-order parameterisation of the edge displacement (figure 13.15). For quadratic variation, at least two integration points are required in order to exactly evaluate I_{ab} . As a consequence, the flux integral must be computed on at least two mesh configurations.

If we instead consider the single side of a 3D tetrahedron in the first-order case (figure 13.17), the integral I_{abc} contains a surface-normal expression quadratic in δ , arising from the cross product of x_{ab} and x_{ac} . Since computing I_{abc} exactly then requires two integration points, the discrete expression for the flux integral must again be evaluated with two mesh geometries.

13.8 Example: A semi-discrete finite-element method (optional section)

Semi-discrete finite-element methods are normally based on a modified ALE form of the conservation laws, derived from considering a fixed reference volume V_0 , which is related to the moving volume V via a coordinate transform $(x_i, t) \leftrightarrow$

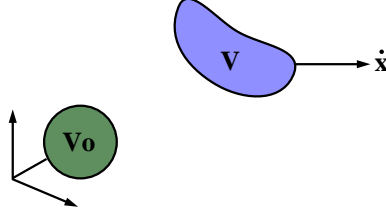


Figure 13.18: Coordinate transform for semi-discrete FEM methods

(ξ_i, t) for which $\partial V = J \partial V_o$ (figure 13.18). The original ALE form then becomes:

$$\frac{d}{dt} \int_{V_o} W J \, dV_o + \int_S (\vec{F} - \vec{x}W) \cdot \vec{n} \, dS = 0 \quad (13.35)$$

Since V_o is fixed, we can bring $\frac{d}{dt}$ inside the integral. By employing the divergence theorem, the following weak form can be derived:

$$\int_{V_o} w \left(\frac{d(WJ)}{dt} + J \nabla \cdot (\vec{F} - \vec{x}W) \right) dV_o = 0 \quad (13.36)$$

where w is the finite-element test function. Normally the second integral is evaluated on V , leading to:

$$\int_{V_o} w \frac{d(WJ)}{dt} dV_o + \int_V w \nabla \cdot (\vec{F} - \vec{x}W) dV = 0 \quad (13.37)$$

A semi-discrete ALE finite-element method can then be defined by considering $\frac{d(WJ)}{dt}$ an unknown which is related to the flow solution via the time-marching algorithm. Satisfaction of the DGCL using such methods requires an analysis similar to that shown for finite-volume schemes in the previous section.

13.9 Example: A space-time finite-element method (optional section)

Space-time (or fully-discrete) discretisations are advantageous as they provide a natural setting for satisfying the DGCL on moving meshes. In fact finite-element space-time discretisations automatically satisfy the DGCL for any order of accuracy in space in time. In order to formulate a space time method, we consider a fixed control volume in space-time, as shown in figure 13.19. If we define a generalised divergence operator and flux vector:

$$\tilde{\nabla} = \left(\frac{\partial}{\partial t}, \frac{\partial}{\partial x}, \frac{\partial}{\partial y} \right); \quad \tilde{F} = (W, f, g, h) \quad (13.38)$$

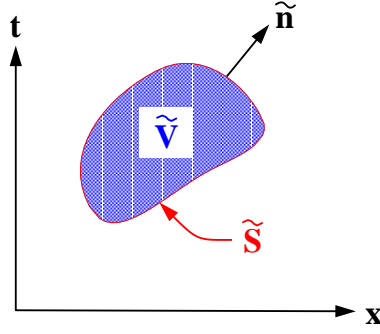


Figure 13.19: A fixed control volume in space-time coordinates

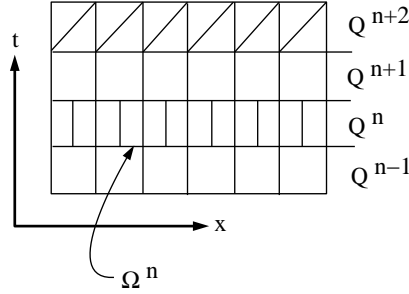


Figure 13.20: The discrete space-time domain

where f, g , and h are the x, y and z components of the space flux vector, \vec{F} , the conservation laws can be written:

$$\int_{\tilde{V}} \tilde{\nabla} \cdot \tilde{F} d\tilde{V} = 0; \quad (13.39)$$

or

$$\int_{\tilde{S}} \tilde{F} \cdot \tilde{n} d\tilde{S} = 0 \quad \text{where} \quad \tilde{n} = (n_t, n_x, n_y) \quad (13.40)$$

To advance the solution, we note that due to causality, only one part of the space-time domain needs to be considered at a time. The space-time domain is therefore split into slabs $Q^n, n = 1..N$ with constant-time boundaries Ω^n at $t = t^n$, as shown in figure 13.20. The solution can then be advanced in time by solving the slabs sequentially. If the mesh topology does not change in time, the number of unknowns in each slab will be comparable to those in standard time-marching techniques.

If a doubling of unknowns can be afforded, one can also choose to make the boundary between slabs discontinuous in time, as shown between the first and

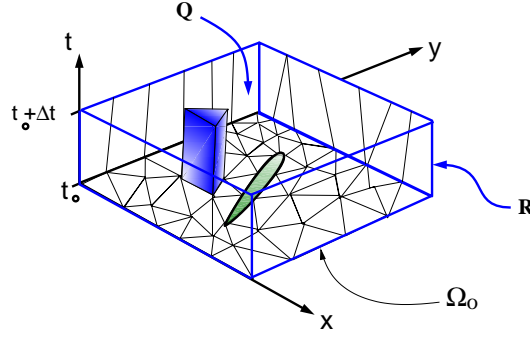


Figure 13.21: A two-dimensional space time mesh

second slabs of figure 13.20. The information from the previous slab is then imposed as a weak boundary condition on Ω_o , the boundary between Q^{n+1} and Q^n :

$$\int_Q w^h \tilde{\nabla} \cdot \tilde{F} dQ + \int_{\Omega_o} w^h (u^{h+} - u^{h-}) = 0 \quad (13.41)$$

This gives enormous flexibility for the generation of moving meshes, as the mesh in one time step can be completely unrelated to the one in the next time step (the total number of elements, for example, can be arbitrarily changed from one time step to another). In order to avoid evaluating the gradient of the flux, (13.41) is usually expanded to:

$$\int_Q -\tilde{F} \cdot \tilde{\nabla} w^h dQ + \int_{\Gamma} w^h \tilde{F} \cdot \tilde{n} d\Gamma \quad (13.42)$$

$$+ \int_{\Omega_o} w^h (u^{h+} - u^{h-}) d\Omega = 0 \quad (13.43)$$

where Γ is the complete surface of Q . This expression maintains a uniform flow, and thus satisfies the DGCL, provided:

$$\int_{\tilde{Q}} \nabla w^h d\tilde{Q} - \int_{\Gamma} w^h \tilde{n} d\Gamma = 0 \quad (13.44)$$

which in the absence of quadrature error, is evaluated exactly by the finite-element procedure. Note that space-time discretisations are necessarily implicit in time, although explicit sub-iteration techniques can be still be used as low-memory solution options.

13.10 Discretisation Error Analysis

The large computational requirements of unsteady simulations means that they are typically performed at the limit of computer resources, and often with

meshes which are coarser than what would be desirable. Consequently, the estimation of discretisation errors due to finite space and time spacings is crucial, especially when considering phenomena as sensitive as flutter.

13.10.1 Grid convergence studies

Space and time grid convergence studies are essential for verifying the quality of unsteady computational solutions. These can also be used to provide direct error estimates. In general, for a method which is n th-order accurate, the discrete solution u_d can be expressed in terms of the exact solution, u_e as:

$$u_d = u_e + gh^n + \text{higher-order terms} \quad (13.45)$$

where g is a function of the gradients of the continuous solution, and h is the step size (Δx or Δt). This results in behaviour of the error $\epsilon = |u_e - u_d|$ similar to that shown in figure 13.22. When h is small, the higher-order terms become

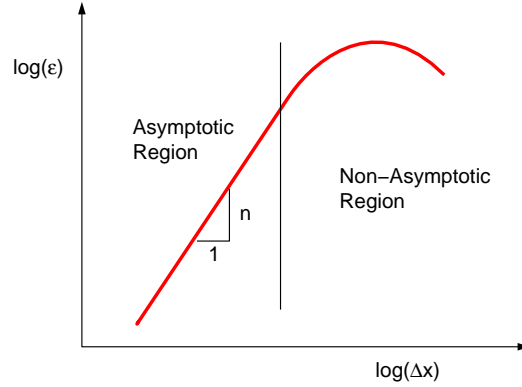


Figure 13.22: Standard behaviour of discretisation error

negligible and the slope on a log-log plot becomes n . The error is then said to be in the asymptotic region.

Results from standard CFD calculations must be in the asymptotic region to be reliable. This can depend on the definition of ϵ , as results for drag may require a finer discretisation than those for lift. In order to have confidence in your results, variations with both $h = \Delta x$ and $h = \Delta t$ must be checked.

In practice, one does not have u_e . Therefore plots similar to figure 13.22 are produced by comparing coarse-mesh solutions to those of the finest mesh in space and time. A straight-forward way to estimate error can then be constructed by considering solutions computed on a sequence of grids with different h .

Consider u_h computed with element size h , and u_{2h} computed with element size $2h$, for a method which is second-order accurate ($n = 2$). g can be eliminated

from the previous equation to obtain:

$$u_e - u_h \approx \frac{u_h - u_{2h}}{3} \quad (13.46)$$

If this error is less than the required tolerance one can assume that the finest numerical solution is adequate. The error estimate can also be used to correct u_h . This is known as Richardson extrapolation.

13.11 Phase and Amplitude Error Analysis

Finite-difference, finite-volume, and finite-element methods, and their associated time-integration schemes, all introduce errors in the representation of flow features as they are convected through the domain. A truncation error analysis of a method will yield its order of accuracy in space and time. It is also useful to examine phase and amplitude errors, however, since methods of the same order can differ significantly from each other in the representation of convective phenomena. The Euler equations can be re-written in a form in which they

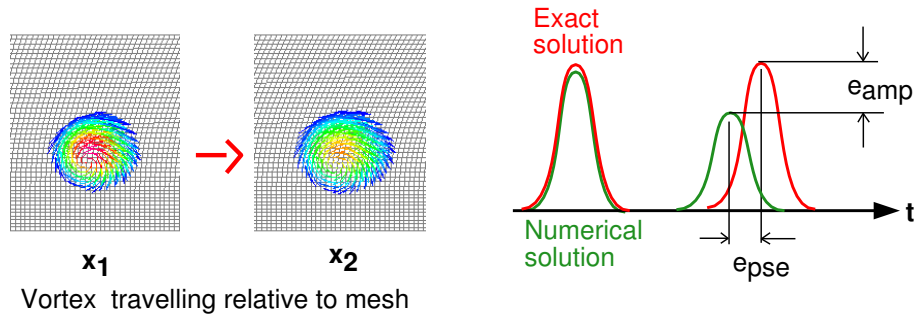


Figure 13.23: Phase and amplitude errors

express:

- The convection of entropy with speed u
- The convection of vorticity with speed u
- The convection of acoustic perturbations with speeds $u + a$ and $u - a$

where u is the local flow speed, and a is the local speed of sound. By analogy, solutions for the linear convection equation:

$$\frac{\partial u}{\partial t} + c \frac{\partial u}{\partial x} = 0 \quad (13.47)$$

are often used to analyse and compare the performance of different numerical methods for the Euler and Navier-Stokes equations.

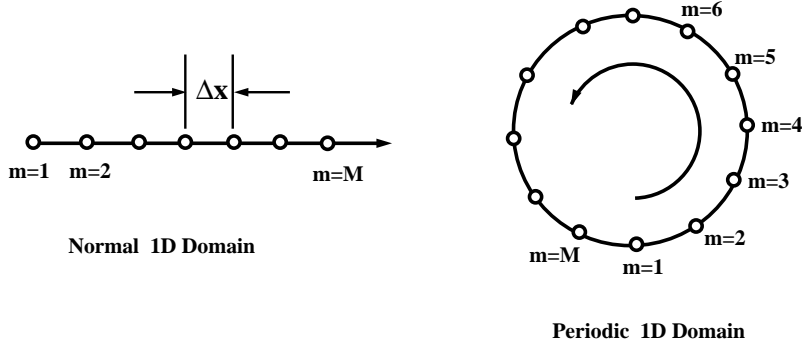


Figure 13.24: Normal and periodic 1D domains

If we consider a 1D periodic domain (figure 13.24), application of a discretisation method to the linear convection equation will lead to a system of the form:

$$\vec{u}^{n+1} = [C]\vec{u}^n \quad (13.48)$$

where \vec{u}^n is the vector containing the unknown values of u at each node or volume. This system can be diagonalised using the similarity transform:

$$\vec{w}^{n+1} \equiv [X]^{-1}\vec{u}^{n+1} \quad (13.49)$$

$$= [X]^{-1}[C][X][X]^{-1}\vec{u}^n \quad (13.50)$$

$$= [\sigma]\vec{w}^n \quad (13.51)$$

where $[X]$ is the matrix of eigenvectors of $[C]$, and $[\sigma]$ is the diagonal matrix of eigenvalues of $[C]$. For a periodic domain, $[C]$ is circulant, and will always have the same eigenvectors, independent of the discretisation method used:

$$X_{jm} = e^{i(2\pi(j-1)(m-1)/M)}; \quad j = 1..M; \quad m = 1..M; \quad (13.52)$$

where j is the number of the eigenvector, m is the node index and M is the total number of nodes.

The eigenvectors of the matrix $[C]$ are a collection of sine waves of different spatial frequencies, with the lowest being a constant, and the highest being a signal which changes sign from node to node (figure 13.25). In the exact solution to the linear convection equation, each of these waves should be convected with constant amplitude with a speed c . This leads to the following definitions of phase and amplitude errors incurred per time step for each wave:

$$e_{amp} = 1 - |\sigma_j| \quad (13.53)$$

$$e_{pse} = \beta_j \frac{c\Delta t}{\Delta x} - \arg(\sigma_j) \quad (13.54)$$

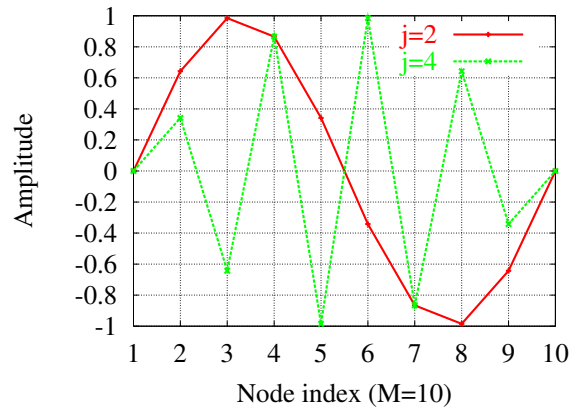


Figure 13.25: Eigenvectors for a 10 node mesh

Where in this case, $\beta_j = 2\pi(j-1)/M$ is the frequency of the eigenvector (wave) associated with the eigenvalue σ_j . For the linear convection equation, the phase and amplitude errors produced by a numerical method are a function of both the wave frequency and the Courant number $= c\Delta t/\Delta x$, where Δt is the time step and Δx is the spacing between nodes. In figures 13.26 to 13.28, phase and amplitude errors for three different numerical methods are given, along with numerical solutions for the convection of a block wave. In the first case, the combination of a second-order accurate finite-difference method with first-order accurate implicit time integration produces a method which is high in phase error at high frequencies (beta) but also has very little damping at high frequencies. The result is a sawtooth effect due to the incorrect speeds of the high-frequency portions of the solution. In the second case, a second-order accurate explicit time integration method is used, with coefficients designed to produced better high-frequency damping, resulting in an improved solution. Finally, results from a third-order accurate space-time method are shown, to which high-frequency damping has been added. The remaining oscillations near the discontinuous part of the solution can be further controlled using operators tuned for shock capturing.

The above observations will also apply to more general flow features convected by similar schemes for the Euler and Navier-Stokes equations. If you think of a flow feature (such as a vortex) as being made up from waves of different frequencies, you can anticipate that its high-frequency components will normally exhibit large phase errors. For a well-designed scheme, these components will also be strongly damped. A side effect will be the smoothing out of the flow feature as it is convected. Marching with higher Courant numbers will tend to produce greater errors. It can also be seen that higher-order schemes can be really worthwhile, provided that their cost is not excessive.

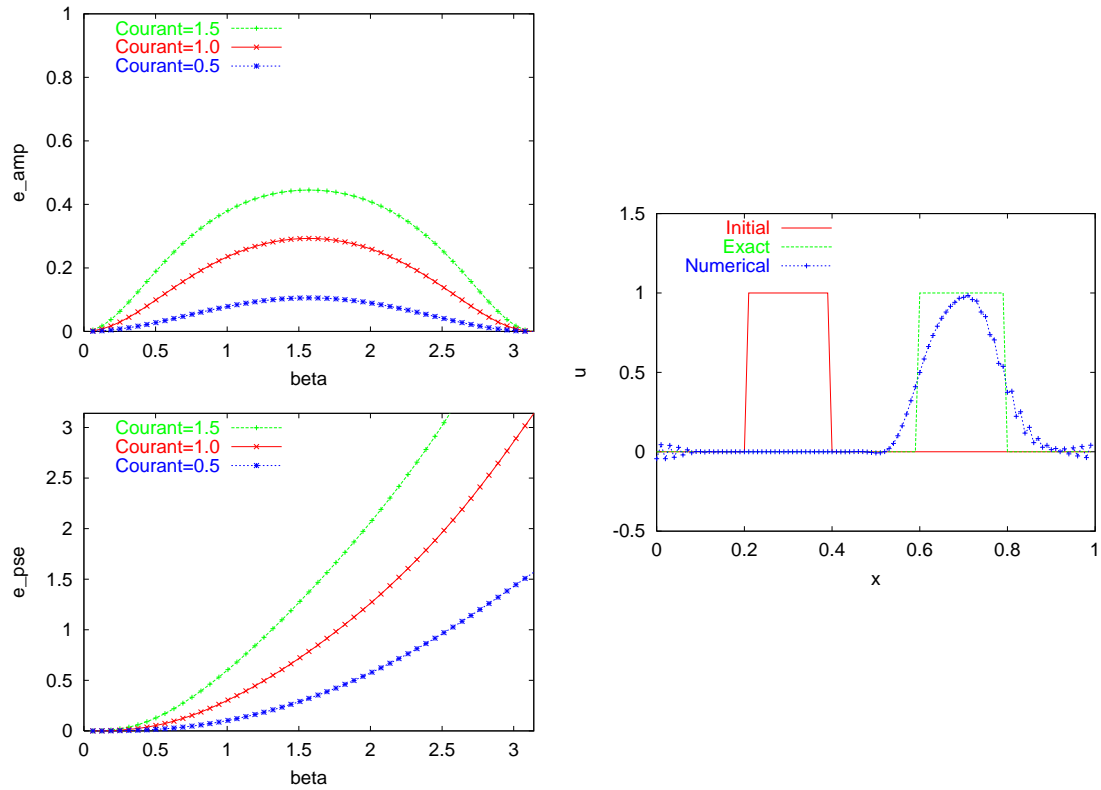


Figure 13.26: Second-order accurate centred finite difference method with first-order accurate implicit time integration: 100 nodes, 80 time steps.

13.11.1 Adjoint-based error estimation

Over the last few years methods for formally estimating the magnitude of local error contributions to quantities of interest, such as lift and moment, have developed rapidly. These involve the solution of dual or adjoint problems which express the sensitivity of the error in the desired quantity to local values of the residual. There is great potential for such methods in the field of aeroelasticity, but there exist two basic complicating issues. The first of these is that the dual problem evolves in the reverse time direction, making its simultaneous computation with the main (primal) problem a bit awkward. The second more serious problem arises from the moving interface between the flow and the structure, which poses serious difficulties for the implementation of the dual problem. The reader is referred to the recent TU Delft thesis of Kris van der Zee for more information and successful strategies.

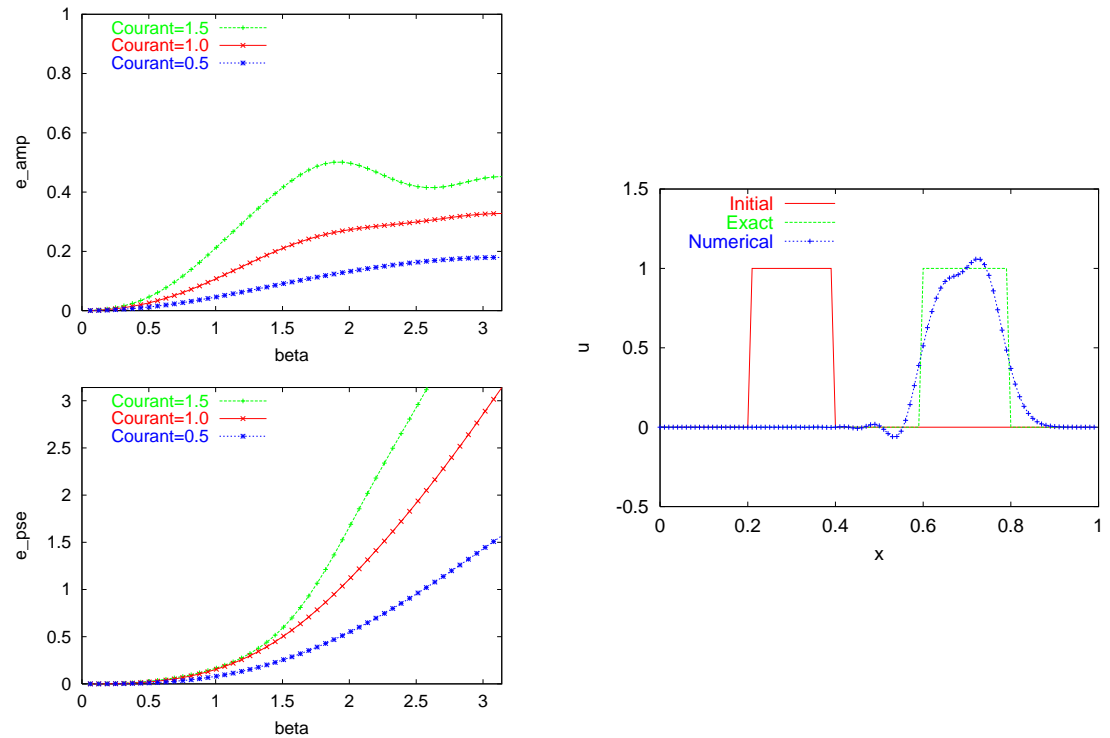


Figure 13.27: Second-order accurate centred finite difference method with explicit second-order accurate Runge-Kutta time integration, 100 nodes, 80 time steps (additional dissipation added for high frequencies).

13.12 Example Unsteady Flow Solutions

In this section we present some example numerical solutions for the transonic flow around the NLR F-5 wing shown in figure 13.29. In the experiment, the wing was subjected to sinusoidal pitching about an axis at 50% of the root chord in a transonic flow. Both experimental and computed results can be found in RTO-TR-26 (October 2000). On initial inspection the TSD (small-disturbance potential) results seem to be superior, but this cannot be true from the theoretical point of view. A possible source of the discrepancy is the relative coarseness of the Euler meshes used. In order to fully compute the effects of convecting vorticity in the unsteady case, a fine mesh in the wake areas is required. Also, since none of the inviscid methods take shock boundary-layer interactions into account, it could also be that the errors present in the TSD model fortuitously cancel errors incurred by neglecting viscosity. This seems to be borne out by the steady results for Euler with boundary layer correction. In summary, one must keep aware of all types of error when interpreting results,

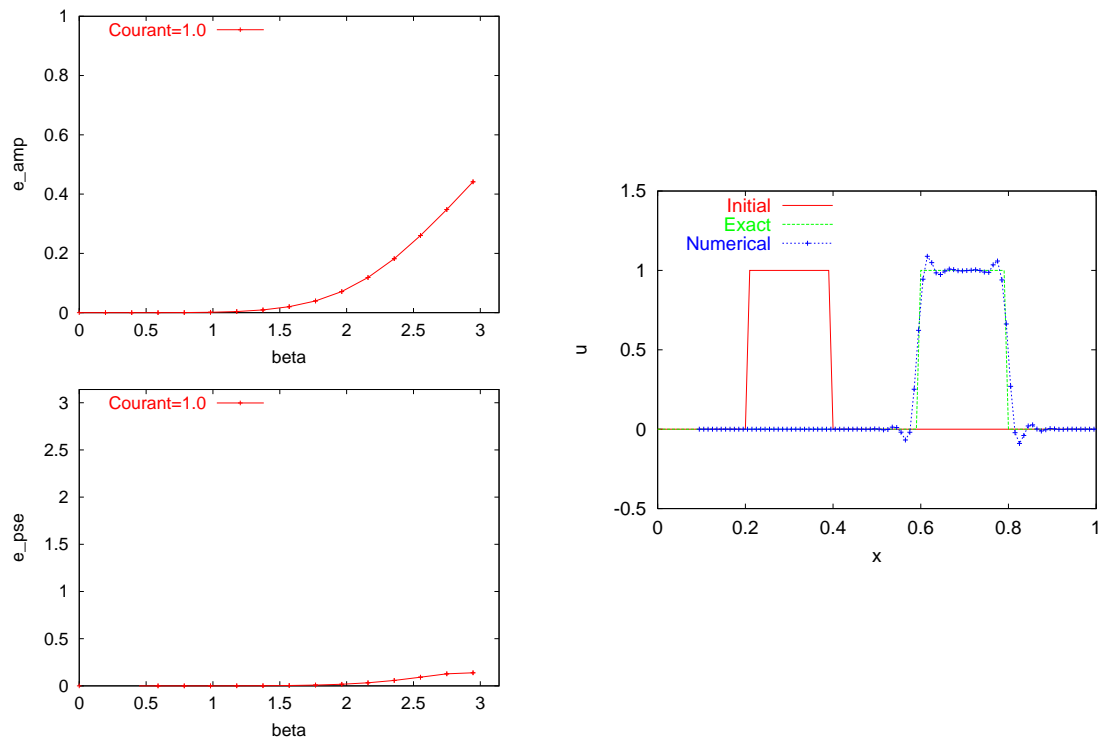


Figure 13.28: Third-order accurate (implicit) space-time discretisation, 50 elements, 2 nodes per element, 80 time steps (additional dissipation added for high frequencies).

including both discretisation and modelling errors.

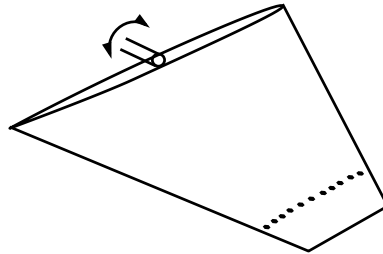
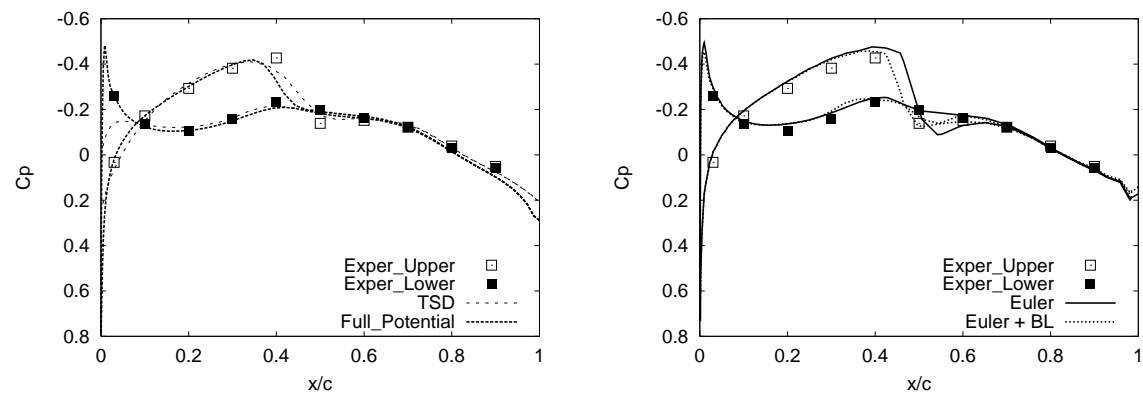


Figure 13.29: NLR F-5 wing


Figure 13.30: Steady Flow $M = 0.896$, $\alpha = 0.5^\circ$, $Re = 5.79 \times 10^6$

TSD:	UTSPV21 (BAe)	96 000 nodes
Full Potential:	TCITRON (Dassault)	85 470 nodes
Euler:	EUGINE (Dassault)	294 851 cells

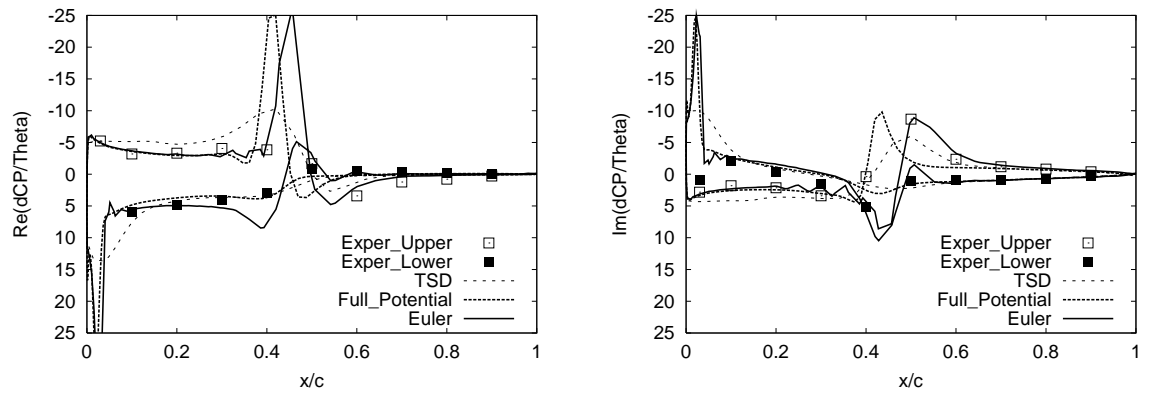
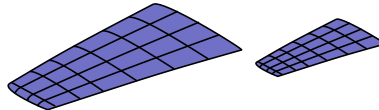


Figure 13.31: Unsteady Flow $M = 0.896$, $\alpha_o = 0.001^\circ$, $\theta = 0.111^\circ$, $k = 0.275$
 Real (left) and imaginary (right) perturbation components

13.13 Practice Problems

p13.13.28 Compare the application of a kernel function method with a panel method for the computation of responses of the wing-tail configuration shown below. What are their advantages and disadvantages?



p13.13.29 Given two solutions u_h and u_{2h} , estimate the error of u_h if both solutions were computed using a first-order accurate method.

p13.13.30 Describe the treatment of moving meshes in the example finite-difference and finite-volume techniques presented in the notes.

p13.13.31 Is amplification error more important than phase error in the prediction of flutter? Discuss in the context of a coarse-mesh Euler discretisation to investigate tail flutter in the wing-tail configuration above.

Chapter 14

Computing Fluid-Structure interactions

As discussed in chapter 11, the repeated application of complete complex aeroelastic simulations is limited in practice due to computational cost. Therefore, most preliminary fully-coupled studies make use of reduced-order models for both the aerodynamic flow and structural response.

As we have already discussed how low-order approximations to structural behaviour can be accomplished, we will start this chapter by describing how compatible low-order aerodynamic approximations can be generated from complex CFD simulations, and used with their structural counterparts to perform aeroelastic simulations.

We will then consider optional methods for coupling fully discretised fluid and structural systems. This is an interesting topic, as standard partitioned approaches to coupling can lead to considerable errors in quantities of interest for aeroelasticity. We will examine a technique for estimating these errors, and then compare the efficiency of partitioned integration methods to that of their strongly-coupled monolithic counterparts.

14.1 Generalised force models from CFD computations

The equations of motion of a discrete fluid-structure system can typically be expressed:

$$[M]\{\ddot{q}\} + [D]\{\dot{q}\} + [K]\{q\} = \{Q(t)\} \quad (14.1)$$

If we choose the generalised coordinates, q , to be the amplitudes of the m most dominant (natural) structural modes, we can construct an efficient reduced-order representation of the fluid-structure system. In this case, the displacement

of the structure, u , can be expressed in terms of the dominant structural mode shapes ϕ , as:

$$u = \sum_{i=1}^m \phi_i q_i \quad (14.2)$$

Examples of the dominant natural mode shapes for a finite wing are shown in figure 14.1.

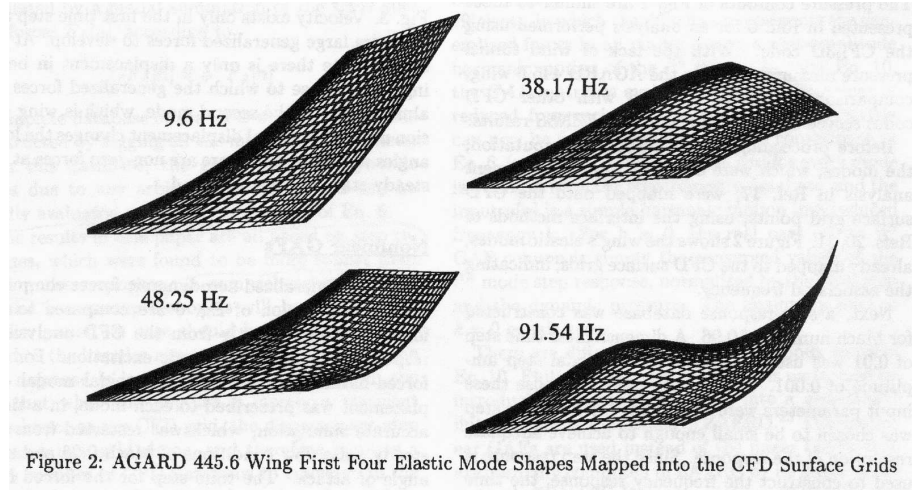


Figure 14.1: Examples of the first four mode shapes ($\phi_i, i = 1..4$) for a wing. (Taken from Raveh, Levy, and Karpel, AIAA paper 00-1325)

Simplified CFD methods are sometimes designed to produce solutions to harmonic excitations. For such methods, generalised forces $Q(t)$ may be constructed using inverse Fourier transforms, as described in previous chapters. More sophisticated CFD methods usually produce time-domain results. For these methods, the computation of harmonic responses is often too time consuming. Several periods of excitation are required to establish a harmonic result, and several computations are required to obtain results over the frequency range required for an inverse transform. Impulse and step responses, in contrast, provide information for a wide range of frequencies within one calculation. Impulse responses require only short time intervals to be computed, but are difficult to realise accurately using a fully discrete representation of the flow. Step responses, on the other hand, are only slightly longer to compute and are far easier to realise computationally. If only a limited frequency content is required, it is also possible to use a smoothed step input.

One of the motivations for performing a complex CFD simulation is to represent non-linear phenomena in the fluid. Depending on the unsteady behaviour of these phenomena, it may also be necessary to represent the unsteady force

response non-linearly. A general approach is to then use a sequence of impulse-response problems to construct a Volterra series:

$$\begin{aligned}
 F(t) = h_0 &+ \int_0^\infty h_1(t-\tau)u(\tau)d\tau \\
 &+ \int_0^\infty \int_0^\infty h_2(t-\tau_1, t-\tau_2)u(\tau_1)u(\tau_2)d\tau_1d\tau_2 \\
 &+ \int_0^\infty \int_0^\infty \int_0^\infty h_3(t-\tau_1, t-\tau_2, t-\tau_3)\dots \\
 &+ \dots
 \end{aligned} \tag{14.3}$$

If sufficient terms are retained, this expression is capable of representing highly non-linear phenomena. Experience has shown, however, that the third and higher-order terms (h_3, h_4, \dots) tend to be negligible for most aerodynamic flows. In fact, it is often sufficient to retain only h_0 and h_1 , even when considering responses of non-linear phenomena such as shock waves, provided the displacements from the steady non-linear condition are reasonably small.

If it is justified to retain only h_0 and h_1 , generalised forces can be quickly constructed using a limited number of impulse or step response computations. For example, the generalised force response to a step excitation with shape $\epsilon\phi_i$ may be expressed as an integral over the surface of the geometry S as:

$$Q_{is}(t) = \frac{1}{\epsilon} \int_S \epsilon\phi_i \cdot G(t) dS \tag{14.4}$$

where $G(t)$ is the computed response of the surface fluid forces due to a step change in the structure geometry of shape ϕ_i and magnitude ϵ . An arbitrary response can then be computed using discrete convolutions for the generalised forces:

$$Q_i(t) = Q_i(0) + \sum_{n=1}^{N=t/\Delta t} Q_{is}(t) \dot{q}_i(t) \Delta t \quad i = 1, 2, \dots \tag{14.5}$$

If it is not sufficient to retain only h_0 and h_1 , then more general expressions for $Q_i(t)$ must be constructed which include terms with multiple mode displacements.

An alternative to the convolution approach is make a reduced-order model of the aerodynamic operator. This can be done by computing the eigensystem of the discrete CFD matrix which expresses the change in the fluid state over a time step. The eigenvectors with largest magnitude are then used to make a simplified model of the fluid response (see, for example Dowell, AIAA Journal Vol 34, No 6, 1996). Although powerful in concept, this approach must be used with care, as due to the multi-scale nature of fluid phenomena, mode truncations can significantly reduce the range of behaviours which can be predicted.

14.2 Coupling of fully-discretised fluids and structures

We now consider the coupled integration of a fully discretised fluid and structural system. For non-linear fluid models, a mesh which fills the volume of the fluid domain is normally required. If the boundary conditions are have not been linearised, then the mesh must also move in response to the deflection of structural components which border the fluid domain. As the movement of the mesh must be determined during the solution procedure, the total problem is often said to be a three-field problem (figure 14.2). The most common approach

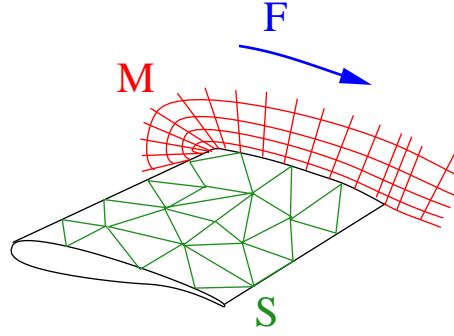


Figure 14.2: Coupled integration as a three-field problem

to treating mesh movement is to use a structural analogy, that is to compute the deflection of the fluid mesh nodes as if they were following the displacement of a fictitious solid which fills the deforming fluid domain. The final system of equations for the three-field problem can then be written:

1. Structural field:
$$M \frac{\partial^2 q}{\partial t^2} + D \frac{\partial q}{\partial t} + K q = F \quad (14.6)$$

2. Fluid field:
$$\frac{d}{dt} \int_V W \, dV + \int_S (\vec{F} - \vec{x}W) \cdot \vec{n} \, dS = 0 \quad (14.7)$$

3. Fluid Mesh field:
$$\tilde{M} \frac{\partial^2 x}{\partial t^2} + \tilde{D} \frac{\partial x}{\partial t} + \tilde{K} x = K_c q \quad (14.8)$$

Where q are the unknowns associated with structural deflections, W are the unknowns associated with the fluid state, and x are the unknowns associated with the fluid mesh position. A visualisation of how the fields are coupled appears

in figure 14.3. Note that the choice of \tilde{M} , \tilde{K} , and \tilde{D} , are in principal arbitrary,

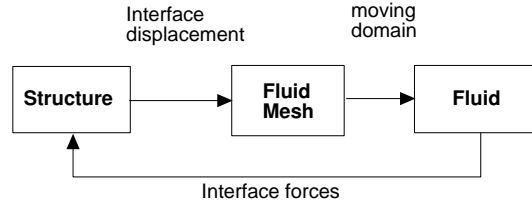


Figure 14.3: Coupling in the three-field representation

as they only affect the dynamics of the fluid-structure system indirectly by determining the quality of the mesh on which the fluid solution is computed. One can choose \tilde{M} and \tilde{D} to be zero, for example, to avoid introducing complex unsteady motion of the mesh. \tilde{K} is normally constructed so that fluid elements in critical regions are stiffer, which prevents them from becoming overly distorted in response to boundary deformations.

Assuming that the mesh responds instantaneously to the structural deformation, we can make the following classification of time integration techniques for the remaining fluid-structure system:

Partitioned

A partitioned method advances the solution in time using one (fully-converged) fluid solution and one (fully-converged) structure solution per time step. Such methods are asynchronous in nature (first fluid, then structure or first structure, then fluid). Extrapolation of previous results is sometimes used to reduced the errors incurred by asynchronicity.

Monolithic

A monolithic method either fully or partially converges the complete fluid-structure interaction system at the end of each time step by using multiple fluid and structure solutions. Depending on the level of convergence, errors incurred by asynchronicity are eliminated.

Mixed

Mixed methods use monolithic techniques on low-order representations of the system (e.g. coarse meshes) and partitioned techniques on higher-order representations (e.g fine meshes). These have low but significant errors incurred by asynchronicity.

14.3 Partitioned Time Integration Techniques

In a partitioned time integration technique, the structure and fluid are each advanced separately in a fixed sequence within the time step. The advantages

of this commonly-used approach are that it is straight-forward to implement, and can be done with completely separate fluid and structural solvers. Its disadvantage is that its inherent asynchronicity introduces new sources of error which can significantly limit the maximum allowable time step for the fluid-structure system. Partitioned solution techniques may be divided into volume-continuous and volume-discontinuous methods, as described below.

14.3.1 Volume-continuous methods

Volume continuous methods are those which maintain a synchronous representation of the position of the structural boundary in the fluid and structure, but as a consequence have an asynchronous representation the forces acting at the boundary. Such a method is visualised in figure 14.4, which shows the sequence of information transfer in a single discrete time step from time t^n to time t^{n+1} . Denoting P^n as the fluid pressure and viscous forces at time level n , and X^n as the structural interface displacement at time level n , the sequence is:

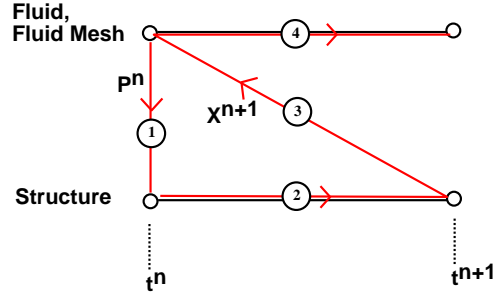


Figure 14.4: Volume-continuous method

1. Transfer P^n to the structure
2. Advance the structure from t^n to t^{n+1}
3. Transfer the new structure location, X^{n+1} , to the fluid mesh
4. Redistribute the fluid mesh and advance the fluid from t^n to t^{n+1}

As a consequence, the fluid mesh interface matches structural mesh interface at each time t_n , but the fluid interface forces do not match those of the structural interface forces at t_n .

14.3.2 Volume-discontinuous methods

In a volume-discontinuous method, the synchronicity of the forces that is maintained in favour of that of the displacements. The sequence, as shown in figure 14.5, is then:

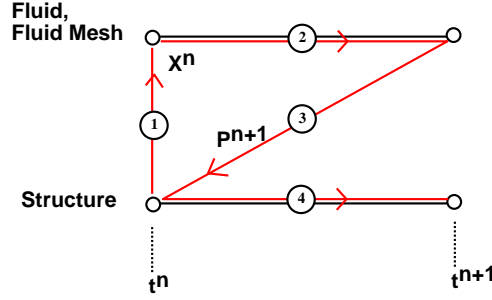


Figure 14.5: Volume-discontinuous method

1. Transfer X^n to the fluid mesh
2. Redistribute the fluid mesh and advance the fluid from t^n to t^{n+1}
3. Transfer P^{n+1} to the from the fluid to the structure
4. Advance the structure from t^n to t^{n+1}

In this case, the forces in the fluid match those applied to the structure at each time t_n , while the displacements of boundary do not match at t_n . In practice the latter mismatch is not not necessarily as disturbing as it sounds, as the fluid and structure interface meshes often differ in interface refinement, and thus already do not match in the steady case.

14.3.3 Analysis of errors due to partitioning

As described above, partitioned schemes cannot simultaneously match both the displacements and forces across the fluid-structure interface. This leads to errors in the transfer of energy between fluid and structure. Assuming the partitioned scheme is consistent, these errors can be reduced by decreasing the time step. For many problems, however, including aeroelastic instability problems, the energy balance is crucial. For such cases, certain partitioned schemes can require very small time steps in order to achieve an acceptable level of accuracy.

In this section we describe a method to estimate the errors introduced partitioning, using the simple one-dimensional piston problem shown in figure 14.6. This can be used to design partitioned methods with relatively low errors in energy conservation. The procedure is described in detail in Piperno and Farhat, *Comput. Meths. Appl. Mech. Engrg.*, vol. 190, No. 24, pp. 3147-3170, (2001). It can be summarised as:

1. Find the change in energy of the fluid, ΔE_F , and the change in energy of the structure ΔE_S , during one time step

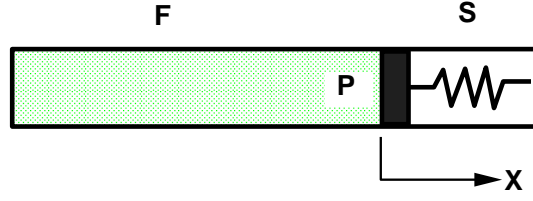


Figure 14.6: A one-dimensional piston problem

2. Estimate the the changes in energy over one period of the oscillation, $(\Delta E_F)_T$ and $(\Delta E_S)_T$, using a continuous approximation for the $n = T/\Delta t$ discrete contributions
3. Determine how accurately the energy balance $(\Delta E_F)_T + (\Delta E_S)_T = 0$ is satisfied by the partitioned scheme under consideration

For simple time-marching techniques, we may express the transfer of energy to the fluid during a single time step Δt as:

$$\Delta E_F = - \int_{t^n}^{t^{n+1}} \dot{X}_F A P_F dt = -(X_F^{n+1} - X_F^n) A \bar{P}_F \quad (14.9)$$

where :

$$A = \text{Surface area of the piston} \quad (14.10)$$

$$\bar{P}_F = P^n \text{ (Euler explicit)} \quad (14.11)$$

$$\bar{P}_F = P^{n+1} \text{ (Euler implicit)} \quad (14.12)$$

$$\bar{P}_F = \frac{(P^{n+1} + P^n)}{2} \text{ (trapezoidal)} \quad (14.13)$$

Similarly, for the structure:

$$\Delta E_S = +(X_S^{n+1} - X_S^n) A \bar{P}_S \quad (14.14)$$

If we consider a harmonic solution such as:

$$X_S(t) = X \cos(\omega t) \quad (14.15)$$

$$P_F(t) = P \cos(\omega t + \phi) \quad (14.16)$$

the energy change over a period can be expressed as the piecewise integration of $\frac{\Delta E}{\Delta t}$ (figure 14.7). As $\frac{\Delta E}{\Delta t}$ represents an average value, This can be related to the integration of a continuous function via the midpoint rule (figure 14.8). We can therefore use the approximate identity:

$$(\Delta E)_T \approx \int_0^{\frac{2\pi}{\omega}} \frac{\Delta E}{\Delta t} dt \quad (14.17)$$

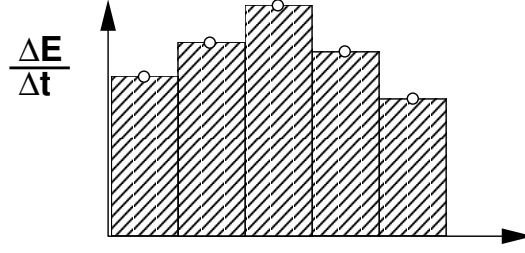


Figure 14.7: Energy change over a period of oscillation

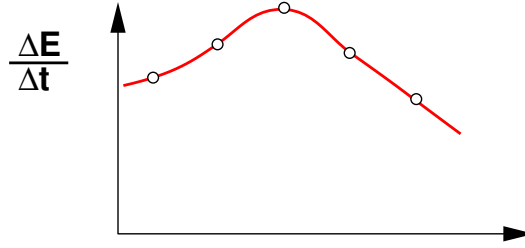


Figure 14.8: Approximation of the discrete integral using a continuous function

in step 2 of the procedure.

Example Problem

Compute the energy-conservation accuracy of a coupled numerical solution procedure for the 1D model piston problem shown in figure 14.6. Consider the case of a volume-discontinuous partitioned solution technique, combined with trapezoidal time integration of both the fluid and the structure.

Solution

We will assume that the piston is oscillating harmonically, so that the discrete solution can be described by:

$$X_S(t^n) = X \cos(\omega t^n) \quad (14.18)$$

$$P_F(t^n) = P \cos(\omega t^n + \phi) \quad (14.19)$$

Step 1: For trapezoidal time integration, the change in the energy of the fluid during one time step may be expressed:

$$\Delta E_F = -(X_F^{n+1} - X_F^n) A \frac{(P_F^{n+1} + P_F^n)}{2} \quad (14.20)$$

Similarly, for trapezoidal integration of the structure:

$$\Delta E_S = (X_S^{n+1} - X_S^n) A \frac{(P_S^{n+1} + P_S^n)}{2} \quad (14.21)$$

where X is the structural displacement, P is the fluid pressure, and A is the surface area of the piston.

In order to express the changes energy in terms of the assumed solution's parameters, we need to consider the differences in the representation of X and P for the fluid and the structure when a partitioned solution technique is used. For a volume-discontinuous technique, the pressure is synchronous, so that:

$$P_S^n = P_F^n = P \cos(\omega t^n + \phi) \quad (14.22)$$

$$P_S^{n+1} = P_F^{n+1} = P \cos(\omega t^n + h + \phi) \quad (14.23)$$

where $h = \omega \Delta t$. The structural displacement is asynchronous, however, so that:

$$X_F^{n+1} = X_S^n = X \cos(\omega t^n) \quad (14.24)$$

$$X_F^n = X_S^{n-1} = X \cos(\omega t^n - h) \quad (14.25)$$

Thus, the change in energy of the fluid and structure during a single time step is:

$$\Delta E_F = -\frac{PAX}{2} [\cos(\omega t^n) - \cos(\omega t^n - h)] [\cos(\omega t^n + h + \phi) + \cos(\omega t^n + \phi)] \quad (14.26)$$

$$\Delta E_S = \frac{PAX}{2} [\cos(\omega t^n + h) - \cos(\omega t^n)] [\cos(\omega t^n + h + \phi) + \cos(\omega t^n + \phi)] \quad (14.27)$$

Step 2: To compute the change in energy over one period of oscillation, we use the approximate identity:

$$(\Delta E)_T \approx \int_0^{\frac{2\pi}{\omega}} \frac{\Delta E}{\Delta t} dt \quad (14.28)$$

For convenience, we define $k = PAX \cos(\phi)$, $d = PAX \sin(\phi)$. Then using the trigonometric formulae from the appendix, the expression for the change in energy in the fluid can simplified and integrated to yield:

$$(\Delta E_F)_T \approx -\frac{k\pi}{2h} [2\sin^2(h)] - \frac{d\pi}{2h} [2\cos(h)\sin(h)] \quad (14.29)$$

Using the trigonometric series expansions, this is approximately:

$$(\Delta E_F)_T \approx k\pi \left[-h + \frac{h^3}{3} \right] + d\pi \left[-1 + \frac{2h^2}{3} \right] \quad (14.30)$$

Employing a similar procedure, we can also express the approximate change in energy over a period for the structure as:

$$(\Delta E_S)_T \approx \frac{d\pi}{2h} [2\sin(h)] \approx d\pi \left[1 - \frac{h^2}{6} \right] \quad (14.31)$$

Step 3: The energy balance over one period of oscillation is given by:

$$(\Delta E_F)_T + (\Delta E_S)_T = k\pi \left[-h + \frac{h^3}{3} \right] + d\pi \left[\frac{h^2}{2} \right] \quad (14.32)$$

The energy conservation accuracy is thus $O(h) = O(\Delta t)$.

Note that although we have used (rather expensive) $O(\Delta t^2)$ accurate trapezoidal integration for both the fluid and the structure, the use of a partitioned solution technique has reduced the time accuracy to $O(\Delta t)$. For lower frequencies, the displacement is out of phase with the change in pressure (pressure is low for large X). Thus $\phi \approx \pi$ and the change in energy of the complete system is positive (note $h > h^2 > h^3$). As a result, this partitioned technique is formally unstable for this undamped problem, and as a consequence the amplitude of the oscillation will grow slowly in time. In the context of aeroelastic instabilities, this means that the flutter speed of a more complex configuration might be underpredicted by such a method.

14.3.4 Improved accuracy by extrapolation

If we are using a volume-discontinuous partitioned method, we can reduce the discrepancy in the interface position as perceived by the fluid and structure using an extrapolation procedure for X^{n+1} , such as:

$$X^{n+1} = X^n + \alpha_1 \dot{X}^n + \alpha_2 \ddot{X}^{n-1} \quad (14.33)$$

This value is then transferred to the fluid in the first part of the partitioned sequence. Using the analysis presented in the previous section, α_1 and α_2 can be chosen in a way which improves the energy-conservation accuracy to $O(\Delta t)^3$. In practice, this can increase the allowable time step by a factor of 10-100.

A similar idea can also be applied to volume-continuous partitioned methods, by transferring an extrapolated estimate for P^{n+1} to the structure in the first step of the sequence. When using extrapolation for the forces, however, some care must be taken near moving discontinuities in the flow.

14.4 Monolithic Time Integration Techniques

In monolithic time integration, the fluid and structure are advanced simultaneously within the time step. In theory, this would lead to a final system of the form:

$$\begin{bmatrix} [FF] & [FM] & [0] \\ [0] & [MM] & [MS] \\ [SF] & [0] & [SS] \end{bmatrix} \begin{Bmatrix} \Delta W \\ \Delta x \\ \Delta q \end{Bmatrix} = \begin{Bmatrix} RHS \end{Bmatrix} \quad (14.34)$$

Where FF , MS , etc denote sub-matrices coupling the fluid, fluid mesh, and structural fields. The complete system is not normally solved simultaneously, however, due to the requirement of having a single program describe both the fluid and the structure, and due to the global stiffness introduced by the very different natures of each sub-matrix. The development of optimal decomposition and preconditioning procedures for the complete matrix remains an interesting research topic, however.

Thus to avoid the issues mentioned above, monolithic methods are usually implemented as an iteration loop involving sequential fluid and structure solution steps performed until the system reaches a specified level of convergence. Since the fluid problem is normally solved by a subiteration procedure within each time step, the communication with the structure can be included in each fluid subiteration with little extra cost.

The prime advantage of monolithic methods is that energy conservation errors at the fluid structure interface can be kept arbitrarily small, or eliminated. Like partitioned methods, it is possible to use extrapolation at the interface to speed the rate of the converge, but this does not influence the final energy conservation property. In principle, energy conservation errors can be controlled even if the accuracy of the solution representation is very different on the fluid and structure sides of the interface (see for example, Van Brummelen, E.H. et al.: Energy Conservation Under Incompatibility for Fluid Structure Interaction Problems, Computer Methods in Applied Mechanics and Engineering, Volume 192, Number 25, 20 June 2003, pp. 2727-2748(22)).

14.5 Efficiency of Monolithic and Partitioned Techniques

To put the application of partitioned and monolithic methods in context, in this section we compare the performance of a volume-discontinuous partitioned with structural extrapolation to that of an energy conservative monolithic method. We consider the case of an oscillating 1 DOF piston connected to a cylinder filled with a gas simulated using the Euler equations. It should be noted that the partitioned method requires only one fluid-structure solution per time step, while the (iterative) monolithic method uses several. Both methods use second-order accurate discretisations for both the fluid and the structure.

The error in the piston's displacement is shown as a function of time step in figure 14.9. An additional non-conservative monolithic method is also shown for comparison. As extrapolation is used in the partitioned case, each of the methods achieves their full second-order accuracy of convergence. The conservative monolithic method is several orders of magnitude more accurate on the same mesh. It is clear that it is the energy-conservation property that is contributing to this result.

An alternate comparison is shown in figure 14.10, which plots the error in the piston displacement versus the total number of fluid and structure solutions

performed to compute one period of oscillation. In this case we (conservatively) assume that the monolithic method's fluid solutions are fully converged before each fluid-structure communication. As a single period of oscillation is considered, the time step of the methods is changing with the number of fluid-structure solutions. It is clear that if higher levels of accuracy are desired, then the monolithic method is considerably more efficient.

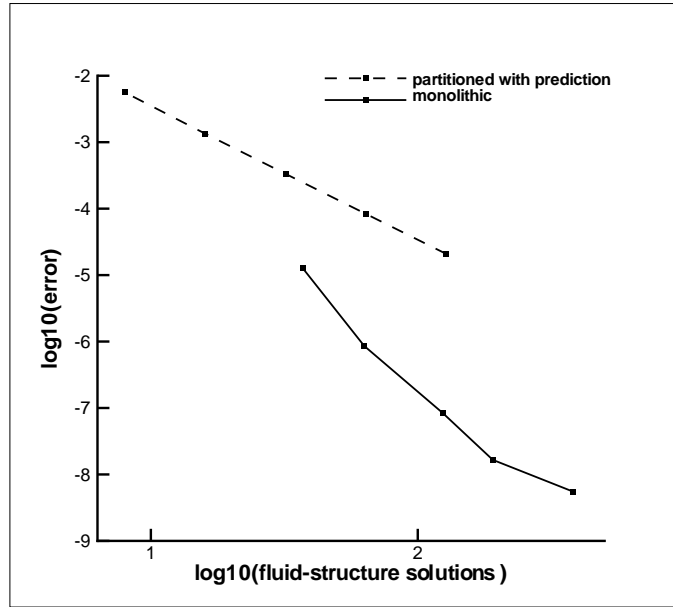


Figure 14.9: Error produced by different coupling methods as a function of time step (plot from C Michler, T.U Delft - LR)

Although illustrative, this problem only considers a single mode of oscillation. If a partitioned method is used in a problem with multiple modal frequencies, it may also be necessary to march at a time step small enough to keep their highest-frequency mode from growing excessively. This can be a severe restriction if only low-frequency accuracy is desired.

Finally, the errors committed due to fluid-structure coupling must be seen in the context of errors introduced by other parts of the discretisation. A summary of the various sources of error in a typical fluid-structure interaction computation is shown in figure 14.11.

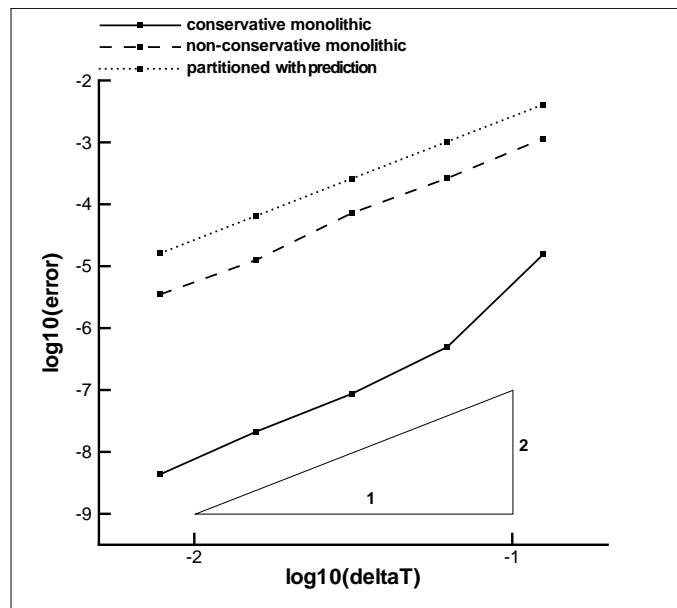


Figure 14.10: Error produced during a period of oscillation vs number of fluid and structure solutions used (plot from C Michler, T.U Delft - LR)

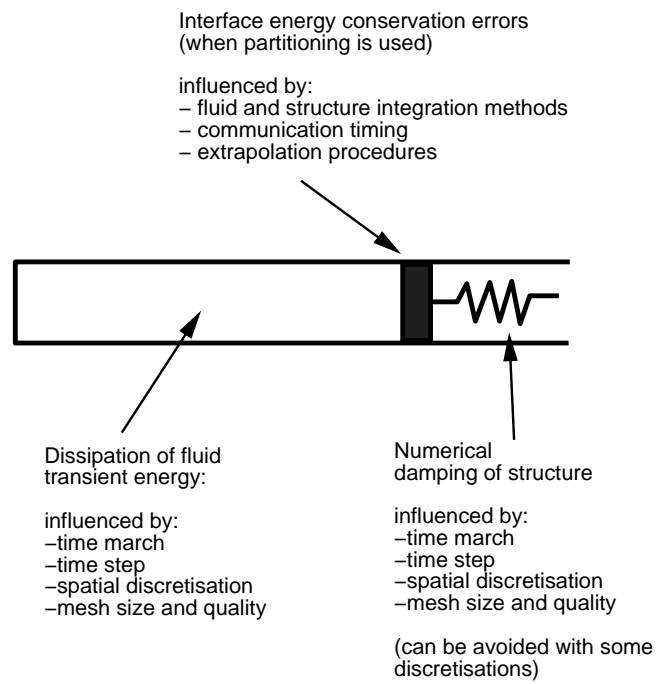


Figure 14.11: Sources of error in the energy balance

14.6 Practice Problems

p14.6.32 Compute the order of accuracy of energy conservation for a volume-discontinuous partitioned integration scheme with a first-order implicit time march for the fluid, and a trapezoidal implicit integration of the structure.

14.7 Handy Formulae

Angle formulae

$$\begin{aligned}\cos(\alpha \pm \beta) &= \cos(\alpha)\cos(\beta) \mp \sin(\alpha)\sin(\beta) \\ \sin(\alpha \pm \beta) &= \sin(\alpha)\cos(\beta) \pm \cos(\alpha)\sin(\beta)\end{aligned}$$

Integrals of sine and cosine products

$$\begin{aligned}\int_0^{\frac{2\pi}{\omega}} \cos^2(\omega t) dt &= \frac{\pi}{\omega} \\ \int_0^{\frac{2\pi}{\omega}} \sin^2(\omega t) dt &= \frac{\pi}{\omega} \\ \int_0^{\frac{2\pi}{\omega}} \cos(\omega t) \sin(\omega t) dt &= 0\end{aligned}$$

Series expansions

$$\begin{aligned}\cos^2(h) &\approx 1 - h^2 + \frac{h^4}{3} \\ \cos(h) &\approx 1 - \frac{h^2}{2} + \frac{h^4}{24} \\ \sin(h) &\approx h - \frac{h^3}{6} + \frac{h^5}{120} \\ \sin^2(h) &\approx h^2 - \frac{h^4}{3} \\ \cos(h)\sin(h) &\approx h - 2\frac{h^3}{3}\end{aligned}$$

(During an exam, all of these formulae will be made available when necessary for completing a question)

Chapter 15

Aeroelasticity in Aircraft Design

15.1 Requirements

There are a large number of design requirements associated with aeroelastic phenomena. The basic bounds for these requirements are set by certification standards. For large aircraft, these can be found in section 25 of the air regulation documents of the relevant country or region (e.g. EASA CS-25, FAR-25, CAR-525 etc). Aeroelasticity is mentioned most explicitly in section 629. Some of the CS-25 aeroelasticity-related standards include:

- The aeroplane must be designed to be free from flutter and divergence for all combinations of altitude and speed encompassed by the VD/MD versus altitude envelope enlarged at all points by an increase of 15% in equivalent airspeed at both constant Mach number and constant altitude, except that the envelope may be limited to a maximum Mach number of 1.0.
- When $MD < 1.0$, A proper margin of damping exists at all speeds up to MD, and there is no large and rapid reduction in damping as MD is approached.
- If concentrated balance weights are used on control surfaces, their effectiveness and strength, including supporting structure, must be substantiated.
- The aeroplane must be designed to be free from control reversal and from undue loss of longitudinal, lateral, and directional stability and control within the previously described VD/MD envelope.
- The aeroplane must be free of flutter or divergence that would preclude safe flight, at any speed up to VD after:

- Failure of any single element of the structure supporting any engine, independently mounted propeller shaft, large auxiliary power unit, or large externally mounted aerodynamic body.
- Absence of propeller aerodynamic forces resulting from the feathering of any single propeller, and, for aeroplanes with four or more engines, the feathering of the critical combination of two propellers.
- Any single propeller rotating at the highest likely overspeed.
- Failure of critical components identified in 25.571 (e.g. wing, empennage, control surfaces fuselage, engine mounting landing gear).
- Any single failure in any flutter damping system.

where MD is the dive Mach number and VD is the dive speed. Normally, compliance with the standards must be demonstrated by analysis, wind tunnel tests, ground vibration tests, flight tests or any other means found necessary by the certification authority. Aside from the certification standards, however, an aircraft producer may have more stringent aeroelastic design requirements, such as those relating to ride quality or control effectiveness.

15.2 Design Process

As aeroelastic design requirements are intimately connected to the operation envelope of the aircraft, it is normally necessary to consider aeroelastic effects at all stages in the design process. This helps to prevent later performance reductions or costly re-designs. Consequently, a sequence of models is normally employed. These become increasingly sophisticated as the details of the configuration are specified. A typical sequence of aeroelastic analysis procedures is given below:

Pre-design stage

- Analytic modelling
- Wind tunnel testing to support modelling of new aeroelastic features

Design iteration stage

- Repeated aeroelastic calculations to verify constraints on or aeroelastically optimize the evolving configuration

Frozen design stage

- Tests of structurally scaled models and comparison with analytic structural models
- Wind tunnel tests with aeroelastically scaled models to verify analytic aerodynamic models and coupling

Prototype stage

- Ground vibration and flexibility tests to provide final validation of structural models
- Analytic calculations to prepare for flight testing
- Flight-test program

We have already discussed various levels of analytic modelling within the course. The remaining sections in this chapter will therefore concentrate on methods for determining aeroelastic characteristics experimentally.

15.3 Wind Tunnel Testing Techniques

Aeroelastic wind tunnel testing is particularly complex, due to the need to match both flow and structural dynamic characteristics at a reduced scale.

In principal an accurate representation of the flow requires the simultaneous matching of both Mach and Reynolds numbers. This is not feasible at the high-Mach and Reynolds numbers combinations at which many aeroelastic instabilities occur. If the phenomena is dominated by either viscous or compressible effects, it can be sufficient to approximate either the flight Reynolds number or Mach number. However for fully-coupled problems, such those accompanied by strong shock boundary-layer interactions, combinations of tests and modelling may be necessary.

The construction of structural models which approximate the dynamic characteristics of the full-size configuration is also not a trivial matter. Scaled skin thicknesses are usually far too small to allow use of materials and attachment methods (e.g. riveting) similar to those on the full-size aircraft. Often plastics are substituted due to their formability, but these typically result in excessive internal damping. Normally the solution is not to attempt to construct a scaled model of the structure, but instead to construct a simplified model which closely reproduces the dynamic characteristics of the real structure. Figure 15.1 shows a full model of a tilt rotor in NASA's Transonic Dynamics Tunnel, and an dynamically-matched underlying structure being prepared for wind-tunnel use. For a simple wing geometry, a dynamically-matched structure might simply match the correct mass, GJ and EI distributions as a function of spanwise position. Normally finite-element methods are used to design and check the structure, while final verification and fine-tuning might make use of vibration test equipment.

There are also problems designing supports when there is significant coupling between aircraft dynamic modes aeroelastic modes. One solution is to support the model using a system of cables designed to allow the excitation of the dynamic mode of interest, as shown in figure 15.2.

Once the configuration of the model has been specified, a careful testing procedure must still be designed to accurately measure aeroelastic phenomena

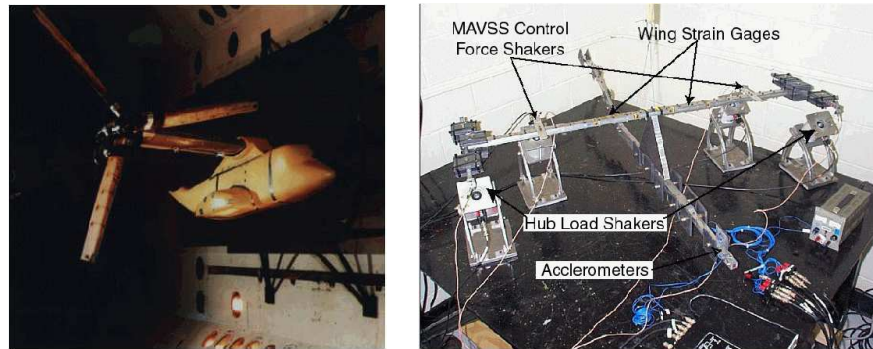


Figure 15.1: Full aeroelastic model in tunnel (left) and a typical underlying structural model (right)

near their points of instability. Normally this is accomplished by using harmonic excitation devices to provide a forced response. These include rotating masses attached to the structure, or oscillating aerodynamic vanes upstream of the model. Frequency sweeps are carried out at multiple fixed operating conditions near the point of instability. Values of damping are then estimated by examining the response characteristics, and a more precise operating condition is chosen.

Special care must be taken, however, when approaching instability points using such procedures. Aeroelastic damping is notoriously hard to extrapolate, as its behaviour can be strongly non-linear. Often expert knowledge is required, or use must be made of advanced computational models which incorporate information obtained in previous tests. As a last resort, a net is normally placed downstream to protect the tunnel from large pieces of debris if the model accidentally crosses an instability boundary.

15.4 Ground Vibration Testing

In the final stages of the design process, full size structures become available, permitting the accurate determination of dynamic characteristics. Normally this is done by ground vibration testing. A typical setup is shown in figure 15.3. The aircraft is placed on supports, and then shakers are applied at strategic points determined by existing finite-element models or previous tests (i.e. away from nodal lines). The supports can be soft if coupling with rigid-body modes is required. The design of the shaker depends on the frequencies of interest and amplitudes required for measurement. Normally mechanical shakers are used for low frequencies (1-100 Hz), electromagnetic for medium frequencies (10-1000 Hz) and acoustic for high frequencies (100-10000 Hz). Measurement is typically carried out using accelerometers, which may be mechanical or electromagnetic. Using advanced identification techniques, structural non-linearities (e.g control surface play) can also be measured. For the ground vibration testing of large

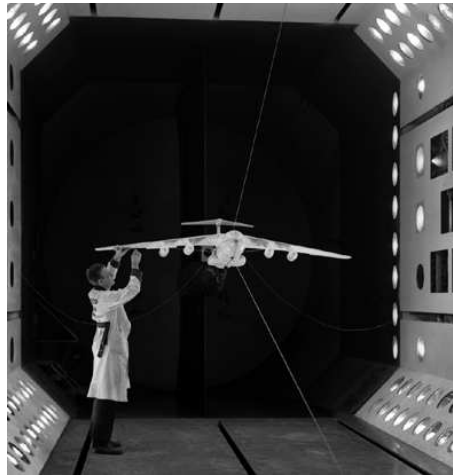


Figure 15.2: Model mounted on cables in NASA's Transonic Dynamics Tunnel

aircraft, as shown in figure 15.4, hundreds of accelerometers may be used. When testing a high-speed aircraft, it may also be necessary to place the structure in a special enclosure to allow the heating to the conditions encountered in flight.

15.5 Flight testing

The first formal flutter tests were carried out in Germany in the mid 1930's by Von Schlippe. His strategy, which is still in use today, was to excite aeroelastic modes of the aircraft in flight and measure the amplitude of the response while gradually increasing the airspeed. An example result is shown in figure 15.5. It can be seen that the flutter condition was quite closely approached in this case, although fortunately the aircraft and crew survived. In general Von Schlippe's technique requires reliable excitation and measurement techniques, and suffers from the complexity inherent in the extrapolation of damping characteristics. In several cases, test aircraft have been lost due to deficiencies one or all of these areas. At the end of the 1958 flight flutter test symposium it was stated that: "It is hoped that ... tests will be considerably less hazardous than they are today" Considerable improvements in measurement and prediction have been made since then, but flight flutter testing remains one of the most hazardous forms of experimental work encountered in aerospace engineering.

15.5.1 Excitation and Measurement

Due to the wide range of flight and loading conditions, normally aircraft require hundreds of test points in order to comply with certification standards. As these often involve diving to achieve limit airspeeds, the tests must be of limited

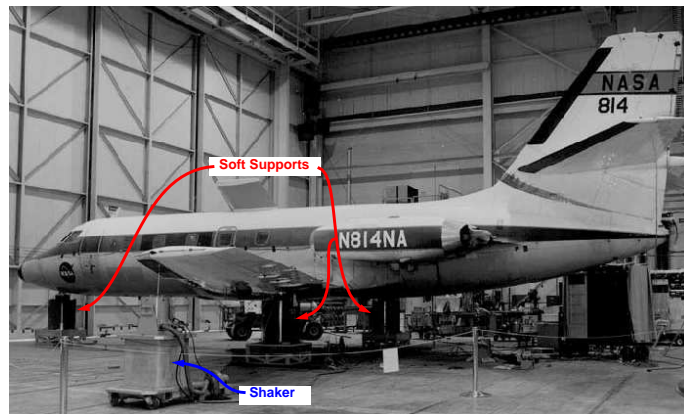


Figure 15.3: Supports and shakers for a ground vibration test

duration to prevent significant changes in test altitude. Therefore the excitation and measurement process must be as quick as possible.

The main requirement for excitation is that it has a sufficient amplitude over the frequency range of interest. Insufficient excitation can lead to both scattered results and inaccurate damping estimations. It is also important that the excitation device alter the configuration as little as possible. Consequently, several excitations techniques have developed, tailored to the phenomena under consideration:

- Pilot control pulses
 - Can provide excitation up to 10Hz
 - Simple, but inconsistent and amplitude often too low
- Oscillating control surfaces
 - Up to 50 Hz
 - Can be semi-random
 - No changes to structure or weight distribution
- Inertial shakers
 - force from rotating-mass systems quadratic in rotation speed: limited at low frequencies, excessive at high frequencies
 - heavy, and often too large to be contained within original surface (affects structural and aerodynamic representation)
 - Not used much since the 1950's, with some exceptions
- Thrusters (Single-use solid-propellant rockets)
 - Run time 15-30ms, thrust up to 4000lbs
 - lightweight
 - limited frequency range
 - difficult to time multiple burns for in or out of phase excitation



Figure 15.4: Large-scale ground vibration tests

- Aerodynamic vanes
 - Good for low frequencies
 - force varies with airspeed
 - can distort aerodynamics
- Atmospheric turbulence
 - No change to aircraft
 - Excites both symmetric and asymmetric modes simultaneously
 - Usually amplitude is too small to provide accurate damping estimate
 - Flight time lost looking for it

A comparison of the measured response levels achieved via a rotating vane and atmospheric turbulence is shown in figure 15.6. Strain gauges have been traditionally used for the measurement of in flight responses, but piezoelectric accelerometers now much more common as they are compact and light, and have good frequency response. The current trend is towards self-contained “stick-on” devices which can transmit data wirelessly to recorders on the aircraft or directly to the ground station.

15.5.2 Ground data processing and damping prediction

Significant advances in air-to-ground telemetry over the last decades have revolutionized flight flutter testing, resulting in a vastly improved capacity for the prediction of instability points.

In the 1970's the first high-speed fast Fourier transforms become possible, allowing rapid estimation of damping ratios at the last measurement point. Data

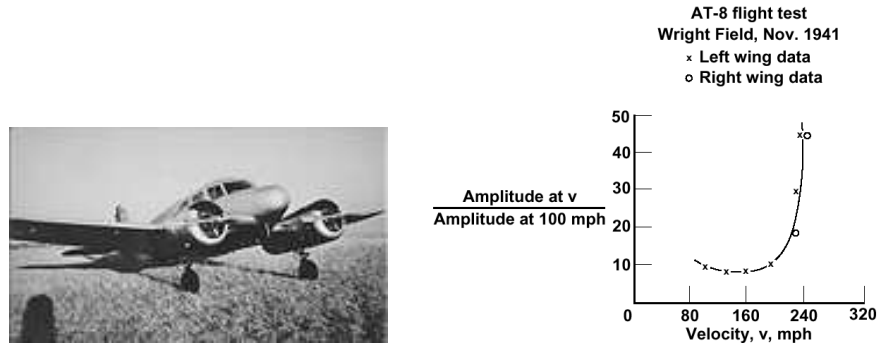
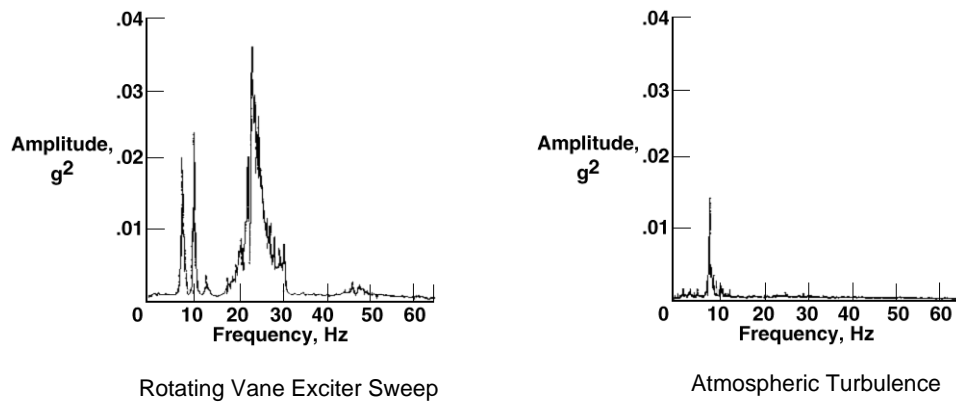


Figure 15.5: Cessna AT8 and flight test result

from range of speeds was then used to estimate the zero-damping point before the next condition was considered. This approach considerably improved safety, although testing in areas with non-linear damping trends remained risky.

Modern on-line flutter prediction methods make use of robust analysis techniques, where a model with uncertainties is constructed using complex numerical aerodynamic and structural representations. As the flight progresses, the flight data is used to conservatively identify the uncertainties in the model, thereby improving the accuracy of the flutter prediction (see figure 15.7). The result is then transmitted back to the aircraft, where it can be shown, for example, as a continuously-adjusted instrument showing the distance from the flutter point. The latter display device is referred to as a “flutterometer” (figure 15.8).



Measured F16XL wing accelerometer responses ($M=0.9$, $h=30\,000$ ft)
(taken from NASA TM -4720)

Figure 15.6: Responses to aerodynamic and atmospheric excitation

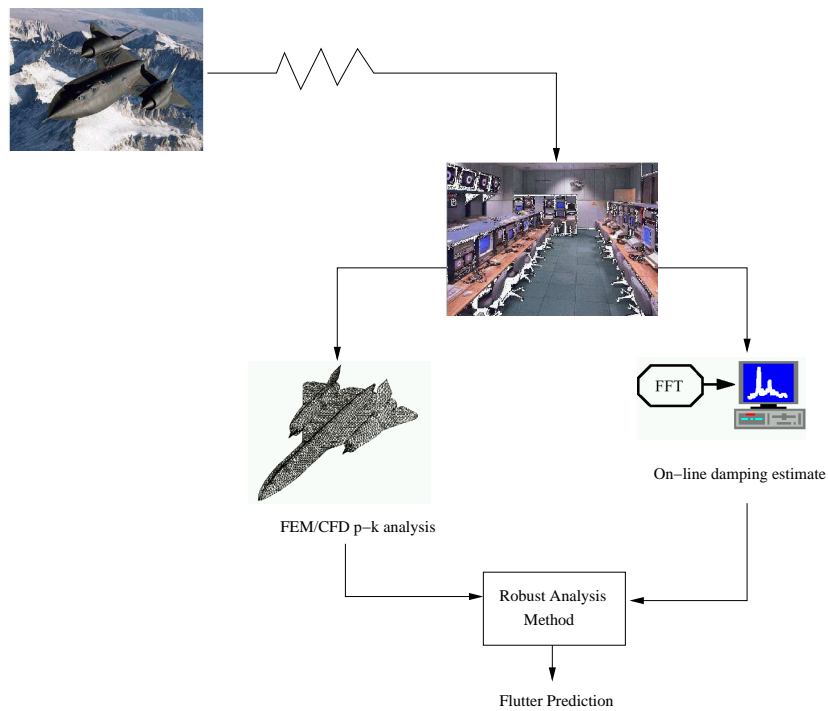


Figure 15.7: Robust analysis for improved on-line flutter prediction (From Lind, R.C, NASA TM-97-206220)

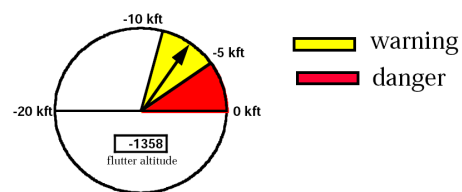


Figure 15.8: Flutterometer (From Lind, R.C, NASA TM-97-206220)